An Evaluation of Computational Fluid Dynamics for Modelling Buoyancy-Driven Displacement Ventilation

Malcolm J. Cook BSc. MSc.

This thesis is submitted to De Montfort University, Leicester, in partial fulfilment of the requirements for the degree of Doctor of Philosophy

August 1998

To Mom and Dad who have always encouraged
me and supported my work

"Only after the last tree has been cut down,
Only after the last river has been poisoned,
Only after the last fish has been caught,
Only then will you find that money cannot be eaten"

Cree Indian Prophecy

Abstract

Environmental concerns and demands for energy efficiency have prompted building designers to reconsider natural ventilation rather than mechanical ventilation and air conditioning. Natural ventilation can be brought about either by wind pressure or by buoyancy forces generated by temperature differences. This research addresses buoyancy-driven flows in a displacement ventilation regime.

Buoyancy-driven displacement ventilation occurs when thermal plumes, which form above heat sources such as occupants and electrical equipment, cause warm, buoyant air to accumulate in the upper part of a space forming a stratified layer. This layer drives a flow out of openings at high level which then draws in fresher air through low level openings. The design of such ventilation strategies must ensure that the layer of stratified air is able to drive a sufficient airflow rate and that the lower level of the stratification remains above the occupants' breathing zone.

Computer models can be used to assist with the design of naturally ventilated buildings. One such tool which has seen increased use with the advent of faster, more affordable, desk-top computers, is *Computational Fluid Dynamics (CFD)*. CFD is a detailed airflow modelling technique which solves the governing equations of air motion to give predictions of, primarily, pressure, velocity and temperature at many locations throughout the geometry under consideration. However, literature to-date points to short-comings in the capabilities of CFD for modelling buoyancy-driven flows.

The aim of this research was to evaluate the accuracy with which CFD is able to model buoyancy-driven flows. This has been done by defining three simple benchmark cases for which both analytical results and salt bath modelling measurements exist. These fundamentally different modelling techniques enable two distinct mechanisms for evaluation. The benchmarks comprise rectangular spaces with point and line sources of buoyancy (heat input) on the floor and openings to the outside air in the top and bottom. The CFD simulations were carried out using the code CFX which comprises solution and modelling techniques (such as turbulence modelling) which are typical of many commercially available CFD programs.

The program gave favourable predictions for the level of the horizontal interface between the warm and cool air, the temperature change across the interface, and the air change rates and flow patterns. Some discrepancies existed in modelling the buoyant plumes produced above the heat sources when using the standard $k-\varepsilon$ turbulence model. These were reduced when employing the more recent $k-\varepsilon$ model based on renormalisation group theory.

The work has shown that careful control of the solution process is needed when modelling buoyancy-driven flows and that care is needed when specifying the conditions at the boundaries separating internal and external air. The work offers guidance to others wishing to use the benchmarks and suggests how these techniques could be used for modelling buoyancy-driven flow regimes in real buildings.

Acknowledgements

This research was supported with funding from De Montfort University, Leicester, and was undertaken within the Environmental Computer Aided Design and Performance (ECADAP) group, and more recently the Institute of Energy and Sustainable Development (IESD).

I would like to thank my director of studies, Prof. Kevin Lomas (De Montfort University) whose support, sound guidance, and meticulous attention to detail throughout this research has been greatly appreciated. I would also like to thank my second supervisors Prof. Andrew Howarth (University of Nottingham) and Dr. Martin Crane (De Montfort University) whose complimentary backgrounds ensured a varied and balanced approach to my research. I am also indebted to Dr. Geoff Whittle (Simulation Technology) and Prof. Paul Linden (University of Cambridge and University of San Diego, California) for their enlightening discussions and for spending many hours advising on the direction of the research and later checking the accuracy of my work.

I would like to thank all of the staff at the IESD for their moral support and encouragement, and for their assistance with IT matters.

It is difficult for me to find words which adequately express my feelings of thanks towards my wife Lisa, whose incredible patience and unfailing loving support, has, without doubt, ensured the completion of this thesis.

Contents

Nomenclature

(-)	dimensionless variable
A^*	effective opening area (m^2)
Ar	Archimedes number (-)
a_u	total area of upper openings (m^2)
a_l	total area of lower openings (m^2)
B	strength of buoyancy source (m^4/s^3)
C	empirical constant in point source plumes (-)
C_1, C_2, C_3, C_μ	turbulence model constants (-)
C_d	discharge coefficient (-)
C_P	specific heat capacity (J/KgK)
c	momentum theorem constant (-)
D	empirical constant in line source plumes (-)
D_ϕ	diffusivity (Γ_ϕ/ρ), (m^2/s)
d_f	length scale for false time-steps (m)
E, E_{He}	wall function constants (-)
G'	plume buoyancy (m/s^2)
G'_H	hypothetical value of G_T at $y = H$ (m/s^2)
g	acceleration due to gravity (m/s^2)
g'	reduced gravity or buoyancy (m/s^2)
g'_h	change in buoyancy across the interface, or stratification strength (m/s^2)
H	height of space (m)
He	total enthalpy (J/Kg)
He^+	normalised enthalpy (-)
He_{ref}	enthalpy reference value (J/Kg)
He_{res}	enthalpy residual (Watts)
He_w	enthalpy at wall (J/Kg)
h	height of interface (m)
he	static enthalpy (J/Kg)

J_{He}	enthalpy flux at wall (J/m^{2}s)
k	turbulent kinetic energy (m^2/s^2)
l	length scale (m)
M	volume flux in plume (m^3/s)
P, p	pressure (Pa)
Pe	Peclet number (-)
P_w	pressure difference due to wind (Pa)
P_s	pressure difference due to stack effect (Pa)
Q	heat flux (W/m^2)
q	mass flux (Kg/s)
q_v	airflow rate (ach^{-1})
Ra	Rayleigh number (-)
Re	Reynolds number (-)
r	radial distance (m)
S_ϕ	source term in ϕ equation (varies)
T	temperature (K)
t	time (s)
t_f	false time-step (s)
u_i	velocity tensor = (u, v, w) (m/s)
u^+	normalised velocity (-)
u^{par}	velocity parallel to wall (m/s)
V	velocity scale (m/s)
v_f	velocity scale for false time-steps (m/s)
v_G	Gaussian axial plume velocity (m/s)
v_T	'Top-hat' axial plume velocity (m/s)
W	heat input (Watts)
x_i	spatial coordinate tensor = (x, y, z) (m):

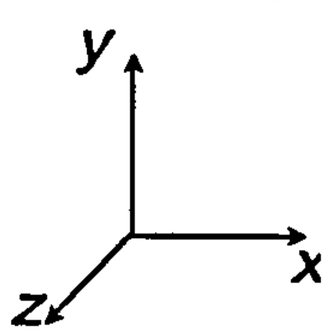

y^+	normalised distance (-)

y_0^+, y_{He}^+	wall function constants (-)
α	plume entrainment (-)
β	coefficient of expansion (K^{-1})
β_o	turbulence model constant (-)
ΔHe_h	change in enthalpy across the interface (J/Kg)
ΔT_h	change in temperature across the interface (K)
δ_{ij}	kronecka delta $= \begin{cases} 1 \text{ if } i = j \\ 0 \text{ if } i \neq j \end{cases}$ (-)
ε	dissipation of turbulent kinetic energy (m^2/s^3)
ϕ	arbitrary variable (varies)
Γ_{eff}	effective diffusivity (Kg/ms)
Γ_{He_t}	eddy diffusivity for enthalpy (Kg/ms)
Γ_ϕ	diffusion coefficient for ϕ (Kg/ms)
η_o	turbulence model constant (-)
κ	wall function constant (-)
λ	thermal conductivity (W/mK)
μ, μ_{eff}	total (effective) dynamic viscosity (Kg/ms)
μ_l	laminar viscosity (Kg/ms)
μ_t	turbulent (or eddy) viscosity (Kg/ms)
θ	azimuth angle (radians)
ρ	density (Kg/m^3)
σ_{He}	turbulent Prandtl number for enthalpy (-)
σ_k	turbulent Prandtl number for k (-)
σ_ε	turbulent Prandtl number for ε (-)
σ_{ij}	shear stress tensor (Pa)
τ	wall shear stress (Pa)
υ	kinematic viscosity (μ/ρ), (m^2/s)
ξ	normalised interface height = h / H

subscripts

Bref	buoyancy reference
Eref	enthalpy reference
ext	external (ambient)
G	Gaussian value (see Appendix B)
int	internal
o	reference value
T	'top-hat' value (see Appendix B)
L	values expressed as a quantity per metre length

superscripts

$k-\varepsilon$	value pertaining to standard $k-\varepsilon$ turbulence model
RNG	value pertaining to RNG $k-\varepsilon$ turbulence model

Glossary and Abbreviations

ach^{-1}	air changes per hour
AIVC	Air Infiltration and Ventilation Centre
BRE	Building Research Establishment
CFD	Computational Fluid Dynamics
CFDS	Computational Fluid Dynamics Services
CIBSE	Chartered Institute of Building Services Engineers
Control Volume	Discrete volumes of space in the computational domain over which the transport equations are solved
ESRU	Energy Systems Research Unit
PLEA	Passive and Low Energy Architecture

Chapter 1

Introduction

1. Introduction

1.1 Preamble

It is necessary to provide buildings with adequate ventilation to ensure both removal of stale air and the supply of fresh air for occupants. This can be provided in different ways, which include: mechanical ventilation, in which fans and ducts are used to move large volumes of air with or without heating the air; air-conditioning, in which the temperature and humidity of air, supplied via fans and ducts, is fully controlled; and natural ventilation which harnesses the naturally occurring driving forces of wind and buoyancy. It is also possible to use a hybrid approach which uses both natural forces and mechanical means (usually fans). These are known as *mixed-mode* systems.

The main disadvantages of air-conditioning are: cost, in terms of capital, running costs and maintenance; and the large amount of space required to house the necessary equipment. Furthermore, there is evidence to suggest that air-conditioning systems are more likely to cause occupant health complaints than natural or mechanical ventilation (Wilson and Hedge (1987)).

Given today's efforts to reduce energy usage and CO_2 emissions, there is an increasing trend to move away from air-conditioned buildings. Consequently, many architects and building designers have turned their attention towards naturally ventilated or mixed mode techniques. Although such buildings use innovative techniques, many have been completed with a high degree of success (Jones et al. (1998)).

Due to the non-predeterminate nature of natural ventilation systems, much care is needed at the design stage to ensure that the ventilation strategy will perform successfully under foreseeable climatic and occupancy scenarios. In particular that acceptable air change rates will be obtained. Predictions of such parameters are much easier in a mechanically-driven system since the designer knows, to a high degree of accuracy, the volume flow rates produced by the various

components that make up the system. When designing natural ventilation strategies however, the only way to predict the flow rates is by means of either a physical or mathematical model. This thesis concerns models of both types.

Physical modelling has been carried out successfully by researchers at Cambridge University (e.g. Lane-Serff et al. (1991)) using the salt bath modelling technique whereby perspex models of a building are inverted and submerged in a tank of fresh water with brine solution used to represent temperature differences. The brine is dyed to enable flow visualisation. This technique enables air change rates and temperature differences to be predicted. However, it does not lend itself well to addressing 'what if' type of questions.

Since the advent of more powerful, affordable, desk-top computers, another tool has become accessible to designers - *Computational Fluid Dynamics (CFD).* This technique considers the airflow in a space by dividing the space into small *cells* and solving the equations which govern the airflow and temperature distribution in each one. This offers the immediate advantage over the salt bath modelling approach of being able to provide information about the flow at many positions throughout the domain of interest. It also enables changes to the geometry and operating conditions to be made more easily, offering an ideal tool for investigating many ventilation options early in the design process.

References cited in the thesis point to limitations in the CFD technique for reliably modelling buoyancy-driven flows. These can be attributed to: the small forces responsible for bringing about buoyancy-driven flows in buildings which can cause instabilities in the solution process; knowledge still lacking in how to accurately model turbulence; and the best way of solving the set of governing equations. Consequently there is still much scope for validation and improvement of CFD codes in the field of buoyancy-driven flows.

1.2 Aims of the Research

The main aims of the research were as follows:

- to evaluate the accuracy of CFD for modelling buoyancy-driven displacement ventilation flows by considering the flows in simple geometries and comparing the results with experimental and analytical predictions of bulk airflow patterns, stratification, and vertical temperature gradients; and
- to provide guidance on the use and reliability of CFD techniques for modelling buoyancy-driven flows.

This thesis is intended to make a significant contribution to the detailed evaluation of CFD applied to buoyancy-driven displacement ventilation. It is intended that the techniques adopted for obtaining the results will be useful to others wishing to model similar flows, and that some of the aspects of CFD responsible for inaccuracies and modelling short-comings will be identified, thereby highlighting areas for improvements in CFD code development or where further research is needed.

1.3 Research Methodology and Thesis Content

After selecting a suitable CFD code for use in this research, it was applied to buoyancy-driven flows in simple (easily defined), idealistic spaces. The predictions were compared with the results obtained using the salt bath modelling technique and the analytical model for that particular flow (both due to Linden et al. (1990)). Both of these modelling techniques are fundamentally different, thereby offering two distinct mechanisms for validation.

In Chapter 2 the motivation for this research is presented followed by a summary of the various techniques available for modelling airflows in buildings. A review of the literature dealing with the application of CFD to airflows in buildings, with emphasis on buoyancy-driven flows, is then presented. An explanation of how a suitable CFD package was selected is given in Appendix A.

Chapter 3 presents the analytical predictions and salt bath modelling of buoyancy-driven displacement ventilation with which the CFD results are to be compared.

Since these flows are driven by buoyant plumes, much of the chapter is devoted to the theory of their behaviour.

Chapter 4 describes the mathematical models of the CFD code used in this research, namely: mass, momentum and heat transfer; buoyancy effects; turbulence modelling; and boundary conditions. The solution techniques and algorithms used to solve the equations presented in this chapter are given in Appendix D.

The results of the inter-model comparisons are given in chapters 5, 6 and 7. Each chapter defines a separate *benchmark case*: **Benchmark 1** - 2D modelling; **Benchmark 2** - 3D modelling of a line source; and **Benchmark 3** - 3D modelling of a point source.

To condense the findings presented in the three results chapters, Chapter 8 is given over to a discussion of the important findings. This is done by offering guidance on how to model the three benchmarks and the accuracy that can be expected from the results, followed by suggestions as to how this might affect CFD modelling of airflows in more complex (real) spaces. In doing this it also suggests areas of research that would benefit from further work. The conclusions of the work, drawn mainly from Chapter 8, are then given in Chapter 9.

References cited throughout the thesis are provided immediately after Chapter 9, followed by a bibliography comprising all publications by the author attained during the course of this research.

Chapter 2

Natural Ventilation and Computational Fluid Dynamics

2. Natural Ventilation and Computational Fluid Dynamics

2.1 Preamble

This chapter explains the motivation for the research by considering the evolution of natural ventilation in temperate/cool climates. Having established the birth of naturally ventilated buildings in a modern context, details of how the airflow in such buildings can be modelled are given.

The chapter begins by outlining the need for ventilation. The use and development of ventilation systems through history, with an emphasis on natural ventilation strategies driven by buoyancy, is given in the next two sections. The following section presents the various methods available for modelling natural ventilation and outlines the advantages and disadvantages of each. A final section then reviews the use of computational fluid dynamics (CFD) for modelling airflows in buildings, paying particular attention to buoyancy-driven flows.

2.2 The Need for Ventilation

In today's technological society, the average person spends more than 90% of their time indoors (Awbi (1991)). It is therefore imperative, for acceptable human performance and well-being, that comfortable environments are maintained. Human comfort involves many parameters which include adequate fresh air provision (and exhaust of stale air) and maintenance of satisfactory temperatures.

Air exchange is necessary to remove stale air and odours, dilute the products of combustion (and respiration), remove harmful chemicals, and combat excess heat. Necessary ventilation rates vary according to the usage of a space, and there is legislation which governs minimum fresh air requirements. Recommendations for minimum fresh air supply rates are given in volume A of the

CIBSE Guide (1986). For example, in cellular offices, average residences and most dance halls, the recommendation is for a minimum fresh air supply rate of 12 litres per second per person.

2.3 Ventilation - a Brief Historical Review

Ventilation can be brought about either by mechanical means whereby large volumes of air are moved around a building by fans, or by natural means where it is driven by wind effects on a building and by temperature differences between internal and external air.

Natural ventilation occurs in almost all dwellings whether it is consciously intended or not. The earliest form of ventilation is probably that occurring in cave dwellings whereby the effects of wind would cause 'exchange flows' at the cave entrance. This bi-directional movement of air would remove stale air and replace it with fresh air. Caves also offered a natural cooling effect due to the absorption of heat into the rock which was important during the day in very hot climates. Camp fires used for warmth during the evening and winter continued to provide ventilation in the absence of wind - the large upward buoyancy forces produced by the fire would drive air out of the cave along its soffit causing fresh air to enter and take its place. A similar phenomenon also occurs in houses with open fires where air is drawn into the room through cracks in the building envelope to replace that which is exhausted via the chimney. Of course this type of natural ventilation offers little or no control over the amount of fresh air entering the space or, more importantly, the temperature of this air. Consequently draughts can be a major problem in older houses.

Until the early 19th century very little (formal) consideration was given to the ventilation of buildings in Britain. Some of the earliest attempts to control ventilation in large buildings can be found in the House of Commons building in 1836 (see CIBSE, 1997) and the Octagon in Liverpool in 1867 (Banham 1984). These buildings used fires to drive large volumes of air upwards through

chimneys. This *thermal syphon effect* was able to 'pull' stale air out of the occupied spaces through openings placed in the ceiling, and into ducts that lead to the base of the chimney. Fresh air, which could be pre-warmed using heat from a steam boiler, was then drawn into the space through low-level openings.

The use of heat sources to drive airflow requires sufficient space for the hot air to move uninhibited. Sufficient space could not always be found, especially in complex structures comprising many rooms. Consequently, research into fan-forced ventilation, which would drive the same volumes of air through *smaller* ducts, began receiving attention. Initially powered by steam and later gas, these fans and their necessary plant were so heavy and large that the only suitable location for them was in basement areas. This raised questions over the 'roundabout and unscientific'[1] way in which air was drawn downwards into the basement over long distances from spaces high up in the building. This problem was resolved by the electrification of the 1880s which meant smaller plant sizes could be achieved, and even enabled fans to be placed in the room that was being ventilated.

During the 19th Century, the use of fans to ventilate large buildings such as The Royal Victoria Hospital, Belfast (Banham 1984) increased. Also, the large buildings necessary to house the heavy industry of the 1890s made it harder to get fresh air into the centre of the space by natural means, so again, massive ductwork was needed.

Using a ducted air system with fans it was also possible to exercise far more control over not only the distribution of air around a building, but also its temperature. Gas powered boilers were used for winter heating and methods for summer cooling were investigated. The latter initially involved placing ice in intake

[1] Banham (1984) attributes this quote to *The Building News*, June 9, 1882: 'A Note on Hospital Ventilation', p.709.

ducts. Later, the use of a refrigeration plant to cool coils was used. It soon became evident however, that this did not always bring about comfortable conditions - the higher levels of humidity that resulted were a particular problem. Fuelled by the intense desire to make buildings more healthy and comfortable (rather than more energy efficient), the concept of full air-conditioning was addressed.

The earliest fully air-conditioned building is believed to be the Milam Building in San Antonio, Texas, completed in 1928 (see Banham 1984). This comprised a large refrigeration plant in the basement with air-conditioning plant distributed at regular height intervals over the twenty-one storey building.

The availability of reliable electric lighting in the early 1900s with its lower heat output helped deeper floor plans to be realised, which could be ventilated and cooled successfully using the new air-conditioning systems. Full air-conditioning quickly became the preferred method of controlling the indoor environment in large, non-domestic buildings - it was relatively easy to control and its operation simple to understand. Tall, rectangular 'sky-scrapers' rapidly emerged (e.g. the United Nations building, New York, in 1970). The size of air-conditioning plant required in such buildings can amount to several entire floors.

In the UK, the economic boom of the 1980s saw the appearance of opulent air-conditioned buildings such as the Lloyds building and the Canary Wharf Tower, both in London. However, people had begun to complain that they were not comfortable in their artificial environments. Complaints included: nausea; eye, nose and throat irritations; headaches; tightness of the chest; and general fatigue. This lead to the term *'sick building syndrome'* (Raw et al. (1992)) and even to certain buildings being referred to as *'sick buildings'*. Amongst other parameters, sick building syndrome is often attributed to poor air quality brought about by insufficient ventilation, or poor maintenance of ducted air systems.

Recently, employers have become increasingly aware of the high costs associated with running an air-conditioned building (see BRECSU 1998 for an example of costs) and the amount of physical space required to house the equipment.

Proposals by the Department of the Environment in 1993 to reduce energy usage in buildings by limiting the use of air conditioning in large, non-domestic buildings (CIBSE, March 1993), and concern over ozone depletion, have encouraged a significant transition to more energy efficient (non air-conditioned) buildings.

2.4 Ventilation - Some Modern Practice Examples

Now that the way has been signalled for energy efficient, naturally ventilated buildings, architects and engineers have began revisiting the natural ventilation strategies of over 100 years ago, and 'reinventing' them in a modern context. The quest to introduce more natural light into buildings also offers opportunities for natural ventilation. Atrium spaces, although not usually designed with energy efficiency in mind, offer ideal circumstances in which buoyancy-driven natural ventilation can take place (Figs. 2.1 and 2.2).

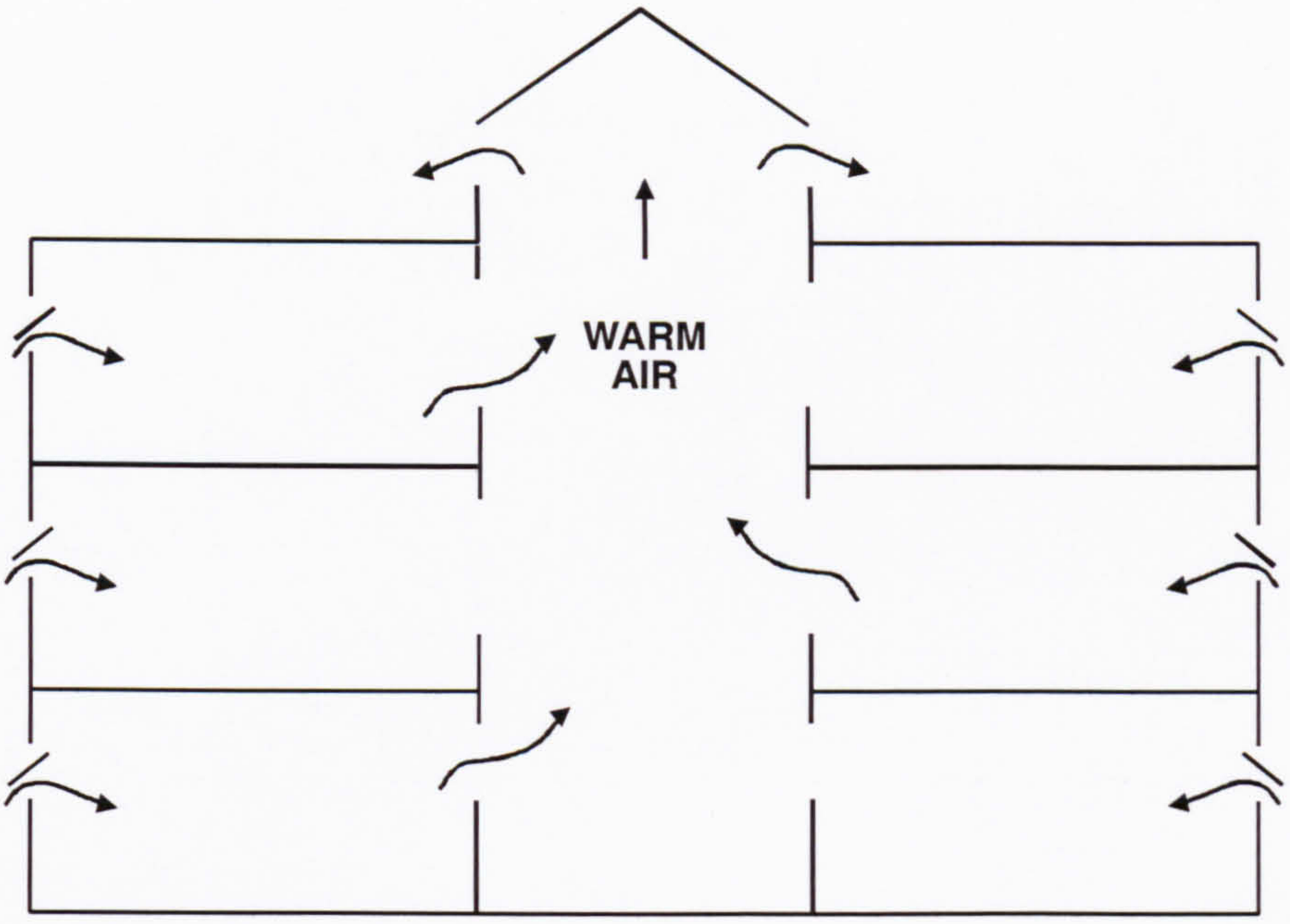

Figure 2.1 Natural ventilation by means of a central atrium space (arrows show intended direction of airflow driven by buoyancy).

Figure 2.2 The library at Anglia Polytechnic University incorporates atria to bring about stack-induced cross ventilation. (Photograph Tony Weller/Builder Group).

The recently published CIBSE Applications Manual: *"Natural Ventilation in Non-Domestic Buildings"* (1997) contains many examples of buildings that are naturally ventilated. Amongst them is the new Learning Resource Centre at Anglia Polytechnic University completed in September 1994, which comprises four storeys with two central atria. The space is cross ventilated, in winter by means of enclosed perimeter heaters which draw in outside air through trickle vents. The air then moves across the floor plate and is drawn into the atrium spaces by the induced 'stack effect' (Figs. 2.1 and 2.2). Stale air is then exhausted at the top of the atria. When no pre-warming is required, the stack effect in the atria is used to draw in outside air through open windows at the perimeter of the surrounding office spaces.

The Engineering School at De Montfort University in Leicester, designed by *Short Ford and Associates* (Fig. 2.3), is said to be "one of the most important projects of the 1990s" (CIBSE, October 1993) due to the way "it could influence a new breed of environmentally sensitive buildings". The building utilises different forms of natural ventilation, for example, shallow plan electrical laboratories are cross ventilated, but due to the deep plan nature of the central section of the building, natural ventilation is by stack effect induced by large exhaust chimneys. The two auditoria are also ventilated in this way. In the auditorium spaces, fresh ambient air enters via a plenum below raked seats (after pre-warming if necessary). A layer of warm air then forms just below the ceiling caused by the internal heat gains produced by occupants, electrical equipment, and lighting. This drives a flow out of the exhaust stacks, drawing in more fresh air below the seats as it does so. At the design stage of this building, *salt bath modelling* was used to gain confidence in the proposed natural ventilation strategy (see §2.5.4 for further details).

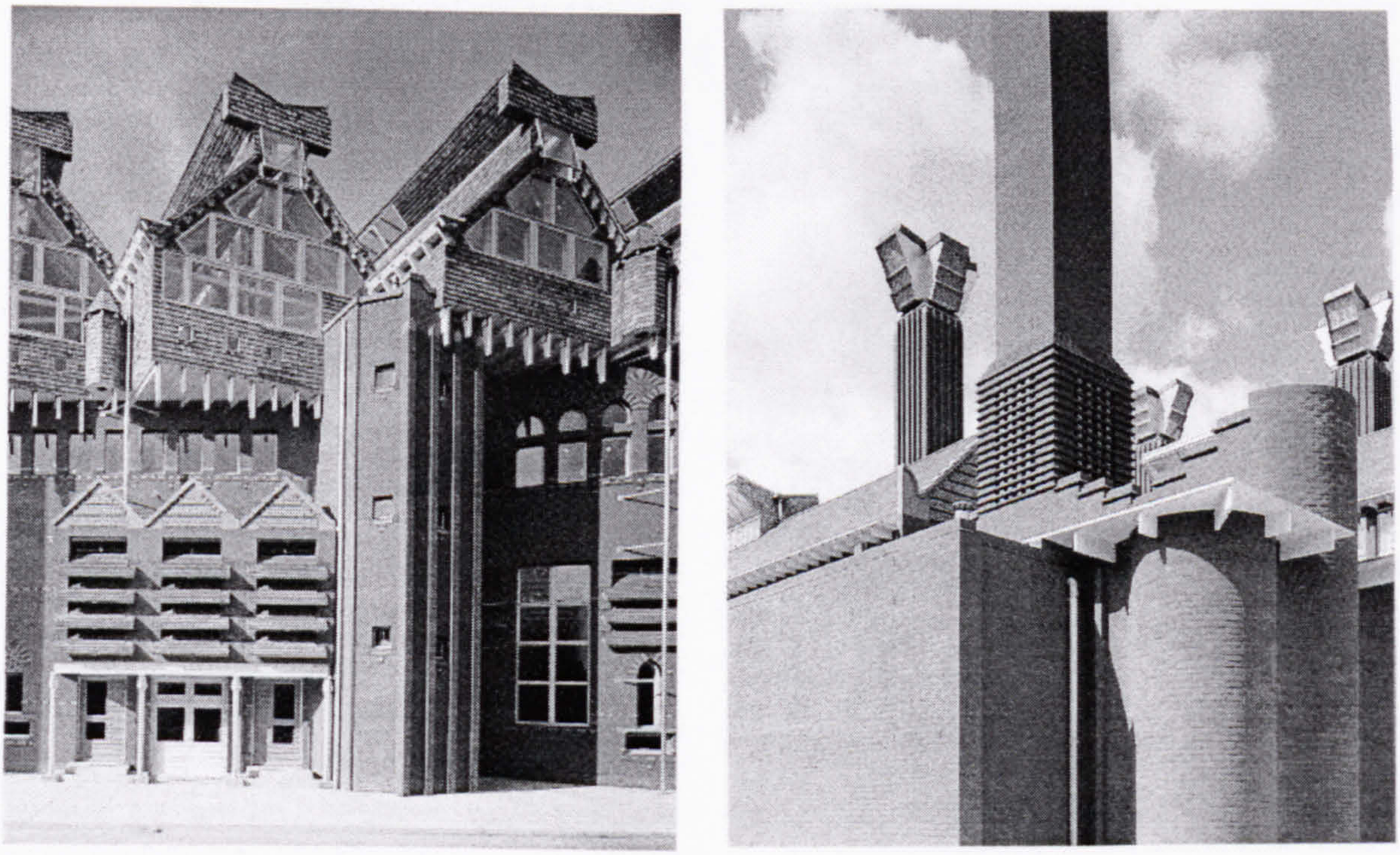

(a) (b)

Figure 2.3 The School of Engineering at De Montfort University, Leicester:
(a) south elevation showing air inlets to an auditorium, (b) exhaust stacks from the central concourse.
(Photographs: Peter Cook).

The Inland Revenue Headquarters building in Nottingham (Fig. 2.4) adopts a mixed mode ventilation strategy. Upward moving air in the stacks located on all four corners of each building draws air across the floor plates and into the stacks where it is exhausted at the top. Air passes into the building through occupant-controlled windows and perimeter inlets in the floor where the flow can be assisted by fans if necessary. Placed at the top of each circular stack is an umbrella-type 'lid' which can be raised or lowered to control the volume flow rate of air through the space.

Figure 2.4 The Inland Revenue Headquarters in Nottingham shows the corner 'turrets' used for natural ventilation. (Photograph: J. Patronis).

Since modern naturally ventilated buildings use innovative ventilation strategies which have not yet been 'tried and tested', it has become important to establish modelling tools capable of predicting the airflows and temperature distributions in these buildings.

2.5 Modelling Natural Ventilation

It is more difficult to size a natural ventilation system than it is a mechanical system, because in the latter, the designer has accurate information regarding the volume flow rates produced by items of equipment (fans, diffusers, duct combinations). In contrast, there is much more uncertainty regarding, for example, the combination of opening sizes and buoyancy-producing heat loads required to drive a certain volume flow in a naturally ventilated regime. It is therefore important that some form of model, physical or theoretical, is used to

optimise key parameters, such as opening sizes and their position, *prior* to construction. The following techniques can all be used to aid the design of naturally ventilated buildings: *Empirical Air Tightness Method; Simplified Theoretical Models; Zonal Models; Salt Bath Modelling; Wind Tunnel Testing;* and *Computational Fluid Dynamics.*

2.5.1 Empirical Air Tightness Method

This is a very approximate method for estimating the rate of air infiltration into a space. The method uses extensive measured data which has allowed average infiltration rates to be correlated with building air tightness (envelope leakage rate at an applied pressure difference of 50Pa). Based on estimates of air tightness, overall infiltration rates can then be calculated as a function of the surrounding terrain and prevailing meteorological conditions.

2.5.2 Simplified Theoretical Models

In these models a single equation is used to estimate the total airflow rate into a space, q_v, where

$$q_v = \text{ELA} \times s(h) \qquad \text{ach}^{-1}. \tag{2-1}$$

The *effective leakage area,* ELA, is a measure of the air tightness of a building at a (reference) pressure difference of 4Pa. This is extrapolated from measurements made at an applied pressure difference of 50Pa. $s(h)$ comprises factors that account for the flow into or out of a space due to temperature differences and wind. Use of this model is exemplified by Sherman (1980).

2.5.3 Zonal Models

Zonal models enable a building to be divided into several discrete *zones* connected by *flow paths.* A zone may be used to represent a room or corridor while flow paths might represent open doors, windows, and cracks (infiltration).

A set of equations to represent the mass flow q, between adjacent zones and between the interior and exterior are then defined by considering the pressure differences ΔP between the two zones. These possess the following general form:

$$q = C(\Delta P)^n \tag{2-2}$$

where C and n are constants.

Pressure differences responsible for driving mass flows through openings on a building façade are brought about by the wind:

$$P_w = \frac{\rho C_{pw} v^2}{2}, \tag{2-3}$$

where:

P_w = wind pressure on façade relative to the static pressure of the free wind;

ρ = density;

C_{pw} = pressure coefficient due to wind; and

v = wind speed,

and by temperature differences (stack effect):

$$P_s = -\rho_0 g \times 273.15 \times \Delta h \times \left(\frac{1}{T_{ext}} - \frac{1}{T_{int}} \right) \tag{2-4}$$

where:

P_s = pressure difference due to stack effect;

ρ_0 = reference density of air;

g = acceleration due to gravity;

Δh = height difference between high level and low level openings;

T_{ext} = external air temperature; and

T_{int} = internal air temperature.

This yields a total driving pressure (pressure difference) between the interior and exterior domains of $\Delta P = P_w + P_s$. This pressure difference drives a mass flow of q according to Equation (2-2). The flow problem is then solved by ensuring that the sum of all the mass fluxes between a zone and its surrounding zones equate to zero, i.e. that the total flow entering each zone is equal to that leaving. Values of pressure in each zone are then found.

Examples of multi-zone models can be found in Walton (1994) and Allard (1990). Such models can be integrated with dynamic thermal simulation programs such as ESP-r (ESRU (1996)) which can be used to predict the variation with time of internal temperatures and other building energy related parameters.

2.5.4 Salt Bath Modelling

This is an experimental technique whereby perspex models of buildings (typically at a scale between 1:20 and 1:100) are inverted and placed in a large tank of fresh water. Brine solutions are then injected into the model to represent sources of heat. Using an inverted camera and dye to colour the brine, the flow characteristics can be visualised. The justification for the use of brine and the various scaling techniques necessary to obtain quantitative full-scale data such as air change rates, are given in Chapter 3.

Salt bath modelling has been used to assist at the design stage of several naturally ventilated buildings. For example, the School of Engineering at De Montfort University, Leicester (Lane-Serff et al. (1991)), the Cable and Wireless building in Coventry (Edwards et al. (1994)) and the New Energy Efficient Office at the Building Research Establishment, Garston (BRE Compact Disc (1997)).

The salt bath technique has also been employed for validating analytical models based on plume theory which can be used to predict some of the main parameters determining buoyancy-driven flows.

2.5.5 Plume Theory

This analytical method is rarely used alone for predicting airflows in buildings and was therefore not included in the list immediately preceding section 2.5.1. However, it was an integral part of the validation process in this research and is therefore introduced here. Further details are given in Chapter 3. The method can be applied to natural ventilation of simple geometries containing clearly defined sources of buoyancy such as line or point sources. The heat sources produce rising plumes for which equations are now well established (Shmidt (1941), Morton et al. (1956), Baines and Turner (1969), and Baines et al. (1990)).

The method begins by postulating a flow pattern and then uses the plume equations for volume, momentum and buoyancy flux to establish macroscopic parameters such as positions of stratification interfaces, and temperature gradients across such interfaces. It is also possible to use the plume equations to find properties such as air change rates through the space. The most noteworthy work carried out so far is that of Linden et al. (1990) who used plume theory to determine the flow in a simple box undergoing mixing and displacement ventilation driven by temperature differences. The contents of this work relevant to this research are discussed in more detail in Chapter 3.

Since plume theory involves approximations and empiricism (see Chapter 3), all the theory derived by Linden et al. (1990) and later Cooper and Linden (1996) and Hunt and Linden (1997) is substantiated using *salt bath experiments*.

2.5.6 Wind Tunnel Testing

This technique enables models of buildings and their surroundings to be subjected to varying (and controlled) wind speeds. Pressure measurements taken over the building façade help to inform parameters of the design such as position of openings and likely air change rates. Flow visualisation is possible using smoke injection. Pressure coefficients calculated from the measurements can be used

for providing boundary conditions at openings in computer based models of internal flows such as computational fluid dynamics.

2.5.7 Computational Fluid Dynamics

This is a detailed modelling technique used primarily for calculating velocities, temperatures and pressures at numerous locations throughout a space to give a detailed picture of the complete flow field. This is achieved by dividing the space up into small *cells* to create a two or three dimensional *mesh*. For example, in a space measuring 2.5m×2.5m×2.5m, the cells might range in size from 0.05m×0.05m×0.05m to 0.3m×0.3m×0.3m. The conservation equations governing fluid flow, namely mass, momentum and energy transfer, are then solved in each cell using the values for velocity, pressure and enthalpy in the neighbouring cells as boundary conditions.

In general, any variable that satisfies a conservation equation (Eq. (2-5)) can be solved for in this way to yield its distribution throughout the space, so, for example, the water vapour content in humid air, and concentrations of brine in water, can be determined.

$$\underbrace{\frac{\partial}{\partial t}(\rho\phi)}_{\text{Transient term}}+\underbrace{\frac{\partial}{\partial x_j}(\rho u_j\phi)}_{\text{Transport of }\phi\text{ by convection}}=\underbrace{-\delta_{ij}\frac{\partial p}{\partial x_j}}_{\text{Pressure gradient}}+\underbrace{\frac{\partial}{\partial x_j}\left(\Gamma_\phi\frac{\partial\phi}{\partial x_j}\right)}_{\text{Transport of }\phi\text{ by diffusion}}+\underbrace{S_\phi}_{\text{Source of }\phi} \qquad (2\text{-}5)$$

where: ϕ = arbitrary variable;

t = time;

x_i = spatial coordinate vector;

ρ = density;

$$\delta_{ij} = \begin{cases} 1 \text{ if } i = j \\ 0 \text{ if } i \neq j \end{cases};$$

p = pressure;

Γ_ϕ = diffusion coefficient; and

S_ϕ = source term.

When all of the equations in each cell have been solved satisfactorily, the results are viewed using some form of *post-processor* - a graphical software module incorporated into most CFD packages. This enables, for example, velocities, pressures, temperatures, and brine concentrations to be represented using vectors and contours.

2.5.8 Advantages and Disadvantages of Each Modelling Technique

Table 2.1 summarises each of the modelling techniques (except plume theory) and outlines the advantages and disadvantages of each. It is seen that computational fluid dynamics, although probably one of the most expensive techniques, offers great potential for building designers. "...Used with care and with the exercise of sound engineering judgement..." (Jones and Whittle, (1992)) it can help to resolve many of the practical problems associated with naturally ventilated buildings such as: avoidance of draughts; correct sizing of openings; and adequate ventilation.

Table 2.1 Advantages and disadvantages of each modelling technique

Technique	Description	Advantages	Disadvantages
Empirical Air Tightness Method	Empirically-based calculation method for predicting building infiltration.	Quick, easy and cheap.	Very approximate. Based on empirical data. Only considers air tightness.
Simplified Theoretical Models	Simple (one-equation) method for calculating approximate airflow rates in a single zone space.	Quick, easy and cheap.	Lacks accuracy, including flow direction. No information on airflow within the space.
Zonal Models	Simple technique for calculating airflow rates between adjacent zones of a multi-zone space.	Quick, easy and cheap. More accurate than simplified theoretical models.	Still no information on airflow within spaces. Some training required.
Salt Bath Modelling	Experimental technique in which perspex models of buildings are submerged in water and brine injected to represent sources of heat.	Visually easy to appreciate. Qualitative flow pattern within a space can be realised and easily photographed. Possible to measure specific parameters.	Expensive to construct accurate models. Time consuming to make geometric changes. Not possible to measure variables at arbitrary positions without intrusive apparatus. Practical experience required. Few equipped laboratories. No heat exchange with structure.
Wind Tunnel Testing	Experimental technique in which models of buildings and their surroundings are subjected to varying (and controlled) wind speeds.	Ideally suited for modelling external airflows. Flow visualisation possible.	Expensive and time consuming. Not possible to model internal flows.
Computational Fluid Dynamics	Computational technique which primarily solves conservation equations of mass, momentum and energy to find velocities, temperatures and pressures throughout the *whole* domain.	Potentially very accurate. Able to predict spatial information giving values for variables throughout the entire flow domain. Easy to investigate changes in geometry and operating conditions. Additional physical models (e.g. radiation models and contaminant dispersion) can be added with relative ease.	Experience required to achieve optimum performance from the code. Very computationally intensive. Detailed simulations of entire buildings or long transient simulations are currently prohibitive. Some validation/development is still required, particularly in the area of turbulence modelling and buoyancy-driven flows.

2.6 Use of Computational Fluid Dynamics for Modelling Building Airflows

This section offers a brief historical review of the application of CFD to modelling airflows in buildings. It focuses mainly on the use of CFD for modelling buoyancy-driven flows, highlighting areas of weakness and thereby pointing towards the motivation for this research.

The birth place of CFD techniques in the UK is widely accepted as being Imperial College, London, where Nielsen (1974) is reported to be the first researcher to model air movement and heat transfer in buildings using computer code developed by Gosman et al. (1969). These early simulations were based on the stream-function/vorticity formulation which significantly simplifies the governing flow equations, and is applicable only in two dimensions. The simulations modelled turbulence using the standard $k-\varepsilon$ model devised by Launder and Spalding (1974) in which the transport of turbulent kinetic energy, k, and its dissipation rate, ε, are modelled. Later Nielsen used a finite difference form (see §A.2.3) of the governing equations, which included additional buoyancy terms, to model "Buoyancy-Affected Flows in Ventilated Rooms" (Nielsen et al. (1979)).

Ideriah (1980), again using finite difference techniques and a buoyant form of the $k-\varepsilon$ turbulence model, simulated flow in a square cavity for various Reynolds and Archimedes numbers[1]. The work showed that when buoyancy effects are significant (Ar > 0.04), numerical instability becomes a problem and under-relaxation techniques (control of the solution process - see §D.7.2) are required to

[1] The Reynolds number provides an indication of the relative magnitudes of inertia and viscous forces and is given by $\mathrm{Re} = \rho UL/\mu$, where U and L are characteristic velocity and length scales respectively.

The Archimedes number provides an indication of the relative magnitudes of buoyancy and inertia forces and is given by $\mathrm{Ar} = g\theta L/TU^2$, where θ, U and L are characteristic temperature difference, velocity and length scales respectively.

ensure convergence of the iterative solution strategy. Also, agreement with experimental data degraded as the flow became more buoyancy-driven rather than momentum-driven. Ideriah suggested that these discrepancies were due to the turbulence modelling technique and suggested possible improvements.

Markatos et al. (1982 and 1984) offer physical justification for not using additional terms in the ε equation when modelling buoyant flows, and obtained satisfactory agreement with experimental data for natural convection flow in a square cavity.

Many authors (e.g. Ideriah (1980), Fraikin et al. (1982), and Thompson et al. (1985)) have reported difficulties in solving buoyancy-driven flows with strong stratification. Jones (1985) explains why these difficulties occur and postulates that tight under-relaxation is necessary to solve buoyancy-driven flows. He suggests that, alternatively, such flows can be solved using the transient form of the governing flow equations and allowing a steady state to emerge. Jones derives a time-scale, $t = 1/f$ (where f is known as the Brundt-Vaisala frequency) over which buoyancy-driven flows should be resolved.

Holmes and Whittle (1987), aware of the rapid growth of CFD use for building design, warned about the potential pit-falls using the phrase "garbage in, garbage out". To help guide users of CFD programs they compiled a list of recommended steps to ensure "accurate and good quality" results. These recommendations included imposition of suitable convergence criteria and the use of experimental data for validation, or when this was not available, work to ensure that further refinement of the computational grid used for representing the flow domain would not influence the results.

With the appearance of modern naturally ventilated buildings, interest grew in the use of CFD to model these flows and the accuracy which could be obtained. Davidson (1989) used a finite difference CFD code developed by Davidson and Hedberg (1986) to model buoyancy-driven displacement ventilation in a simple space containing a single heat source. The medium used was water as this enabled easier flow visualisation in the experiments which were used to validate

the program's predictions. The results showed good qualitative agreement in that the CFD model accurately predicted the occurrence of stratification. However, discrepancies existed in the height of the interface separating the warm water above from the cooler water below. Davidson concluded that more work was needed to investigate the feasibility of using numerical techniques to model buoyancy-driven flows.

Whittle (1990) used CFD to analyse winter and summer conditions in a large atrium space. He notes that CFD codes do not deal well with strongly buoyant flows and that often long run times are needed to obtain a solution.

McGuirk and Whittle (1991) realised the need for benchmarks. They proposed a 2D benchmark in which a cool jet issues into a warm space at ceiling level. As the buoyancy of the incoming jet was increased, a degradation of convergence was observed and tighter under-relaxation was needed. In the most buoyant cases, a time-dependent flow was observed.

In 1992 Jones and Whittle reviewed the current status and capabilities of CFD for building airflow prediction. In the summary of their paper, they outlined what was needed in a CFD code to successfully model airflows in buildings and what they thought were the major short-comings and limitations of most codes. One limitation noted was turbulence modelling, and the need for faster convergence of buoyancy dominated flows.

In 1992, there was an important step forward in the use of two equation ($k-\varepsilon$) turbulence models. Yakhot, Orszag et al. (1992) used *Renormalisation Group* (RNG) theory taken from their earlier work (Yakhot and Orszag (1986)), coupled with a double expansion technique, to derive modified forms of the k and ε equations originally derived by Launder and Spalding (1974). A detailed mathematical description underlying the RNG $k-\varepsilon$ model is far too complex to be included here and is not necessary in understanding its use in this research. Briefly however, the technique enables small scale degrees of freedom, say at the atomic level, to be represented in terms of larger scale motions, thereby removing

the task of solving the motion at the atomic level. This removal and re-representation of degrees of freedom is continued iteratively until the resulting set of equations obtained can be solved on relatively coarser grids such as those used in a CFD model. Since the constants in the k and ε equations are derived from mathematical theory, the empiricism of the standard $k-\varepsilon$ model (Launder and Spalding (1974)) is removed. The model possesses high and low Reynolds number forms, which have the potential to obviate the need for wall functions in the low Reynolds number regions. It is also claimed that the RNG model handles stratification and swirl effects better than the standard $k-\varepsilon$ model. Various CFD software vendors have incorporated the RNG form of the $k-\varepsilon$ model into their codes and have reported great improvements in prediction over the standard model when compared with experimental data for certain flow types (for example, see FLUENT Inc. (1993) where flow over a backward-facing step with heat transfer is considered). Versteeg and Malalasakera (1995) note the excitement that has been brought about by the potential of the RNG $k-\varepsilon$ model, but emphasise the need for its extensive validation.

Jacobsen (1993) used the standard $k-\varepsilon$ model of Launder and Spalding (1974) to model displacement flows. He notes that the short-comings of the standard model are inherent in its eddy viscosity concept because isotropic turbulence is assumed. This implies that turbulence acts equally in all directions, (showing no preference to the direction of motion or gravity force). He also suggests that some discrepancies are due specifically to an ill-defined ε equation. Despite these short-comings he proposes that the standard $k-\varepsilon$ model is a good compromise between accuracy and the risk of numerical instabilities which is a feature of the more CPU-intensive techniques, especially turbulence models which consider the motion of individual Reynolds stresses and heat fluxes (see, for example, Murakami et al. (1992)).

Over the last few years, developers of commercial CFD codes have improved the modelling techniques used to represent turbulence. They are also continually

improving the user interface, thereby making CFD accessible to an ever wider user-base.

2.7 Selecting CFD Software

It was not the aim of this research to develop and validate a new CFD code, rather, it was to use a readily (commercially) available package, and to evaluate its ability to model buoyancy-driven displacement ventilation. The selection process undertaken is given in Appendix A, which identifies the important factors that were considered along with the elimination process that took place. Although the search criteria will change over time, and vary depending upon the intended CFD application, its underlying methodology is potentially useful. Following the search, which took place in March 1993, CFX, developed by *Computational Fluid Dynamics Services* (Atomic Energy Authority, Harwell) was selected.

2.8 Summary

This chapter has stated the need for ventilation of buildings and briefly discussed the progress of ventilation systems up to the present day. Government bodies, architects and clients are becoming increasingly aware of the importance to reduce energy usage and CO_2 emissions, resulting in an increasing number of naturally ventilated or mixed-mode buildings being constructed. It is imperative, at the design stage of such (innovative) projects, that architects and engineers can demonstrate to their clients that adequate and appropriate ventilation of the occupied spaces will be achievable.

Computational Fluid Dynamics (CFD) is potentially a very useful tool for assisting in the design of naturally ventilated buildings. However, the published literature points to limitations in the technique. Although much work is being conducted to overcome these, such as the development of new turbulence models, much validation work is still required, both to test the new modelling techniques and to establish exactly where the limitations lie, and their severity. It is hoped that the

research reported in this thesis will make a significant contribution to the evaluation of CFD techniques for modelling buoyancy-driven displacement ventilation.

Chapter 3

The Theory and Salt Bath Modelling of Buoyancy-Driven Displacement Ventilation

3. The Theory and Salt Bath Modelling of Buoyancy-Driven Displacement Ventilation

3.1 Preamble

This chapter describes buoyancy-driven displacement ventilation. The analytical work established by Linden et al. (1990) is summarised and the salt bath modelling technique which was used to verify this work is described. Fundamental to the operation of buoyancy-driven displacement ventilation are thermal plumes, so much of this chapter is devoted to plume theory.

The chapter concludes with a strategy for using the analytical and salt bath modelling work for evaluating the accuracy with which CFX is able to model buoyancy-driven displacement ventilation flows.

Displacement ventilation flows are made possible by the existence of *buoyancy sources* and it is useful to address this issue first.

3.2 Buoyancy Sources

Buoyancy is a force brought about by local density differences in a fluid subject to gravity. When a 'parcel' of fluid is *lighter* than its surroundings, the buoyancy force can be thought of as a *reduced gravity force*, g' acting *upwards* on the 'parcel' of fluid, (Eq. (3-1)).

$$g' = g\frac{\Delta\rho}{\rho_1} \tag{3-1}$$

where: g = acceleration due to gravity;

$\Delta\rho$ = difference in density between the 'parcel' of fluid being considered and that of its surrounding fluid (local density difference); and

ρ_1 = some reference density.

The density difference in Equation (3-1) can be expressed as a temperature difference, ΔT, as follows:

$$g' = g\beta\Delta T \tag{3-2}$$

where, for a perfect gas:

β = coefficient of thermal expansion $1/T_1$ for some reference temperature, T_1.

A buoyancy *source* is the origin of a density difference, e.g. the point of entry of brine into fresh water, or heat into air. In the first case, the buoyancy force acts vertically downwards (same direction as *g*) since brine is denser than fresh water, and in the second, vertically upwards, *opposing g*, hence the term *reduced gravity*. From here onwards, the reduced gravity g', will simply be referred to as the buoyancy.

The strength of a buoyancy source is called the *buoyancy flux*, *B*, and is defined as the product of the buoyancy and the volume flux, *M* (Eq. (3-3)).

$$B = Mg' \tag{3-3}$$

For a source of brine in fresh water, the buoyancy flux can simply be written as follows using Equation (3-1):

$$B = \frac{Mg\Delta\rho}{\rho_1} \tag{3-4}$$

where: M = volume flux of brine at the source; and

$\Delta\rho$ = density difference between incoming brine and the (ambient) fresh water.

The source strength due to a heat input of *W* watts in air, is derived as follows:

$$W = qC_p\Delta T = \rho MC_p\Delta T \tag{3-5}$$

where: q = mass flux induced by source;

C_p = specific heat capacity; and

ΔT = temperature difference produced by the heat source.

Substituting Equation (3-2) into Equation (3-3), and using Equation (3-5) to eliminate ΔT, yields

$$B = \frac{g\beta W}{\rho C_P}. \tag{3-6}$$

The theory in this chapter, and the CFD simulations that follow, neglect radiation and model convection heat transfer only. Consequently, all of the energy input specified at the heat source is used in the formation of a buoyant plume.

3.3 Qualitative Description of Buoyancy-Driven Displacement Ventilation

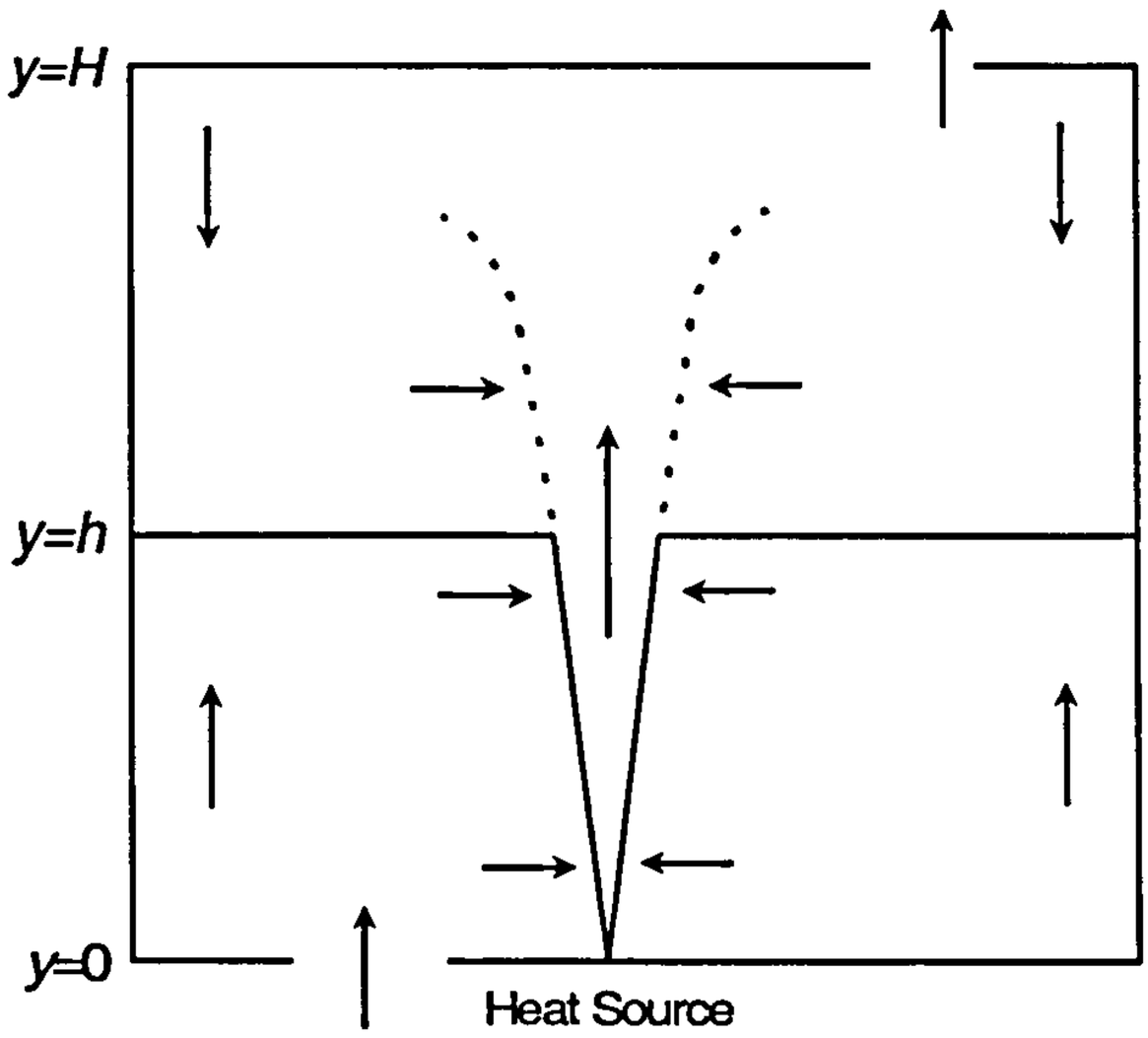

Figure 3.1 Steady displacement flow in a space containing a source of constant heat injection, after Linden et al. (1990), (arrows show the direction of air movement).

Consider displacement ventilation of the space in Figure 3.1 driven by a point source of buoyancy in the centre of the floor. The increased temperature caused by the heat source produces buoyancy forces in the vicinity of the source according to Equation (3-2). These upward forces cause the air in this region to

rise. This vertically moving, lighter air, entrains the surrounding (ambient) air forming a plume. The entrainment leads to a plume which widens with height as the volume flux increases and the temperature decreases. The latter effect yields a gradually decreasing buoyancy force with height. Upon reaching the top of the space, some of the air is recirculated. The plume, therefore, begins to entrain some of this lighter-than-ambient air and so becomes lighter than if it were entraining the ambient air. A layer of warm, buoyant air forms in the upper region of the space. This drives a flow through the upper openings since the hydrostatic pressure difference between the top and the bottom of the layer is smaller inside the space than between the same heights outside the space. A *stable stratification* develops (Fig. 3.1) in which an interface forms at height $y = h$ separating the warmer, buoyant air above it from the cooler (ambient) air below.

Note that the flow direction outside the plume, both above and below the interface, is always *towards* the plume. Even along the interface there is flow towards the rising plume. It will be shown later that above the interface, the plume is no longer driven by density differences but is purely a momentum jet.

Linden et al. (1990) have shown through their experiments (§3.6) that the steady state in Figure 3.1 is very robust. If temporary changes are made to the driving conditions, and the interface at $y = h$ moves, the original flow pattern (and value of h) is recovered upon returning to the previous set of conditions. So the flow regime is reproducible (and predictable) for a given set of operating conditions.

In order to describe the displacement flow (i.e. the interface height and the change in buoyancy across the interface), it is necessary to quantify the parameters of the plume which are responsible for bringing about the flow.

3.4 Governing Equations for a Plume Emanating from a Point Source of Buoyancy

The basic equations of plume theory were presented by Morton et al. (1956). Three main assumptions were made:

i. the rate of inflow of fluid into the plume at a given height is proportional to the vertical velocity on the axis of the plume at that height;
ii. the mean velocity profiles and mean buoyancy profiles in the plume are similar at all heights; and
iii. the fluids are incompressible and do not change volume on mixing, and the largest local variations in density are small compared to some reference density.

The last assumption enables the use of the *Boussinesq approximation* in which the density variations in the inertia terms of the governing Equations of motion are neglected, but those in the buoyancy force term are retained, where they are of primary importance. (See chapter 1 of Turner (1973) for further details).

It has been shown (Rouse et al. (1952)) that the measured velocity and buoyancy profiles of a plume can be represented using Gaussian profiles thus:

$$v(y,r) = v(y)e^{-r^2/b_G^2} \tag{3-7}$$

and

$$G'(y,r) = G'(y)e^{-r^2/\lambda^2 b_G^2} \tag{3-8}$$

where: v = vertical velocity in plume;

y = height above the source (m);

r = radial distance from the plume axis;

b_G = Gaussian plume width;

G' = buoyancy in the plume; and

λ = ratio between the widths of the Gaussian buoyancy profile and the Gaussian velocity profile.

Uncertainties exist in the value of the empirical constant λ. Rouse et al. (1952) found a value of 1.16 while Kofoed (1991) established a value just below 1). A value of 1 will be used throughout this work.

For mathematical ease, *'top-hat'* profiles can be used to represent their Gaussian counterparts (assumption (ii) above). To do this it is necessary to define the dimensions of the 'top-hat' such that both profiles give the same total momentum, volume and buoyancy fluxes. This mathematical analysis is presented in Appendix B.1.

In Figure 3.2, b_G is the radial distance from the plume axis to the point at which the velocity has fallen to 1/e of its axial value. It determines the shape of the Gaussian plume profile and is used as a characteristic width for the plume. The rate of increase of b_G with height provides a measure of the rate of entrainment, α_G, into the plume. α_G is the proportionality constant relating the inflow of fluid at the edge of the plume (at $r = b_G$) to the vertical velocity on the plume axis (assumption (i) above) (see Eq. (3-9)).

$$u_G(y = y_1) = \alpha_G v_G(y = y_1) \tag{3-9}$$

where: u_G = velocity towards the plume axis at a distance of $x = b_G$ from the axis and a height y_1 above the source;

v_G = velocity on the plume axis at a height y_1 above the source.

When using 'top-hat' profiles, the associated entrainment α_T occurs at $r = b_T$ (Fig. 3.2) and is related to the 'top-hat' velocity v_T. α_T is related to its Gaussian counterpart by the expression given by Jin (1993):

$$\alpha_T = \sqrt{2}\alpha_G \tag{3-10}$$

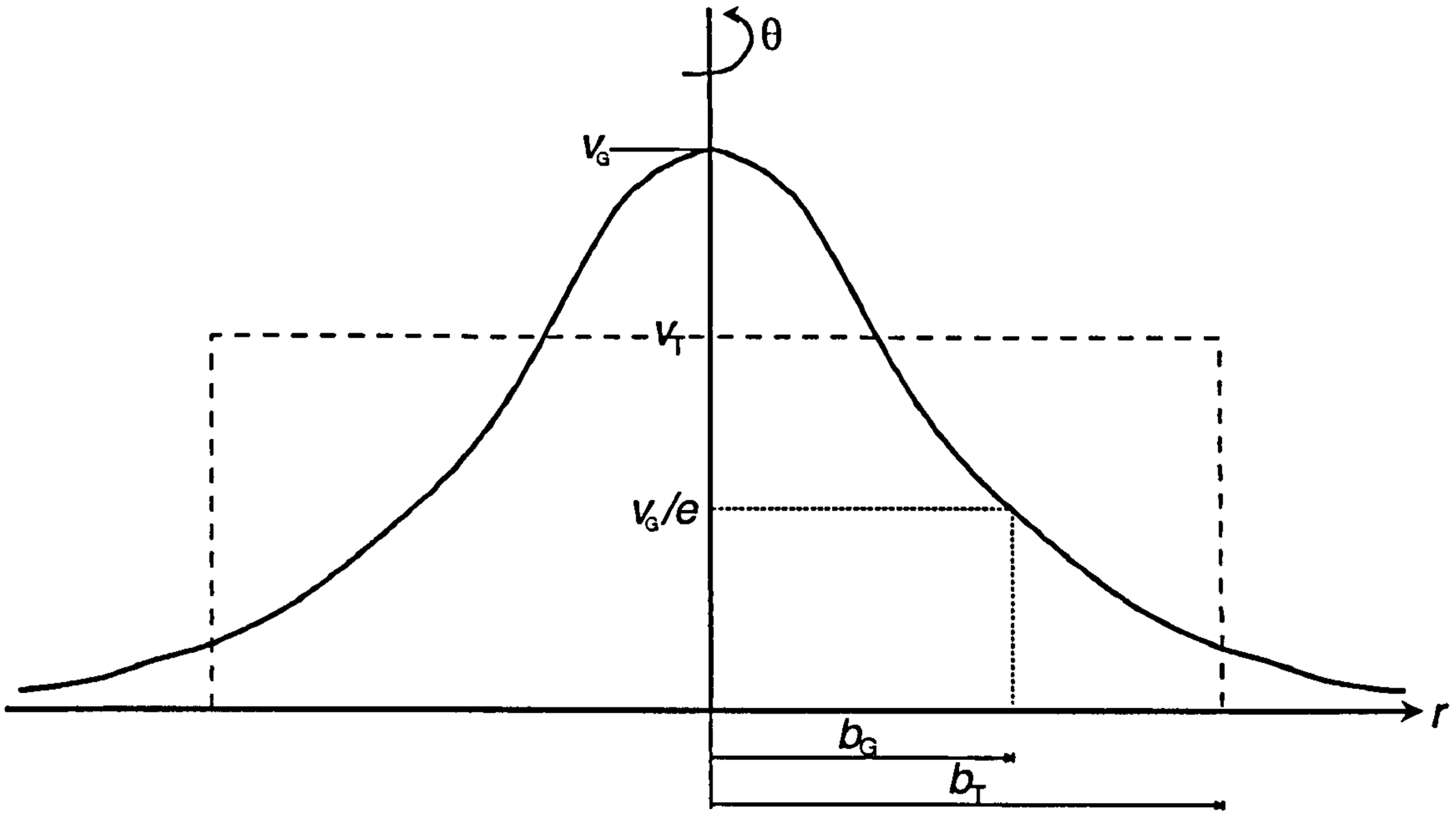

Figure 3.2. Cross section of an axi-symmetric plume comparing Gaussian and 'top-hat' profiles.

Great difficulties exist in measuring the empirical constant α_G (Morton et al. (1956) found $\alpha_G = 0.093$, Rouse et al. (1952) measured $\alpha_G = 0.083$ and Baines and Turner (1969) used $\alpha_G = 0.1$). Linden et al. (1990) used a value of $\alpha_T = 0.1$ (pre-supposing a value of $\alpha_G = 0.07$), which is the value used throughout this work.

Using the three assumptions above, Morton et al. (1956) derived the governing equations for a plume in a large body of stationary, *unstratified*, ambient fluid by considering conservation of volume, momentum and buoyancy. The resulting equations for a rising plume emanating from a *point source* of buoyancy can be written as follows:

$$b_T = \frac{6}{5}\alpha_T y \tag{3-11}$$

$$v_T = \frac{5}{6\alpha_T}\left(\frac{9}{10}\alpha_T \frac{B}{\pi}\right)^{1/3} y^{-1/3} \tag{3-12}$$

$$G'_T = \frac{5}{6\alpha_T}\frac{B}{\pi}\left(\frac{9}{10}\alpha_T\frac{B}{\pi}\right)^{-1/3} y^{-5/3} \tag{3-13}$$

where B is the source strength and y is the height above the source. The variables b_T, v_T and G'_T are given by their Gaussian (real) counterparts as shown in Appendix B.1.

The plume properties required in generating a theory for displacement ventilation are the volume flux, $M(y,B)$, and the buoyancy, $G'_T(y,B)$. These can be extracted from equations (3-11) - (3-13) to give:

$$M(y,B) = C\left(By^5\right)^{1/3} \tag{3-14}$$

$$G'_T(y,B) = \frac{\left(B^2y^{-5}\right)^{1/3}}{C} \tag{3-15}$$

where $C = \frac{6}{5}\alpha_T\left(\frac{9}{10}\alpha_T\right)^{1/3}\pi^{2/3}$.

The buoyancy flux, B, in Equations (3-14) and (3-15) is given by Equation (3-3) as follows:

$$B = G'_T(y,B)M(y,B). \tag{3-16}$$

This product is *constant* at all heights in the plume and is equal to the strength of the source. Recall that $G'(y,B)$ decreases with height due to the entrainment of dense fluid, and $M(y,B)$ increases.

3.5 Quantitative Description of Buoyancy-Driven Displacement Ventilation

3.5.1 Flow from a Point Source of Buoyancy

Displacement ventilation flows are defined by deriving equations for the interface height, h, and buoyancy change across the interface, g'_h, also referred to as the stratification strength.

The fluid flow in Figure 3.1 is assumed to be incompressible, so the volume flux of fluid entering the space is equal to that leaving, F, say. Since the only vertical motion at the interface is in the plume, F is equal to the volume flux of fluid in the plume at the interface height:

$$F = M(y = h, B). \tag{3-17}$$

Using Bernoulli's theorem (see chapter 3 of Batchelor (1974)), the flux through the space is found to be

$$F = A^{*}\left(g'(H-h)\right)^{1/2} \tag{3-18}$$

where A^{*} is an *effective area* of the openings given by

$$A^{*} = \frac{a_u a_l}{\left(1/2\left(a_u^2/c + a_l^2\right)\right)^{1/2}} \tag{3-19}$$

where: a_u = total area of upper openings[1];

a_l = total area of lower openings[1]; and

c = constant in the momentum theorem.

[1] Upper openings are assumed to be *above* the interface and lower openings *below*. The theory holds for openings in the sides as well as in the top and bottom of the space, however, openings close to the interface may result in *exchange* flows (flow both in *and* out). All cases presented in this work have horizontal openings in the top and bottom, as did most of the experimental boxes of Linden et al. (1990).

The constant c results from the momentum theorem (see chapter 5 of Batchelor (1974)), and is used to account for the sudden expansion, and therefore loss of pressure head, as the fluid enters the space. c lies between 0.5 for a sharp expansion, and 1 for a perfectly smooth expansion. $c=1$ was used in the work of Linden et al. (1990).

It is interesting to note that A^* depends primarily on the *smaller* of a_u and a_l. Thus, increasing the size of the openings at one level once they are larger than those at the other level, produces little extra flow.

The same argument used to obtain Eq. (3-17) can be used to give the following expression relating buoyancy fluxes:

$$g'_u F = G'_T(h,B)M(h,B)$$

$$\Rightarrow \quad g'_u = G'_T(h,B) \tag{3-20}$$

where $g'_u = g'(y=H)$, the buoyancy at the upper opening.

Therefore, g' has the same value above the interface both inside *and* outside the plume. The plume is therefore a *momentum jet* above the interface level. The reduced gravity throughout the whole space, except in the plume below the interface, is therefore given by:

$$g'(y) = \begin{cases} G'_T(h,B) & h \le y \le H \\ 0 & 0 \le y < h \end{cases}. \tag{3-21}$$

Note that $g'(y)$ for $0 \le y < h$ has been set to zero as there are no buoyancy sources producing density differences in the region outside the plume below the interface. From equations (3-21) and (3-15), the value of g' above the interface, g'_h, can be written as

$$g'_h = g'(h \le y \le H) = \frac{B^{2/3}}{Ch^{5/3}}. \tag{3-22}$$

Using equations (3-14) and (3-18), Equation (3-17) can be written as

$$A^{*}\left(g'(H-h)\right)^{1/2} = CB^{1/3}h^{5/3}$$

which can be expressed as follows using $\xi = h/H$ and $g' = G'_T(y=h,B)$:

$$\frac{A^{*}}{H^2} = C^{3/2}\left(\frac{\xi^5}{1-\xi}\right)^{1/2} . \qquad (3\text{-}23)$$

This equation illustrates the important aspect of the theory of buoyancy-driven displacement ventilation, that *the interface height does not depend on the source strength* (or floor area) as might be expected. It depends only on the height of the space, the sizes of the openings, and plume entrainment. The buoyancy change across the interface can be usefully normalised using G'_H, the (hypothetical) value of the plume buoyancy at $y = H$, giving

$$\frac{g'_h}{G'_H} = \left(\frac{H}{h}\right)^{5/3} . \qquad (3\text{-}24)$$

Equations (3-21) and (3-23) are the governing equations which define a displacement ventilation flow produced by a single point source of buoyancy in an unstratified fluid.

3.5.2 Flow from a Line Source of Buoyancy

The mathematical analysis of a plume produced by an infinite line source of buoyancy was not covered by either Morton et al. (1956) or Linden et al. (1990), so it is presented here in Appendix B.2.

The governing equations resulting from this theory ((B-27), (B-29) and (B-30)) can be used to give the following expressions for the volume flux *per unit length*, $M_L(y,B_L)$ and reduced gravity, $G'(y,B_L)$ in a line plume:

$$M_L(y,B_L) = DB_L^{1/3}y \qquad (3\text{-}25)$$

$$G'_T(y,B_L)=\frac{B_L^{2/3}}{yD} \tag{3-26}$$

where $B_L(=M_L G'_T)$ is the buoyancy flux *per unit length at the source*, and $D=(2\alpha_T)^{2/3}$.

Equating volume and buoyancy fluxes as in §3.5.1, the following governing equations for displacement ventilation flow in a space containing a line source of buoyancy in an unstratified fluid are found:

$$\frac{A_L^{\bullet}}{H}=D^{3/2}\left(\frac{\xi^3}{1-\xi}\right)^{1/2} \tag{3-27}$$

$$g'_h=g'(h\le y\le H)=G'_T(y=h,B_L)=\frac{B_L^{2/3}}{hD}. \tag{3-28}$$

Again, $g'(0\le y<h)=0$.

Analogously with M_L and B_L, the variables a_u, a_l and $A_L^{\bullet}$ are all specified *per unit length* of the source.

Normalisation of the buoyancy change across the interface yields

$$\frac{g'_h}{G'_H}=\frac{H}{h}. \tag{3-29}$$

3.6 Salt Bath Modelling

Linden et al. (1990) verified their theory for point and line sources by carrying out *salt bath experiments*. This involved submerging small perspex boxes (typically $0.3\text{m}\times0.25\text{m}\times0.2\text{m}$), with various sized holes in the top and bottom, into a large tank ($0.6\text{m}\times0.6\text{m}\times13\text{m}$) of fresh water. Buoyancy forces were produced by introducing brine into the box. Since brine is denser than water, the buoyancy forces acts downwards, so the perspex models were inverted to enable

a flow to be driven through the space. Using dye to colour the brine, it was the intention that this configuration would produce an inverted image of what happens when a heat source drives a flow in air. The large volume of ambient fluid meant that its density could be assumed to be constant throughout the experiment.

To ensure consistency between the discussions of air and brine flows, *lower openings* will be referred to as those on the same level as the source, and *upper openings* as those on the opposite side of the box. Similarly, the floor of the space will be used to refer to the plane containing the source, and 'below the interface' will be used to indicate the region between the interface and the floor, etc.

Linden et al. (1990) assumed that the volume flux of brine emitted by the source was small compared with that in the plume, so that the flow was being driven largely by buoyancy, not a source of momentum. Typical values used in the experiments for the volume and buoyancy fluxes at the source, were $2\times10^{-5}\,m^3/s$ and $1\times10^{-5}\,m^4/s^3$, respectively.

Experiments were initiated by starting the flow of brine into the box, and removing plugs to form upper and lower openings. Figure 3.3 shows a set of photographs illustrating the development of the flow.

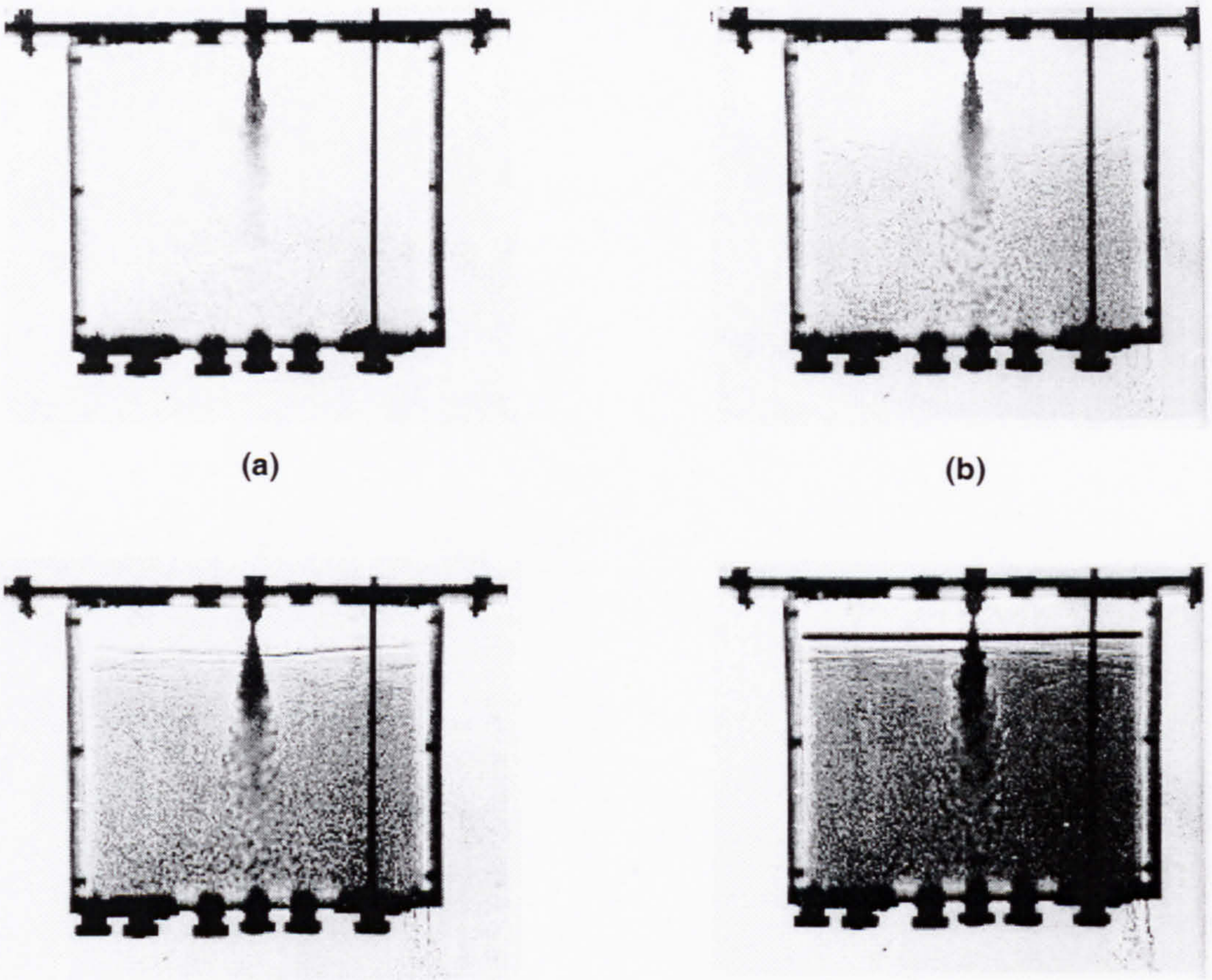

Figure 3.3 The development of steady displacement flow in a box containing a line source of brine (after Linden et al. (1990)).

Note the formation of the interface in Figure 3.3(b) and the subsequent sharpening of it, and darkening of fluid above it, as more and more (dyed) dense fluid enters the box (Figs. 3.3(c) and (d)). As predicted, a steady state develops in which there is inflow through the lower openings, entrainment into the plume in which the fluid crosses the interface separating the dense and light fluid, and outflow through the upper openings. Figure 3.4 shows a density profile measured just after photograph 3.3(d) was taken using a vertically traversing conductivity probe (+ upward traverse, × downwards traverse). Note the definition of the interface at 22cm and the uniformity of the density below 17cm. Here, 0cm corresponds to the top of the box.

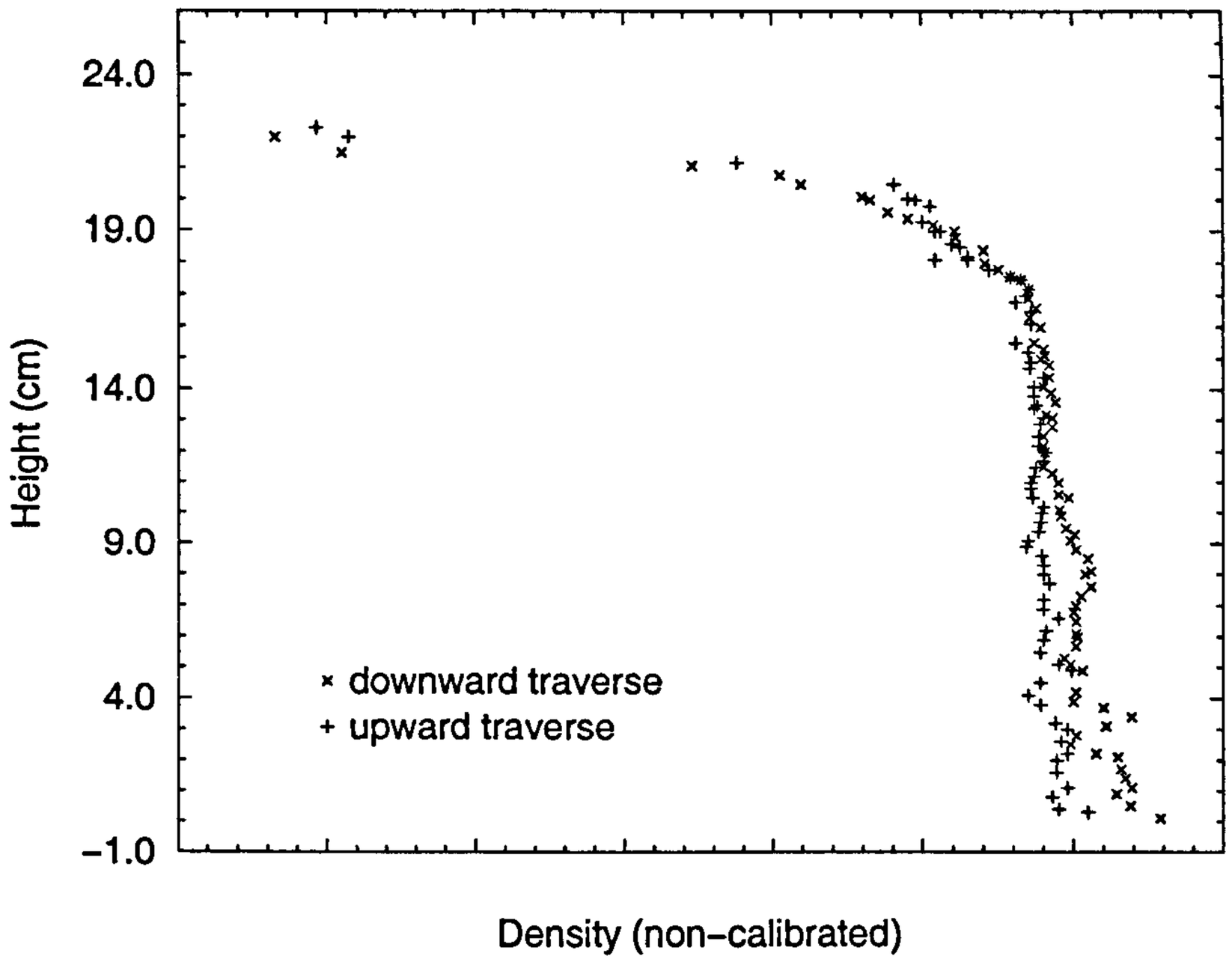

Figure 3.4 Density profile of a steady displacement flow containing a line source of brine (after Linden et al. (1990)).

Increasing or decreasing the source strength caused temporary movement of the interface as the new buoyancy and volume fluxes were resolved. The flow then resumed the steady state again with the interface height returning to its original level.

The quantitative results from the experiments are shown in Figures 3.5 - 3.8, where the measured values of the interface height, h, and $g'(h \le y \le H)$ for point and line sources are compared with the theoretical values. Note the normalisation of h with respect to the height of the space, H, and g' with respect to G'_H (the reduced gravity in the plume if it were to reach a height $y = H$). A value of $c = 1$ was used when calculating $A^{\bullet}_{(L)}$.

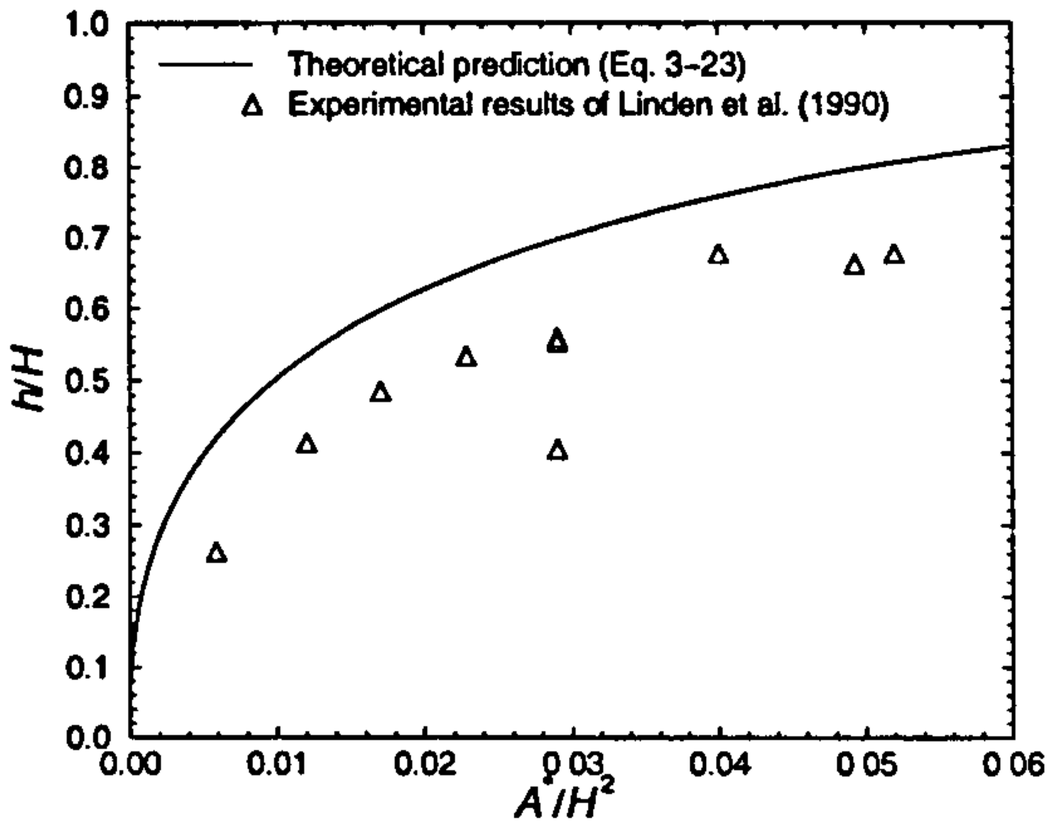

Figure 3.5 Variation of interface height with effective opening area for a displacement ventilation flow driven by a point source of buoyancy.

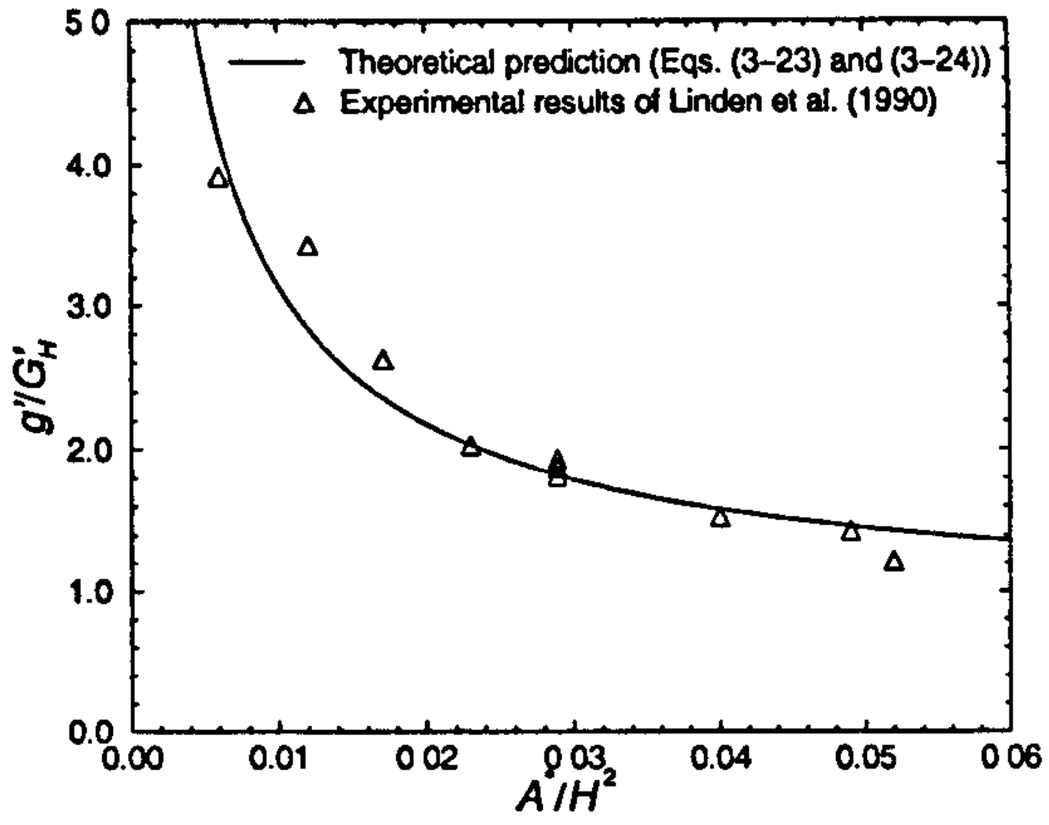

Figure 3.6 Variation of buoyancy change across the interface with effective opening area for a displacement ventilation flow driven by a point source of buoyancy.

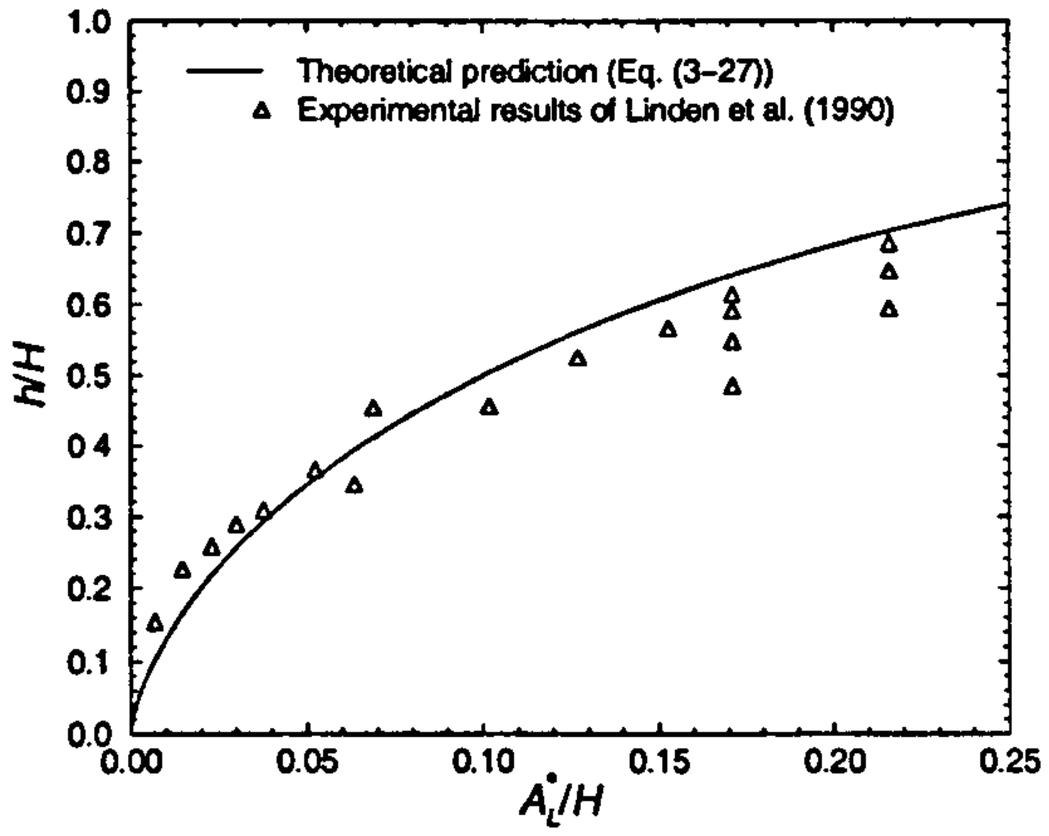

Figure 3.7 Variation of interface height with effective opening area (per unit length) for a displacement ventilation flow driven by a line source of buoyancy.

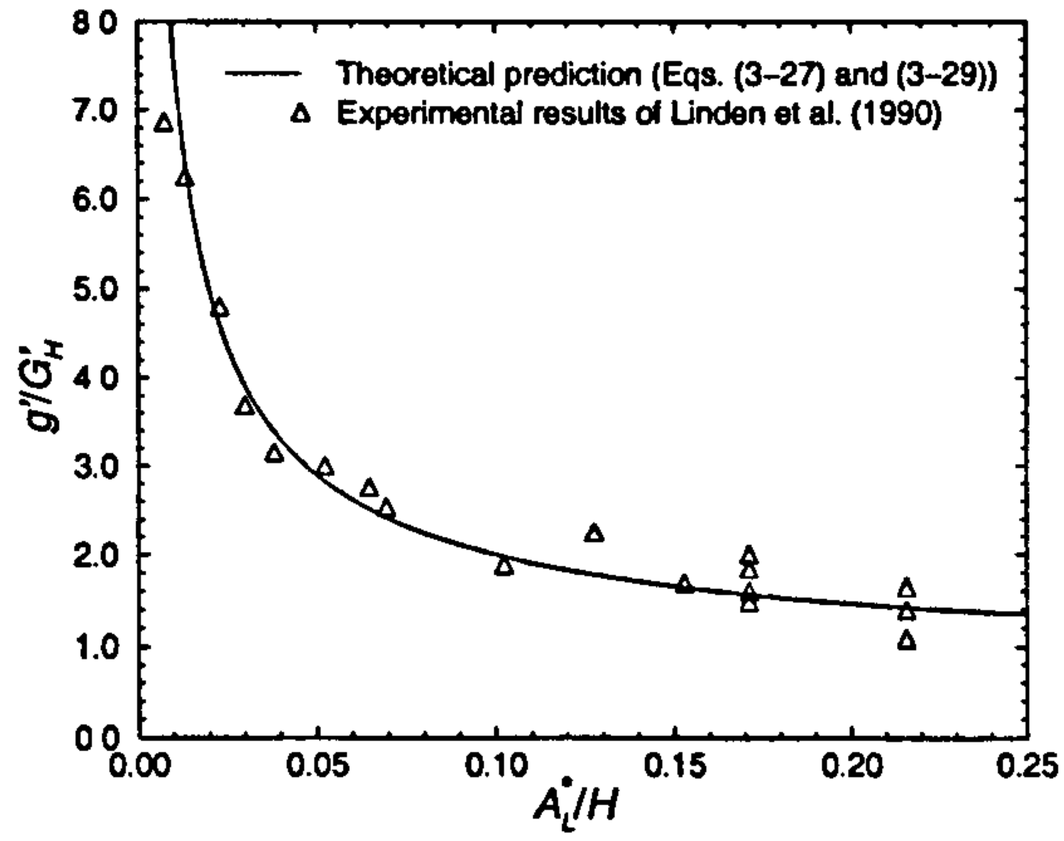

Figure 3.8 Variation of buoyancy change across the interface with effective opening area (per unit length) for a displacement ventilation flow driven by a line source of buoyancy.

Reasonable agreement was achieved in all the comparisons, except in Fig. 3.5 where the experimental results for a point source show a lower interface height than predicted. This is thought to be due largely to an inaccurate definition of A^* which will be discussed in Chapter 8.

3.7 Validity of Salt Bath Models

It is useful to address, briefly, the validity of using salt bath experiments for modelling buoyancy-driven airflows, and in particular, to consider what is necessary in applying the salt bath model results to airflows at full scale.

Flows in buildings have high Reynolds (Re) and Peclet (Pe) numbers. These are dimensionless quantities used to compare inertia forces with friction forces, and inertia forces with diffusion forces, respectively, and are given by

$$\mathrm{Re} = \frac{VL}{\upsilon} \tag{3-30}$$

and

$$\mathrm{Pe} = \frac{VL}{D_\phi} \tag{3-31}$$

where: V = typical velocity scale, (e.g. the largest velocity in the plume);

L = typical length scale, (e.g. the height of the space);

υ = (μ/ρ), kinematic viscosity of fluid; and

D_ϕ = (Γ_ϕ/ρ), diffusivity of heat in air, or brine in water.

Provided Re and Pe remain large, the flow can be regarded as independent of the molecular properties (viscosity and diffusion) of the fluid. Therefore, (small scale) salt bath models can be used to represent thermal buoyancy effects in air, since water is much denser than air and has a lower viscosity. Dynamic similarity is also enforced by the fact that brine diffuses in water much less than heat in air. Salt baths therefore produce the high Re and Pe numbers required.

The observations made from salt bath experiments can be applied to airflows at full scale using dimensional analysis as follows.

The dimensions of the buoyancy flux, $[B]$, are given by

$$[B] = L^4 T^{-3} \tag{3-32}$$

where: L = length scale; and

T = time scale.

Therefore, buoyancy fluxes in the model can be related to those at full scale by

$$\frac{B_M}{B_F} = \left(\frac{L_M}{L_F}\right)^4 \left(\frac{T_F}{T_M}\right)^3 \tag{3-33}$$

where the subscripts M and F denote model and full scale properties, respectively.

When using a model to represent a given full scale situation, L_F, B_F and L_M are known. B_M is then chosen to be some suitable value[1]. Using these four *known* quantities, the ratio T_F/T_M can be found using Equation (3-33). This then enables properties at full scale to be determined from the model results using Equations (3-34) and (3-35).

$$\frac{g'_F}{g'_M} = \left(\frac{L_F}{L_M}\right)\left(\frac{T_M}{T_F}\right)^2$$

$$\Rightarrow \qquad g'_F = g'_M \left(\frac{L_F}{L_M}\right)\left(\frac{T_M}{T_F}\right)^2 \tag{3-34}$$

and

$$\frac{u_F}{u_M} = \left(\frac{L_F}{L_M}\right)\left(\frac{T_M}{T_F}\right)$$

$$\Rightarrow \qquad u_F = u_M \left(\frac{L_F}{L_M}\right)\left(\frac{T_M}{T_F}\right) \tag{3-35}$$

Similarly, the volume flux through the space, q_F is given by:

$$q_F = q_M \left(\frac{L_F}{L_M}\right)^3 \left(\frac{T_M}{T_F}\right) \tag{3-36}$$

---

[1] At the source, $B_M = G'_M M_M = g(\Delta\rho/\rho)_M M_M$ (Eqs. (3-1) and (3-16)). The model is intended to represent a *buoyancy-driven* flow. It is therefore important to drive the flow in the model using the density difference, rather than the volume flux. M_M is therefore given a value as small as possible, whilst $(\Delta\rho/\rho)_M$ is given some value large enough to drive the flow, typically, $(\Delta\rho/\rho)_M \cong 0.04$.

Note that it is not necessary to reproduce the same g' (i.e. density differences) in the experiments as those which occur at the full scale. Rather it should be chosen to give large enough Reynolds and Peclet numbers, so that dynamic similarity is achieved.

3.8 Methods for Evaluating the CFD code

The analytical predictions of Linden et al. (1990) have been shown to be reasonably accurate by comparison with salt bath experiments. In chapters 5-7, the ability of CFX to accurately model buoyancy-driven displacement ventilation flows is evaluated using both the analytical and experimental work described in this chapter.

The evaluation was carried out by comparing various qualitative and quantitative aspects of the preceding theory of plumes and displacement flows with the CFD results. Table 3.1 shows the main comparisons that were conducted and how they were implemented. The analysis is divided up into properties of the overall flow (displacement flow analysis), and plume properties (plume analysis). In the displacement flow analysis, the CFD predictions were compared with both the salt bath results [S] and the analytical work [A], whilst in the plume analysis, comparisons were made between the CFD predictions and the analytical work only.

The two dimensional CFD simulations can be readily compared with the theory for a line source, since this is a good representation of a space containing a line source that is infinite in the direction of the source. This is also the way in which CFX models a 2D slice (see §D.3.1).

Table 3.1 List of Qualitative and Quantitative Comparisons for use in CFD Evaluation.

Ref.	Points of comparison and cross references	Method of comparison
Displacement flow analysis		
1	Flow pattern (§3.3). [S, A]	This included a general comparison of the flow field. In particular, the presence of the following were noted: a plume from the source; inflow through lower openings; outflow through upper openings; stratification of the flow (i.e. an interface separating light, warm air above from dense cool air below and across which there is very little vertical motion); and direction of the flow above and below the interface.
2	Independence of the interface height on the source strength (Eqs. (3-23) and (3-27)). [S, A]	This was carried out by measuring the interface height as a fraction of the height of the space for different source strengths. The interface height was defined as that height at which there was least vertical motion outside the plume. The source was varied by changing the heat input at the source.
3	Variation of interface height with opening areas (Eqs. 3-23 and 3-27). [S, A]	For each simulation, values of h/H were plotted on Figures 3.5 (3D) and 3.7 (2D).
4	Variation of reduced gravity across the interface with opening areas (Eqs. 3-24 and 3-29). [S, A]	For each simulation, values of g'_h/G'_H were plotted on Figures 3.6 (3D) and 3.8 (2D).
Plume analysis		
5	Plume entrainment. [A]	Values of α_T were calculated from the gradient of the graph b_T vs. y and compared with the value of 0.1 used by Linden et al. (1990).
6	Volume flux in plume. [A]	Values were taken from a graph of $M_{(L)}$ vs. y and compared with the theory.
7	Is $M_{(L)}$ proportional to $B_{(L)}^{1/3}$ for some constant height (Eqs. (3-14) and (3-25))? [A]	For the different source strengths investigated, a measure of the volume flux in the plume was made at some height and the graph $M_{(L)}$ vs. $B_{(L)}^{1/3}$ analysed.
8	3D: Is M proportional to $y^{5/3}$ (Eq. (3-14))? 2D: Is M_L proportional to y (Eq. (3-25))?	The volume flux $M_{(L)}$ was calculated at regular vertical intervals in the same plume (same value of $B_{(L)}$) and the graphs M vs. $y^{5/3}$ (3D) and M_L vs. y (2D) analysed.
9	Plume buoyancy (Eqs. (3-15) (3D) and (3-26) (2D)) [A]	Values were taken from the graph G'_T vs. y and compared with the theory.
10	Is G'_T proportional to $B_{(L)}^{2/3}$ for some constant height (Eqs. (3-26) and (3-15))? [A]	As 7 but G'_T rather than $M_{(L)}$, and G'_T vs. $B_{(L)}^{2/3}$ analysed.
11	3D: Is G'_T proportional to	As 8 but G'_T was measured in the plume and the

	$y^{-5/3}$ (Eq. (3-15))? 2D: Is G_T' proportional to y^{-1} (Eq. (3-26))? [A]	graphs G' vs. $y^{-5/3}$ (3D) and G_T' vs. y^{-1} (2D) analysed.

[A] Comparisons made between CFD predictions and analytical work.

[S, A] Comparisons made between CFD predictions and both analytical work and salt bath experiments.

3.9 Summary

This chapter has outlined the theory derived by Linden et al. (1990) for buoyancy-driven displacement ventilation based on point and line sources of buoyancy. This was approached qualitatively and then quantitatively using the governing equations for buoyant plumes. The main parameters used to define the flow are interface height and buoyancy change across the interface.

The salt bath modelling technique has been described, and the results obtained by Linden et al. (1990) in verifying their theory, presented. The experiments showed good agreement with the theory in most cases.

A table of flow parameters to be used as a basis for comparison between the CFD results and the work of Linden et al. (1990) has been compiled.

Chapter 4

Mathematical Models of CFX

4. Mathematical Models of CFX

4.1 Preamble

This chapter presents the various mathematical models used in CFX (version 4.1) for representing: transfer of mass, momentum and heat; buoyancy effects; turbulence; boundary conditions; and fluid properties. The solution of the equations that govern these processes is detailed in Appendix D.

All of the equations in this chapter are written in cartesian form as this is the coordinate system used to define geometries throughout the research. Conventional tensor notation is employed (see Appendix C).

4.2 The Governing Equations of CFD

All the fluids investigated in this research are *Newtonian*. This means that there exists a linear relationship between the shear stress, σ_{ij}, and the rate of shear (the velocity gradient). In CFX, this is expressed as follows:

$$\sigma_{ij} = -p\delta_{ij} + \mu\left(\frac{\partial u_i}{\partial x_j} + \frac{\partial u_j}{\partial x_i}\right) \tag{4-1}$$

where: p = pressure;

u_i = velocity;

x_i = cartesian coordinate directions;

$\delta_{ij} = \begin{cases} 1 \text{ if } i = j \\ 0 \text{ otherwise} \end{cases}$; and

μ = dynamic viscosity.

The equations that govern the motion and thermal behaviour of Newtonian fluids can be derived by considering the conservation laws of physics over a volume of fluid (see Patankar (1980) and Shaw (1992)). These laws are the conservation of

mass, momentum and internal energy (thermal energy). In CFX, these laws are expressed in the following form:

Conservation of mass (continuity equation):

$$\frac{\partial \rho}{\partial t} + \frac{\partial}{\partial x_j}(\rho u_j) = 0 \tag{4-2}$$

Conservation of momentum:

$$\frac{\partial}{\partial t}(\rho u_i) + \frac{\partial}{\partial x_j}(\rho u_i u_j) = \frac{\partial}{\partial x_j}\underbrace{\left[-p\delta_{ij} + \mu\left(\frac{\partial u_i}{\partial x_j} + \frac{\partial u_j}{\partial x_i}\right)\right]}_{\text{shear stress}} + B_i \tag{4-3}$$

Conservation of energy:

$$\frac{\partial}{\partial t}(\rho He) + \frac{\partial}{\partial x_j}(\rho u_j He) - \frac{\partial}{\partial x_j}\left(\lambda \frac{\partial T}{\partial x_j}\right) = \frac{\partial p}{\partial t} \tag{4-4}$$

where: B_i = body force;

He = enthalpy;

T = temperature;

t = time;

λ = conductivity; and

ρ = density.

H is the *total* enthalpy, given in terms of the static (thermodynamic) enthalpy, h:

$$He = he + \frac{1}{2}u_i^2 \tag{4-5}$$

The only body force encountered in this research is gravity, so $B_i = \rho g_i$, where g_i is the acceleration due to gravity (= (0,-9.8,0)).

The above equation set is closed by adding the equation of state:

$$\rho = \rho(T, p) \tag{4-6}$$

and the constitutive equation:

$$he = he(T, p) \tag{4-7}$$

All the flows considered in this research are assumed to be *incompressible* and possess a *steady state*. Therefore, the governing equations become:

$$\frac{\partial u_k}{\partial x_k} = 0 \tag{4-8}$$

$$\frac{\partial}{\partial x_j}(\rho u_j u_i) = \frac{\partial}{\partial x_j}\left(-p\delta_{ij} + \mu\left(\frac{\partial u_i}{\partial x_j} + \frac{\partial u_j}{\partial x_i}\right)\right) + \rho g_i \tag{4-9}$$

$$\frac{\partial}{\partial x_j}(\rho u_j He) - \frac{\partial}{\partial x_j}\left(\lambda \frac{\partial T}{\partial x_j}\right) = 0 \tag{4-10}$$

and the equation of state becomes:

$$\rho = \text{ constant, } \rho_0, \text{ say} \tag{4-11}$$

For incompressible flows, it is assumed that the kinetic energy term in the total enthalpy is negligible relative to the static enthalpy, therefore, equation (4-5) simply becomes:

$$He = he(T, p) \tag{4-12}$$

CFX assumes fluids to be thermally perfect in that the static enthalpy varies with temperature only. The constitutive equation is therefore given using the specific heat at constant temperature, C_p, as follows:

$$he = C_p(T - T_{Eref}) \tag{4-13}$$

Since enthalpy is arbitrary to within an additive constant, an *enthalpy reference temperature*, T_{Eref}, is used to define the temperature at which $he = 0$.

It is reiterated that these equations (Eqs. (4-8) - (4-13)) are valid *only* for incompressible, steady flows. For flows involving compressibility and transient effects, more mathematical detail is needed at almost every stage in the following sections. Such work will not be detailed. Interested readers should consult the CFX User Manual (CFDS, (1995)).

4.3 Heat Transfer

Heat transfer, and hence temperature distribution, is determined using the energy equation (Eq. (4-10)) and the constitutive equation (Eq. (4-12)).

By using the relationship in Equation (4-14), the temperature in Equation (4-10) can be replaced by the convected variable, *He*. This relationship is only valid for incompressible (or weakly compressible) flows, in which $He = he$, since it ignores the kinetic energy term.

$$\frac{\partial T}{\partial x_j} = \frac{1}{C_p}\frac{\partial He}{\partial x_j} \tag{4-14}$$

This enables the energy equation to be written in a *'convection-diffusion'* form (Eq. 4-15), similar to the momentum equation.

$$\frac{\partial}{\partial x_j}\left(\rho u_j He\right) - \frac{\partial}{\partial x_j}\left(\frac{\lambda}{C_p}\frac{\partial He}{\partial x_j}\right) = 0 \tag{4-15}$$

The benefits of having the governing equations in a similar form are appreciated when writing algorithms to solve them.

Note that the energy transport equation only models heat transfer by convection (and diffusion). Radiation is omitted in this research.

4.4 Buoyancy

For the incompressible flows considered, the *Boussinesq approximation* is used to model buoyancy effects. Here, the density is set to be a constant, ρ_0 (by the equation of state), except in the momentum equation where the following expression is used:

$$\rho = \rho_{Bref}\left(1 - \beta\left(T - T_{Bref}\right)\right) \tag{4-16}$$

which results from a Taylor series expansion of:

$$\rho = \rho_{Bref} + \left(\rho - \rho_{Bref}\right) \tag{4-17}$$

where: ρ_{Bref} = buoyancy reference density;

T_{Bref} = *buoyancy reference temperature;*

T = local temperature; and

β = thermal expansion coefficient given by $-\frac{1}{\rho}\frac{\partial \rho}{\partial T}$. (4-18)

Either T_{Bref} or ρ_{Bref} must be set by the user. In this research the reference temperature was specified and the reference density calculated (automatically) using equations (4-16) and (4-11).

Using Equation (4-17), the body force term and the pressure gradient term on the right-hand side of the momentum Equation (4-9) can be rewritten as

$$\rho g_i - \frac{\partial p}{\partial x_j}\delta_{ij} = (\rho - \rho_{Bref})g_i - \frac{\partial P}{\partial x_j}\delta_{ij} \tag{4-19}$$

where P is a *modified* pressure with the hydrostatic part removed:

$$P = p - \rho_{Bref} g_i x_i \tag{4-20}$$

$(\rho - \rho_{Bref})g_i$ effectively becomes the body force term which can be written as $-\rho_{Bref}\beta(T - T_{Bref})$ using Equation (4-16).

4.5 Turbulence Modelling

4.5.1 Background

Most flows occurring in reality are turbulent. That is, they exhibit a random, fluctuating, time-dependent behaviour. For example, a rising smoke plume from a lighted cigarette may appear smooth and *laminar*, but may instantaneously change into a highly complex, *turbulent* flow. The plume may subsequently alternate between laminar and turbulent regimes.

The governing equations used in CFX (Eqs. (4-2) - (4-4)) are the *exact* equations for laminar flow. Turbulent flows can be thought of as highly complex, rapidly varying, time-dependent, *laminar* flows. Consequently, if fine enough meshes (§D.2) and small enough time steps were used, these equations could be used to

model turbulent flows. Unfortunately, current computing power prevents such an approach. Instead, CFD packages use *turbulence models*.

4.5.2 Mathematical Description of Turbulence using Reynolds Averaging

If $f = f(t)$ and $g = g(t)$ are two turbulent quantities, then each can be represented as follows:

$$f = \bar{f} + f' \tag{4-21a}$$

$$g = \bar{g} + g' \tag{4-21b}$$

where: f = instantaneous value of f;

$\bar{f}$ = time-averaged, or *Reynolds-averaged*, value of f defined by $\bar{f} = \lim_{t_1 \to \infty} \frac{1}{t_1} \int_{t_0}^{t_0+t_1} f(t)dt$ where t_1 is large relative to the period of the fluctuations; and

f' = fluctuating component of f.

Similarly for g.

When combining two turbulent quantities, the following laws of averaging exist:

$$\bar{\bar{f}} = \bar{f} \quad \overline{f'} = 0 \tag{4-22}$$

$$\overline{af + bg} = a\bar{f} + b\bar{g} \text{ where } a \text{ and } b \text{ are constants} \tag{4-23}$$

$$\overline{\bar{f}\,\bar{g}} = \bar{f}\,\bar{g} \tag{4-24}$$

$$\overline{fg} = \bar{f}\,\bar{g} + \overline{f'g'} \tag{4-25}$$

$$\overline{\left(\frac{\partial f}{\partial x_j}\right)} = \frac{\partial \bar{f}}{\partial x_j} \tag{4-26}$$

By expressing the primitive variables (u_i, p, and He) in the same way as Equation (4-21a) and Reynolds averaging each of the governing equations (Eqs. (4-8), (4-9), and (4-15)), the following set of *Reynolds-averaged equations* are obtained.

Reynolds averaged continuity equation:

$$\frac{\partial \overline{u_k}}{\partial x_k} = 0 \tag{4-27}$$

Reynolds averaged momentum equation:

$$\frac{\partial}{\partial x_j}\left(\rho \overline{u_j}\ \overline{u_i}\right) = \frac{\partial}{\partial x_j}\left(-\overline{p}\delta_{ij} + \mu\left(\frac{\partial \overline{u_i}}{\partial x_j} + \frac{\partial \overline{u_j}}{\partial x_i}\right) - \rho\overline{u_i' u_j'}\right) + \rho g_i \tag{4-28}$$

Reynolds averaged energy equation:

$$\frac{\partial}{\partial x_j}\left(\rho \overline{u_j}\ \overline{He}\right) - \frac{\partial}{\partial x_j}\left(\frac{\lambda}{C_p}\frac{\partial \overline{He}}{\partial x_j} - \rho\overline{u_i' He'}\right) = 0 \tag{4-29}$$

It is noticed that, after the time averaging process, the continuity equation has remained unchanged, but additional terms, comprising products of the fluctuating components, have appeared in both of the other governing equations. These terms have arisen from the (non-linear) convection term and are called:

$$\text{Reynolds stresses} = \rho\overline{u_i' u_j'} \tag{4-30}$$

and

$$\text{Reynolds fluxes} = \rho\overline{u_i' He'} \tag{4-31}$$

So, in addition to solving for the various primitive variables, when modelling a turbulent flow, it is also necessary to solve for all the Reynolds stresses (six in a three dimensional flow) and any Reynolds fluxes arising from scalar transport equations. Since at present there are more variables than equations, additional work is required to produce solutions for the Reynolds stresses and fluxes. This can be done, either by using the eddy viscosity hypothesis (§§4.5.3-4.5.5), or by using second order closure models (§4.5.6).

4.5.3 Eddy Viscosity Models

The turbulence modelling approach employed in this research uses the *eddy viscosity* hypothesis which assumes that the Reynolds stresses have a similar form to that of the laminar viscous stresses by expressing them as:

$$-\rho\overline{u_i'u_j'} = \mu_t\left(\frac{\partial\overline{u_i}}{\partial x_j}+\frac{\partial\overline{u_j}}{\partial x_i}\right)-\frac{2}{3}\rho k\delta_{ij} \tag{4-32}$$

where μ_t is the *eddy viscosity*, or *turbulent viscosity*, and k is the *turbulent kinetic energy* given by:

$$k = \frac{1}{2}\overline{u_i'u_i'} \tag{4-33}$$

The additional term involving k in Equation (4-32) serves to make the relation accurate for incompressible flows (when $i = j$).

Similarly, an *eddy diffusivity* hypothesis exists for the Reynolds fluxes to give

$$-\rho\overline{u_i'He'} = \Gamma_{He_t}\frac{\partial\overline{He}}{\partial x_j} \tag{4-34}$$

where Γ_{He_t} is the *eddy diffusivity* for enthalpy. This is related to the eddy viscosity as follows:

$$\Gamma_{He_t} = \frac{\mu_t}{\sigma_{He_t}} \tag{4-35}$$

where σ_{He_t} is the *turbulent Prandtl number* for enthalpy. It is this value that is specified when defining the eddy diffusivity, not the eddy diffusivity itself.

Using these hypotheses, the Reynolds-averaged equations become:

$$\frac{\partial}{\partial x_j}\left(\rho\overline{u_j}\,\overline{u_i}\right) = \frac{\partial}{\partial x_j}\left(-\overline{p_0}\delta_{ij}+\mu_{eff}\left(\frac{\partial\overline{u_i}}{\partial x_j}+\frac{\partial\overline{u_j}}{\partial x_i}\right)\right)+\rho g_i \tag{4-36}$$

$$\frac{\partial}{\partial x_j}\left(\rho\overline{u_j}\,\overline{He}\right)-\frac{\partial}{\partial x_j}\left(\underbrace{\left(\frac{\lambda}{C_p}+\frac{\mu_t}{\sigma_{He_t}}\right)}_{\Gamma_{He_{eff}}}\frac{\partial\overline{He}}{\partial x_j}\right)=0 \tag{4-37}$$

μ_{eff} and $\Gamma_{He_{eff}}$ are the *effective* viscosity and diffusivity given by the sum of their laminar and turbulent components as follows:

$$\mu_{eff} = \mu_l + \mu_t \tag{4-38}$$

$$\Gamma_{He_{eff}} = \Gamma_{He} + \Gamma_{He_t} \tag{4-39}$$

Γ_{He} can be inferred from Equation (4-15):

$$\Gamma_{He} = \frac{\lambda}{C_P}. \tag{4-40}$$

p_0 represents a further modification to the pressure which, for buoyant flows, is given by Equation (4-41) (c.f. (4-20) that was used for describing laminar flows).

$$p_0 = p - \rho_{Bref} g_k x_k + \frac{2}{3}\rho k \tag{4-41}$$

It is now observed that the governing equations for momentum and heat transfer developed for turbulent flow using the eddy viscosity hypothesis (Eqs. (4-36) and (4-37)) have the same form as the laminar flow equations with μ and Γ_{He} replaced with μ_{eff} and $\Gamma_{He_{eff}}$. That is, the viscosity and diffusion have been enhanced by turbulent components. Consequently, all that is left to do to solve the set of equations for turbulent flow when using the eddy viscosity hypothesis, is to determine μ_t. ($\Gamma_{He_{eff}}$ can then be found using equations (4-35) and (4-39)).

Determining the eddy viscosity, μ_t

Much research has been carried out into developing satisfactory methods for determining the eddy viscosity. Prandtl (1925) suggested using the relationship

$$\mu_t = \rho C_\mu l^2 \left(\frac{\partial \overline{u_i}}{\partial x_j} + \frac{\partial \overline{u_j}}{\partial x_i} \right) \tag{4-42}$$

and carrying out experiments of simple turbulent flows to determine the (empirical) constants, C_μ and length scale l. However, these constants are only accurate for the type of flows from which they were derived and so the model lacks generality. So-called *one-equation* models were therefore investigated which increase the generality by solving an additional transport equation for the turbulent kinetic energy, k. μ_t can then be found using an expression of the form

$$\mu_t = \rho C_\mu l k^{1/2}. \tag{4-43}$$

But again, these sort of models rely on the empirical determination of l and C_μ.

The most widely used technique today for determining μ_t goes one step further and uses both k and its dissipation rate, ε, to express a formula for μ_t, and solving additional transport equations for each. Such models are known as *two-equation*, $k-\varepsilon$ *models*, and eliminate the need to specify a length scale, l, for the flow. This has now become the industry standard turbulence modelling technique owing to its acceptable accuracy in modelling a wide range of flows.

It should be noted that eddy viscosity models assume isotropic turbulence which results in diffusion (a scalar quantity), acting equally in all directions. There is thus no preference given to either the direction of the flow, or the gravity vector in buoyant flows, both of which may play an important part in producing an accurate solution.

4.5.4 The Standard $k-\varepsilon$ model in CFX

Most CFD codes, including CFX, provide the user with a k-ε model based on that described by Launder and Spalding (1974). The eddy viscosity is then given by

$$\mu_t = C_\mu \rho \frac{k^2}{\varepsilon} \tag{4-44}$$

where $C_\mu = 0.09$ (empirical), and the transport equations are as follows.

For k:

$$\frac{\partial}{\partial x_j}\left(\rho \overline{u_j} k\right) - \frac{\partial}{\partial x_j}\left(\left(\mu_l + \frac{\mu_t}{\sigma_k}\right)\frac{\partial k}{\partial x_j}\right) = P + G - \rho\varepsilon \tag{4-45}$$

and for ε:

$$\frac{\partial}{\partial x_j}\left(\rho \overline{u_j} \varepsilon\right) - \frac{\partial}{\partial x_j}\left(\left(\mu_l + \frac{\mu_t}{\sigma_\varepsilon}\right)\frac{\partial \varepsilon}{\partial x_j}\right) = C_1 \frac{\varepsilon}{k}\left(P + C_3 \max(G,0)\right) - C_2 \rho \frac{\varepsilon^2}{k} \tag{4-46}$$

P and G represent production of k due to shear stresses and body forces respectively:

$$P = \mu_{eff} \frac{\partial \overline{u_i}}{\partial x_j}\left(\frac{\partial \overline{u_i}}{\partial x_j} + \frac{\partial \overline{u_j}}{\partial x_i}\right) \tag{4-47}$$

$$G = \frac{\mu_{eff}}{\sigma_{He_t}} \beta g_k \frac{\partial \overline{T}}{\partial x_k} \tag{4-48}$$

The set of empirical constants used in CFX are:

$C_1 = 1.44$; $C_2 = 1.92$; $C_3 = 0.0$ (see below); $\sigma_k = 1.0$; $\sigma_\varepsilon = 1.217$; and $\sigma_{He_t} = 0.9$.

These are the recommended constants of Launder and Spalding (1974), except σ_ε and C_3. σ_ε has a recommended value of 1.3 but is set in CFX using the formula

$$\sigma_\varepsilon = \frac{\kappa^2}{(C_2 - C_1)\sqrt{C_\mu}} \tag{4-49}$$

where κ is the Von Karman constant (= 0.4187). The C_3 term in the ε equation was not included in the model by Launder and Spalding (1974) but was suggested by Ideriah (1980) in an attempt to model buoyancy more accurately. Throughout this research it is seldom used so $C_3 = 0$. When it is used, a value of $C_3 = 1.0$ is used. However, there is much debate concerning the form of this term and other values have been used, (see for example Jacobsen (1993) and Chen et al. (1990)).

It should be noted that in the near-wall region, or *boundary layer*, laminar viscosity dominates over turbulent viscosity and therefore has a significant influence on the production, destruction and diffusion of turbulent kinetic energy. Consequently, the $k-\varepsilon$ model becomes inaccurate in such regions. To overcome these difficulties, *wall functions* are used (§4.6.1).

4.5.5 The RNG $k-\varepsilon$ model in CFX

One of the most recent attempts to model turbulence more accurately is due to Yakhot and Orszag (1992) who used Renormalisation Group (RNG) theory to determine the constants in the k and ε equations, thereby removing the

empiricism of the model. A brief description of the underlying theory of the RNG model was given in section 2.6. Many CFD codes now offer a RNG alternative to the standard $k-\varepsilon$ model. The RNG equations in CFX take the following form.

For k:

$$\frac{\partial}{\partial x_j}\left(\rho\overline{u_j}k\right)-\frac{\partial}{\partial x_j}\left(\left(\mu_l+\frac{\mu_t}{\sigma_k}\right)\frac{\partial k}{\partial x_j}\right)=P+G-\rho\varepsilon \tag{4-50}$$

and for ε:

$$\frac{\partial}{\partial x_j}\left(\rho\overline{u_j}\varepsilon\right)-\frac{\partial}{\partial x_j}\left(\left(\mu_l+\frac{\mu_t}{\sigma_\varepsilon}\right)\frac{\partial \varepsilon}{\partial x_j}\right)=(C_1-C_{1RNG})\frac{\varepsilon}{k}(P+C_3\max(G,0))$$

$$-C_2\rho\frac{\varepsilon^2}{k} \tag{4-51}$$

where

$$C_{1RNG}=\frac{\eta\left(1-\frac{\eta}{\eta_0}\right)}{1+\beta_0\eta^3} \tag{4-52}$$

and

$$\eta=\left(\frac{P}{\mu_l}\right)^{1/2}\frac{k}{\varepsilon}. \tag{4-53}$$

The model constants are: $C_1 = 1.42$, $C_2 = 1.68$, $C_3 = 0.0$, $\sigma_k = 1.0$, $\sigma_\varepsilon = 0.7179$, $C_\mu = 0.085$, $\beta_0 = 0.015$, and $\eta_0 = 4.38$.

Note that the difference between this turbulence model and the standard $k-\varepsilon$ model lies in the form of the ε equation and the set of constants used, which reflects the opinion that the ε equation has long thought to be a source of inaccuracy in the standard version of the model (Versteeg and Malalasekera (1995)).

4.5.6 Second Order Closure Models

Although the two-equation eddy viscosity approach has proved very reliable for modelling a wide range of turbulent flows, in order to solve *anisotropic* (direction dependent) turbulence, a second order closure model should be used. These are sometimes called stress transport models since they model the motion of the

individual Reynolds stresses (Eq. (4-30)) and Reynolds fluxes (Eq. (4-31)). This is done by solving an additional transport equation for *each* of the Reynolds stresses and fluxes.

It can be deduced that for a non-isothermal turbulent flow, stress transport models involve the solution of an extra *seven* transport equations. Although it has been reported (Jones and Whittle (1992)) that some second order models are able to deal better with swirl and reattaching flows, Clarke and Wilkes (1988) reported an increase in computing time of about 100%.

Second order closure models are *not* investigated during this research. Their inclusion here is intended to highlight possible deficiencies in the $k-\varepsilon$ model that may be eliminated if a second order closure model were adopted.

4.6 Mathematical Description of Boundaries

Four types of boundary are employed in this research. This section explains the function of each and the mathematical conditions imposed on them.

4.6.1 WALL Boundaries

These are used at all fluid-solid interfaces and enable users to specify conditions for velocity and heat transfer.

For all solid boundaries in this work, the so-called 'no-slip' condition was imposed on velocity ($u_i = 0$). For most solid boundaries, heat transfer was zero (adiabatic). At heat sources, constant heat flux was imposed.

WALL boundaries are also used to implement *wall functions* which are employed to account for the rapid variation in fluid properties close to solid boundaries in turbulent flows. This obviates the need for ultra-fine meshing close to boundaries which would be required to capture the true physics of the flow, and eliminates the inaccuracies of the $k-\varepsilon$ turbulence model in these regions.

4.6.1.1 Wall functions for velocity

When fluid flows past a solid surface, a *boundary layer* forms. This can be thought of as comprising three regions (Fig. 4.1): a laminar sub-layer; a log-law layer in which the fluid velocity can be expressed as a logarithmic function of the distance from the wall; and an outer layer which represents the interface between the boundary layer and the free stream flow.

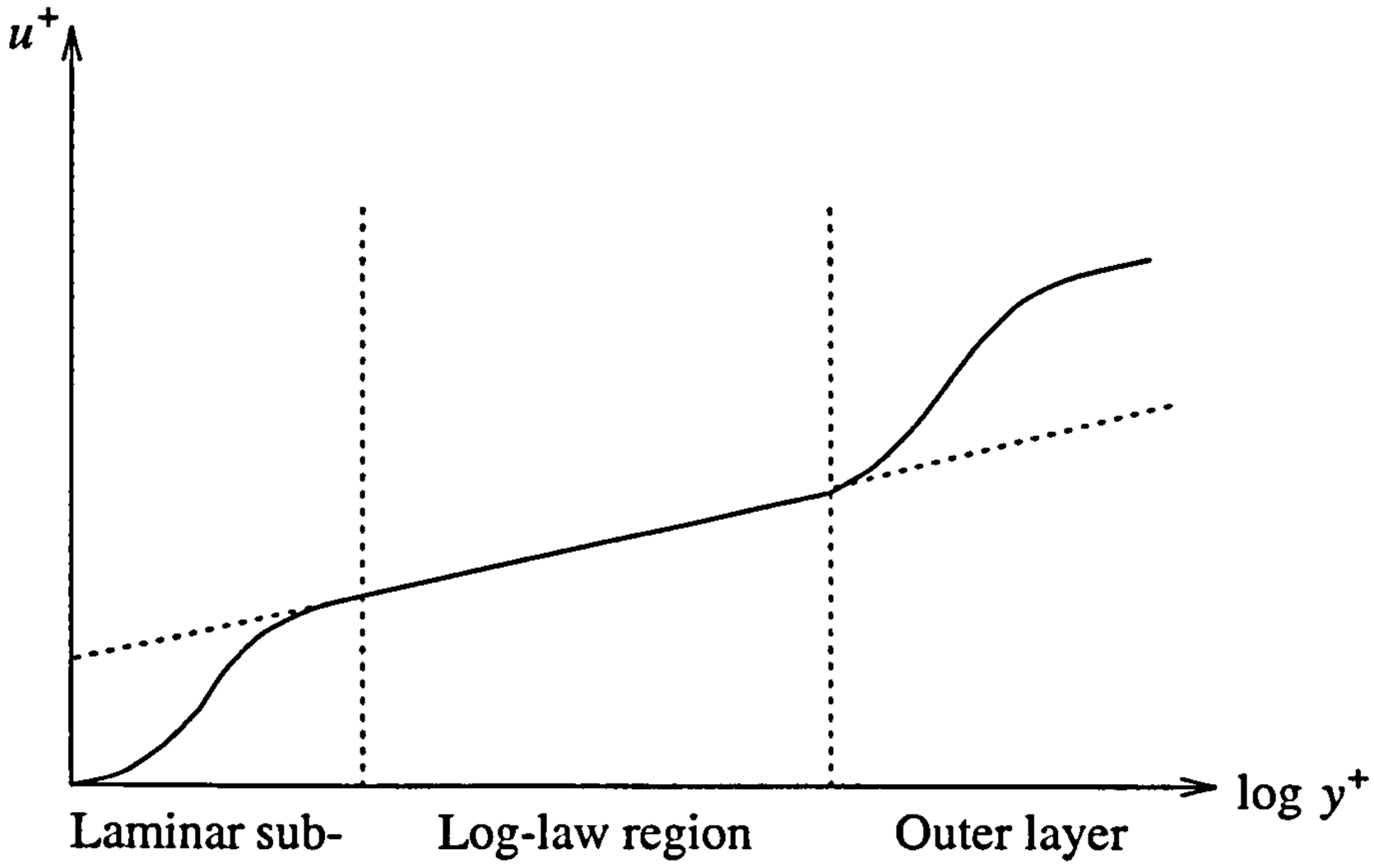

Figure 4.1. Velocity variation near a wall (after Shaw (1992)).

At some point in the log-law region of a fully developed boundary layer, it is found that (Launder and Spalding (1974)),

$$\tau^2 = C_\mu \rho^2 k^2 . \tag{4-54}$$

Using this, a new quantity, $\tau_k = |\tau|$ is defined thus

$$\tau_k = C_\mu^{1/2} \rho k \tag{4-55}$$

in which the *k* subscript should not be confused with tensor notation.

This quantity is used to define the following, non-dimensional variables:

$$u^+ = \frac{(\rho \tau_k)^{1/2}}{\tau_k} u^{par} \tag{4-56}$$

$$y^+ = -\frac{(\rho\tau_k)^{1/2}}{\mu}(d-y) \tag{4-57}$$

where u^{par} is the component of velocity parallel to the wall and y is the perpendicular distance from the wall which is assumed to be at $y = d$.

The velocity parallel to the wall is then defined as follows.

$$u^+ = \begin{cases} y^+, & \text{for } y^+ < y_0^+ \\ \frac{1}{\kappa}\log(Ey^+), & \text{for } y^+ > y_0^+ \end{cases} \tag{4-58}$$

where y_0^+ is the cross-over point between the laminar sub-layer and the log-law region, i.e. the upper root of

$$y_0^+ = \frac{1}{\kappa}\log(Ey_0^+). \tag{4-59}$$

This gives a value of $y_0^+ = 11.23$. E and κ are constants of the wall function and take the values, $E = 9.793$ and $\kappa = 0.4187$ (Von Karman constant).

By employing wall functions, the user is able to place the first grid node of the mesh anywhere in the log-law region ($11.23 < y^+ < 150$ (approx.)) and allow the wall functions to take care of the rapid variation in variables close to the wall.

The value of the turbulent kinetic energy, k, is represented by its transport equation (Eq. (4-45) or (4.50)) in the control volume immediately adjacent to the solid boundary. Using this, the value for τ_k can be found. The transport equation for ε (Eq. (4-46) or (5.51)) is particularly inaccurate close to solid boundaries, so the value of ε in the control volume nearest the wall is calculated independently using the relationship in Equation (4-60) in which k has been calculated from its transport equation.

$$\varepsilon = \frac{C_\mu^{3/4} k^{3/2}}{\kappa(d-y)} \tag{4-60}$$

4.6.1.2 Wall functions for enthalpy

Using the value for τ_k (Eq. (4-55)), enthalpy, *He* is non-dimensionalised as follows.

$$He^+ = \frac{(\rho\tau_k)^{1/2}}{J_{He}}(He_W - He) \tag{4-61}$$

where: $J_{He} = \left(\frac{\partial He}{\partial n}\right)_W$ (flux of *He* at the wall); and

He_W = value of *He* on wall.

Again, making the three layer assumption at solid boundaries, the value of the enthalpy is given by

$$He^+ = \begin{cases} \sigma_{He} y^+, \text{ for } y^+ < y^+_{He} \\ \dfrac{\sigma_{He_t}}{\kappa}\log\left(E_{He} y^+\right), \text{ for } y^+ > y^+_{He} \end{cases} \tag{4-62}$$

where σ_{He} is the *laminar* Prandtl number (or Shmidt number) for enthalpy given by

$$\sigma_{He} = \frac{\mu}{\Gamma_{He}}. \tag{4-63}$$

The log-layer constant, E_{He}, is given by the formula of Jayatilleke (1969):

$$E_{He} = E\exp\left[9.0\kappa\left(\left(\frac{\sigma_{He}}{\sigma_{He_t}}\right)^{3/4} - 1\right)\left(1 + 0.28\exp\left(-0.007\frac{\sigma_{He}}{\sigma_{He_t}}\right)\right)\right] \tag{4-64}$$

which gives a value of $E_{He} = 4.429$, and a cross-over point of $y^+_{He} = 12.08$.

4.6.2 PRESSURE Boundaries

PRESSURE boundaries are *flow boundaries* and are used at solution domain boundaries where the user knows the pressure of the fluid relative to the rest of the domain. Fluid can flow into, or out of the solution domain, across a pressure boundary. The conditions imposed in each case are as follows.

4.6.2.1 Inflow through a PRESSURE boundary

Fluid entering the domain across a fluid boundary is assumed to enter normal to the cell face. *Dirichlet* conditions (constant values assigned directly to variables) are set on pressure and temperature. Zero normal gradients (unchanging conditions), known as *Neumann* conditions, are imposed on velocity and turbulence quantities.

4.6.2.2 Outflow through a PRESSURE boundary

When fluid flows out of the domain across a PRESSURE boundary, the only value fixed (Dirichlet condition) is pressure, all others are designated a Neumann condition.

4.6.2.3 Other notes on PRESSURE boundaries

Pressure is arbitrary to within an additive constant, therefore, the solution procedure requires some reference pressure from which all other pressures can be calculated. When using PRESSURE boundaries, the reference pressure is taken as that specified by the user at the pressure boundary.

For both inflow and outflow across PRESSURE boundaries, the zero gradient condition is imposed on velocity. This implies a fully developed flow assumption which may be inaccurate in some situations, for example, if the boundary is located at a sudden contraction or expansion. To avoid such problems, PRESSURE boundaries should ideally be located in regions of unchanging geometry, so that if the zero gradient condition had not been set explicitly, the flow would nevertheless have settled down to a fully developed flow in this region.

4.6.3 SYMMETRY PLANE Boundaries

In many CFD applications, the geometry and boundary conditions are symmetric about some plane. In such cases it is common practice to use a SYMMETRY PLANE boundary condition. This both reduces the required computation and aids convergence by reinforcing symmetry.

The conditions imposed at these boundaries are:

$$\frac{\partial u_i^{par}}{\partial n} = 0\,,\ \frac{\partial \phi}{\partial n} = 0\,,\ \text{and}\ u_i^{perp} = 0 \qquad (4\text{-}65)$$

where u_i^{par} and u_i^{perp} are the components of velocity parallel and perpendicular to the boundary, ϕ represents the scalar variables: p; k; ε; and H, and n represents the direction normal to the boundary.

`SYMMETRY PLANE` boundaries are also used on the two plane faces used to represent a 2D slice of a room (see §D.3.1).

4.6.4 `INTER BLOCK` Boundaries

The other boundary type used in this work is the `INTER BLOCK` boundary which is created automatically by the code when defining a multi-block geometry (see §D.2).

4.7 Fluid Properties

Before the governing equations can be solved, various fluid properties still remain to be specified. For non-isothermal simulations of airflow these are: β; λ; μ; ρ; and C_P. These are set by defining a *standard fluid*. This assumes all the fluid properties, except the coefficient of thermal expansion, are functions of temperature only, expressed as

$$\Psi = a + bT + cT^2 + dT^3 + eT^4 \qquad (4\text{-}66)$$

where: Ψ = value of fluid property

T = *standard fluid reference temperature*

a, ..., e are constants

All the user is required to do then, is simply specify the *standard fluid reference temperature*, T, at which the various fluid properties are to be calculated. The expansion coefficient β, was defined in Equation (4-18).

4.8 Summary

The governing equations in CFX used for modelling steady, turbulent, non-isothermal flows have been described, along with the mathematical conditions imposed at solid and flow boundaries. The techniques used to solve the governing equations are described in Appendix D.

Chapter 5

Two Dimensional Modelling of Buoyancy-Driven Displacement Ventilation

5. Two Dimensional Modelling of Buoyancy-Driven Displacement Ventilation

5.1 Preamble

This chapter describes the two dimensional simulations that were carried out as an important preliminary exercise to modelling full three dimensional flows.

The chapter begins with the definition of a reference case which is referred to as **Benchmark 1.** The initial difficulties encountered in modelling this case and how they were overcome are discussed. The final (satisfactory) result for this reference case is fully documented and then used as a basis for investigating the effects of varying certain numerical and physical parameters.

The CFD results are compared with the work of Linden et al. (1990) for a 2D line source of buoyancy (§3.5.2).

5.2 Definition of Benchmark 1

Displacement ventilation in a 2D slice of a simple space, driven by a source of buoyancy in the centre of the floor, was considered (Fig. 5.1).

In CFX, 2D simulations are defined by considering a one-cell-thick slice of a geometry that is infinitely long in the *z* direction (§D.3.1). The length of the cell in the *z* direction was set to 1m, which enabled all quantities such as opening areas and source strengths to be expressed in quantities 'per metre in the *z* direction'.

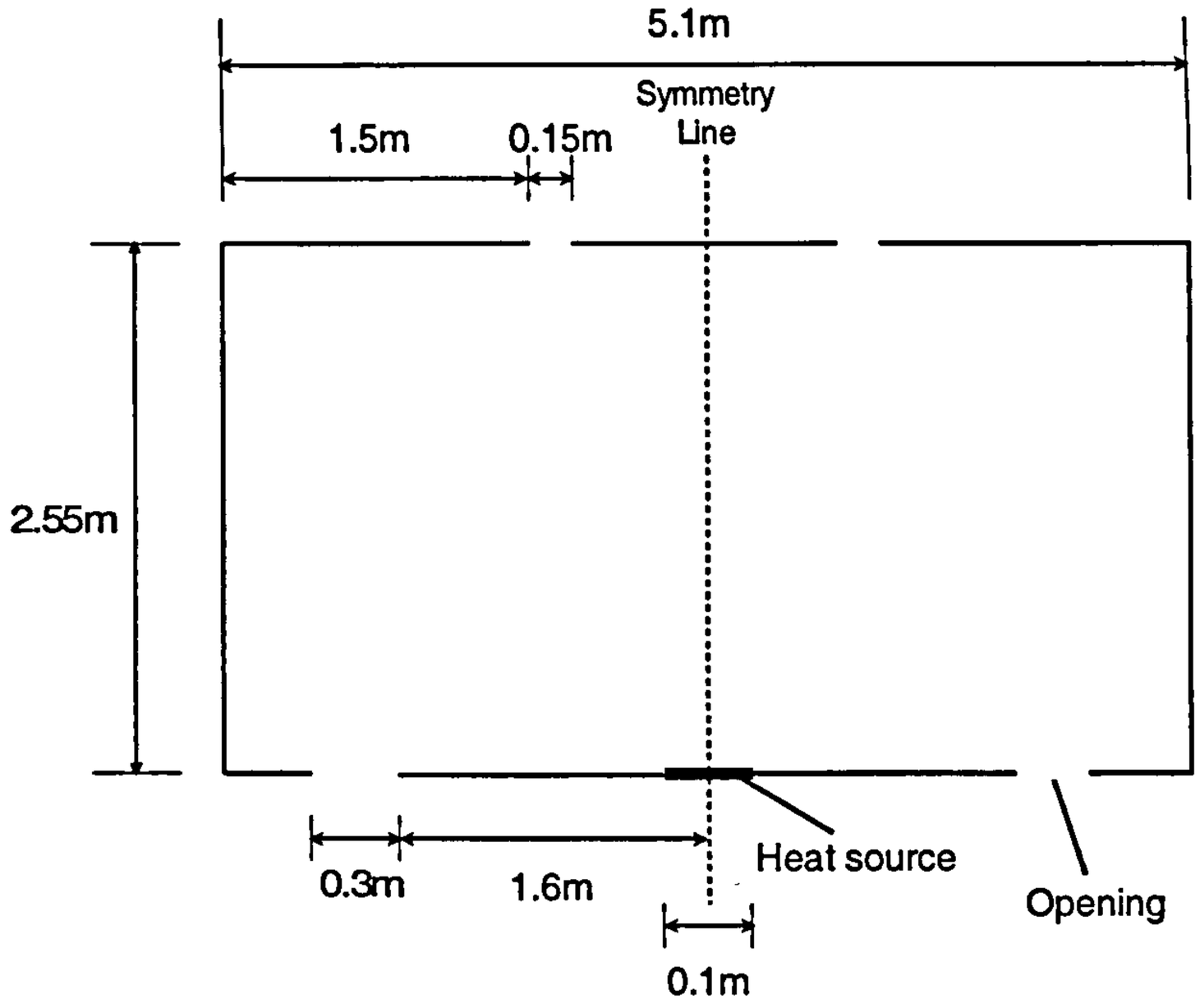

Figure 5.1 Geometrical description of Benchmark 1.

The ambient air temperature was set to 18°C and it was assumed that the walls, ceiling and floor (except to source) were adiabatic. The space is symmetrical about its centre and air was able to move freely into or out of the space via the upper and lower openings.

5.3 Initial Simulations

5.3.1 Setting Boundary Conditions

One of the main difficulties in modelling natural ventilation flows lies in deciding what boundary conditions to set at the openings between the interior and exterior. In particular, what conditions to impose on pressure, velocity and turbulence quantities. In mechanical ventilation, this issue is far simpler since these conditions are determined by the equipment being used. In this work however, the only driving force is the single heat source in the centre of the floor inside the space (Fig. 5.1).

It was anticipated that the flow in the vicinity of the openings would be complex - the air is rapidly contracted and then expanded as it passes through the openings

which causes complex, rapidly changing pressure fields. Such pressure changes would have an effect on the airflow inside the space and so it was thought necessary to model the air explicitly as it passed through the openings. The computational domain was therefore extended beyond the room so that any potential errors caused by specifying inaccurate boundary conditions at the openings were removed. It should be noted that by including some of the exterior space in the computational domain, it was not sought to obtain accurate predictions for the flow field in these regions. It was used purely in an attempt to eliminate possible inaccuracies in the results *inside* the space. The amount of exterior modelled was estimated for the initial simulations but is investigated further in §5.10.

The task of specifying boundary conditions at the openings had now been replaced with the task of deciding what conditions to impose at the extremities of the exterior domain. In reality the exterior region is infinite so the boundary conditions used should reflect this as closely as possible. This was done by setting zero normal gradient (i.e. unchanging conditions) on the velocity components and turbulence quantities, and explicitly specifying values for temperature and pressure. The value for temperature is only used when the flow is *into* the domain and is set equal to the ambient temperature. Pressure was set to be a constant ($p = 0$ for convenience) at all points on the exterior boundary. This was possible since pressure is arbitrary to within an additive constant, i.e. the value of pressure on the boundary was simply used as a reference, relative to which, all other pressures were calculated. Pressure differences due to height, (h_1, say), ($\Delta p = \rho g h_1$), were automatically accounted for in the momentum equation (Eq. (4-9)). This sort of boundary is called a `PRESSURE` boundary in CFX (see §4.6.2 for more details).

It is normal in steady-state CFD simulations for geometrically symmetric problems to be modelled as such, and so a `SYMMETRY PLANE` boundary was used as shown in Figure 5.2

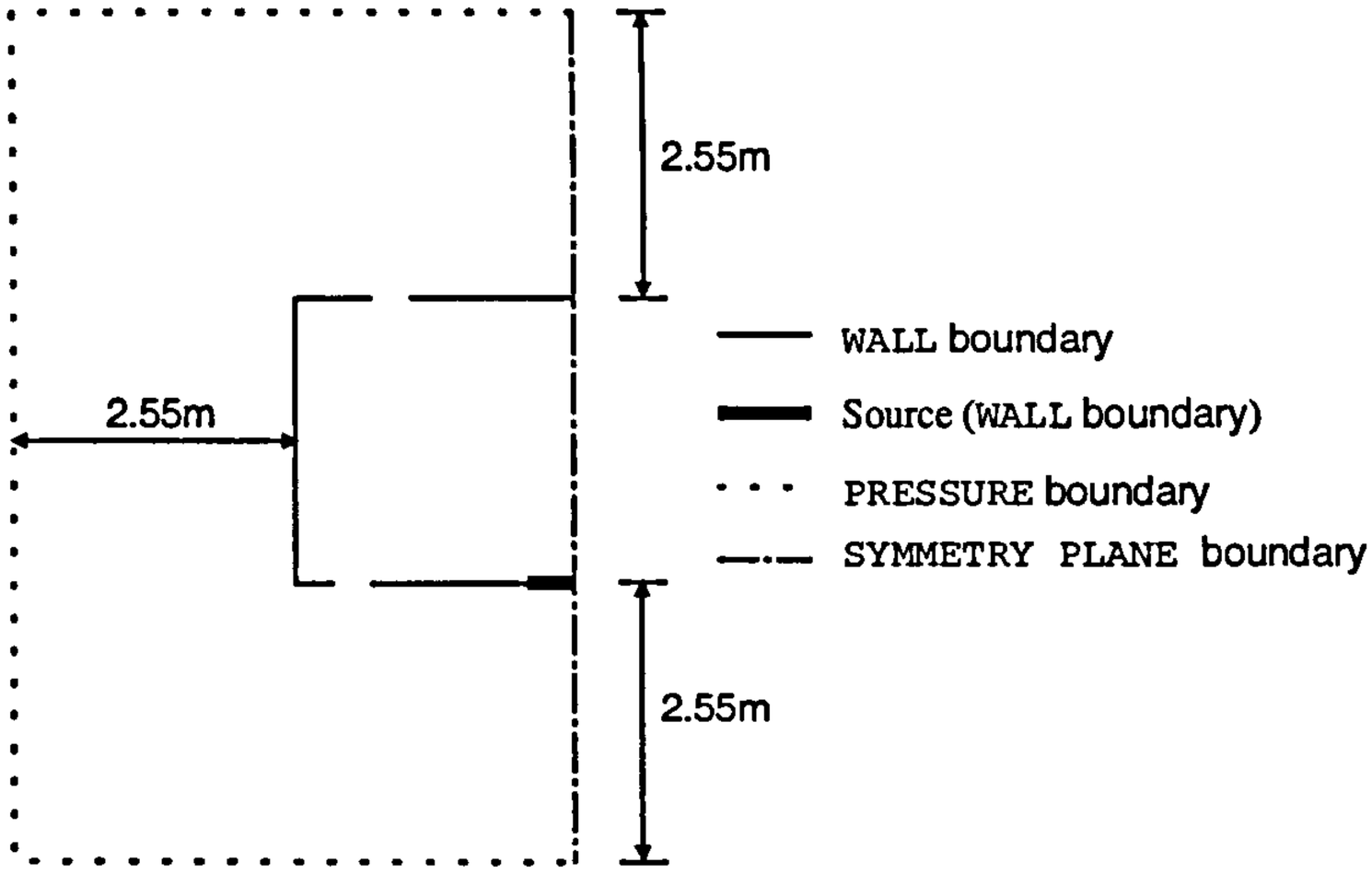

Figure 5.2 Representation of Benchmark 1 in CFX.

5.3.2 Enthalpy and Buoyancy Reference Temperatures

In flows with heat transfer and buoyancy effects, reference temperatures for enthalpy, T_{Eref}, and buoyancy, T_{Bref}, need to be specified (see §§4.2 and 4.4). In these simulations, the buoyancy reference temperature needs to be set to the same value as the ambient temperature, since T_{Bref} is used in the calculation of the pressure field as follows.

Recall from Chapter 4 that the pressure field in a turbulent flow is given by Equation (4-41):

$$p_0 = p - \rho_{Bref} g_k x_k + \frac{2}{3}\rho k \qquad \text{(Eq. 4-41).}$$

Using Equation (4-16)

$$\rho = \rho_{Bref}\left(1-\beta\left(T - T_{Bref}\right)\right) \qquad \text{(Eq. 4-16),}$$

Equation (4-41) can be written as

$$p_0 = p - \frac{\rho g_k x_k}{1-\beta\left(T - T_{Bref}\right)} + \frac{2}{3}\rho k. \qquad (5\text{-}1)$$

So in order for $p_0 = p - \rho g_k x_k + \frac{2}{3}\rho k$ (i.e. zero net pressure force) on the PRESSURE boundary as required, T_{Bref} had to be set equal to the temperature on

the PRESSURE boundary, i.e. the ambient temperature. In order to obtain the same result for a different buoyancy reference temperature, it would have been necessary to alter the value of p set on the PRESSURE boundary. It was easier simply to set $p = 0$ on the PRESSURE boundary and T_{Bref} equal to the ambient temperature.

The enthalpy reference temperature has no effect on the solution as it is simply a numerical parameter used for specifying the temperature at which the static enthalpy is zero (Eq. (4-13)). For convenience, this too was given the same value as the ambient temperature.

5.3.3 Specification of Fluid Properties

Physical fluid properties were set using the *standard fluid reference temperature* method available in CFX (§4.7). A temperature of 2°C above ambient was used, which gave the following values:

$C_p = 1004\,\text{J/KgK}$;

$\lambda = 0.02571\,\text{W/mK}$;

$\mu = 1.812\times10^{-5}\,\text{Kg/ms}$; and

$\rho = 1.208\,\text{Kg/m}^3$.

The thermal expansion coefficient is calculated (automatically) using Equation (4-18) ($\beta = -(1/\rho)\partial\rho/\partial T$) and was given the value

$\beta = 0.003394\,\text{K}^{-1}$.

5.3.4 Mesh Definition

For the initial simulation, the mesh shown in Figure 5.3 was used (72×90). The mesh density and orthogonality is investigated later in more detail (§5.5).

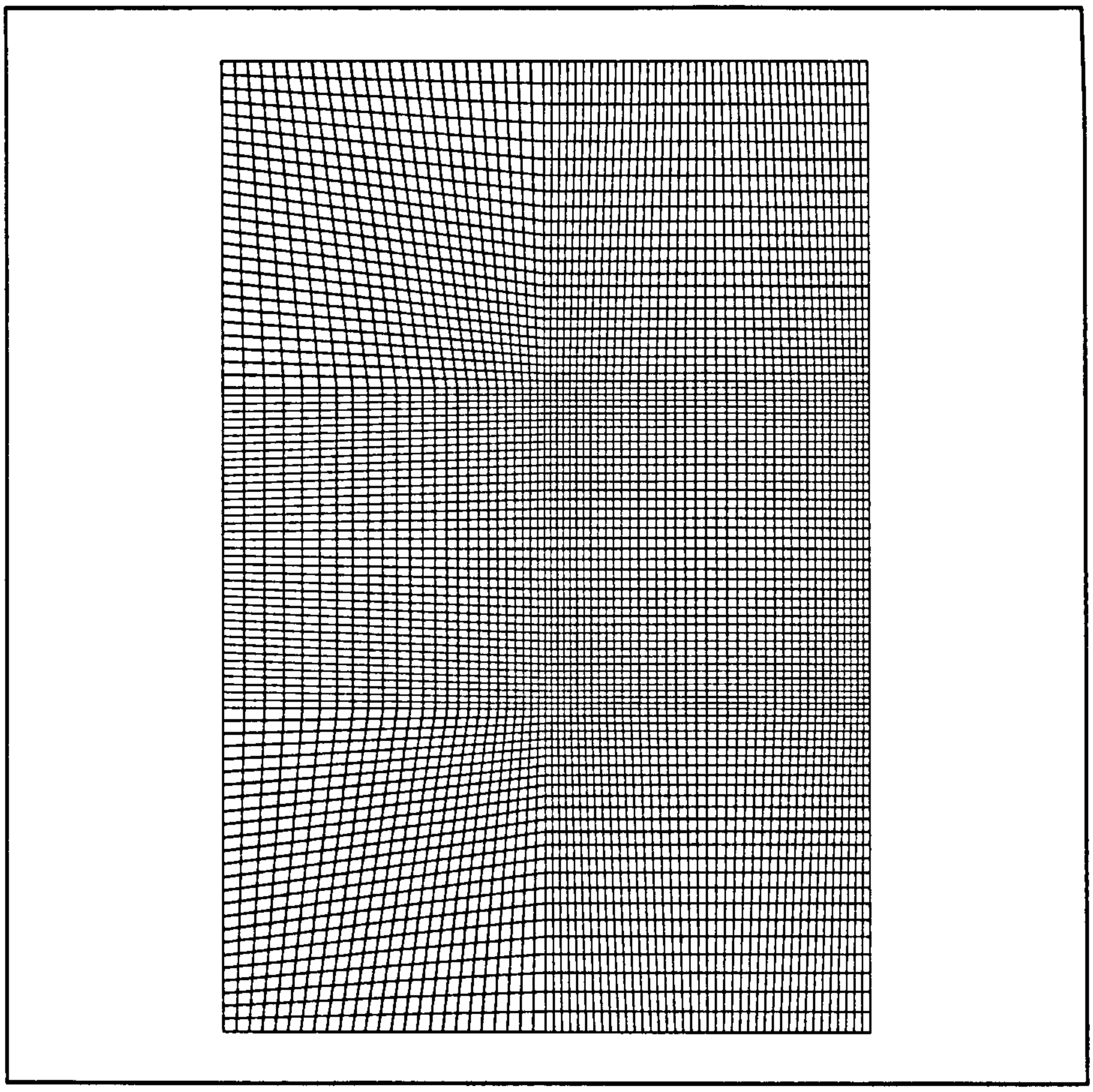

Figure 5.3 Mesh used in the initial simulation of Benchmark 1 (range of cell dimensions: 4.75cm - 16cm).

5.3.5 Convergence Criteria

It was necessary to decide upon appropriate convergence criteria that should be met before a solution was deemed accurate (see §D.7.4). The following criteria were used:

i. the enthalpy residual should be less than 1% of the total heat entering the domain; and
ii. the absolute values at the monitoring point (§D.7.1) should not change by more than about 0.1%.

In all simulations, the monitoring point was placed in the centre of the upper opening.

5.3.6 Obtaining a Solution

Satisfactory convergence (i.e. adherence to the above criteria) could not be achieved for Benchmark 1 using the default solution techniques (see Appendix D). The enthalpy residual was too large (Fig 5.4) and none of the absolute values were constant (Fig. 5.5).

For non-converging simulations, it is important to first check that the model has been accurately set up according to the problem definition, and also that this definition is an accurate numerical representation of the real problem. If convergence difficulties persist, it is necessary to consider the numerical techniques being employed to solve the discretised equations. Since there are only small oscillations in the absolute value plot (Fig. 5.5), it may be possible to obtain satisfactory convergence by using a more stable solution procedure. This can be achieved by imposing tighter *under-relaxation factors* which make the solution matrix more *diagonally dominant* and hence the solution procedure more stable (see §D.7.2). The trade-off attached to this approach is a degradation in convergence rate (i.e. the rate of decrease of the residuals is slower).

Many different combinations of under-relaxation factors were investigated, e.g. under-relaxation on the momentum equations only, under-relaxation on enthalpy only, under-relaxation on all equations, etc. Although all combinations had the effect of slowing down the solution procedure, none were able to eliminate the small oscillations on the absolute values or reduce the enthalpy residual sufficiently.

It was thought that the under-relaxation used was not specific enough to the type of flow being solved. The other type of under-relaxation available is *false time-stepping* (§D.7.2). This is less straight forward to apply, since a knowledge of the time-scale over which the flow is oscillating is required, which is of course difficult to determine prior to conducting the simulation. However, it was observed by analysing the flow field predictions of the non-converged solution, that although the default solution technique did not produce constant absolute values, it did produce a good *approximation* to the expected flow pattern in the region of

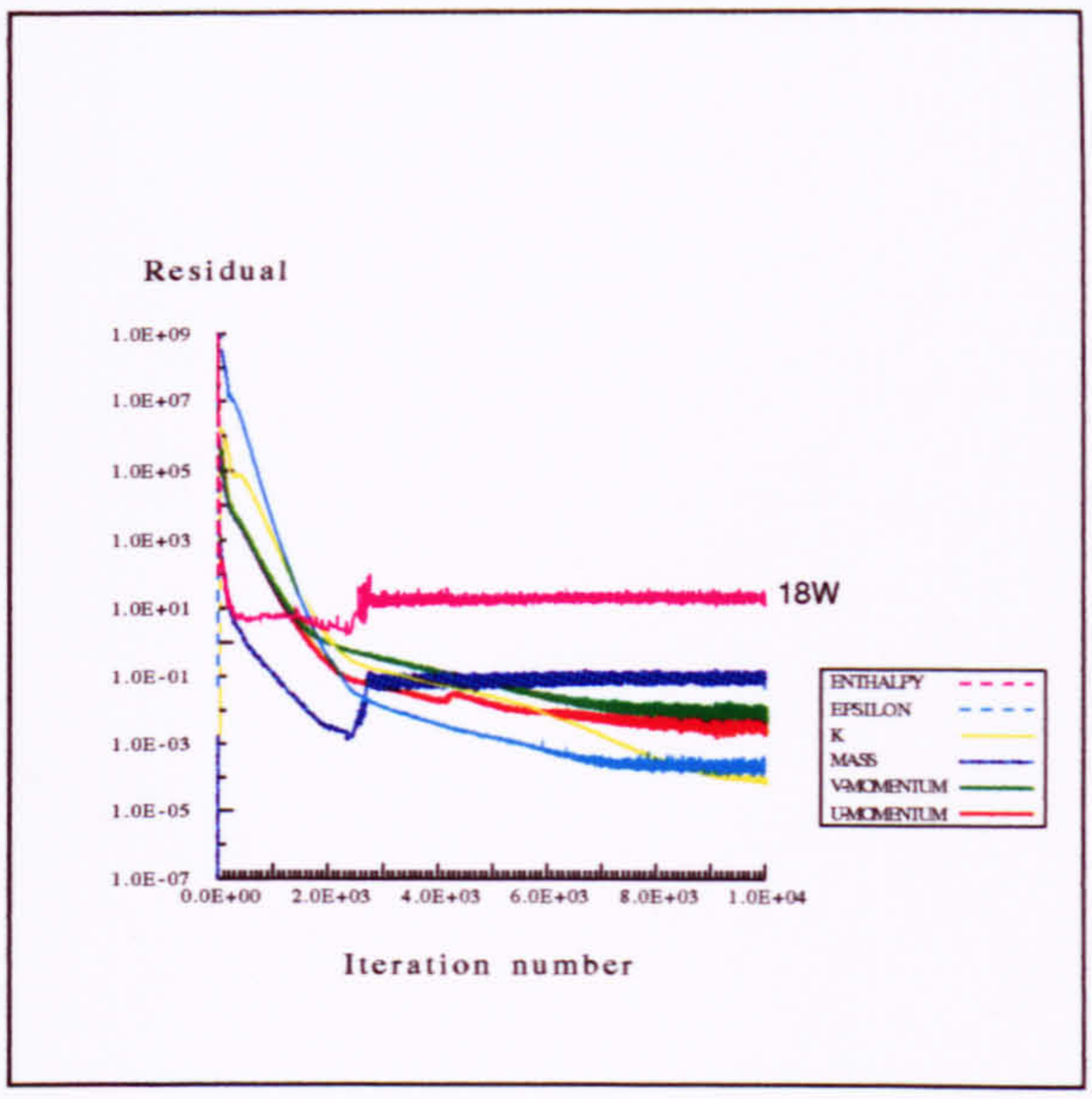

Figure 5.4 Equation residuals obtained throughout the solution process.

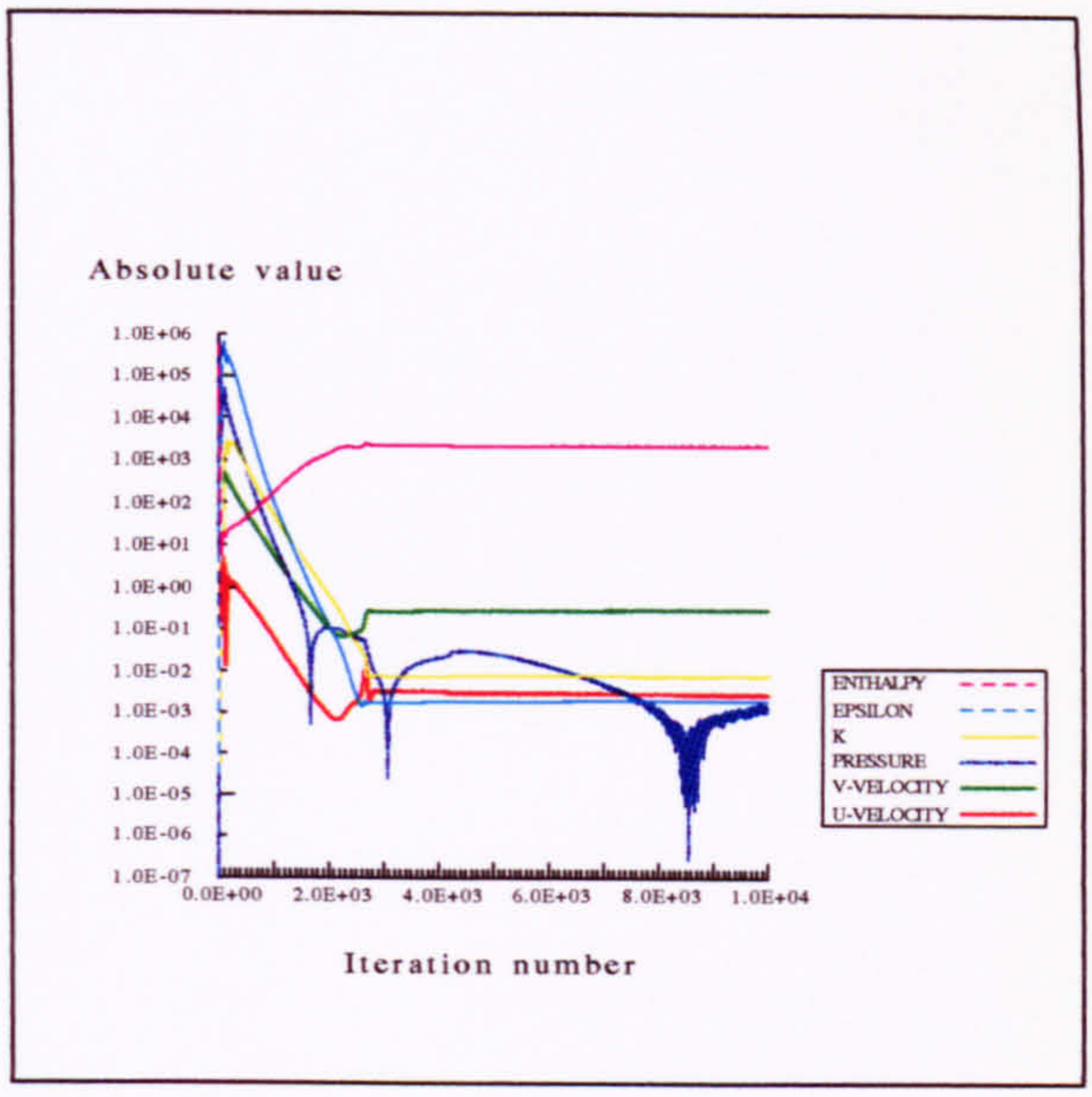

Figure 5.5 Absolute values at the monitoring point obtained throughout the solution process.

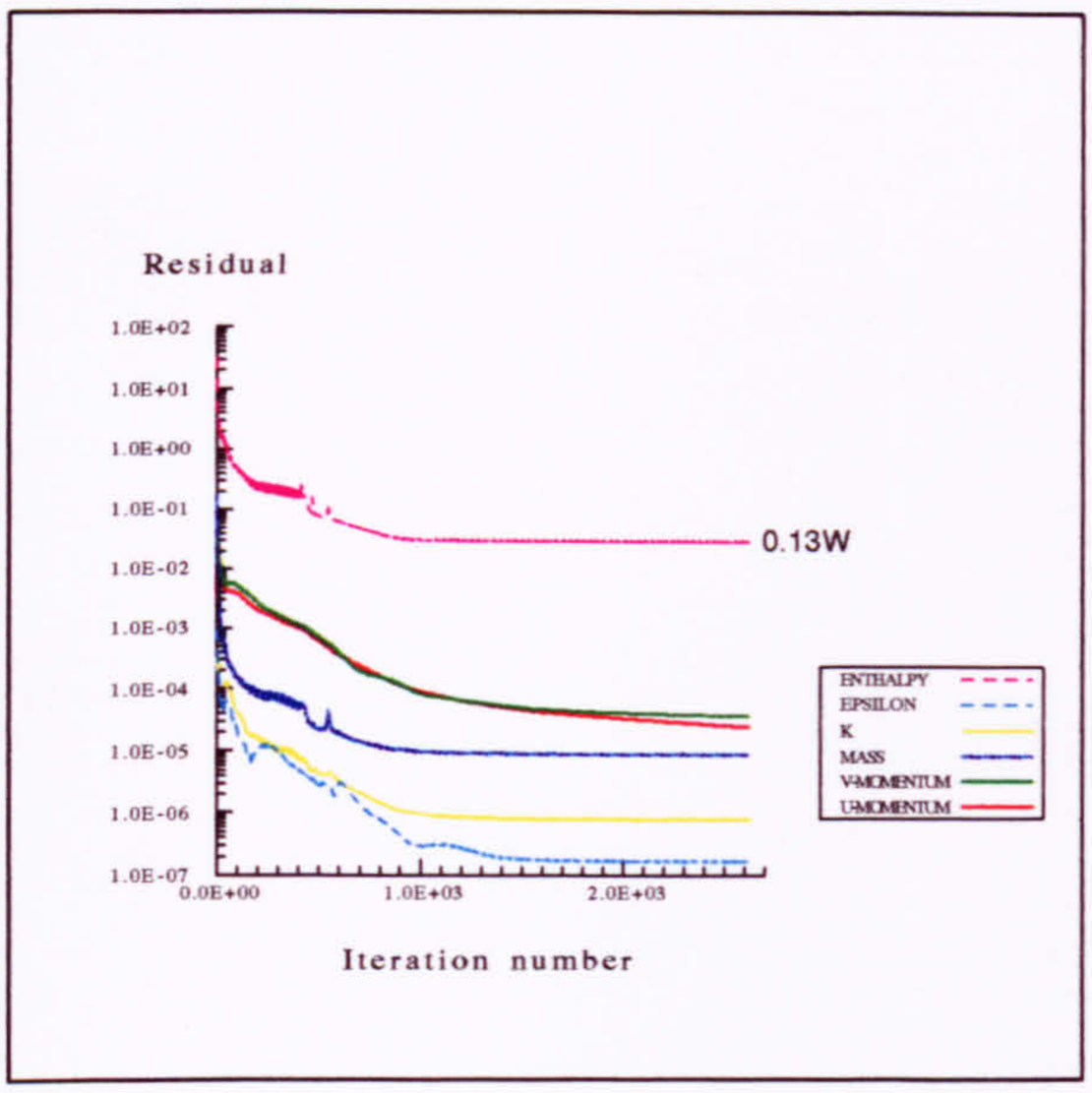

Figure 5.6 Equation residuals obtained throughout the solution process when using false time-steps of 0.1s on each momentum equation (restart of initial simulation).

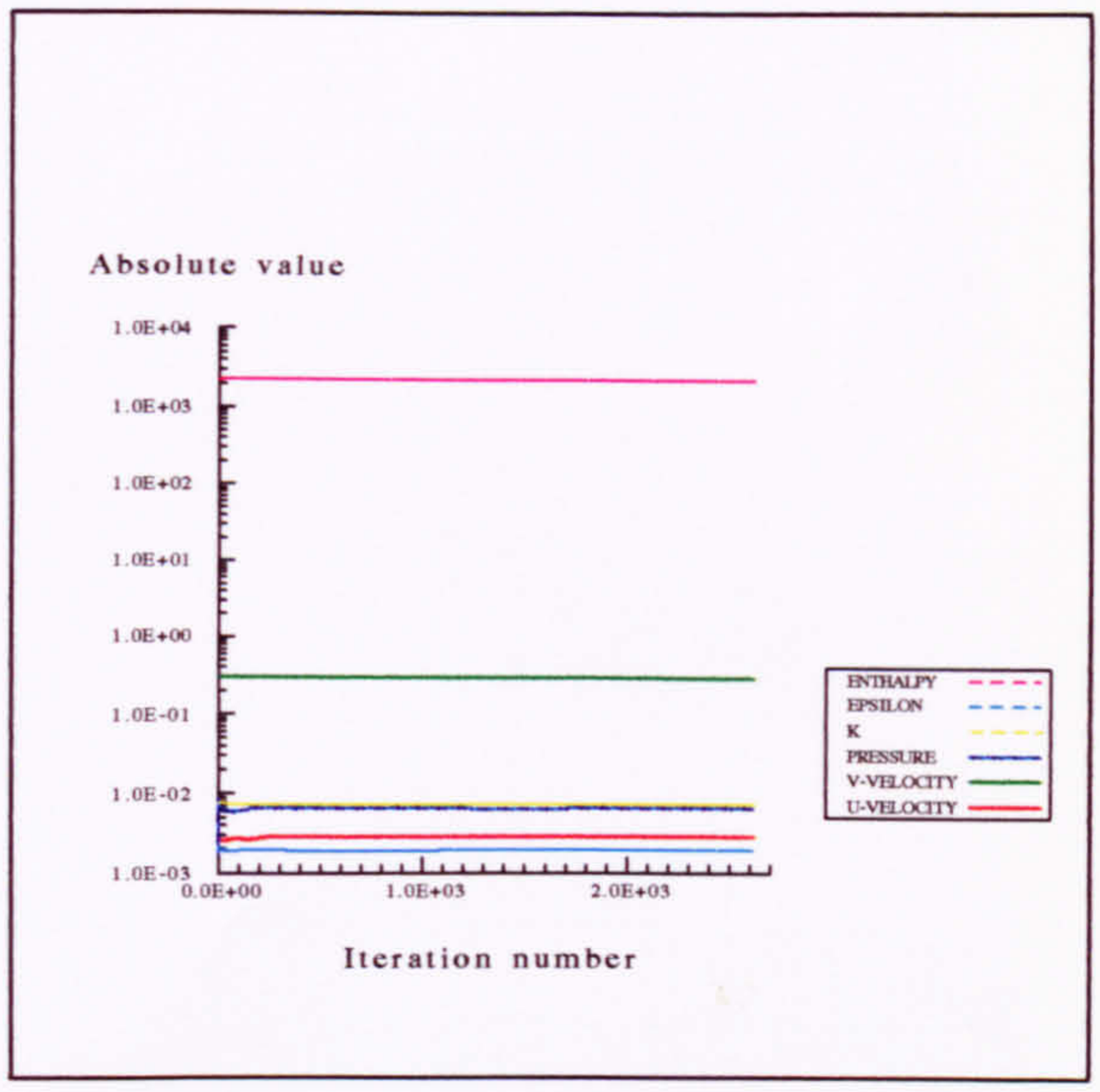

Figure 5.7 Absolute values at the monitoring point obtained throughout the solution process when using false time-steps of 0.1s on each momentum equation (restart of initial simulation).

interest (inside the space). This is an approximation in the sense that, since the iteration procedure adopted was unable to establish a definitive set of absolute values, it oscillated within a range of values close to the solution. Consequently, the result obtained using the default under-relaxation factors and no false time-stepping could be used to calculate a suitable time-scale for use as an initial guess to the false time-step required, by expressing the time-scale, t_f, as

$$t_f = \frac{\text{typical cell dimension (m)}}{\text{typical velocity (m/s)}} = \frac{d_f}{v_f}. \qquad (5\text{-}2)$$

v_f was calculated by finding the average velocity throughout the domain and d_f by using Equation (5-3).

$$d_f = \sqrt{\frac{\text{area of domain}}{\text{number of cells}}} \qquad (5\text{-}3)$$

It should be noted that a precise value of t_f was not sought and indeed not required to obtain an accurate solution. It simply acted as a time-scale factor that *controlled* the solution procedure.

Using equations (5-2) and (5-3), a value of about 2s was found. A *restart* simulation using this false time-step on the two momentum equations produced smaller oscillations in the absolute values but did not eliminate them completely. Another restart was run using the smallest cell dimension in the domain to calculate d_f, giving $t_f = 1.2s$. This produced further improvement but did not achieve constant absolute values. More simulations were carried out in which the false time-steps were gradually decreased. An optimum value of 0.1s imposed on the two momentum equations was established, whereby all convergence criteria were met (Figs. 5.6 and 5.7).

It is useful to investigate this value of t_f and compare it with equations (5-2) and (5-3). By using the smallest cell dimension for d_f ($= 0.0475\text{m}$) and the highest velocity in the plume ($\approx 0.32\,\text{m/s}$) for v_f (which is surely a characteristic velocity of

the flow), a value of $t_f = 0.15$s is found, which compares favourably with the optimum value used.

Now that a fully converged result had been obtained for Benchmark 1, this could be used as a reference with which variations in physical and numerical parameters could be compared. The detailed results for Benchmark 1 are now discussed.

5.4 Analysis of Benchmark 1 Results

Table 5.1 provides a summary of the numerical parameters and techniques used to obtain this result.

Table 5.1 Summary of numerical parameters and techniques used to obtain a solution for Benchmark 1.

Parameter/Technique	Details
Solution procedure	Hybrid differencing was used on all convection terms except in the mass conservation equation where central differencing was used. Pressure correction was carried out using the SIMPLEC algorithm. For further details see §§D.3.3 and D.4.2).
Turbulence	Standard k-ε (§4.5.4).
Enthalpy reference temperature	Ambient (= 18°C).
Buoyancy reference temperature	Ambient (= 18°C).
Under-relaxation factors	Default (momentum: 0.65, mass: 1.0, turbulent kinetic energy and dissipation: 0.7, energy: 0.7).
False time-steps	0.1s on u and v momentum equations in restart simulations.
Mesh	72×90 (see Fig. 5.3).
Boundary conditions	All surfaces are adiabatic ($Q = 0$) except the source ($Q = 200\ \mathrm{W/m^2}$) and possess the no-slip condition ($u_i = 0$) and wall functions described in §4.6.1. The domain boundary is made up of `SYMMETRY PLANE` boundaries (§4.6.3) and `PRESSURE` boundaries (§4.6.2) where $p = 0$ and $T = 18$ °C.

5.4.1 Discussion of the Flow Field

The resulting velocity field (Figs. 5.8 and 5.9) shows the rising plume from the heat source as expected. This forms a layer of warm, buoyant air in the upper

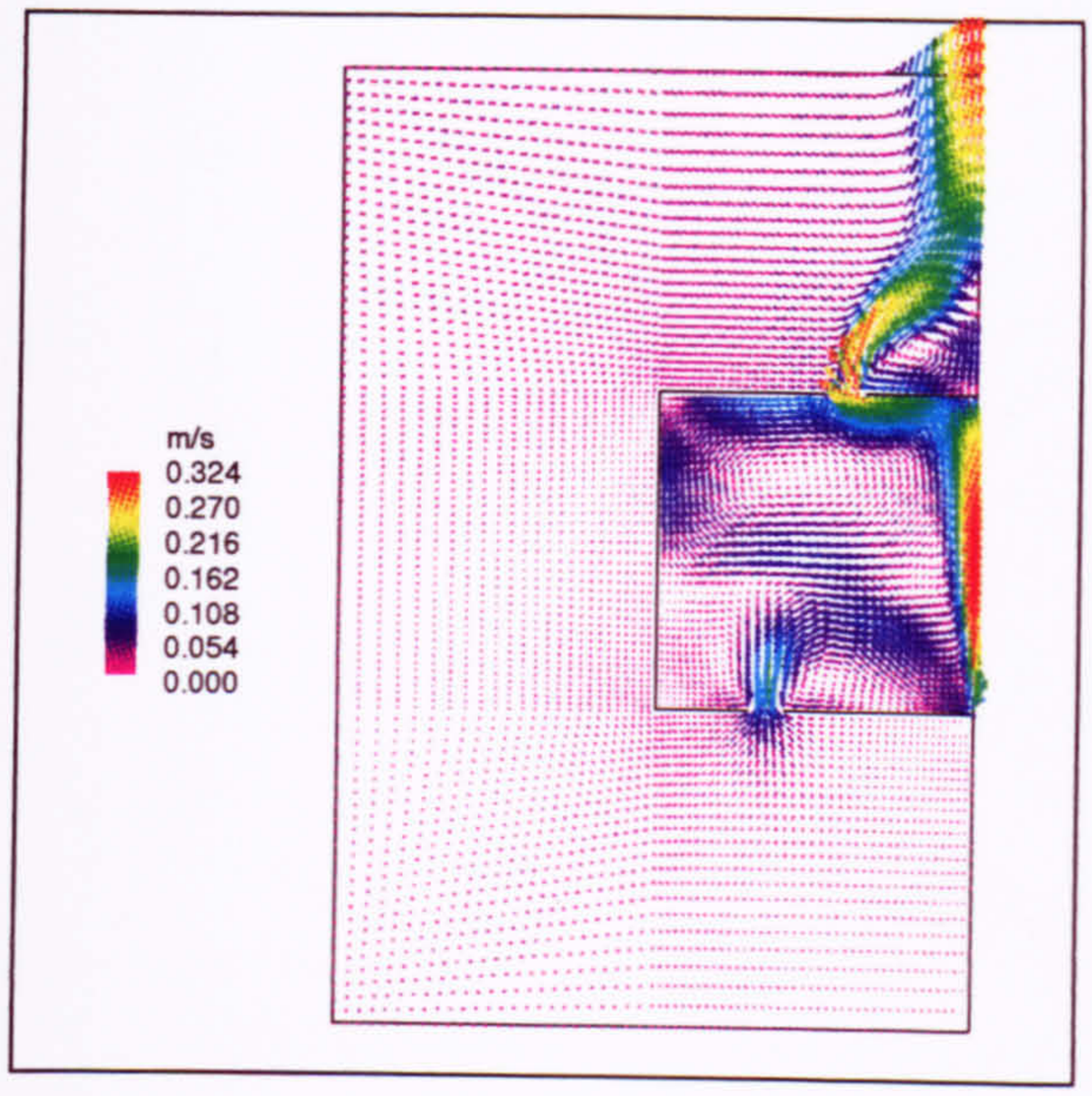

Figure 5.8 Predicted velocity field in whole domain for Benchmark 1.

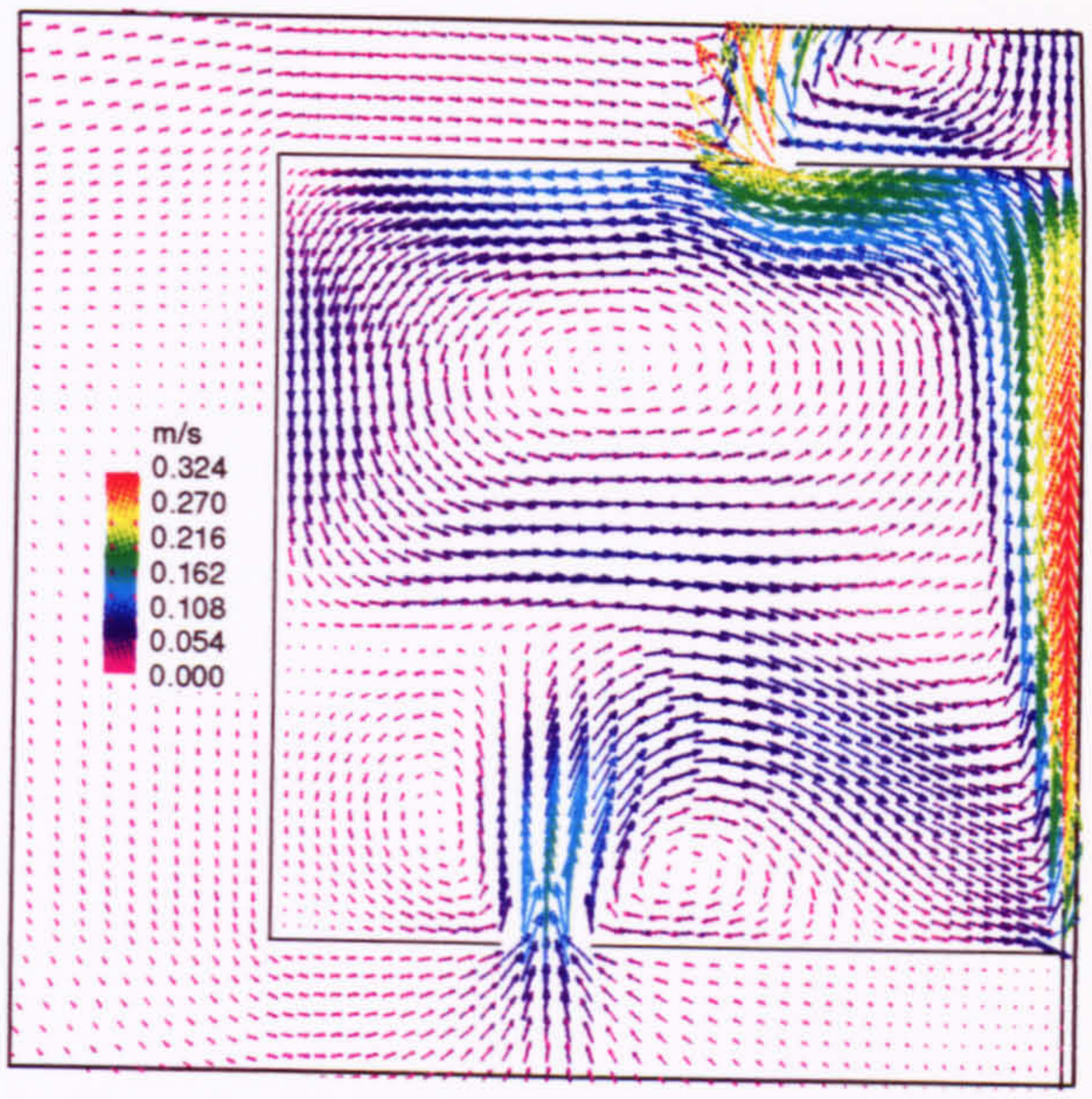

Figure 5.9 Predicted velocity field in space for Benchmark 1.

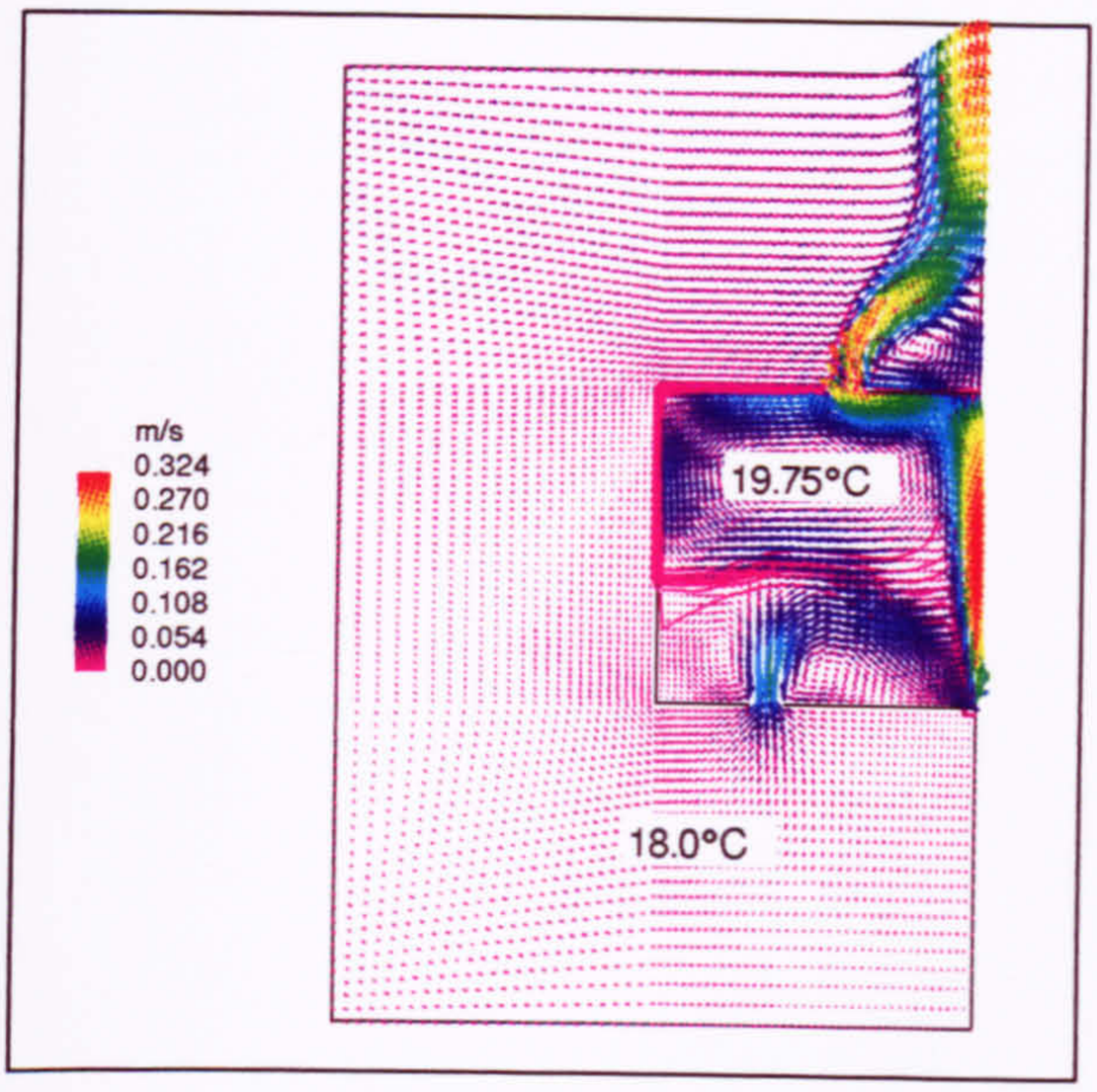

Figure 5.10 Predicted velocity and temperature field in whole domain for Benchmark 1 (contour interval = 0.25°C).

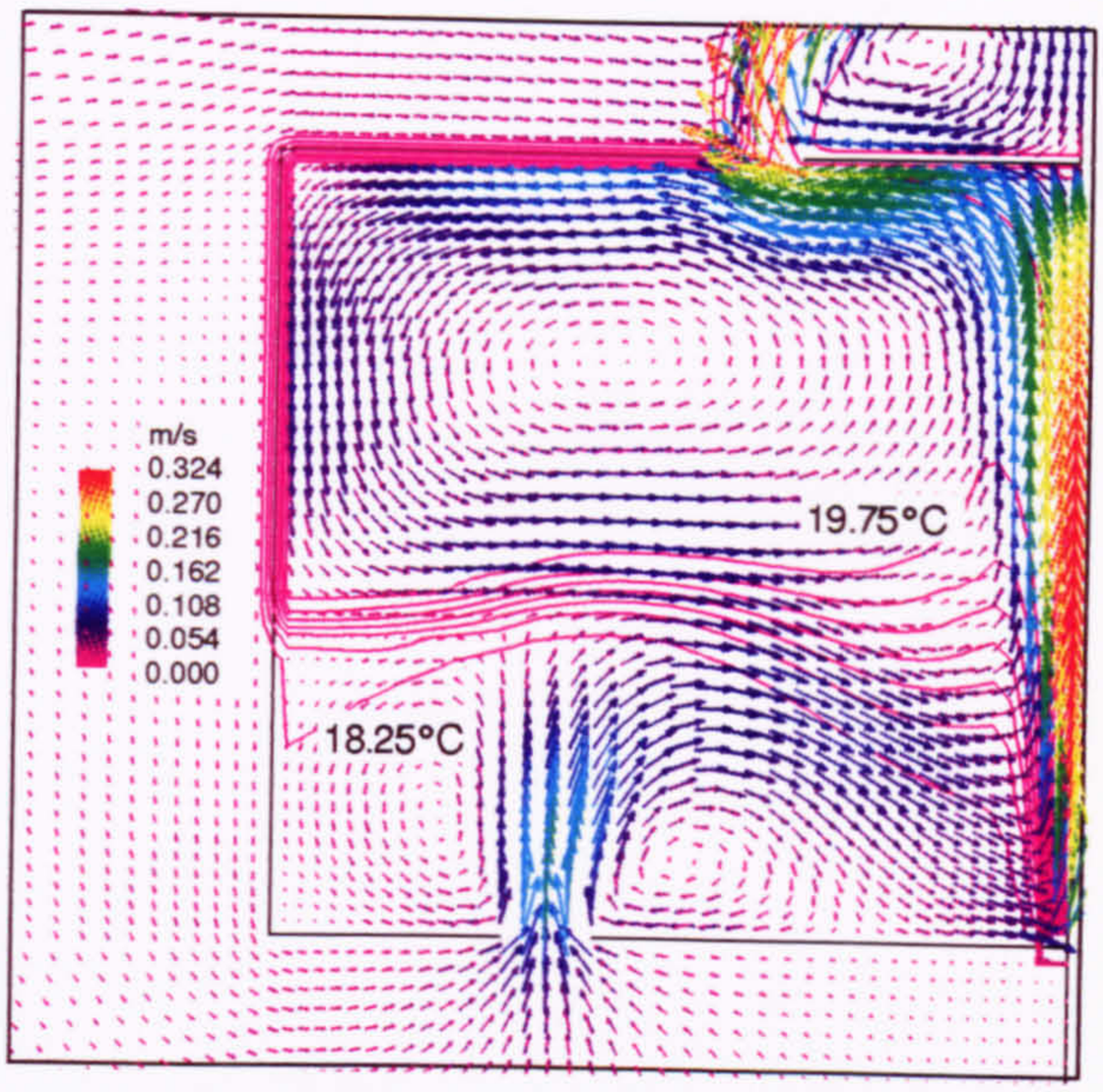

Figure 5.11 Predicted velocity and temperature field in space for Benchmark 1 (contour interval = 0.25°C).

region of the space which stratifies causing an interface to form separating the warm, buoyant air above, from the cooler, ambient air below (Figs. 5.10 and 5.11).

The interface is identified by the height at which there is least vertical motion outside the plume, and is accompanied by a sharp change in temperature. A steady state was achieved in which the rising plume entrains fresh, ambient air below the interface, and carries it into the upper part of the space where it recirculates and exits through the upper openings.

This flow pattern compared favourable with the description by Linden et al. (1990). The only slight cause for concern was the impingement of the incoming air on the interface. It was therefore considered prudent to measure the interface height *away* from this region, i.e. at the far left-hand-side of the box. Linden et al. (1990) predicts the airflow below the interface to have a vertical component toward the interface and a horizontal component toward the plume (Fig. 3.1). However, due to the infinite length of the openings in the CFD model (inherent in a 2D simulation), two recirculation zones were established below the interface, either side of the incoming air. Consequently, some of the air below the interface possesses a vertically *downwards* component.

As intended by the boundary conditions imposed, there is virtually zero flow in the exterior space, other than the rising plume forced out of the space by the layer of buoyant air in the space, and the surrounding air that it entrains.

A plot of the pressure field (Fig. 5.12) clearly shows a net pressure difference between air at the interface height inside the space, and that at the same height outside the space. This again supports the theory of Linden et al. (1990) by showing that the accumulated layer of warm air causes a hydrostatic pressure difference which drives the flow out of the space. Recall the following:

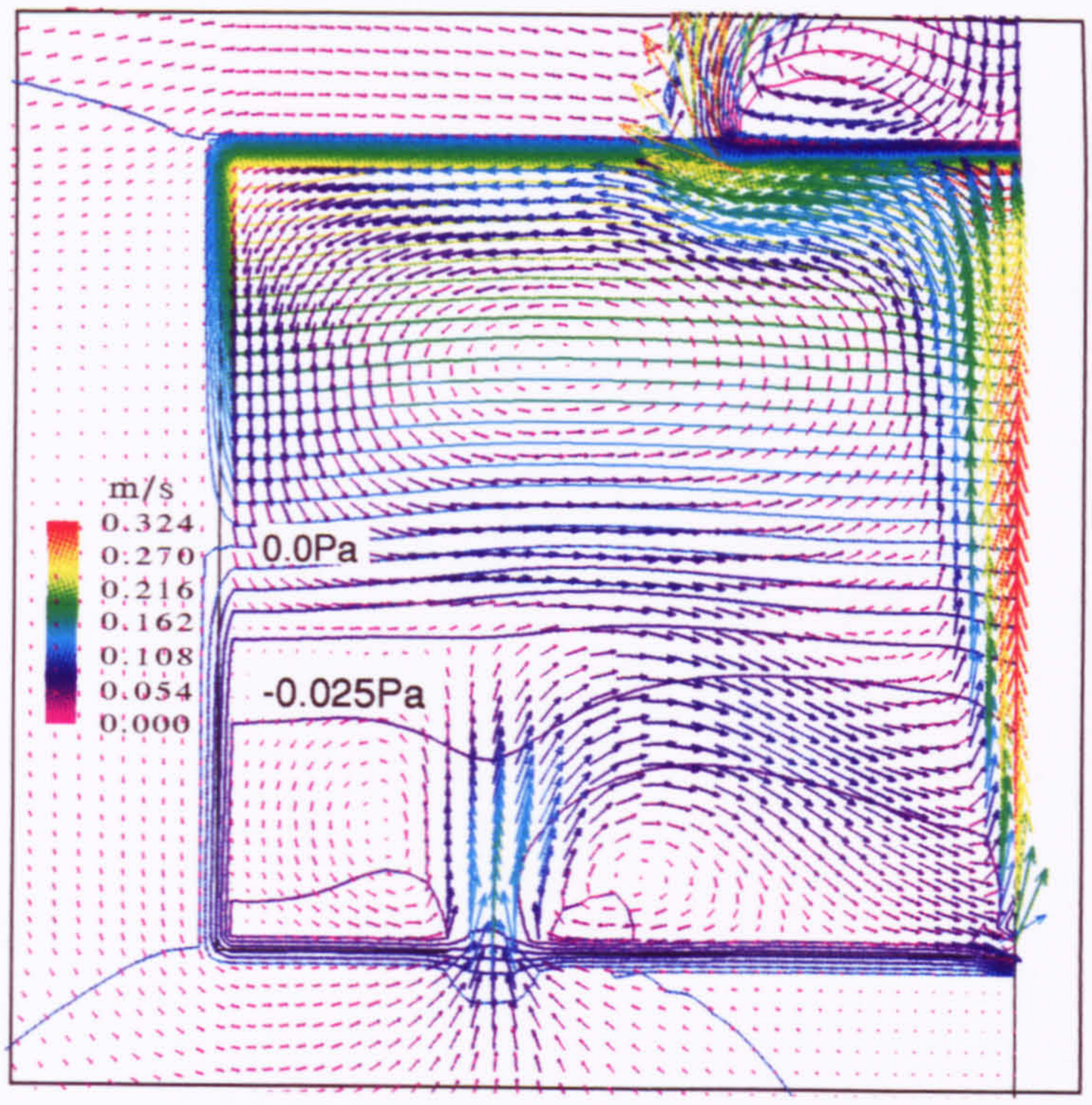

Figure 5.12 Predicted velocity and pressure fields for Benchmark 1 (all pressures are relative to $p = 0$ on the pressure boundary and the contour interval is 0.005Pa).

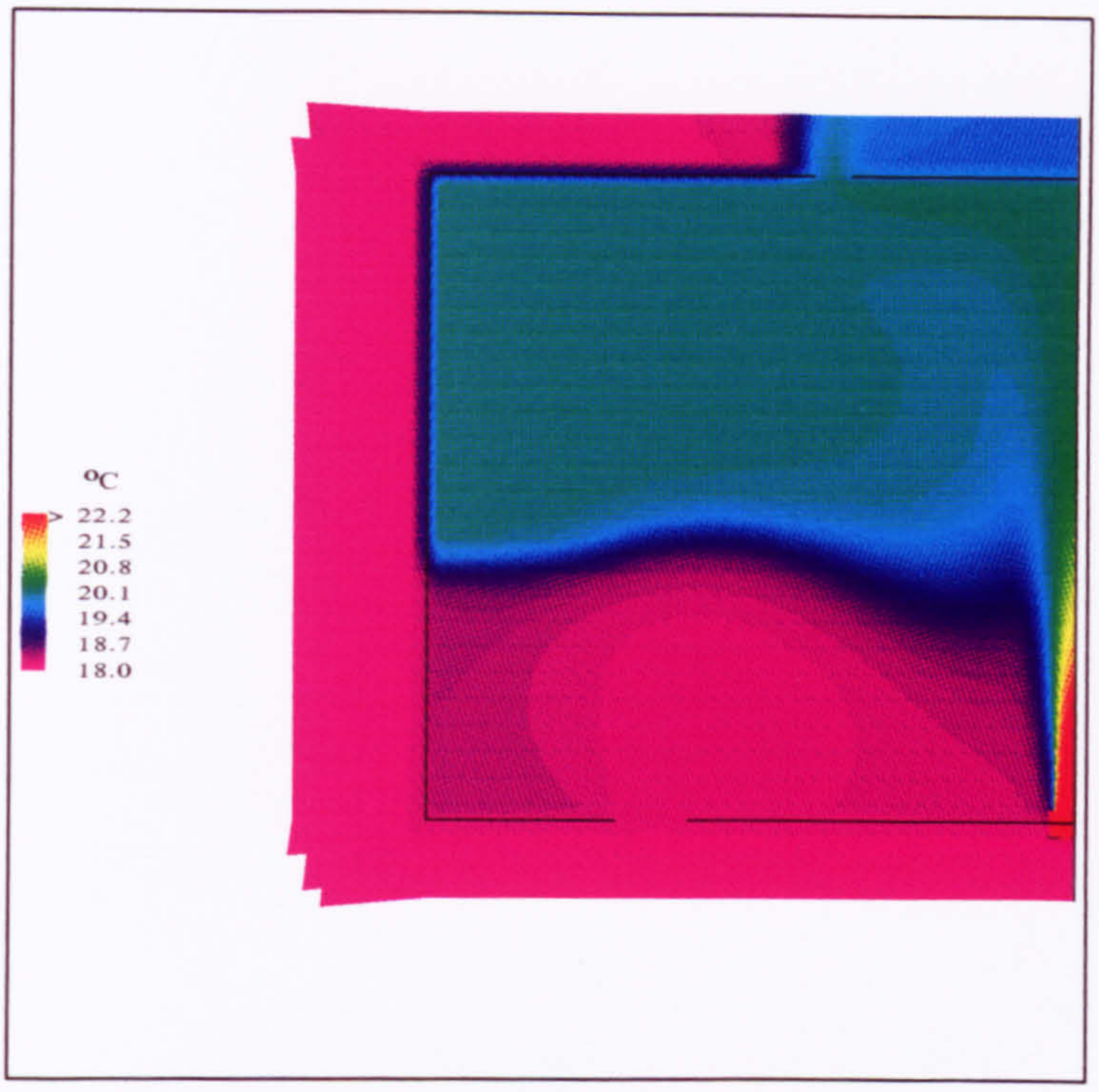

Figure 5.13 Temperature distribution for Benchmark 1 showing stratification of warm air above cool, ambient air.

> "... the layer of buoyant fluid near the ceiling will drive a flow through the openings since the hydrostatic pressure difference between the top and bottom of the layer will be smaller than that between the same heights in the denser fluid outside the space."
>
> Linden et al. (1990)

5.4.2 Vertical Density Profile

The stratification of the flow is shown clearly in a shaded contour plot of the temperature (Fig. 5.13). Buoyancy, g', was measured along vertical lines at five distances from the left-hand wall of the space (Fig. 5.14). The buoyancy is expressed in terms of enthalpy using Equation (3-2) ($g' = g\beta\Delta T$), and the relationship between temperature and enthalpy ($\Delta T = \Delta He/C_p$) to give:

$$g' = g\beta\Delta T = \frac{g\beta\Delta He}{C_p} = \frac{g\beta(He - He_{ref})}{C_p} = \frac{g\beta He}{C_p} \qquad (5\text{-}5)$$

where the reference value of enthalpy, He_{ref}, is taken to be the ambient value (= 0) since the ambient air temperature is the same as the enthalpy reference temperature at which enthalpy is defined to be zero (§5.3.2).

All buoyancy profiles, except that in the plume, show a sudden increase in density in the range $0.34 < h/H < 0.51$, suggesting an interface in this region. The most clearly defined interface was given by the profile at $x = 0.075$m, again suggesting that the best x-location for measuring h/H was in this vicinity (this is also the approximate location at which Linden et al. (1990) used a conductivity probe to measure the density in Figure 3.4).

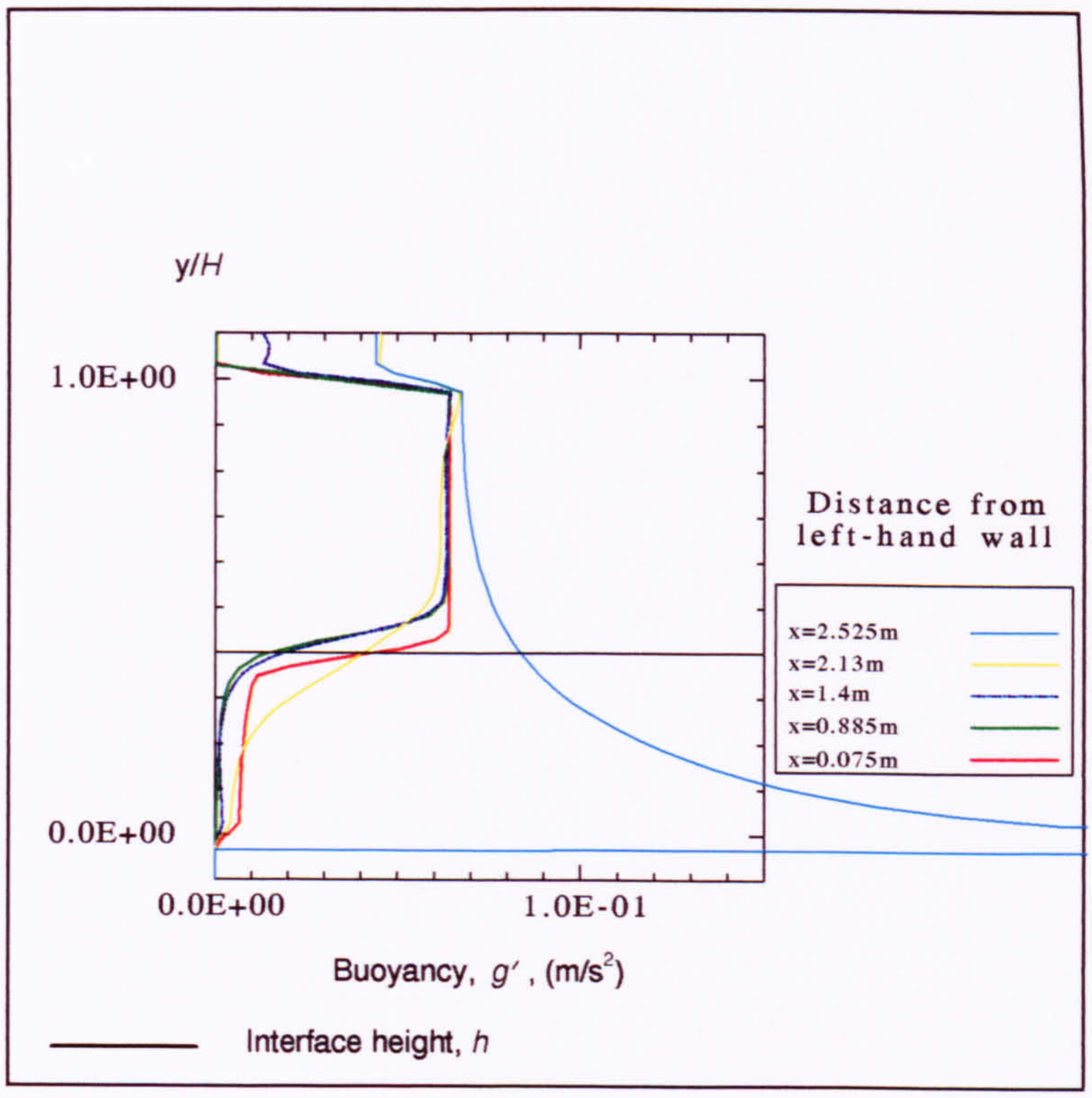

Figure 5.14 Buoyancy profiles for various *x*-locations along the space.

The profile plotted in the plume (at $x = 2.525\text{m}$) shows a large buoyancy value close to the source due to the large temperature difference produced. This gradually reduces as more and more ambient air is entrained. The theory states that all air above the interface should be of uniform buoyancy, *equal to that in the plume at the interface height* (Eq. 3-21). Figure 5.14 shows excellent agreement with the first part of this statement. The reason for the higher plume buoyancy at the interface level is because the theoretical prediction of the buoyancy above the interface is based on a plume-width-average of the buoyancy in the plume (not the value on the plume axis). In this case, a 'top-hat' profile is assumed which possesses a lower value than the axial value shown in the $x = 2.525\text{m}$ profile ($G'_T = G'_G / 2$ (Eq. (B-11)).

5.4.3 Interface Properties

The interface is estimated from Figure 5.11 at the $x = 0.075\text{m}$ location. This result is compared with the analytical prediction of Linden et al. (1990) in Table

5.2 along with the value of g'_h (the buoyancy change across the interface). Note that h is normalised with respect to the height of the space, and g'_h with respect to G'_H (the value of plume buoyancy at (the hypothetical) height H).

Table 5.2 Comparison of interface properties for Benchmark 1.

	CFD	Theory (Linden et al (1990))
h / H	0.390	0.603
g'_h / G'_H	1.84	1.66

These discrepancies are investigated as the chapter progresses.

5.4.4 Plume Behaviour

Accurate modelling of the plume is imperative if reliable results for the displacement ventilation flow pattern are to be obtained. The volume flux in the plume, M_L, determines the interface height, h, (since the interface forms when M_L is equal to the volume flux through the space), and the buoyancy change across the interface, g'_h, is determined by the reduction in buoyancy achieved after height h in the plume. By way of assessing the ability of the CFD program to model the plume, a measure of the entrainment into the plume (§3.4) was made. The 'top-hat' value of entrainment, α_T, was calculated as follows.

Vertical velocity profiles were plotted (Fig. 5.15) at 10cm vertical height intervals above the source in the vicinity of the plume. From these graphs it was possible to measure the characteristic plume width, b_G, from the plume axis to the point at which the axial velocity v_G had fallen by a factor of 1/e. The corresponding 'top-hat' values were then calculated (Table 5.3) and the variation of the 'top-hat' plume width b_T with height above the source plotted (Fig. 5.16). Enthalpy (He_T) which is also included in Table 5.3 is not plotted since only the axial value was required.

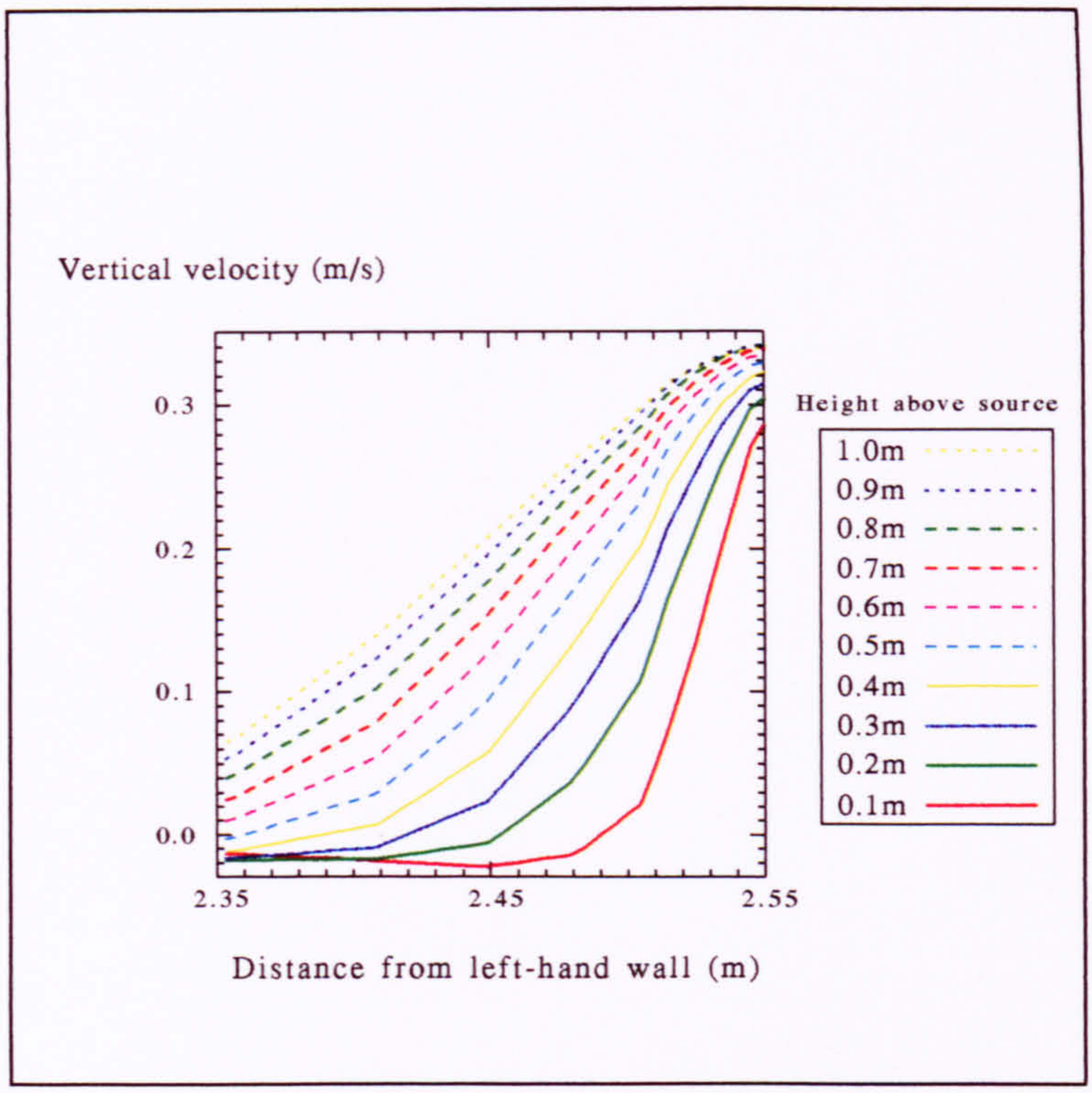

Figure 5.15 Vertical velocity profiles at 10cm height intervals in the vicinity of the plume.

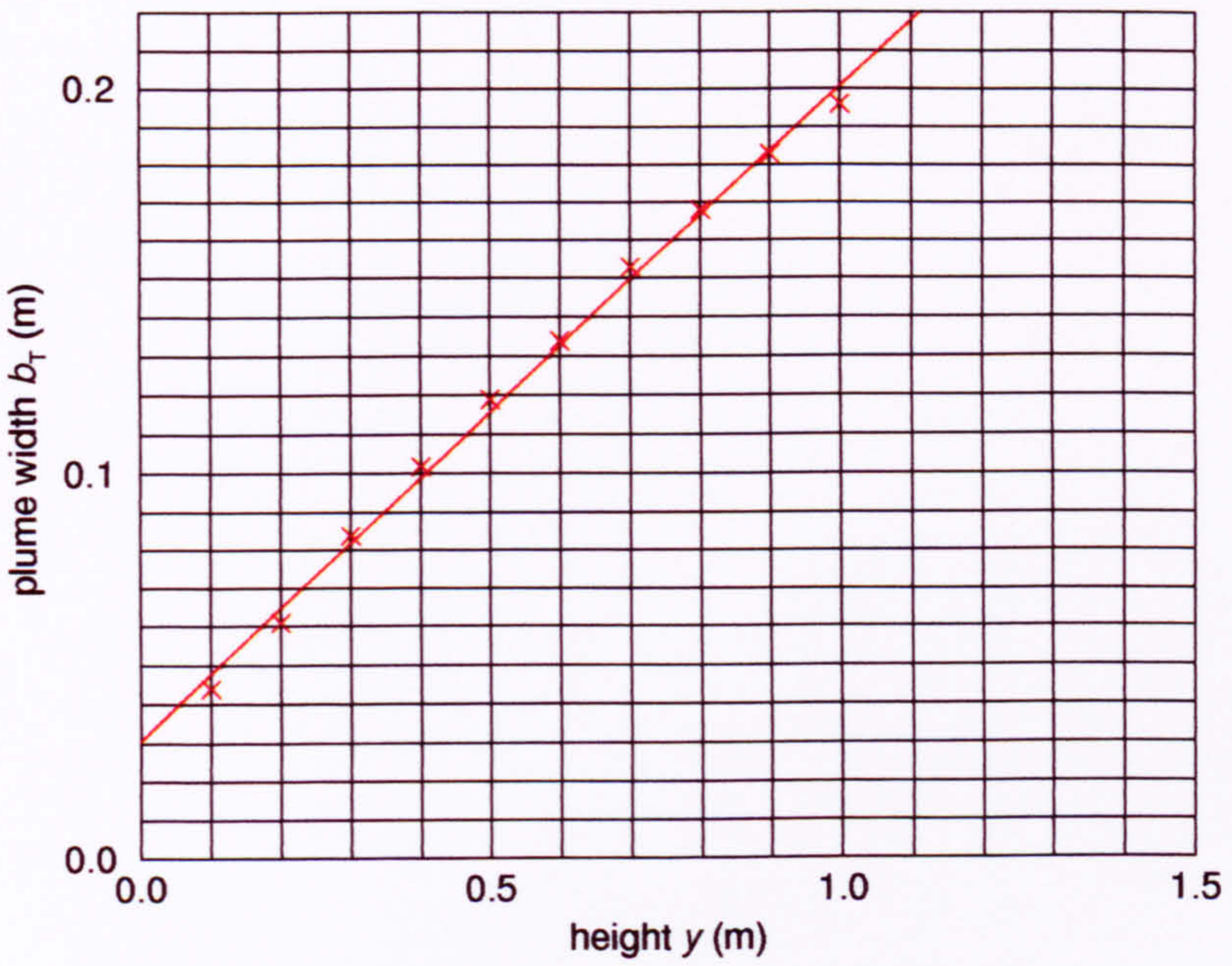

Figure 5.16 Variation of plume width with height above the source.

Table 5.3 'Top-hat' plume data calculated for Benchmark 1.

Height above source (m)	$v_T = \frac{v_G}{\sqrt{2}}$ (*)	$b_T = \sqrt{\frac{\pi}{2}} b_G$ (*)	$He_T = \frac{He_G}{2}$ (*)
0.1	0.203	0.044	5730.0
0.2	0.216	0.061	4142.8
0.3	0.223	0.084	3246.3
0.4	0.228	0.102	2683.6
0.5	0.233	0.119	2294.7
0.6	0.236	0.134	2013.8
0.7	0.240	0.153	1803.7
0.8	0.241	0.168	1643.8
0.9	0.241	0.183	1518.6
1.0	0.240	0.196	1420.8

(*) See Appendix B for derivation of these formulae.

From Equation (B-29): $b_T = \alpha_T y$, it is deduced that the gradient of the graph in Figure 5.16 is equal to α_T, therefore

$$\alpha_T^{k-\varepsilon} = 0.17.$$

It is simply noted at this point that the CFD model has predicted a larger value of entrainment than that used by Linden et al. (1990), and found experimentally by previous researchers (Morton et al. (1956), Rouse et al. (1952), and Baines and Turner (1969)).

Using the 'top-hat' plume quantities given in Table 5.3, the variations of volume flux in the plume per metre length, M_L, and buoyancy in the plume, G'_T, were calculated using

$$M_L = 2 b_T v_T \tag{5-6}$$

and

$$G'_T = \frac{g\beta(He_T - He_{ref})}{C_P} \tag{5-7}$$

respectively, where the reference value He_{ref} is equal to the ambient value of enthalpy (=0).

The variations of M_L and G'_T with height above the source are compared with the theoretical predictions using $\alpha_T = 0.1$ (used by Linden et al. (1990)) and $\alpha_T = 0.17$ as predicted by the CFD simulation (Figs. 5.17 and 5.18).

The equation relating volume flux in the plume with height above the source is Equation (3-25), which when rearranged as $y = \frac{M_L}{DB_L^{1/3}}$ can be compared directly with the linear graphs in Figure 5.17. Since the CFD model has predicted a linear relationship, this suggests that the CFD plumes are behaving qualitatively well. The difference in the gradient between the CFD prediction and the theory (for $\alpha_T = 0.1$) can be attributed to the higher value of entrainment predicted by the CFD model. Note the similarity in gradients between the CFD model and the theoretical line for $\alpha_T = 0.17$. The differences in the *y*-axis intercept are thought to be due to the assumption of an infinitesimally narrow line source in the theoretical analysis. In the CFD simulations, the source has a finite area which implies the existence of a '*virtual origin*' at some point *below* the source. Consequently, at $y = 0$ the CFD simulation predicts a non-zero volume flux, i.e. the volume flux that would be present had there been an infinitesimally narrow source at the virtual origin ($y \approx -0.12$).

The graph showing variation of plume buoyancy with height (Fig. 5.18) does not compare as well with the theory as the volume flux variation. The equation of the curve fitted to the CFD points is:

$$G'_T = 0.05y^{-0.6}$$

c.f. theory using $\alpha_T = 0.17$ (Eq. 3.26):

$$G'_T = 0.06y^{-1}.$$

From these equations and Figure 5.18, it is observed that the discrepancy in plume buoyancy is not caused solely by the discrepancy in entrainment. Rather, the CFD has predicted a different *variation* of G'_T with B_L, α_T, and *y*. This is substantiated by the non-linear variation between G'_T with y^{-1} (Fig. 5.19).

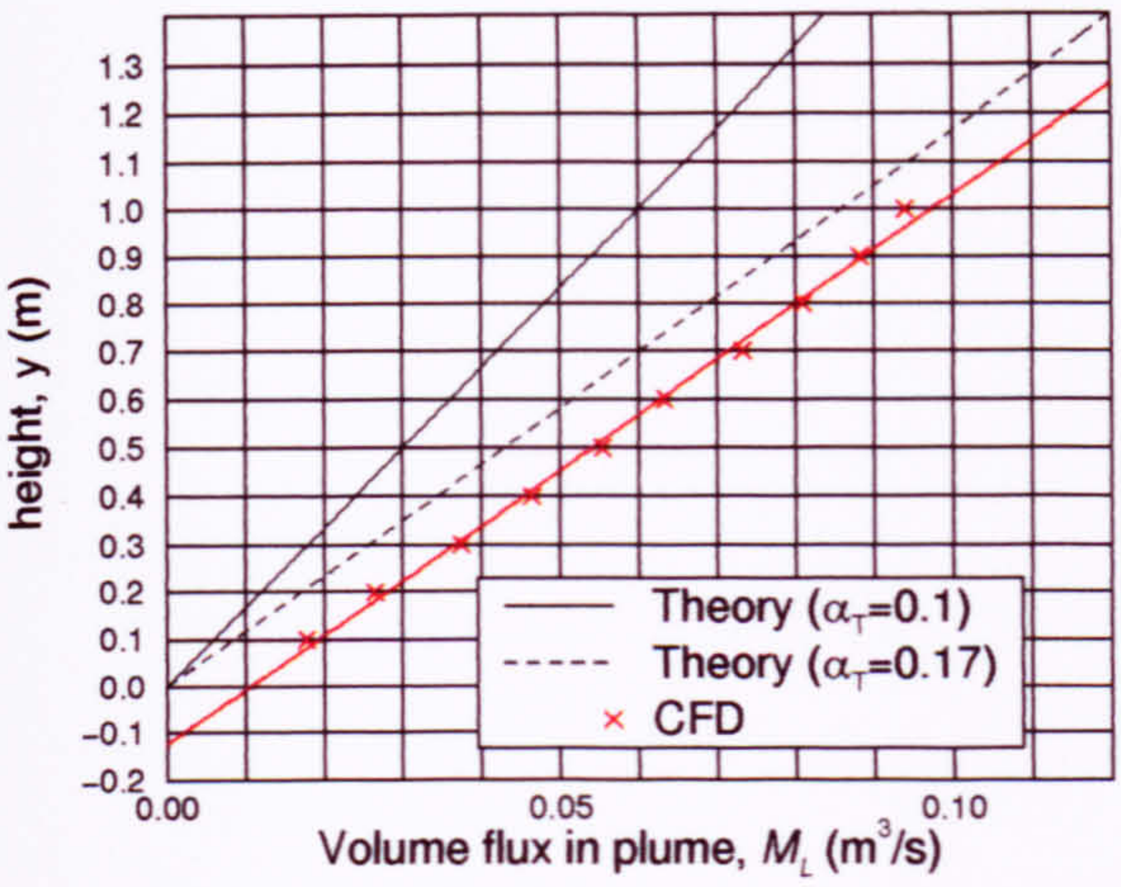

Figure 5.17 Variation of volume flux in the plume with height.

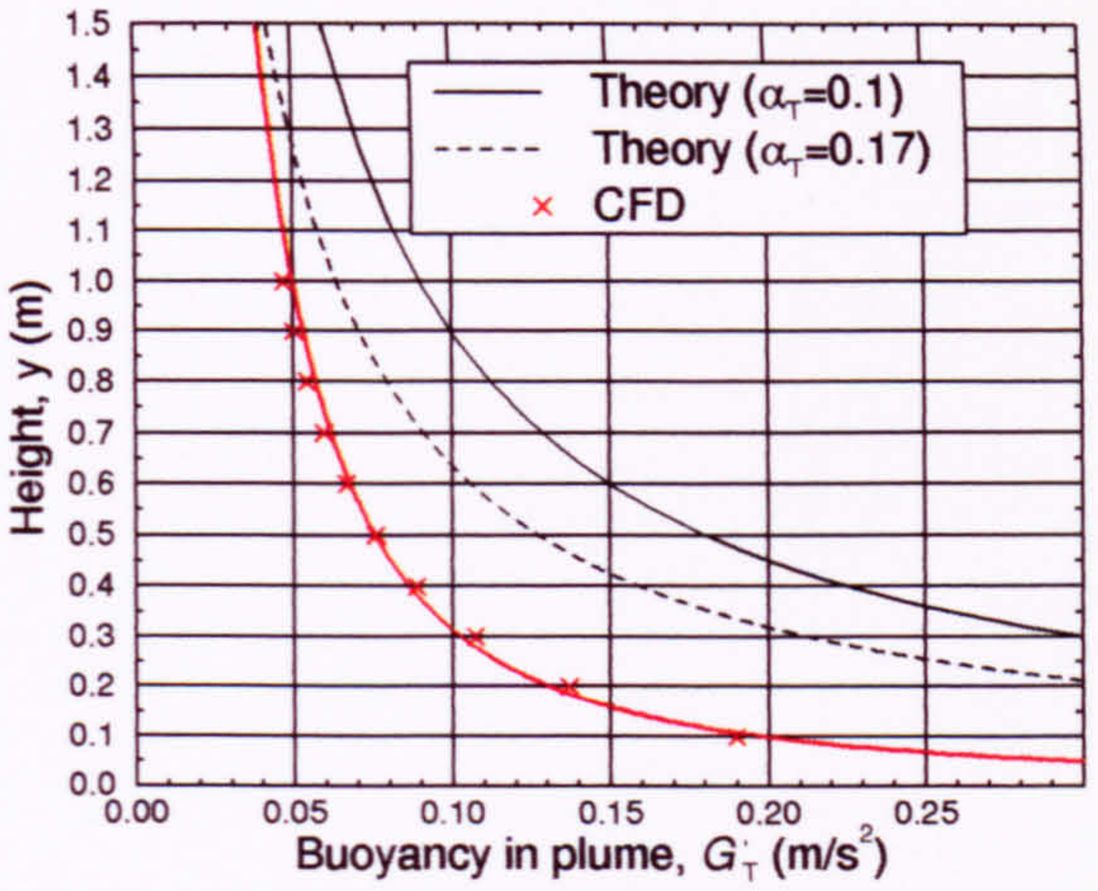

Figure 5.18 Variation of buoyancy in the plume with height.

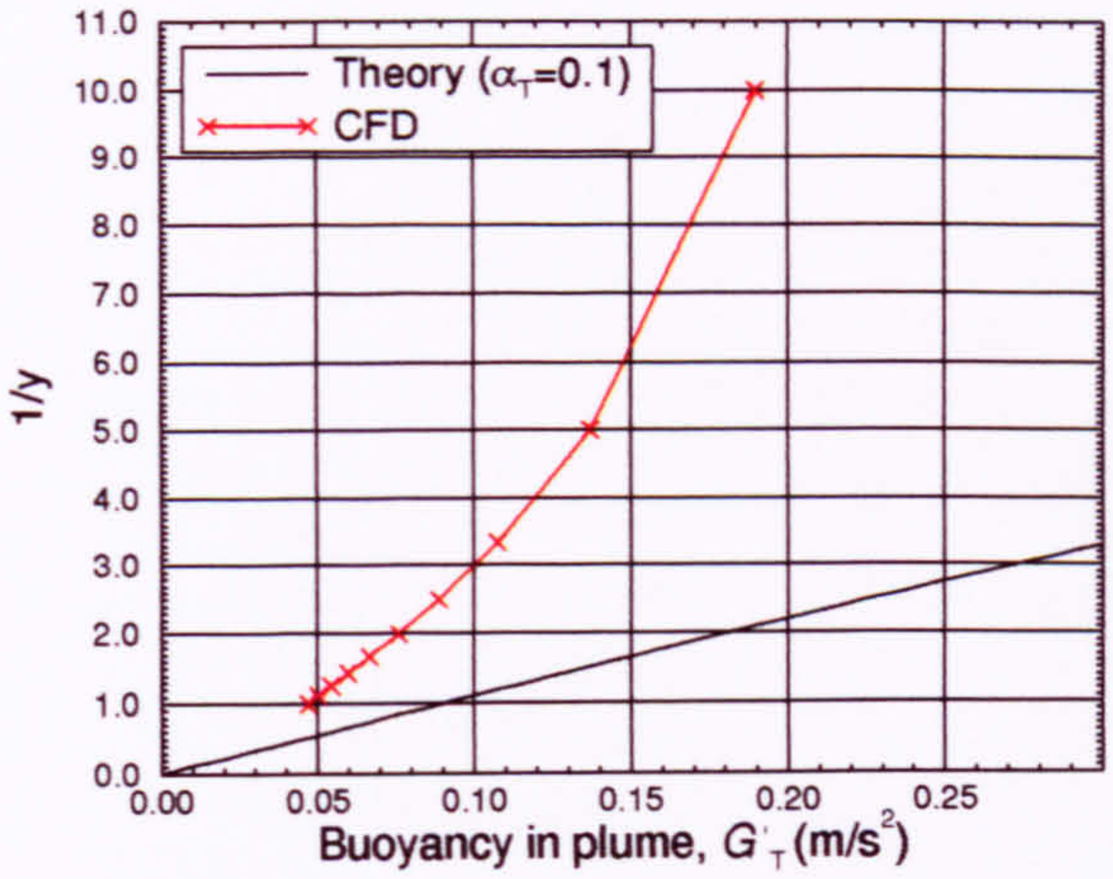

Figure 5.19 Variation of buoyancy in the plume with y^{-1}.

One factor contributing to this phenomenon is the virtual origin. Recall from Figure 5.14 that there exists a large buoyancy gradient low down in the plume. The effect of the virtual origin is to remove the lower part of the plume where the large values of buoyancy occur. As a result, the values predicted by the CFD model are less than the theoretical values, and the larger values close to the source are omitted. Consequently, the buoyancy gradient is altered. This is discussed further in Chapter 8 (§8.3.3).

5.5 Mesh Investigation

Mesh dependency in CFD simulations can potentially provide a source of error in the results. It is therefore important to investigate the effect of the mesh on the solution, and ensure that an adequately detailed mesh is being used.

All CFD simulations must begin with an estimate as to how dense the mesh should be and in which areas more grid nodes are likely to be needed. This can then be used as a starting point from which to alter the mesh density so that a *mesh independent solution* (one that does not depend significantly on further refinement) is obtained within an acceptable amount of computing time.

Although the mesh density is sometimes accountable for discrepancies, it should be remembered that, at best, the mesh can only be expected to give accurate results for the *mathematical* model being solved. For example, in this work, once a value for the interface height, h, had been established such that further mesh refinement produced no significant changes in h, even if this value did not agree with that obtained experimentally, it would have been pointless to continue the refinement in the hope that, eventually, a result much closer to that of the experiment would be found.

The properties used to determine whether or not a mesh independent solution had been established were the vertical velocity profiles in the vicinity of the plume and the buoyancy change across the interface, g'_h. Five different meshes were investigated (Table 5.4).

Table 5.4 Meshes used to identify optimum mesh density and refinement.

Case	Description	Resolution (*x*-direction vs. *y*-direction)
MESH1	This is the reference case already investigated (Fig 5.3).	65 × 90
MESH2	Finer than MESH1, but same block structure*.	101 × 134
MESH3	Finer than MESH2, but same block structure*.	157 × 210
MESH4	Coarser than MESH1, but same block structure*.	38 × 44
MESH5	Same resolution as MESH1 in room, but coarser, non-orthogonal (skewed) mesh, in exterior (Fig 5.20). This mesh uses a different block structure to the other four meshes with the aim of reducing simulation times.	Interior: 42 × 40 Exterior: 25 × 124**

* For information on block topology in CFX see §D.2.

** 124 is the number of cells around the perimeter of the domain (excluding the symmetry line).

Convergence was extremely difficult to achieve for MESH5 (the highly skewed mesh). For the default under-relaxation factors, the solution process rapidly diverged (i.e. the residuals rapidly increased to values that could no longer be stored in the computer, resulting in no solution being attained). Even reducing the false time-steps could not prevent divergence. Convergence could only be achieved by specifying under-relaxation factors of 0.1 on the two momentum equations. As already pointed out (§5.3.6), any type of under-relaxation slows down convergence. Under-relaxation factors of 0.1 are considered to be extreme constraints on the iteration process and therefore undesirable due to high simulation times. The rapid divergence was thought to be due to the deferred correction approach adopted in the CFX solver algorithm (§D.9). On non-orthogonal grids, this can cause very small values of ε at a localised set of points, giving rise to unphysically high values of the turbulent viscosity, μ_t $(= C_\mu \rho \frac{k^2}{\varepsilon})$. This is discussed further in section 8.2.2.

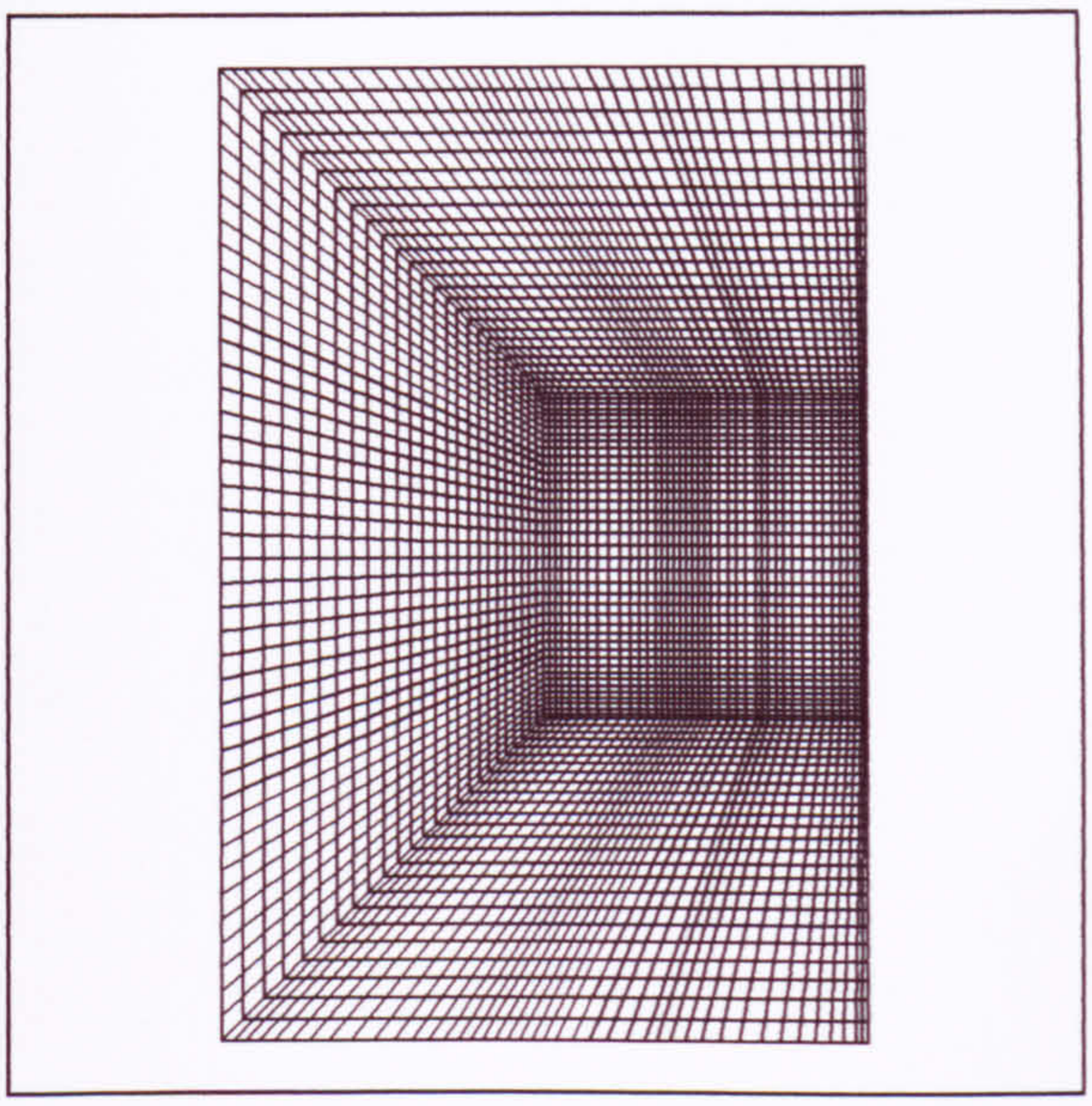

Figure 5.20 Non-orthogonal mesh (MESH5 in Table 5.4) used to produce a coarser mesh in the exterior domain.

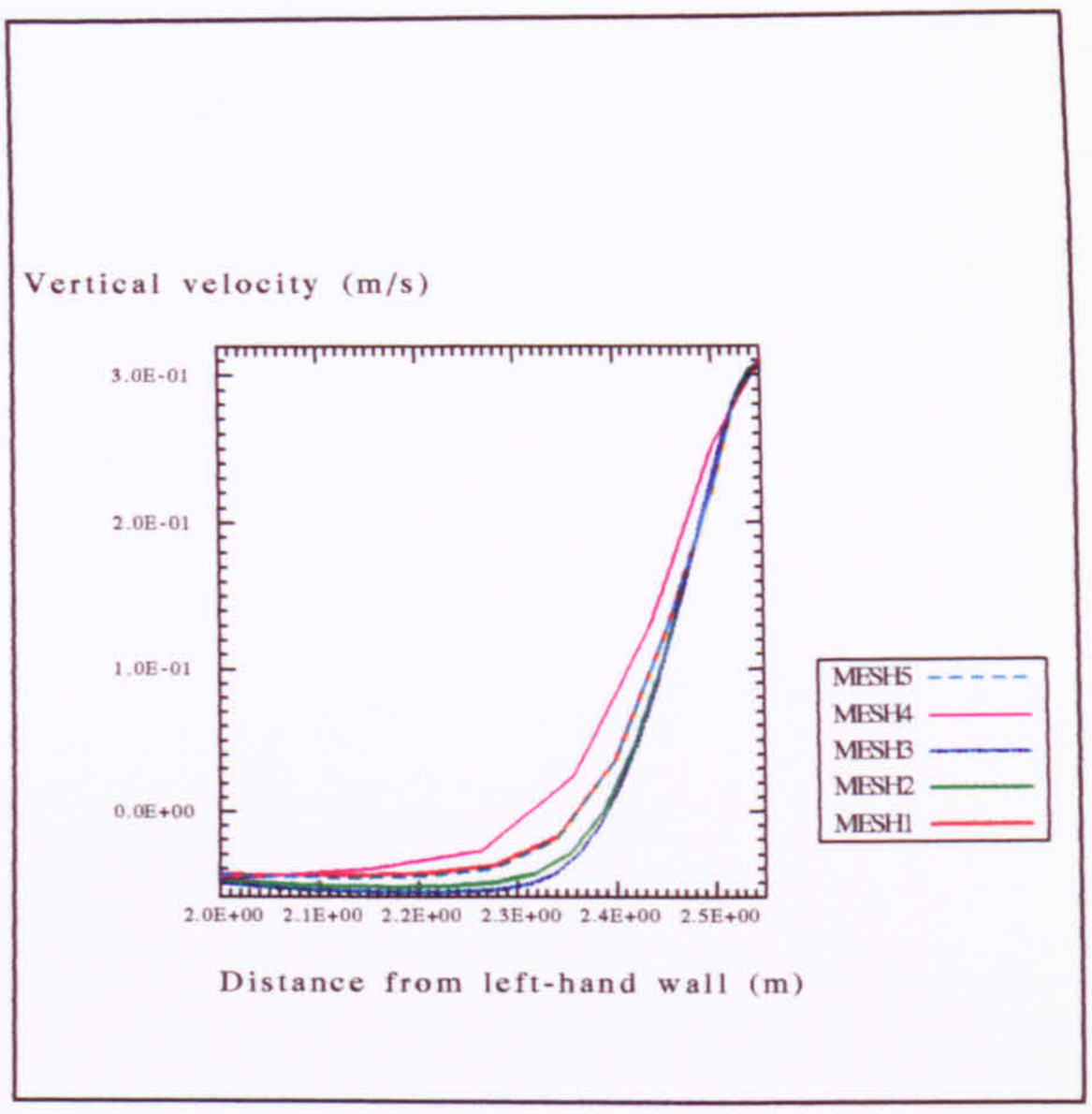

Figure 5.21 Vertical velocity profiles at 0.3m above the floor for various meshes (Table 5.4).

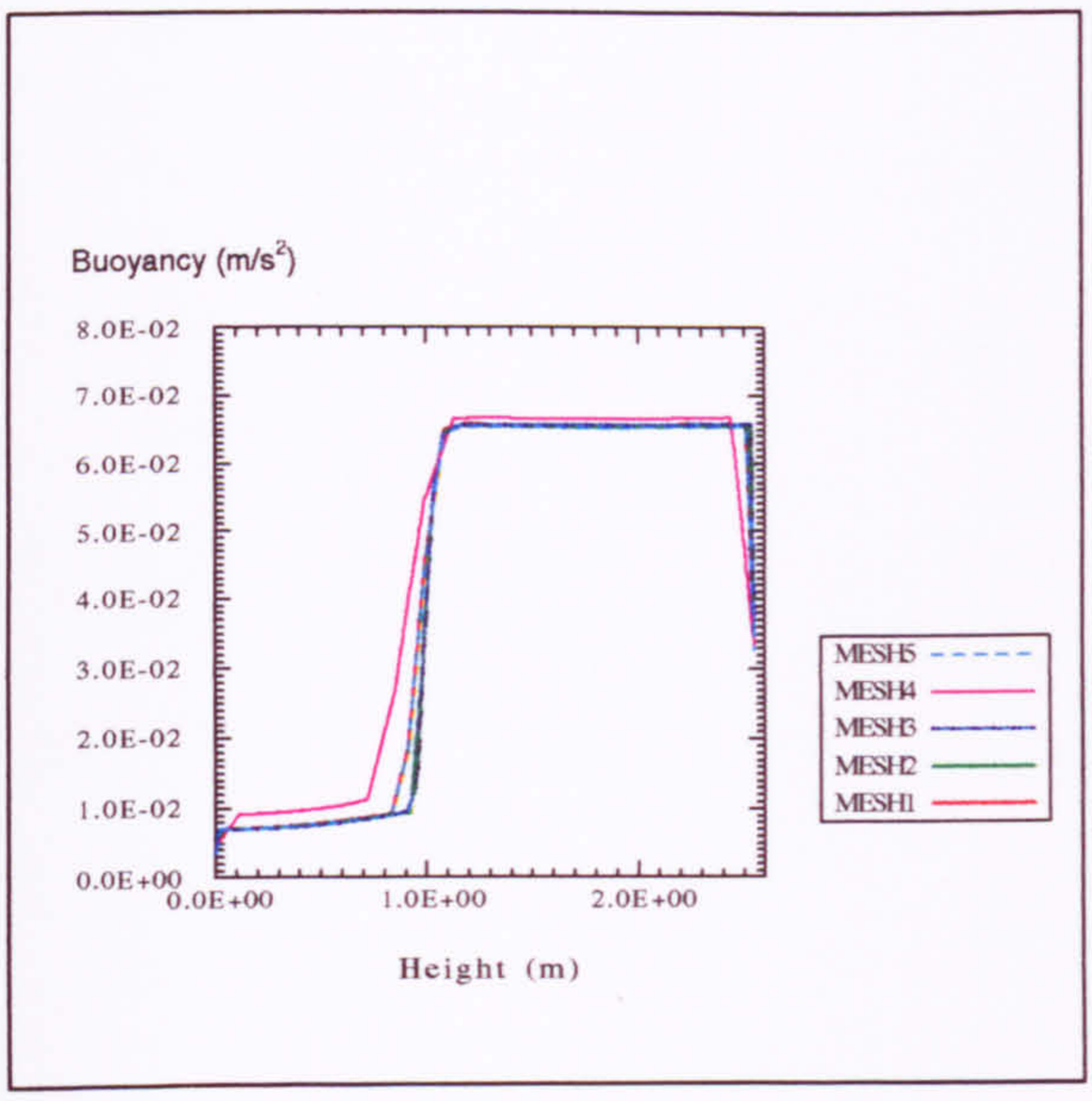

Figure 5.22 Change in buoyancy along line $x = 0.2$m for various meshes (Table 5.4).

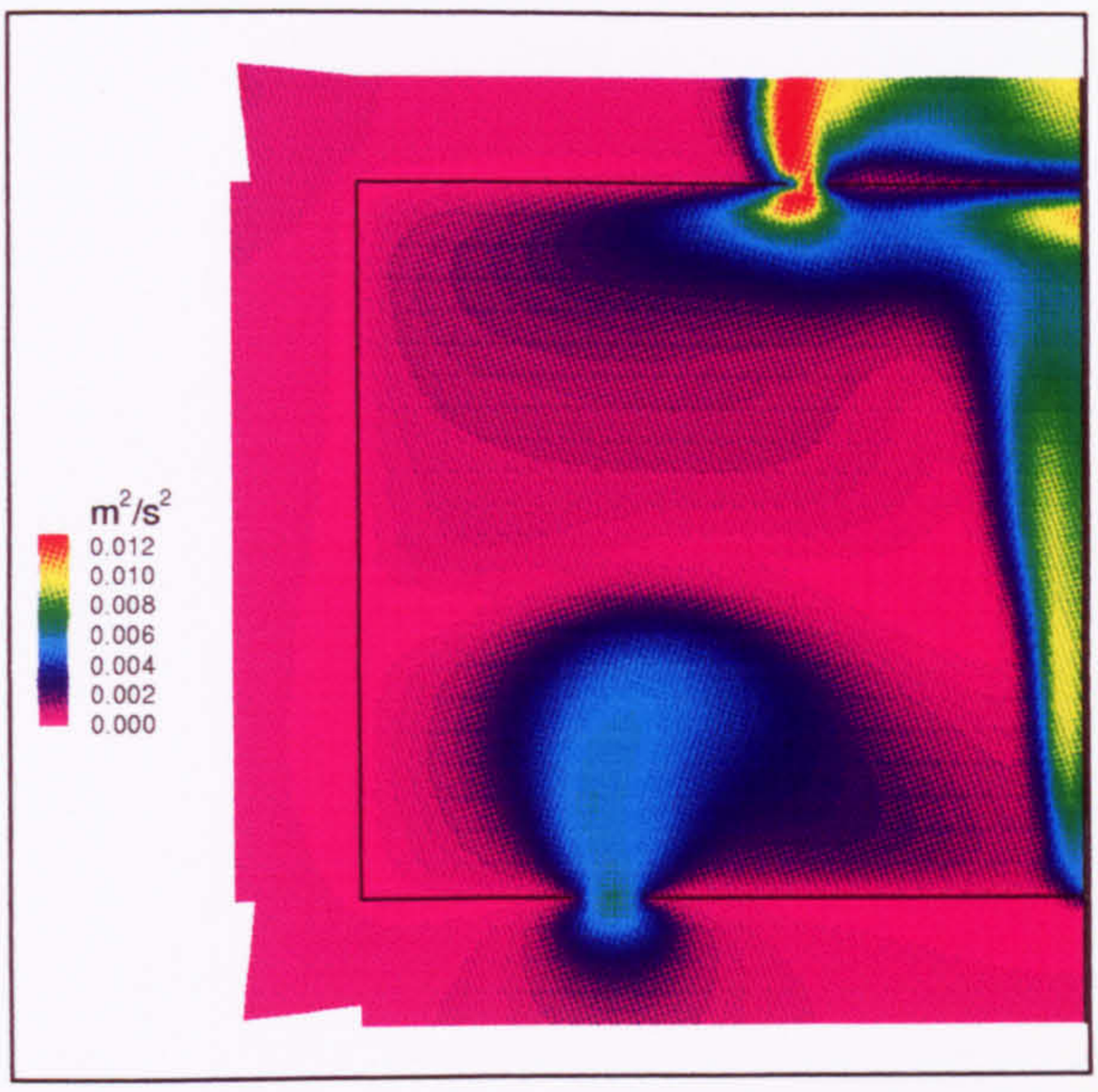

Figure 5.23 Distribution of turbulent kinetic energy k.

The vertical velocity profiles predicted by each mesh in the vicinity of the plume show very similar results (Fig. 5.21). The largest differences are observed in MESH4 where a wider plume is predicted. However, to enable accurate prediction of the axial plume properties v_G and He_G, it was deemed necessary to use a mesh resolution in the plume with a length scale smaller than the width of the heat source - cells of dimension 1cm × 1cm were used. The comparison in the predicted values of g'_h (Fig. 5.22) also shows the largest differences to be in the MESH4 results where a more diffuse interface is predicted.

It was decided that MESH1 (with a finer mesh in the plume[1]) gave a sufficiently mesh-independent solution to enable accurate measurement of flow properties such as plume width, interface height and stratification strength. However, due to potential convergence problems when using non-orthogonal grids, all non-orthogonalities in MESH1 were removed.

5.6 Effect of Turbulence Model

Another important consideration in CFD modelling is the method used for representing turbulence. This is of particular importance when modelling buoyancy-driven flows since the plume, which governs these flows, induces additional turbulence effects (Fig. 5.23).

An indication of whether or not a buoyancy-driven flow is turbulent is given by the Rayleigh number, Ra:

$$\mathrm{Ra} = \frac{\beta g \rho^2 l^3 \theta C_p}{\mu \lambda} \qquad (5\text{-}8)$$

where, for the plume:

l = typical length scale, h say, and

[1] Following feedback of the work in this section to §5.4.4 (plume behaviour), all of the plume properties (α_T, M_L, G'_T, etc.) were calculated from simulations which employed a finer mesh in the plume.

θ = temperature difference between plume axis and entrained air, say.

The flow in the plume has a Rayleigh number of the order of 1×10^9. The onset of turbulence is said to occur in the range $10^6 < \mathrm{Ra} < 10^9$ (Jones and Whittle (1992)). It is therefore reasonable to assume that the flows investigated here are turbulent.

So far, the standard $k-\varepsilon$ turbulence model of Launder and Spalding (1974) has been employed. This was used as it is widely accepted as being the industry standard turbulence model capable of modelling many different flow types to an acceptable degree of accuracy. However, some researchers (Ideriah (1980), Fraikin et al. (1982), and Thompson et al. (1985), and more recently Chen et al. (1995)) have reported difficulties when using the standard $k-\varepsilon$ model to simulate buoyancy-driven flows.

Many researchers have tried improving the standard $k-\varepsilon$ model so that buoyancy-driven flows are more accurately represented. For example, Ideriah (1980) added a buoyancy term to the ε equation of the form

$$\rho g \beta \mu_t \theta \frac{\varepsilon}{k}. \tag{5-9}$$

Many CFD codes incorporate such a term. However, the exact form of the term remains subject to debate and so the default in most codes is to exclude the term. CFX uses the term in the form shown in Equation (4-46). A simulation including this term ($C_3 = 1$ in Eq. (4-46)) produced marginal increases in the axial plume values for velocity and enthalpy (typically about 1.5%), but no measurable difference in either h/H or g'_h/G'_H. This is thought to be due to the fact that the flows considered here are stable, stratified flows in which the vertical temperature gradient, $\partial T/\partial y$ is everywhere positive, resulting in a negative value for G in the ε equation since $G = \frac{\mu_{eff}}{\sigma_{He_t}} \beta g_k \frac{\partial \overline{T}}{\partial x_k}$ (Eq. 4-48), and hence nullifying the C_3 term. Although $\partial T/\partial y$ is negative in the plume and the G term in the equation is invoked, its influence is evidently small.

Yakhot and Orszag (1986) used Renormalisation Group (RNG) theory to derive, *mathematically*, a new set of constants for the $k-\varepsilon$ model (see §2.6 and §4.5.5). By using mathematical theory to derive the constants in the model, all empiricism of the standard $k-\varepsilon$ model was removed.

Benchmark 1 was run using the RNG $k-\varepsilon$ model incorporated into CFX (§4.5.5). The convergence criteria were successfully attained, and the flow pattern showed qualitatively similar results (Fig. 5.24) to those obtained using the standard $k-\varepsilon$ model. However, the interface height and buoyancy change across it were slightly different and compared more favourably with the predictions of Linden et al. (1990) (Table 5.5).

Table 5.5 Comparison of results predicted by the standard and RNG $k-\varepsilon$ models with the predictions of Linden et al. (1990).

	Theory (Linden et al (1990))	Standard $k-\varepsilon$ model	RNG $k-\varepsilon$ model
h/H	0.603	0.390	0.490
g'_h/G'_H	1.66	1.84	1.88
air change rate (ach^{-1})	25.66	22.42	21.90

Table 5.5 also compares the predictions of air change rate (ach^{-1}) with that predicted by Linden et al. (1990). The latter is calculated using the theoretical value of M_L (Eq. 3-25) at $y=h$ where h is the interface height predicted by Linden et al. (1990).

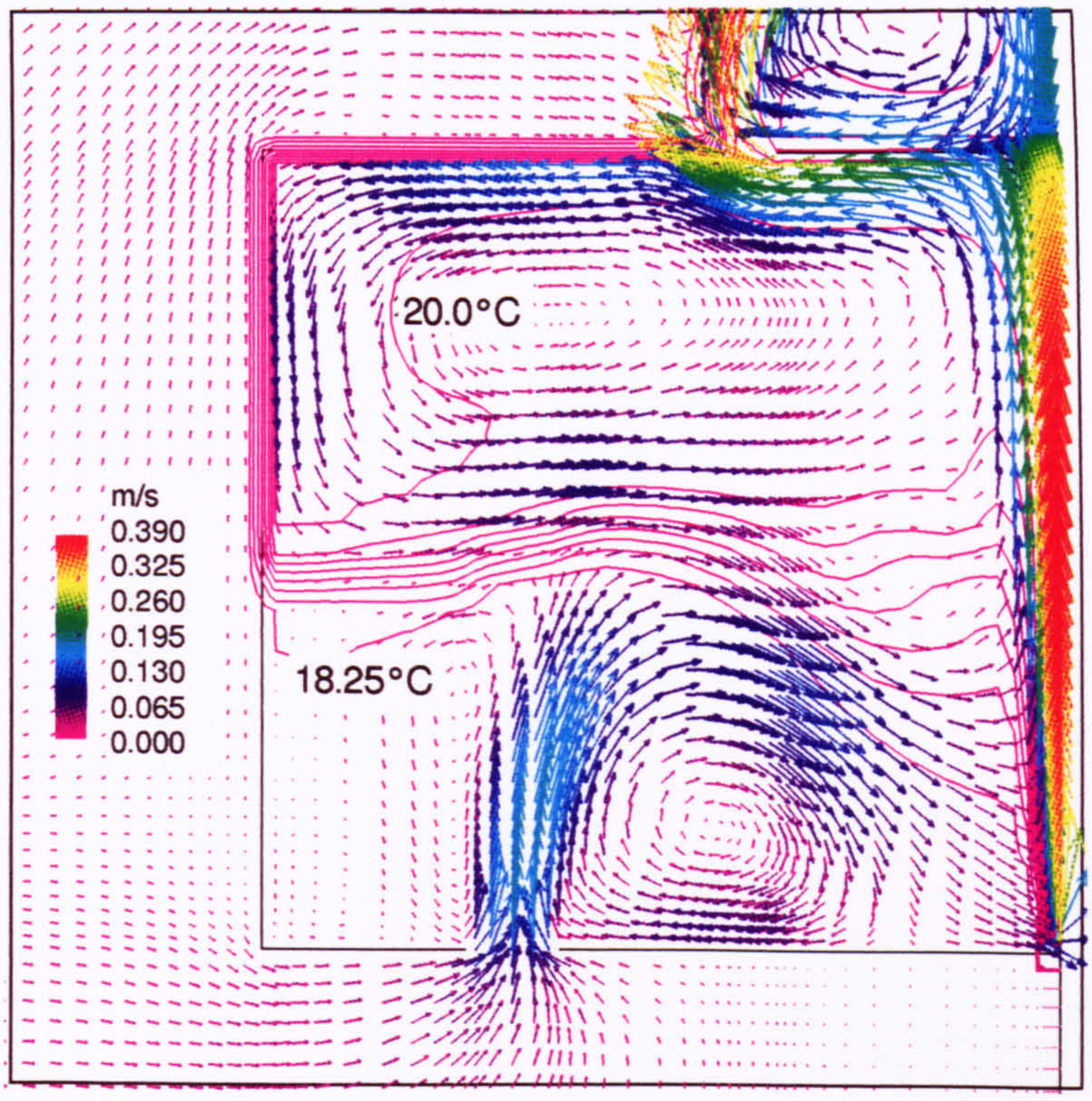

Figure 5.24 Flow pattern and temperature contours for Benchmark 1 when using the RNG $k-\varepsilon$ turbulence model (c.f. Fig. 5.11).

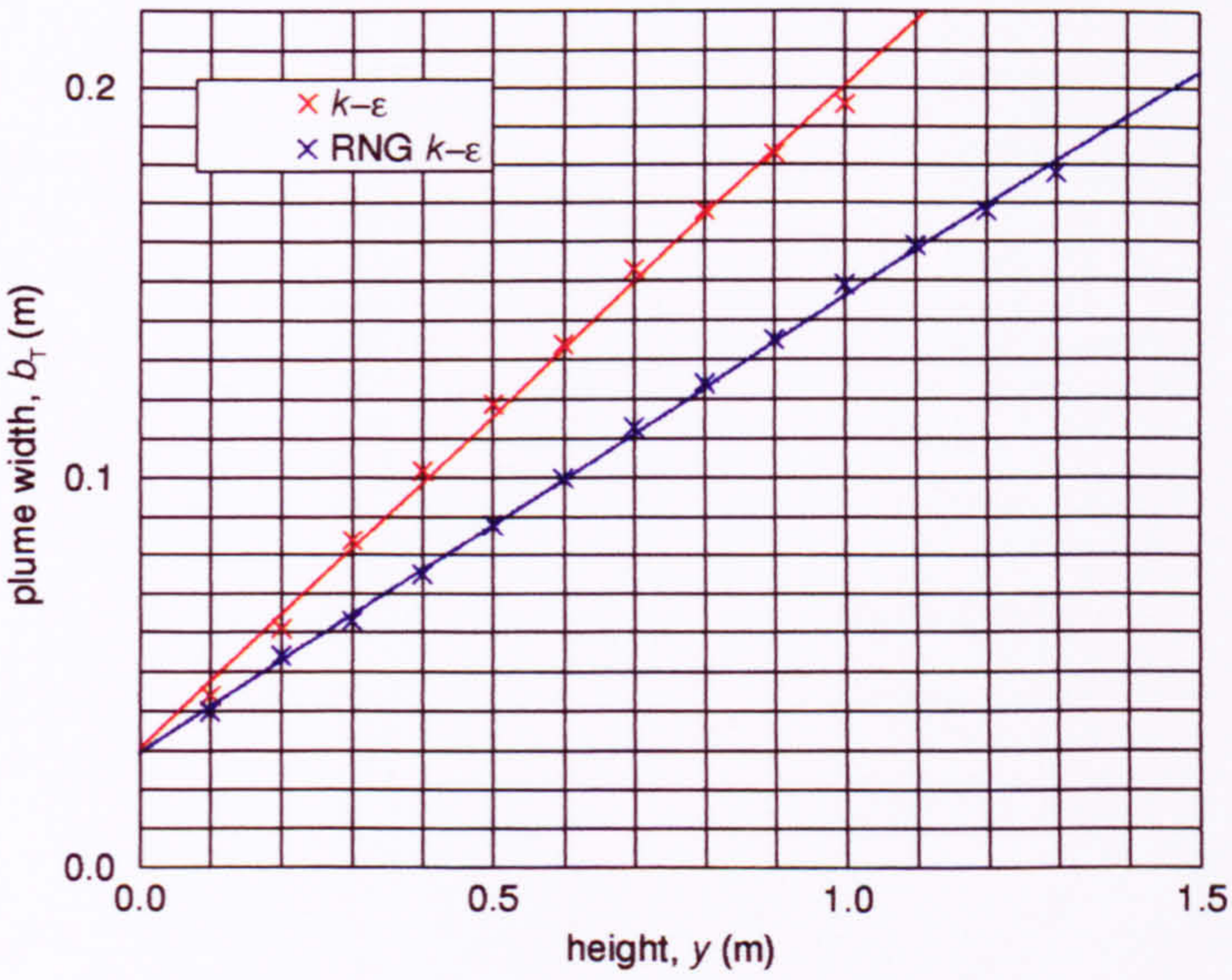

Figure 5.25 Variation of plume width with height above the source using the standard and RNG $k-\varepsilon$ models (gradient = α_T (Eq. (B-29)).

Table 5.6 'Top-hat' plume data calculated for Benchmark 1 (standard and RNG $k-\varepsilon$ models).

Height above source (m)	$v_T = \frac{v_G}{\sqrt{2}}$ (*)		$b_T = \sqrt{\frac{\pi}{2}} b_G$ (*)		$He_T = \frac{He_G}{2}$ (*)	
	$k-\varepsilon$	RNG	$k-\varepsilon$	RNG	$k-\varepsilon$	RNG
0.1	0.203	0.209	0.044	0.040	5730.0	5898.0
0.2	0.216	0.231	0.061	0.054	4142.8	4498.4
0.3	0.223	0.242	0.084	0.063	3246.3	3643.1
0.4	0.228	0.250	0.102	0.075	2683.6	3073.1
0.5	0.233	0.256	0.119	0.088	2294.7	2663.2
0.6	0.236	0.262	0.134	0.100	2013.8	2356.1
0.7	0.240	0.267	0.153	0.113	1803.7	2117.5
0.8	0.241	0.269	0.168	0.124	1643.8	1928.3
0.9	0.241	0.272	0.183	0.135	1518.6	1773.9
1.0	0.240	0.274	0.196	0.149	1420.8	1648.3
1.1		0.274		0.159		1546.7
1.2		0.272		0.168		1462.6
1.3		0.269		0.178		1393.7

(*) See Appendix B for derivation of these formulae.

By repeating the analysis carried out in section 5.4.4, it was shown that the RNG $k-\varepsilon$ model had predicted a narrower plume and therefore a smaller value of the entrainment constant (Fig. 5.25 and Table 5.6):

$$\alpha_T^{RNG} = 0.12.$$

This compared more favourably than the standard $k-\varepsilon$ model with that used by Linden et al. (1990) and measured by previous researchers (Morton et al. (1956), etc.).

The more favourable agreement of entrainment prediction between the theory and the RNG model yields similar gradients for the variation in plume volume flux with height (Fig. 5.26). However, since the RNG model has predicted a narrower plume than the standard $k-\varepsilon$ model, its virtual origin is lower, at $y \approx -0.16\text{m}$. As expected the difference in entrainment between the two turbulence models is also reflected in the variation of plume buoyancy with height (Fig. 5.27). Although the RNG model has predicted values closer to the theoretical line than the standard

model, the shape and position of the CFD curve is still substantially different to the theoretical prediction.

The final simulation investigated in this section incorporated the additional buoyancy term in the ε equation (Ideriah (1980)) into the RNG turbulence model ($C_3 = 1$ in Eq. 4-46). However, as with the standard $k-\varepsilon$ model, and for the same reasons, there were no changes in the results.

5.7 Effect of Sizes and Positions of Openings

To investigate the dependence of the interface parameters on opening sizes, simulations were carried out for various effective opening areas A_L^*, where

$$A_L^* = \frac{a_u a_l}{\left(1/2\left(a_u^2/c + a_l^2\right)\right)^{1/2}} \qquad \text{(Eq. 3-19).}$$

The results show good qualitative agreement for both turbulence models (Figs. 5.28 and 5.29) - note the favourable agreement of interface height between the theoretical prediction when an entrainment value of $\alpha_T = 0.17$ is used and the CFD results for the standard $k-\varepsilon$ model. Quantitatively, the prediction of interface height is closer to that of Linden et al. (1990) when using the RNG $k-\varepsilon$ model owing to its lower prediction of entrainment. The CFD results for buoyancy change across the interface do not vary much depending on the turbulence model used, and both models offer favourable quantitative agreement with the theory. The similarity in results between the two models is caused by a cancelling effect as follows. The theory states that $g_h' = G_T'(y = h)$ (Eq. (3-21)). So factors affecting buoyancy in the plume at the interface can potentially cause changes in g_h'. Now plume buoyancy reduces with height or if entrainment increases. Therefore, when moving from the standard $k-\varepsilon$ model to the RNG $k-\varepsilon$ model, the interface rises causing an increase in h and a corresponding reduction in

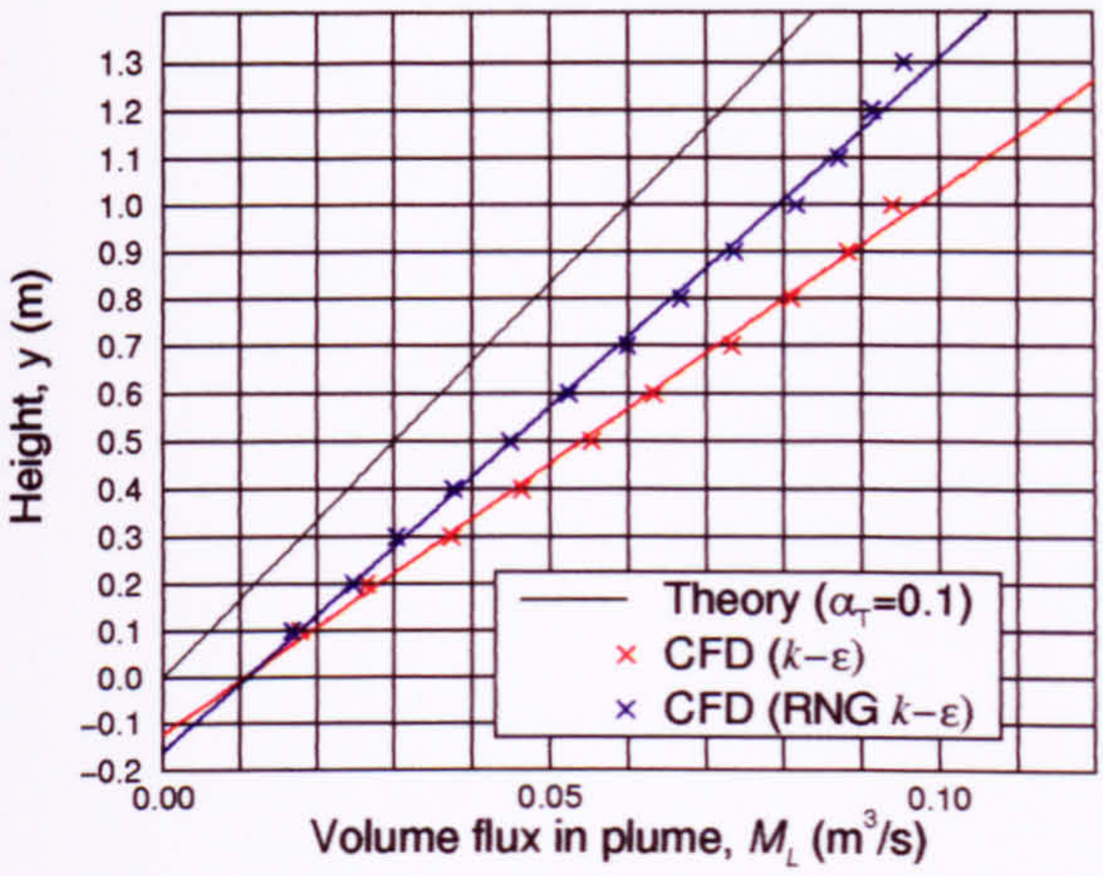

Figure 5.26 Variation of volume flux in the plume with height for both turbulence models.

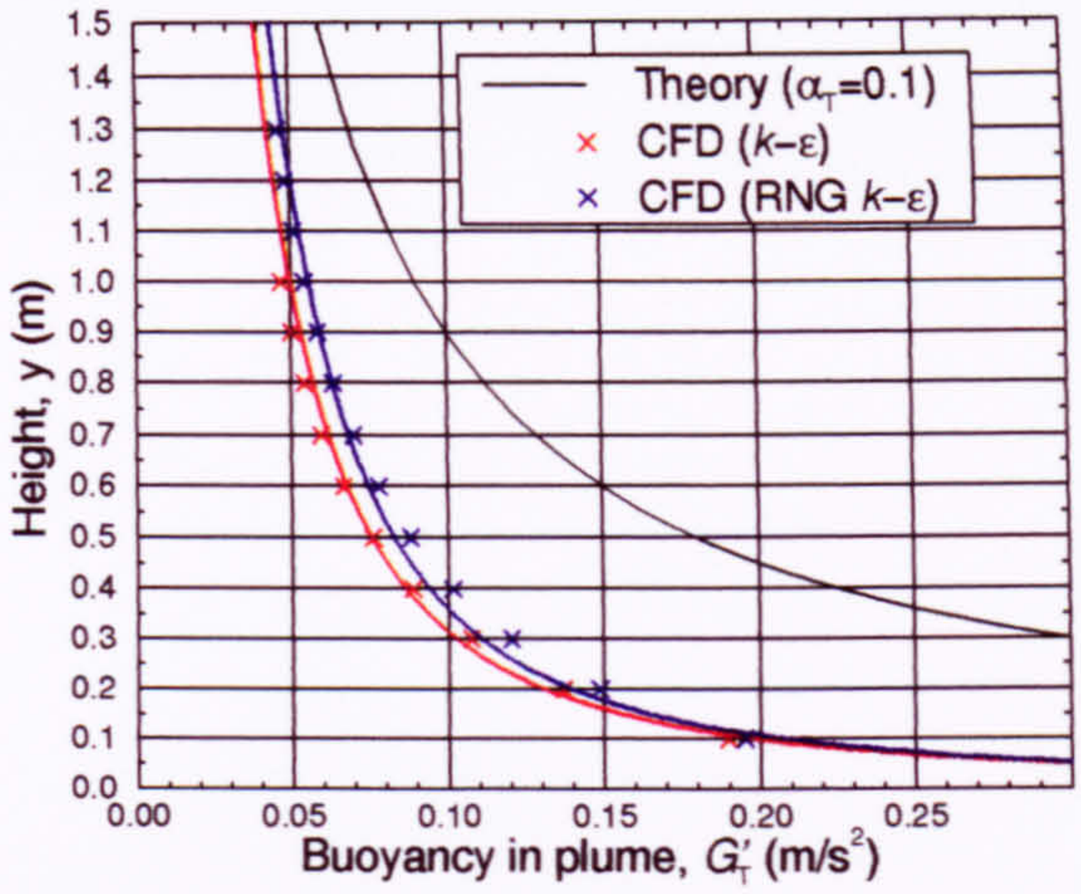

Figure 5.27 Variation of buoyancy in the plume with height for both turbulence models.

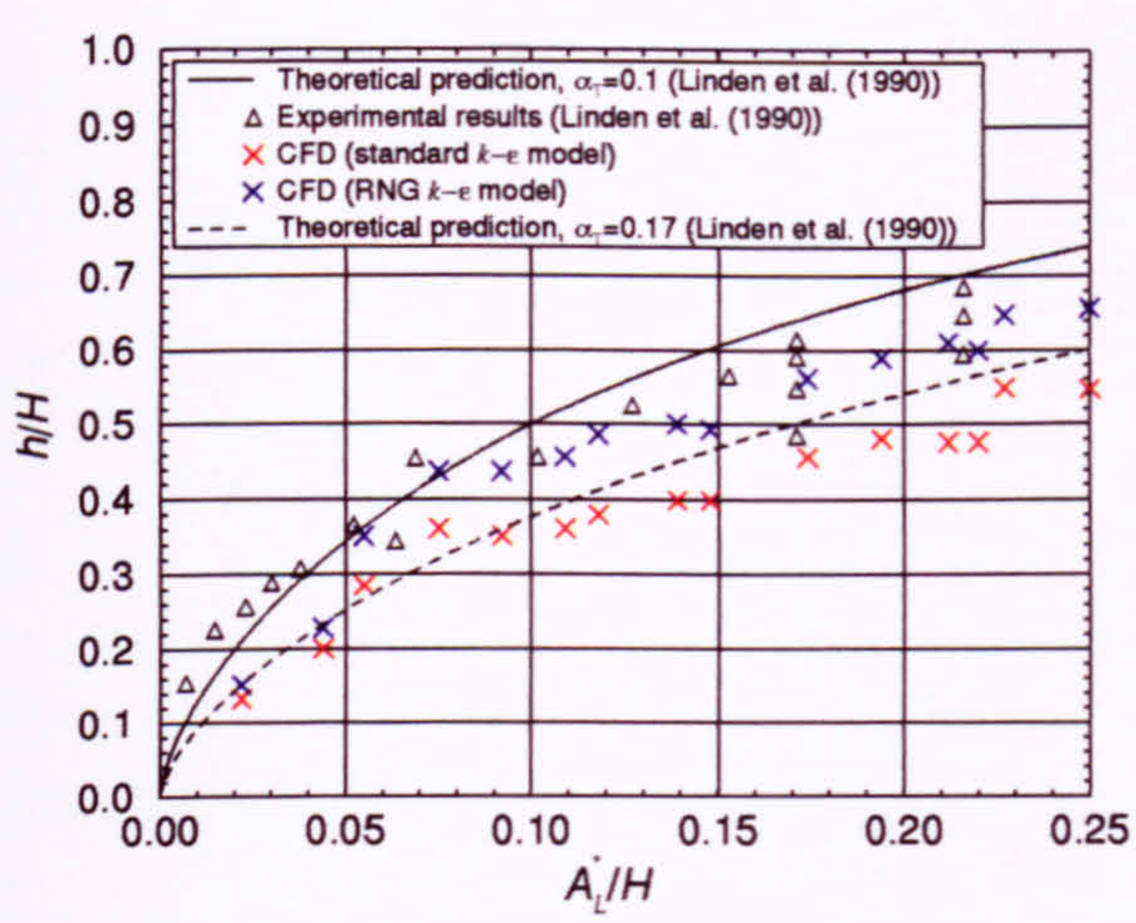

Figure 5.28 Variation of interface height with effective opening area for both turbulence models.

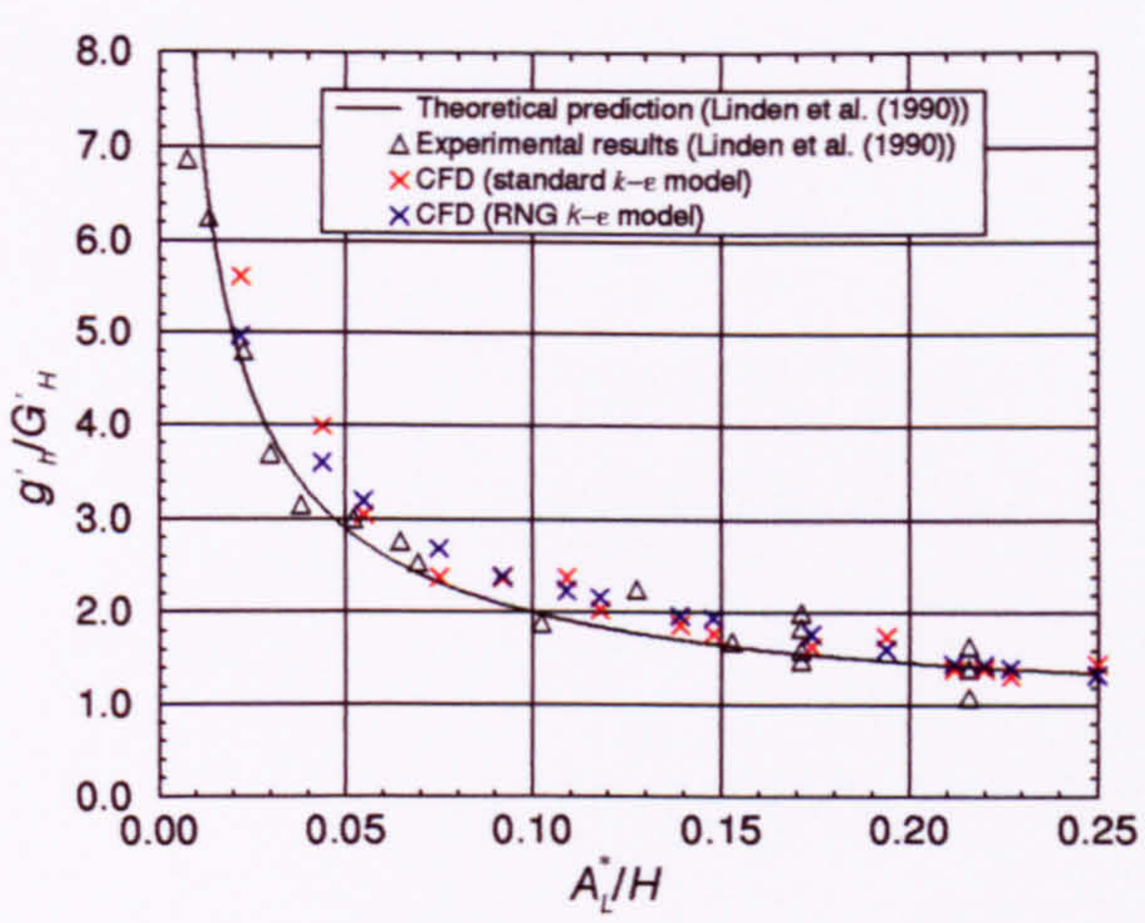

Figure 5.29 Variation of buoyancy change across the interface with effective opening area for both turbulence models.

$G'_T(y=h)$. However, simultaneously the entrainment reduces causing an *increase* in $G'_T(y=h)$. These two effects, if not completely, do at least act to cancel each other out, giving

$$G'_T\left(y=h^{k-\varepsilon}\right) \approx G'_T\left(y=h^{\mathrm{RNG}}\right)$$

$$\Rightarrow \quad g'^{\,k-\varepsilon}_h \approx g'^{\,\mathrm{RNG}}_h .$$

The general trend of the CFD results in Figure 5.28 does not follow a perfect curve. This is thought to be due to the lower openings being smaller than the upper ones in some cases, causing a larger momentum flux through the lower openings. This momentum force impinges on the interface (Fig. 5.30) forcing it upwards in that region, making the interface height difficult to measure.

Simulations in which openings were placed at different horizontal locations produced favourable agreement with the theory (Figs. 5.31 - 5.33).

5.8 Effect of Space Dimensions

Simulations were carried out for a 'tall' space (5.1m wide $\times$5.1m high) and a 'wide' space (10.2m wide $\times$ 2.55m high). The theory of Linden et al. (1990) states that the interface parameters, h/H and g'_h/G'_H, are independent of the floor area. This was verified subject to a small discrepancy in the interface height (Fig. 5.34 and Table 5.7). The slightly lower interface predicted by Benchmark 1 is thought to be due to the larger velocities in the upper region of the space causing downward momentum forces on the interface at the measurement point.

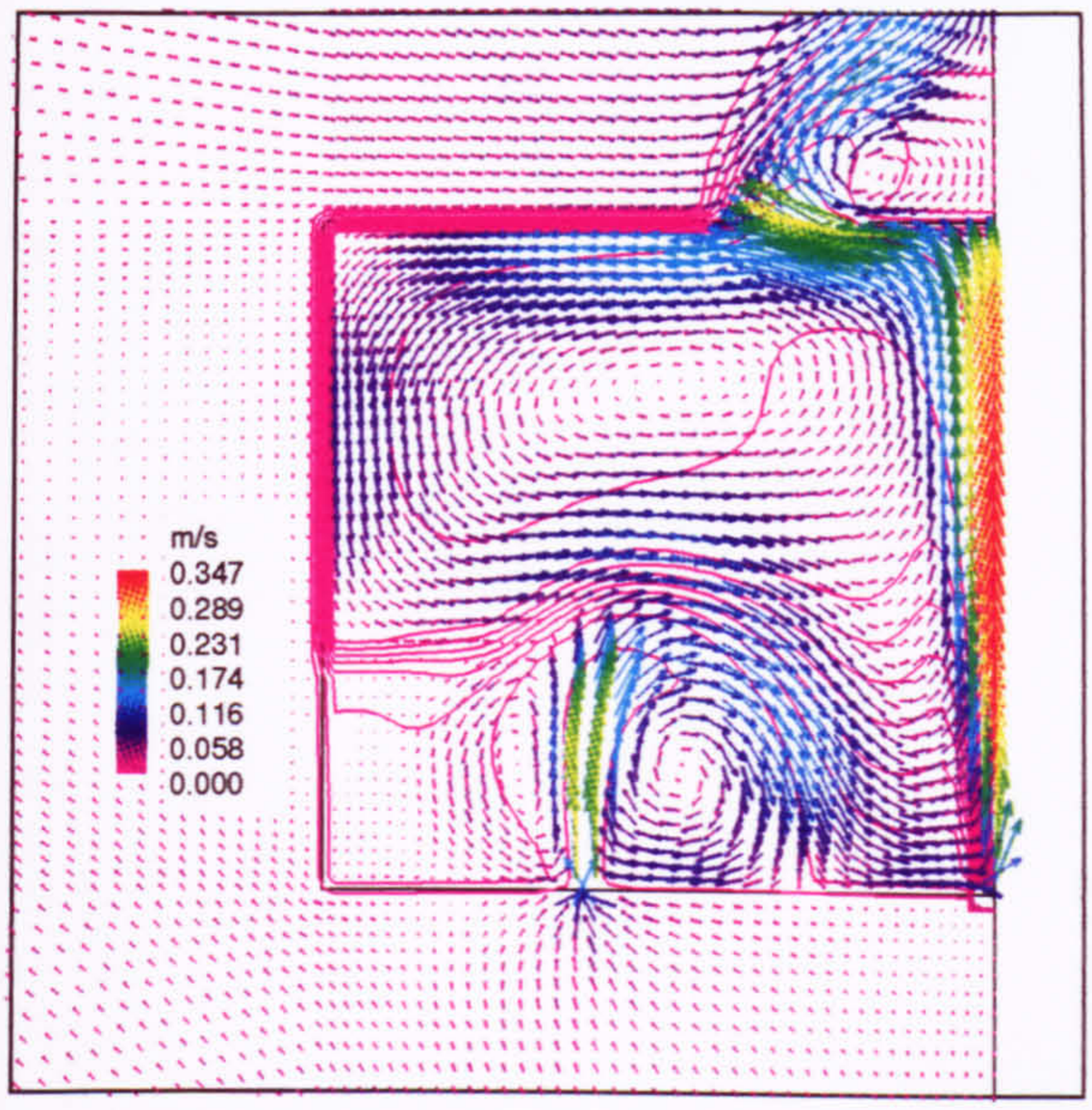

Figure 5.30 Incoming air impinging on the interface due to a smaller lower opening than upper opening.

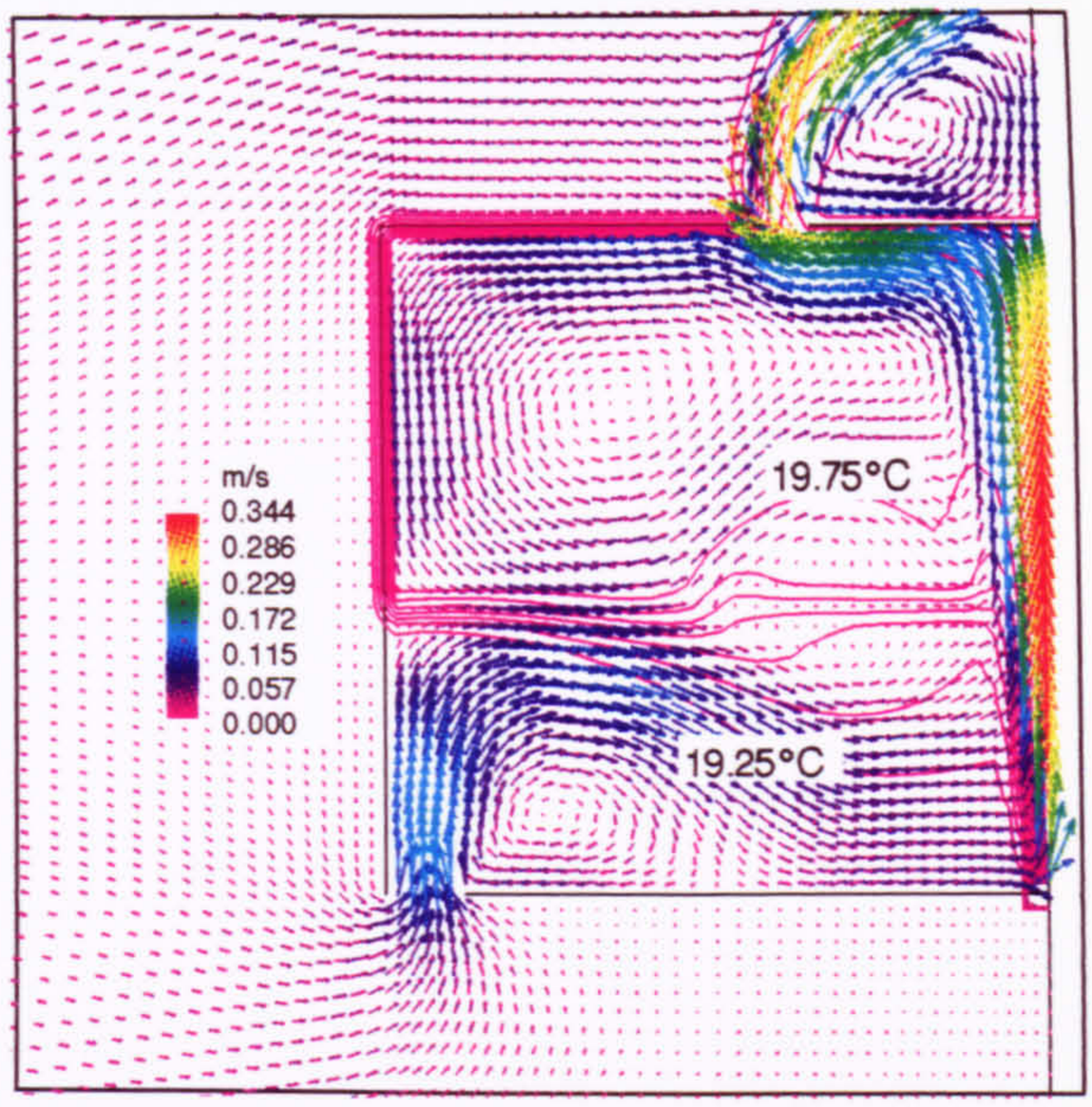

Figure 5.31 Resulting flow pattern for lower openings against walls using standard $k-\varepsilon$ model ($A_L^*/H = 0.15$, $h/H = 0.438$, $g'_h/G'_H = 1.80$).

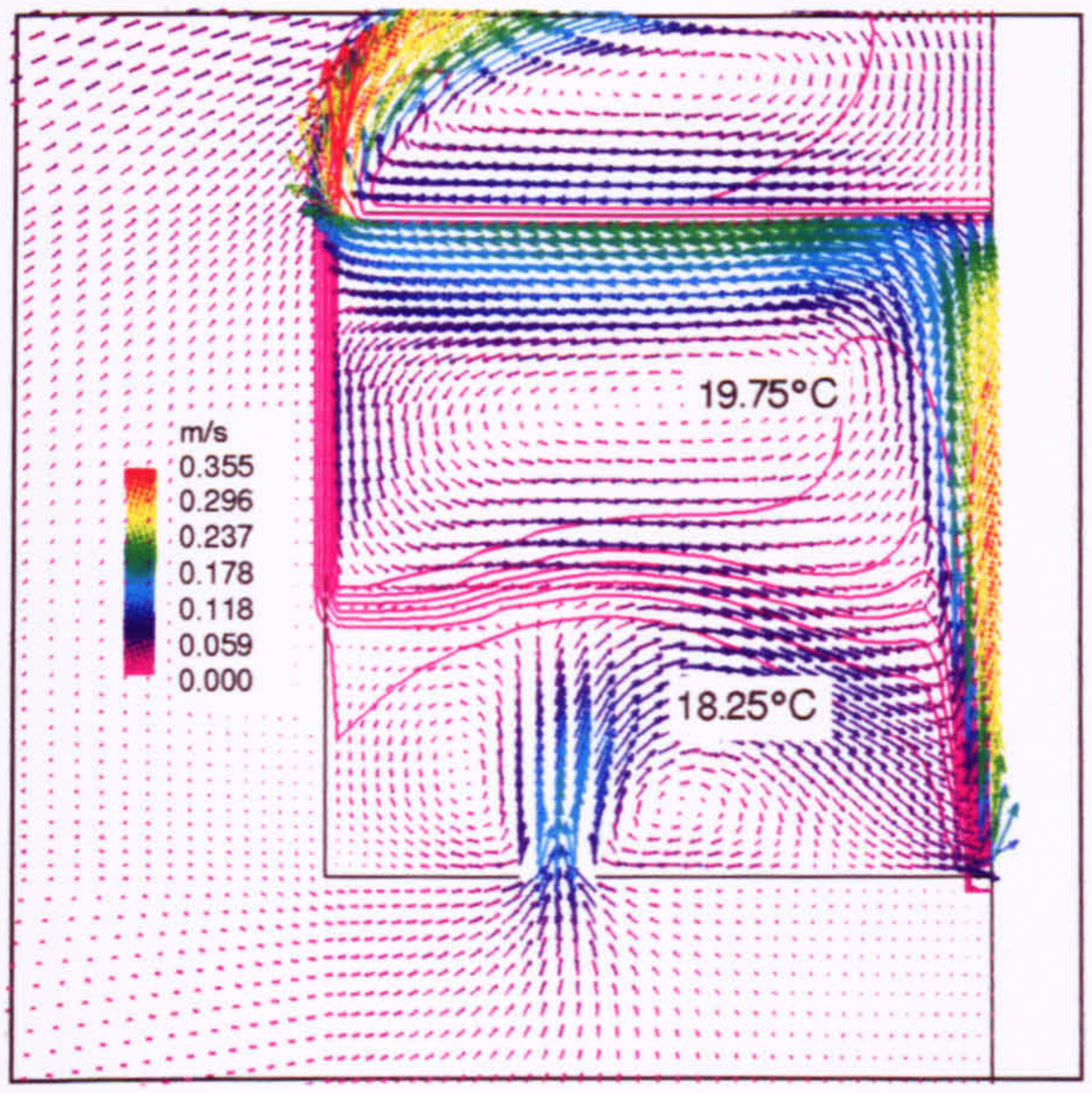

Figure 5.32 Resulting flow pattern for upper openings against wall using standard $k-\varepsilon$ model ($A_L^*/H = 0.148$, $h/H = 0.4$, $g'_h/G'_H = 1.72$).

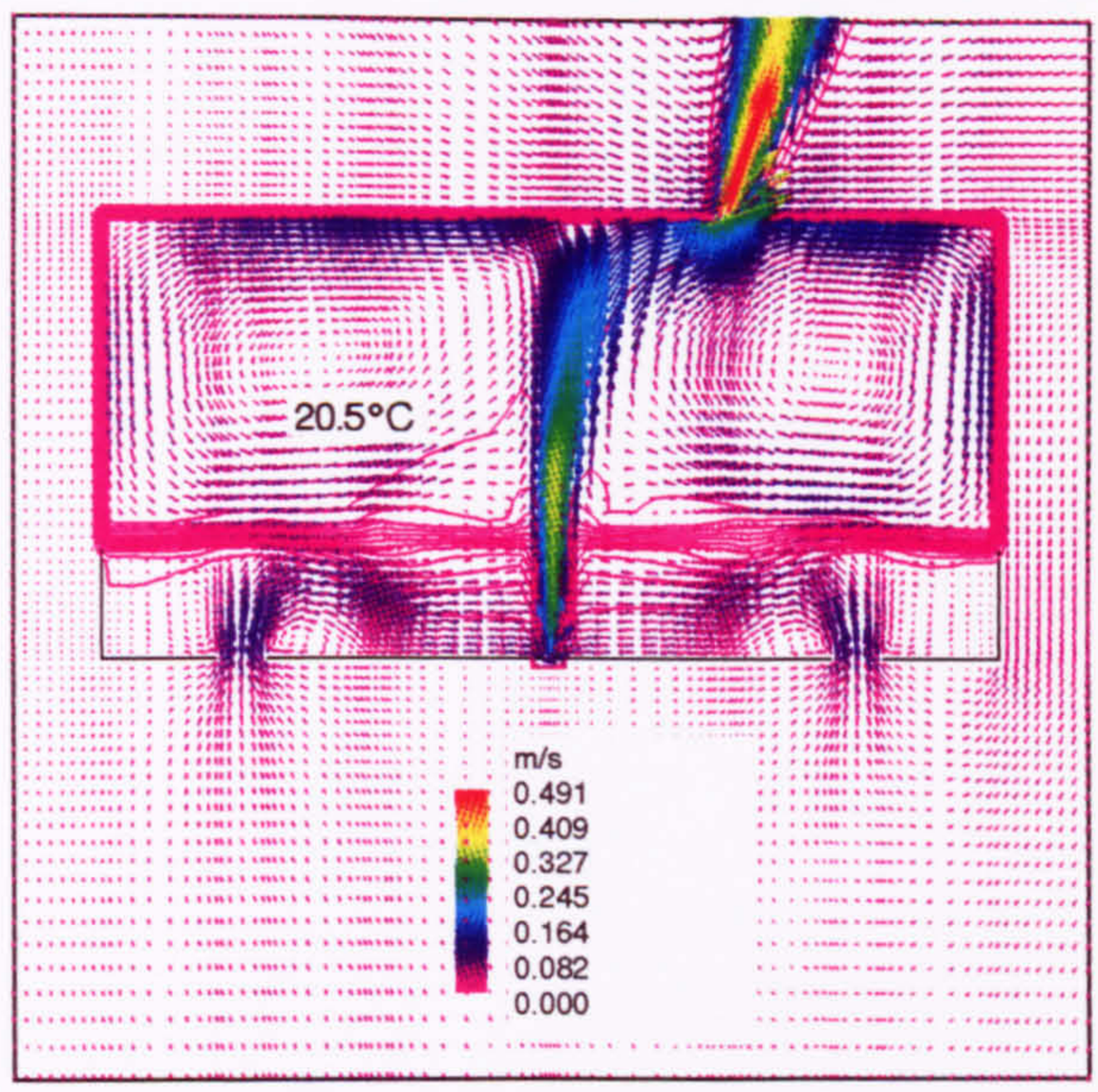

Figure 5.33 Resulting flow pattern for only *one* upper opening using standard $k-\varepsilon$ model ($A_L^*/H = 0.072$, $h/H = 0.26$, $g'_h/G'_H = 2.85$).

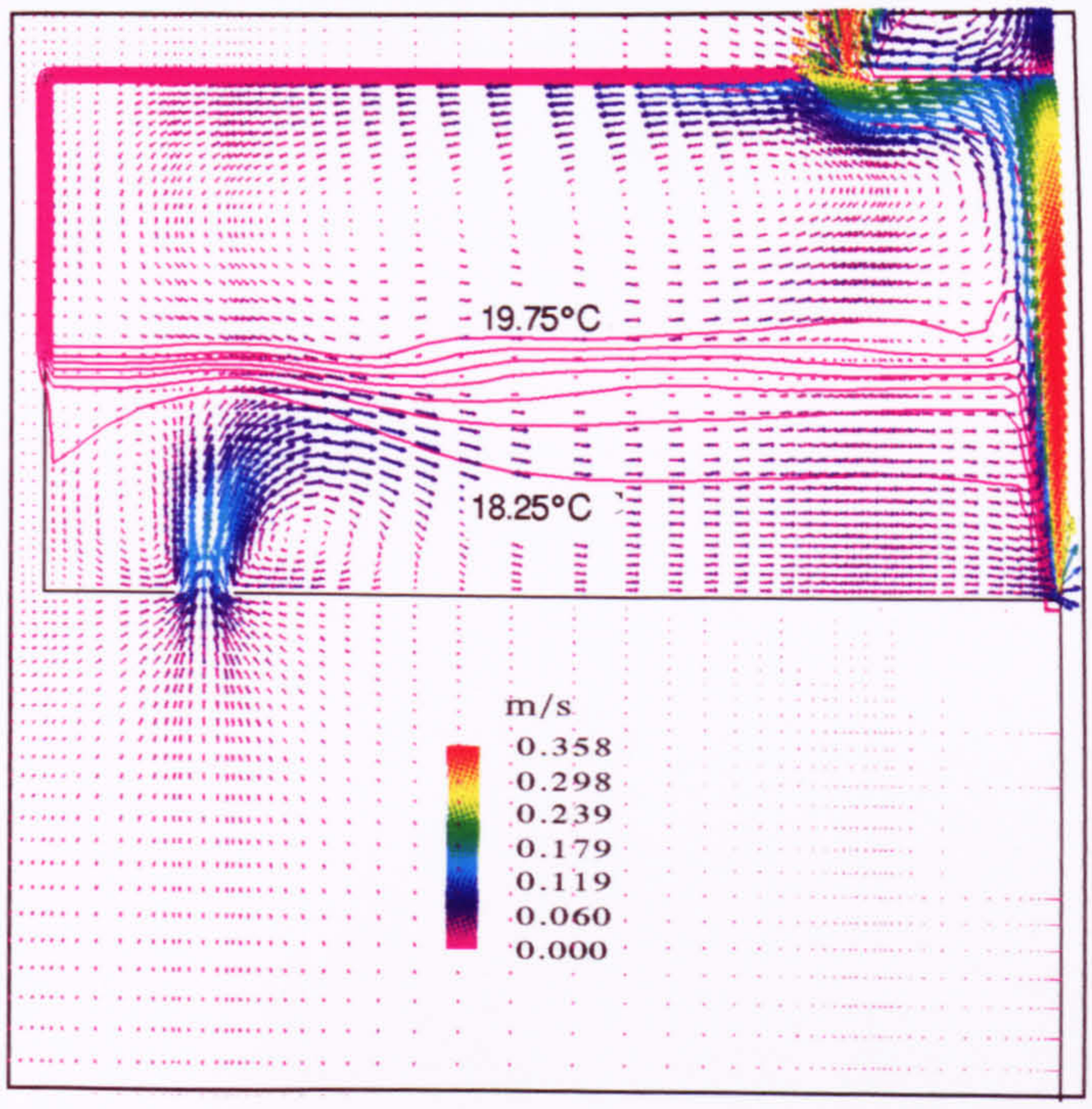

Figure 5.34 Resulting flow pattern for 'wide' space ($A_L^*/H = 0.148,\ Q = 200\text{W}$).

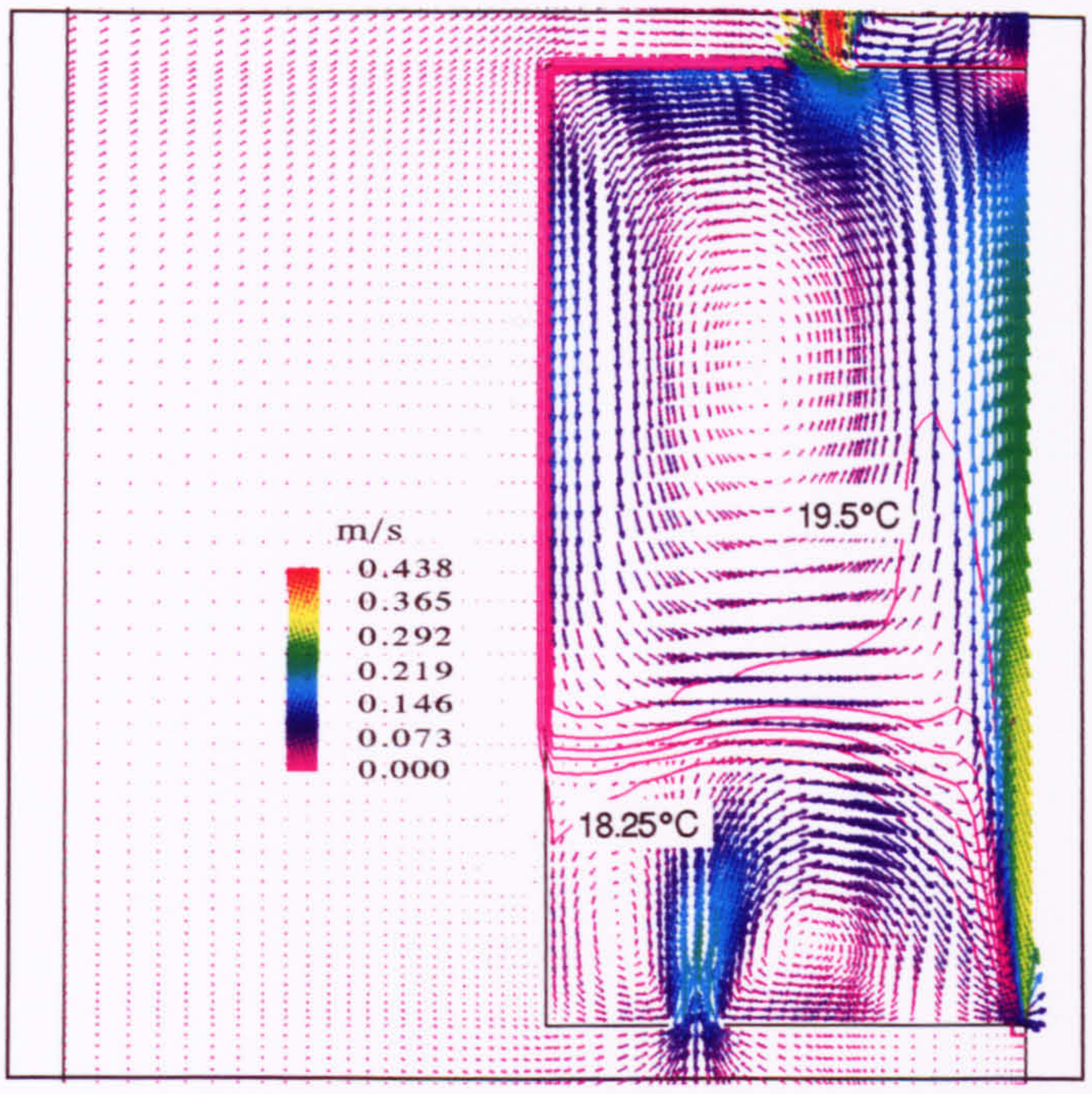

Figure 5.35 Resulting flow pattern for 'tall' space ($A_L^*/H = 0.074,\ Q = 200\text{W}$).

Table 5.7. Comparison of flow parameters for different space dimensions using the $k-\varepsilon$ turbulence model.

	h/H	g'_h/G'_H	ach^{-1}
'Wide' space (Fig. 5.34)	0.440	1.86	14.8
'Tall' space (Fig. 5.35)	0.285	2.86	11.2
Benchmark 1 (Fig. 5.11)	0.390	1.84	22.4

The simulation of the taller space resulted in a lower value for h/H and a higher value for g'_h/G'_H as predicted (Figs. 3.7 and 3.8). Although the normalised interface height h/H has reduced, the actual height of the interface ($h = 1.45$m) has risen, as the volume fluxes in the plume and through the openings reach a steady state. Therefore, the plume propagates further before breaking down to form the interface which results in a lower value of $G'_T(y=h)$ and thus g'_h.

5.9 Effect of Source Strength on the Flow

Various source strengths were simulated using the same effective opening area defined for Benchmark 1. The results for 50W and 1000W using both turbulence models (Figs 5.36 - 5.39) show clearly the effects of varying this key physical parameter.

As expected, the temperature change across the interface increases as the source strength increases, as do the induced velocities and therefore the volume flux in the plume. The plume properties M_L and G'_T compare qualitatively well with the theoretical predictions and vary linearly with $B_L^{1/3}$ and $B_L^{2/3}$ respectively as predicted (Figs. 5.40 - 5.43).

The quantitative discrepancies in the volume flux curves (Fig. 5.40) can be attributed to the larger value of entrainment predicted by the CFD code for both turbulence models, and the existence of the virtual origin. Those in the buoyancy curve (Fig. 5.41) are more substantial. Although the linear variation of G' with

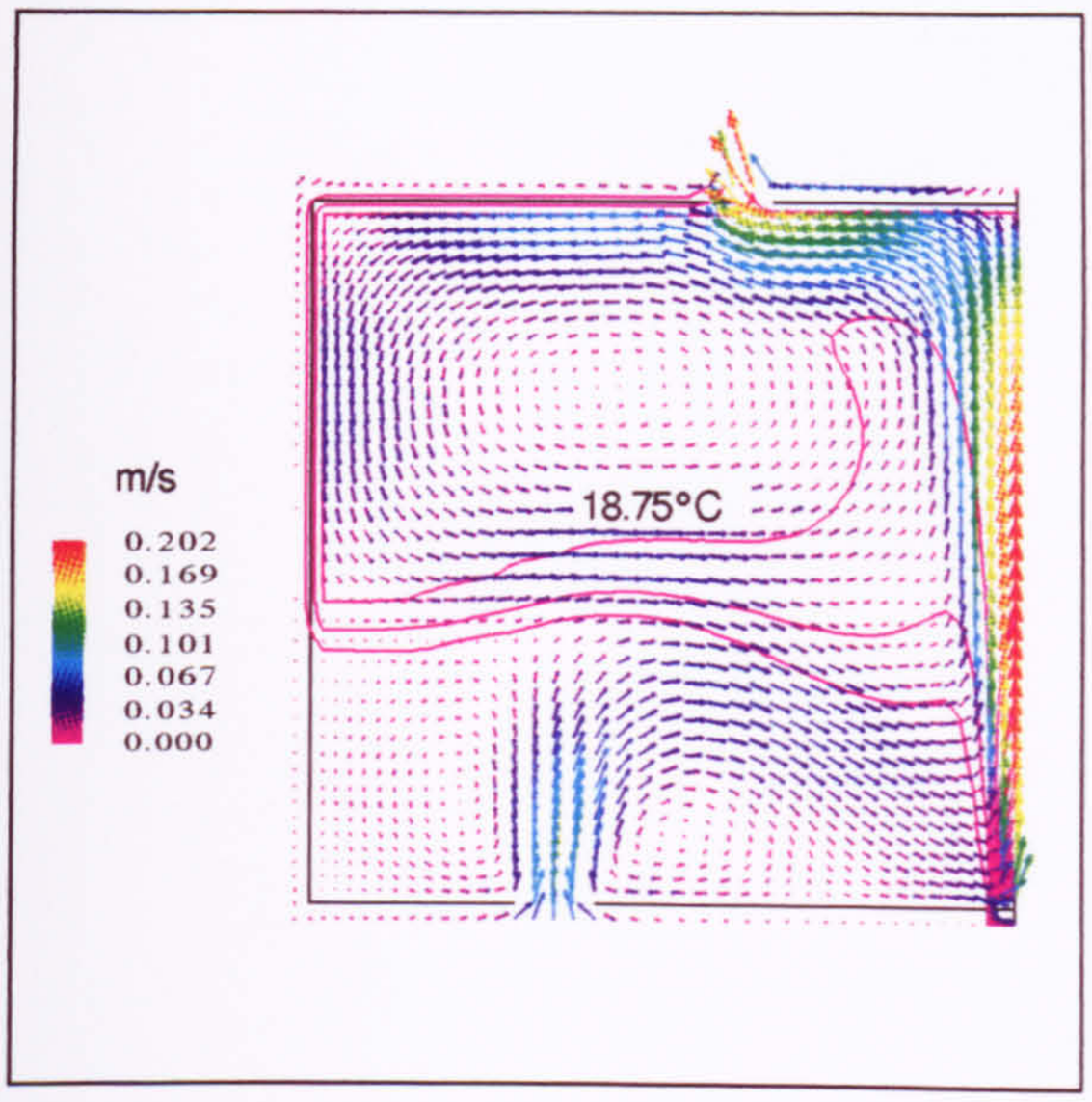

Figure 5.36 Flow pattern for Q = 50W using the standard $k-\varepsilon$ model.

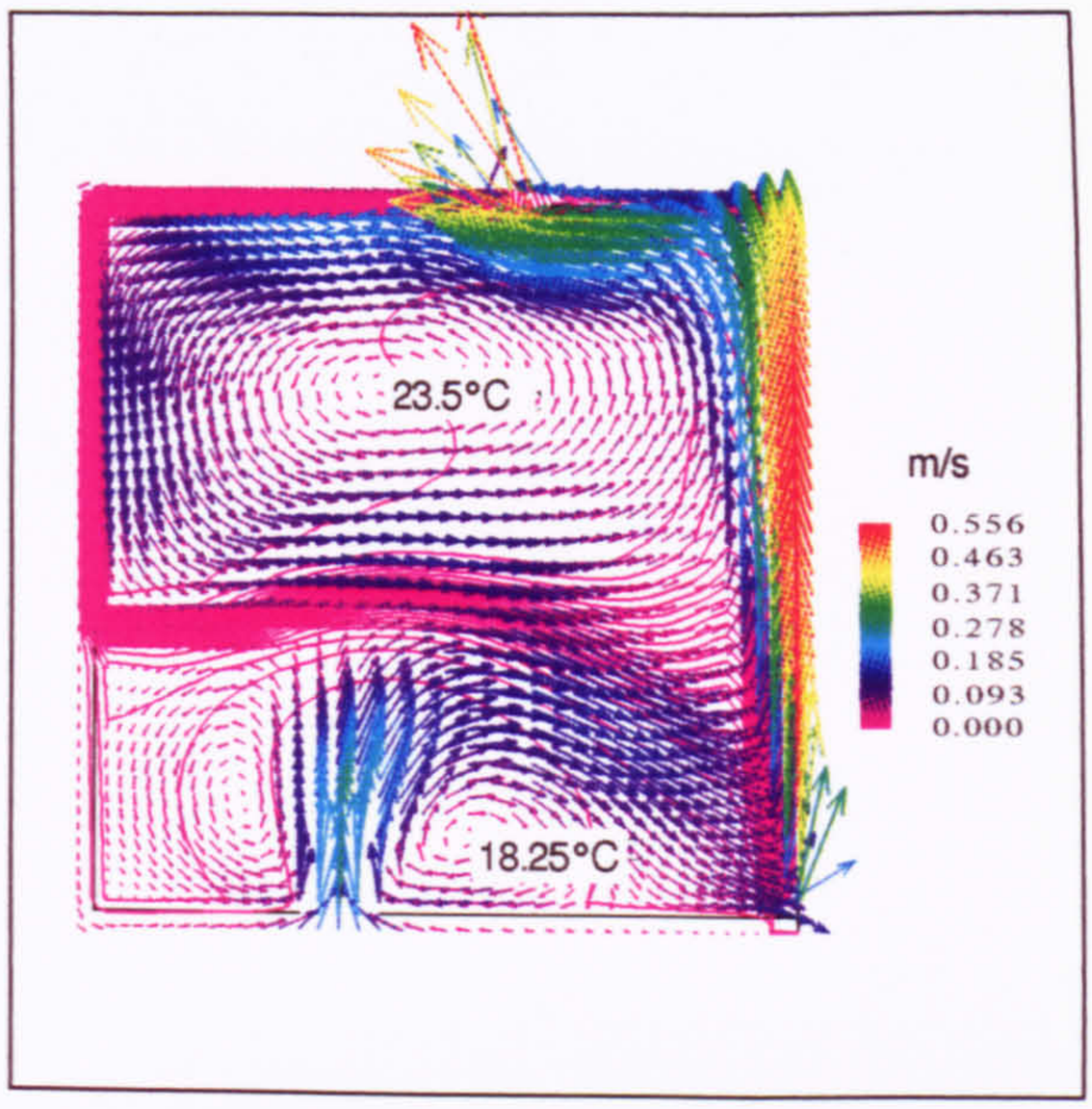

Figure 5.37 Flow pattern for Q = 1000W using the standard $k-\varepsilon$ model.

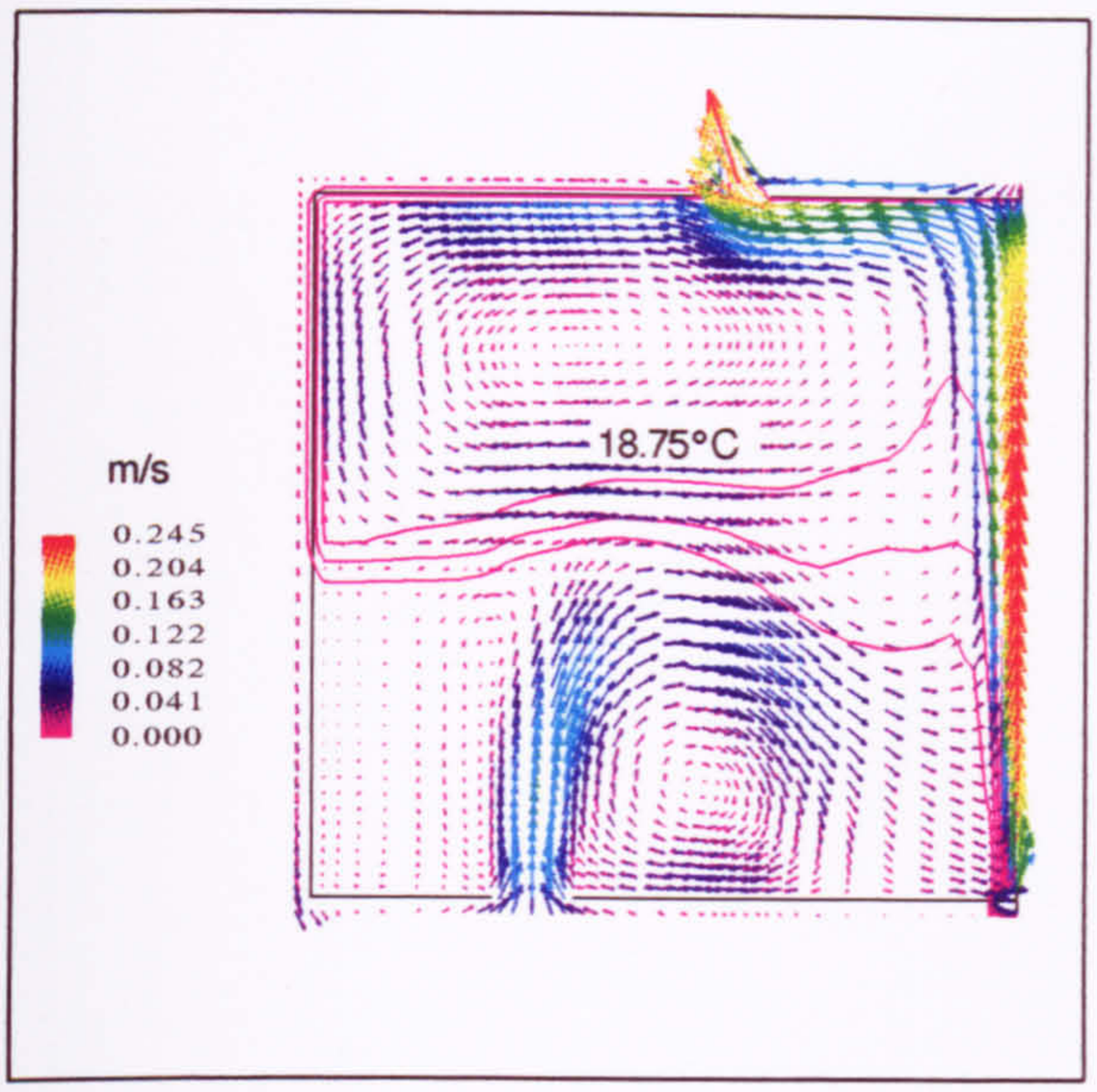

Figure 5.38 Flow pattern for Q = 50W using RNG $k-\varepsilon$ model.

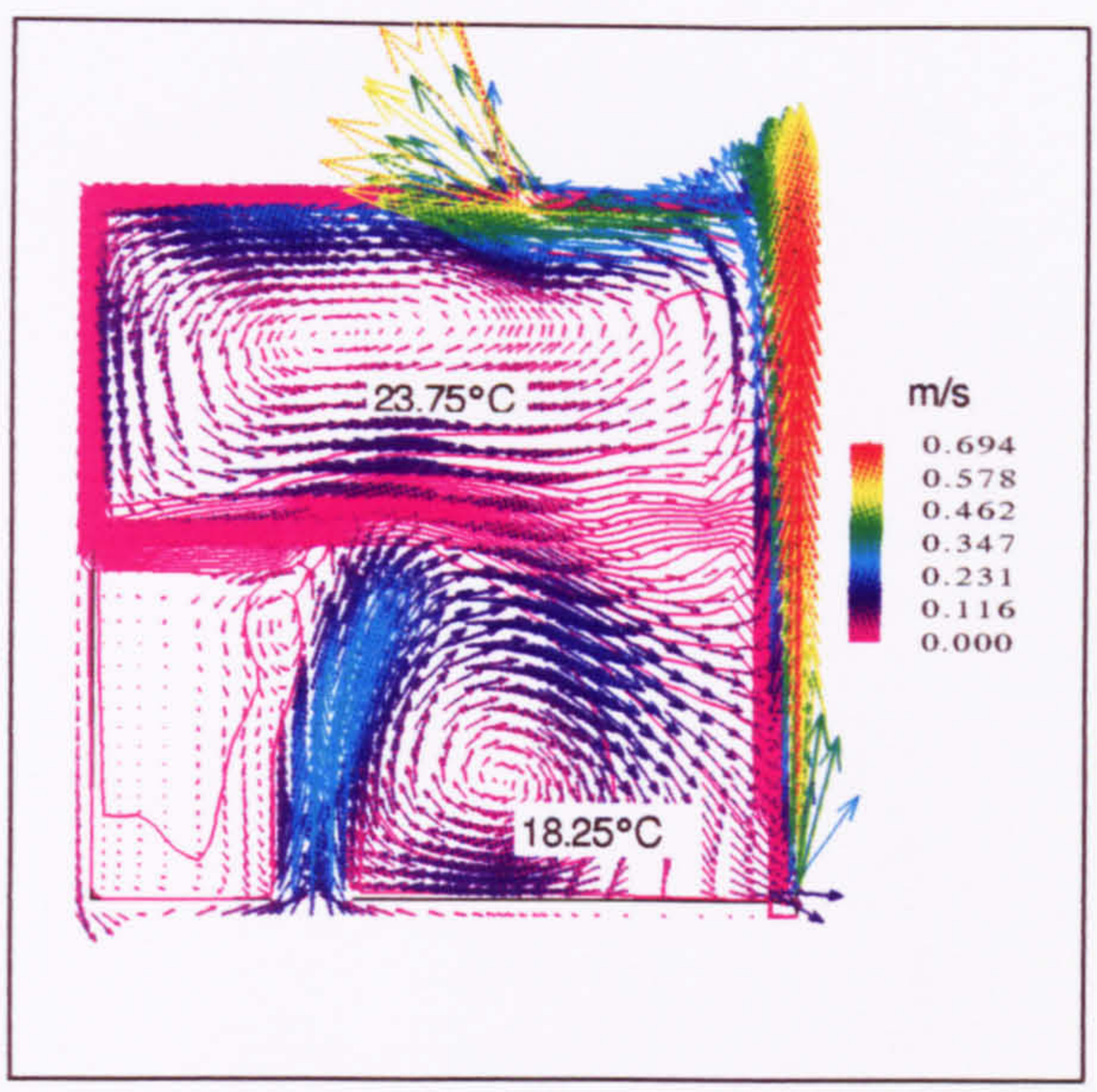

Figure 5.39 Flow pattern for Q = 1000W using RNG $k-\varepsilon$ model.

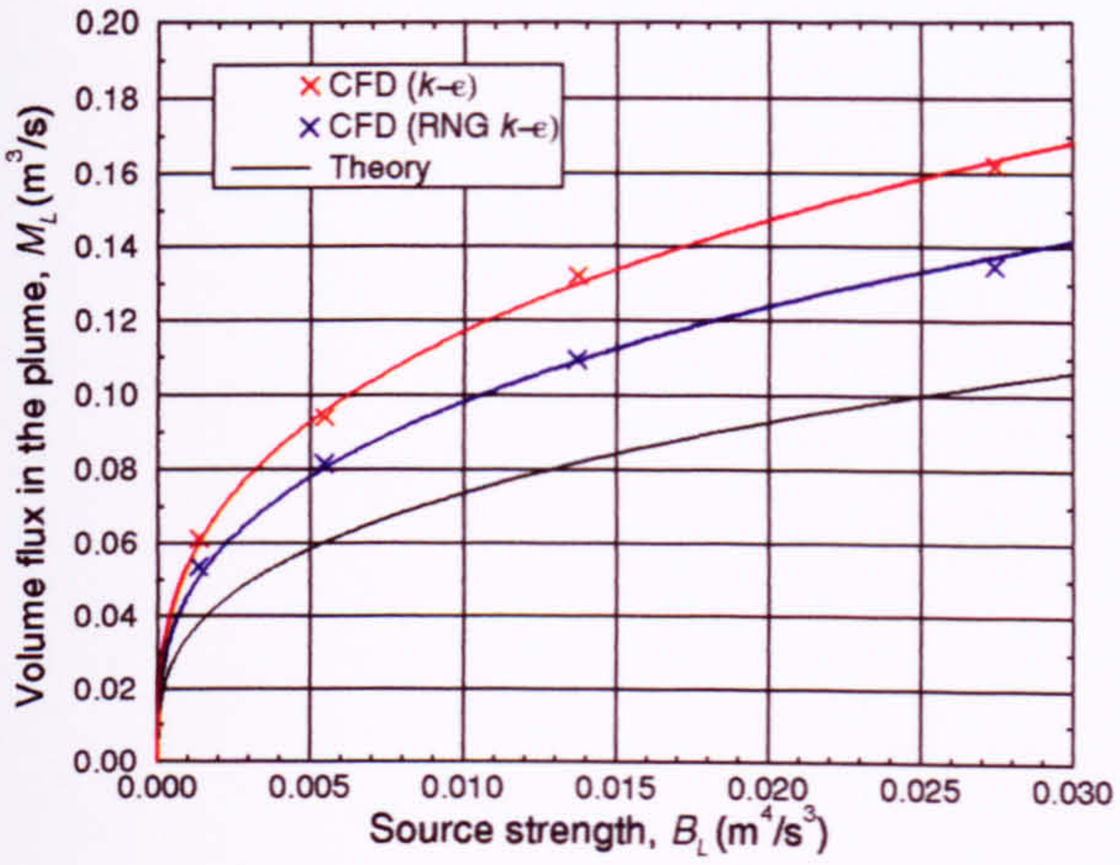

Figure 5.40 Variation of volume flux in the plume with source strength at 1m above the source.

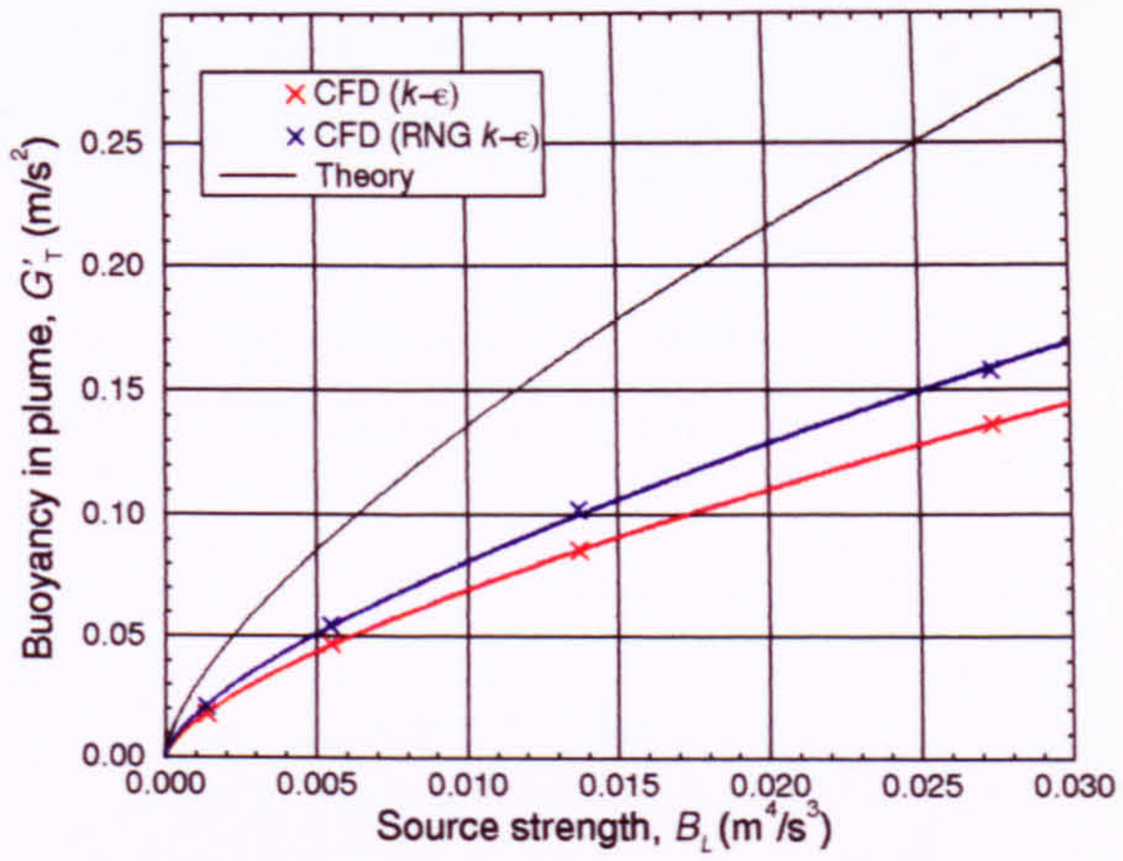

Figure 5.41 Variation of plume buoyancy with source strength at 1m above the source.

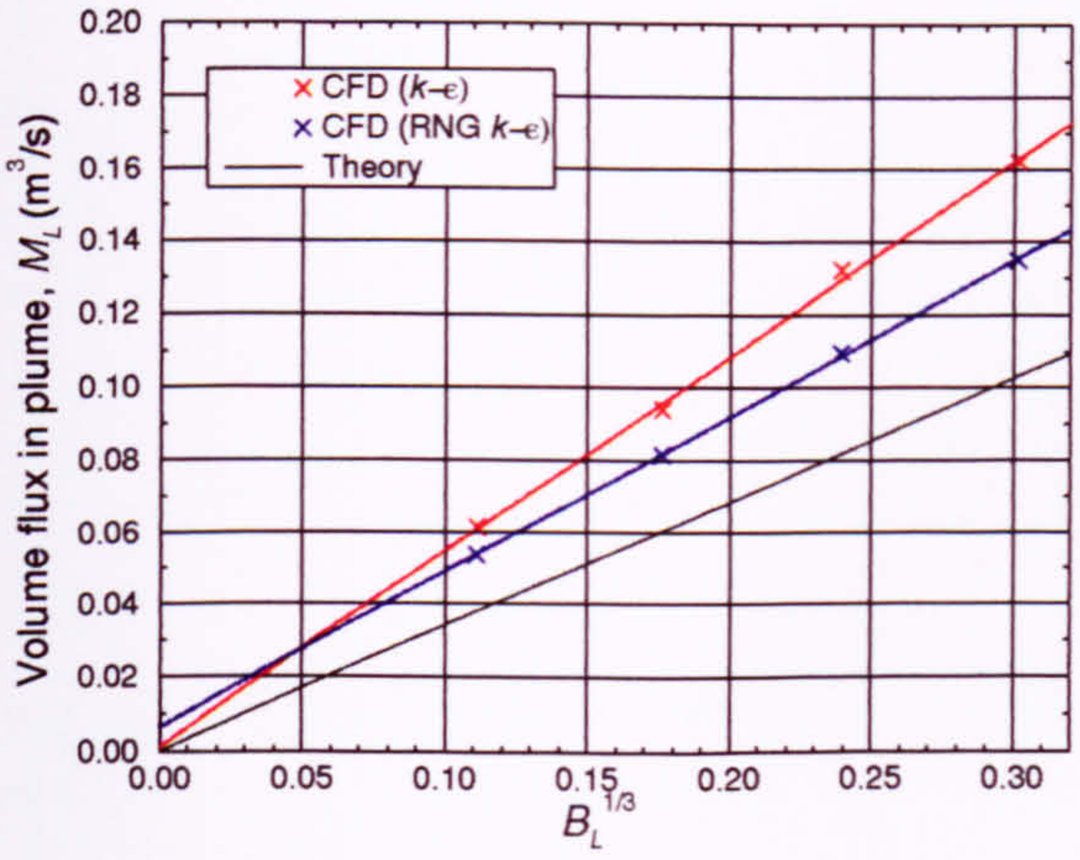

Figure 5.42 Variation volume flux in the plume with $B_L^{1/3}$.

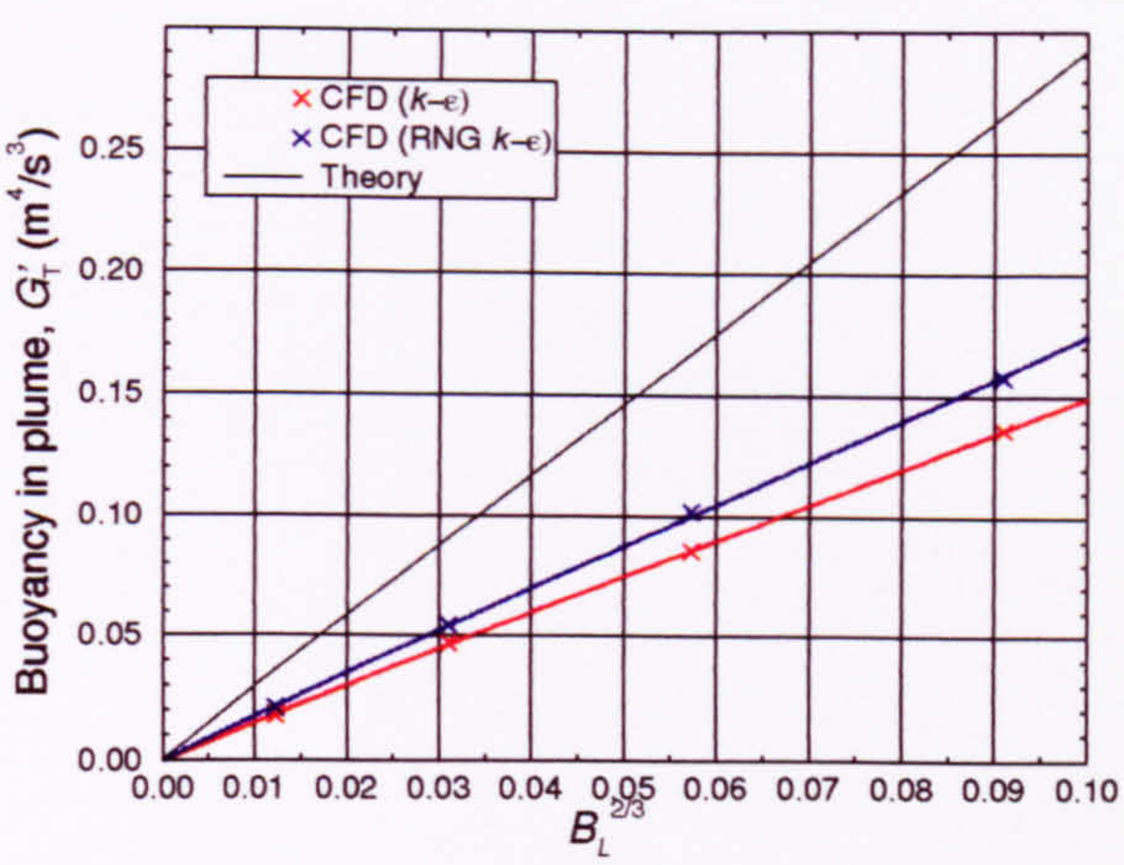

Figure 5.43 Variation of plume buoyancy with $B_L^{2/3}$.

$B_L^{2/3}$ is successfully predicted (Fig. 5.43), its *rate* of variation is not, which gives rise to the discrepancies in Figure 5.41. It is evident from Figures 5.41, 5.43 and 5.19 that the inaccurate prediction of plume buoyancy lies in the variation of buoyancy with *height*.

However, the most important observation to be made in this section is the prediction that the interface height is independent of the source strength (Table 5.8).

Table 5.8 Effect of source strength on displacement ventilation flow parameters.

Source strength (W)	h/H		g'_h/G'_H		ach^{-1}	
	$k-\varepsilon$	RNG	$k-\varepsilon$	RNG	$k-\varepsilon$	RNG
50	0.390	0.473	1.86	1.89	14.12	13.84
200	0.390	0.490	1.84	1.88	22.42	21.87
500	0.390	0.479	1.85	1.89	30.45	29.34
1000	0.390	0.528	1.84	1.87	38.48	37.65

The slight difference in interface height when using the RNG model will be discussed in Chapter 8. However, these differences must be put into perspective. It is noticed in the RNG simulation of Benchmark 1 (e.g. Fig. 5.24), that most of the temperature change at the interface occurs in the range $0.444 < h/H < 0.537$. The variation in h/H with source strength for the RNG model (Table 5.8) lies within this range suggesting that the difference is not a major cause for concern.

5.10 Investigation of Exterior Space Modelled

Various amounts of the exterior domain were modelled to investigate how much of this space could be eliminated without affecting the final result. This has the advantage of reducing run times which would become increasingly important when addressing three dimensional simulations.

All simulations gave qualitatively similar results for the displacement ventilation flow inside the box (Figs. 5.44 - 5.47). The unrealistically high velocities in the exterior space in Figure 5.44 are thought to be caused by *artificial entrainment*

across the PRESSURE boundaries. This is a common problem when using Neumann boundary conditions on surfaces facing each other, since many different flow solutions exist that satisfy the conditions $p = 0$ and $\partial\phi / \partial n = 0$ (i.e. no change across the boundary) on both boundaries. Air can be entrained across two facing PRESSURE boundaries at *any* velocity provided there is no pressure change between the two boundaries, i.e. the air leaves the domain at the same velocity at which it entered. It may be possible to eliminate this effect by imposing very tight under-relaxation factors or very small false time-steps. Despite this misrepresentation of flow outside the box in Figure 5.44, the interface parameters defining the flow inside the box compare favourably with Benchmark 1 for all cases (Table 5.9).

Table 5.9 Interface parameters for various exterior domains.

	h / H	g'_h / G'_H
Benchmark 1	0.390	1.84
Exterior Space 1	0.388	1.91
Exterior Space 2	0.367	2.00
Exterior Space 3	0.390	1.85
Exterior Space 4	0.392	1.87

It was decided, based on the data in Table 5.9, that an exterior domain above and below the space to an extent equal to the height of the room would be adequate. This is provided upper and lower openings are positioned *away* from the sides of the box. If they are not, then this results in user-defined PRESSURE boundaries being located adjacent to openings, which is the potential source of error that the exterior space modelling is seeking to avoid (§5.3.1).

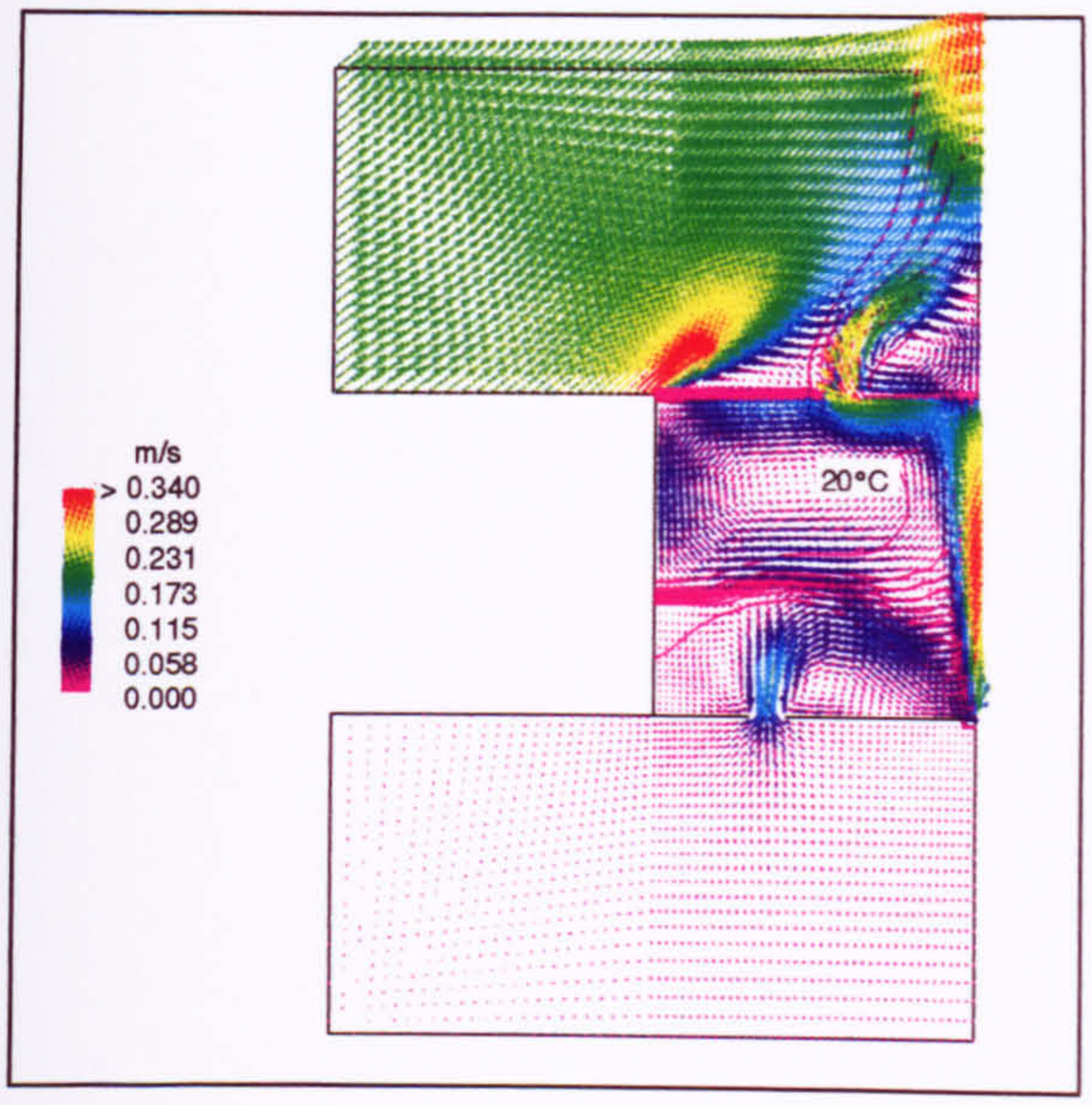

Figure 5.44 Exterior Space 1.

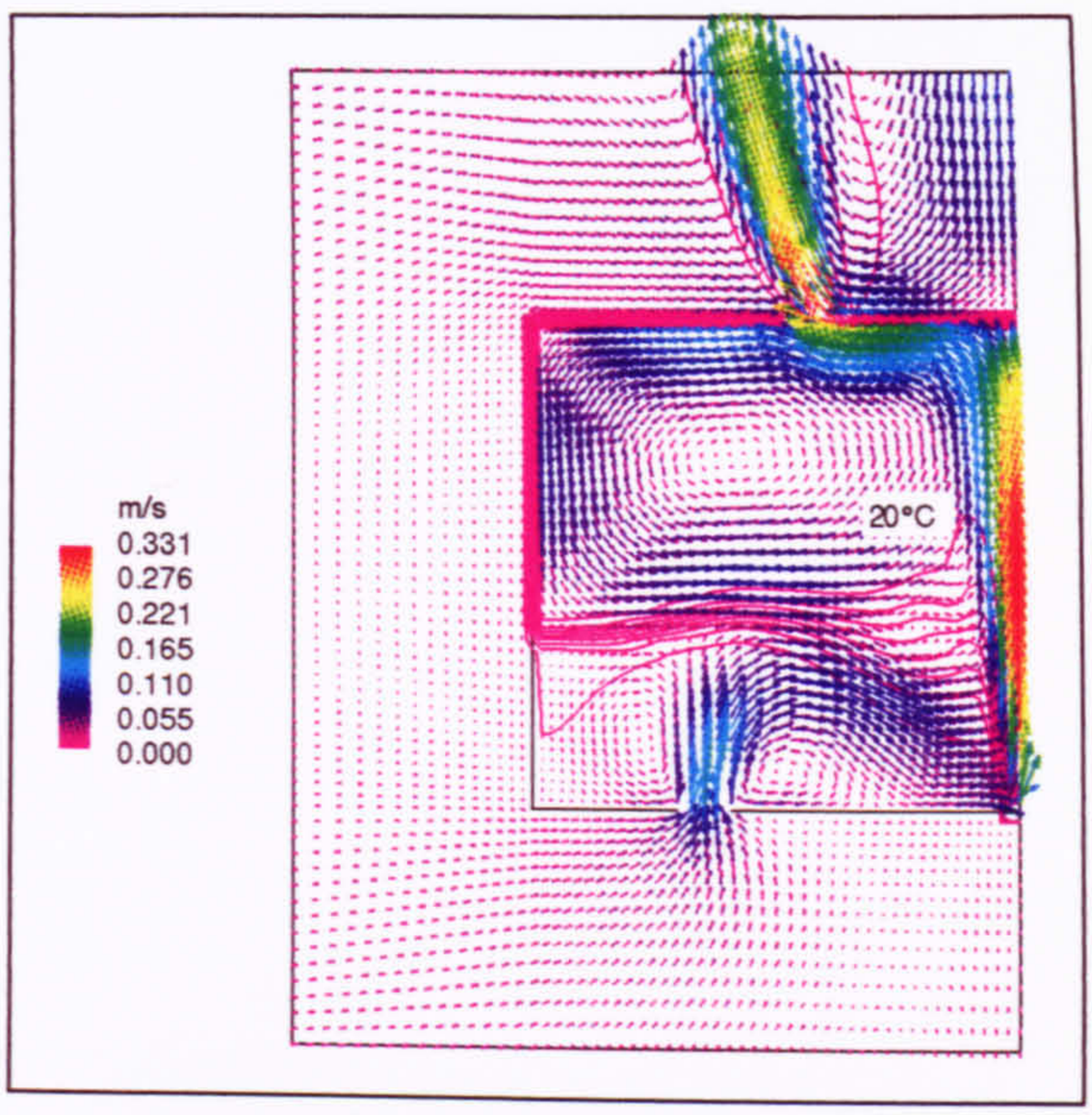

Figure 5.45 Exterior Space 2.

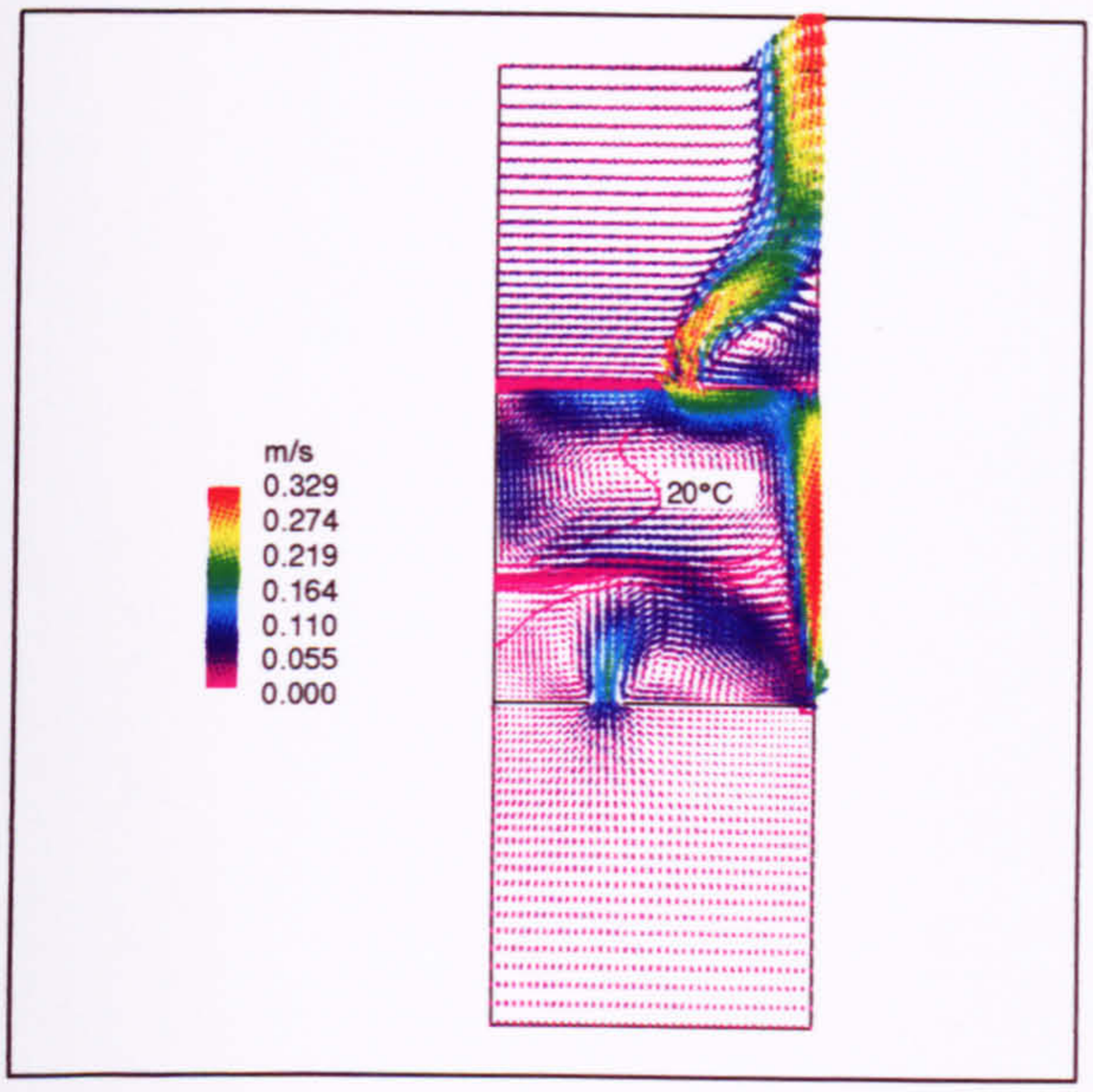

Figure 5.46 Exterior Space 3.

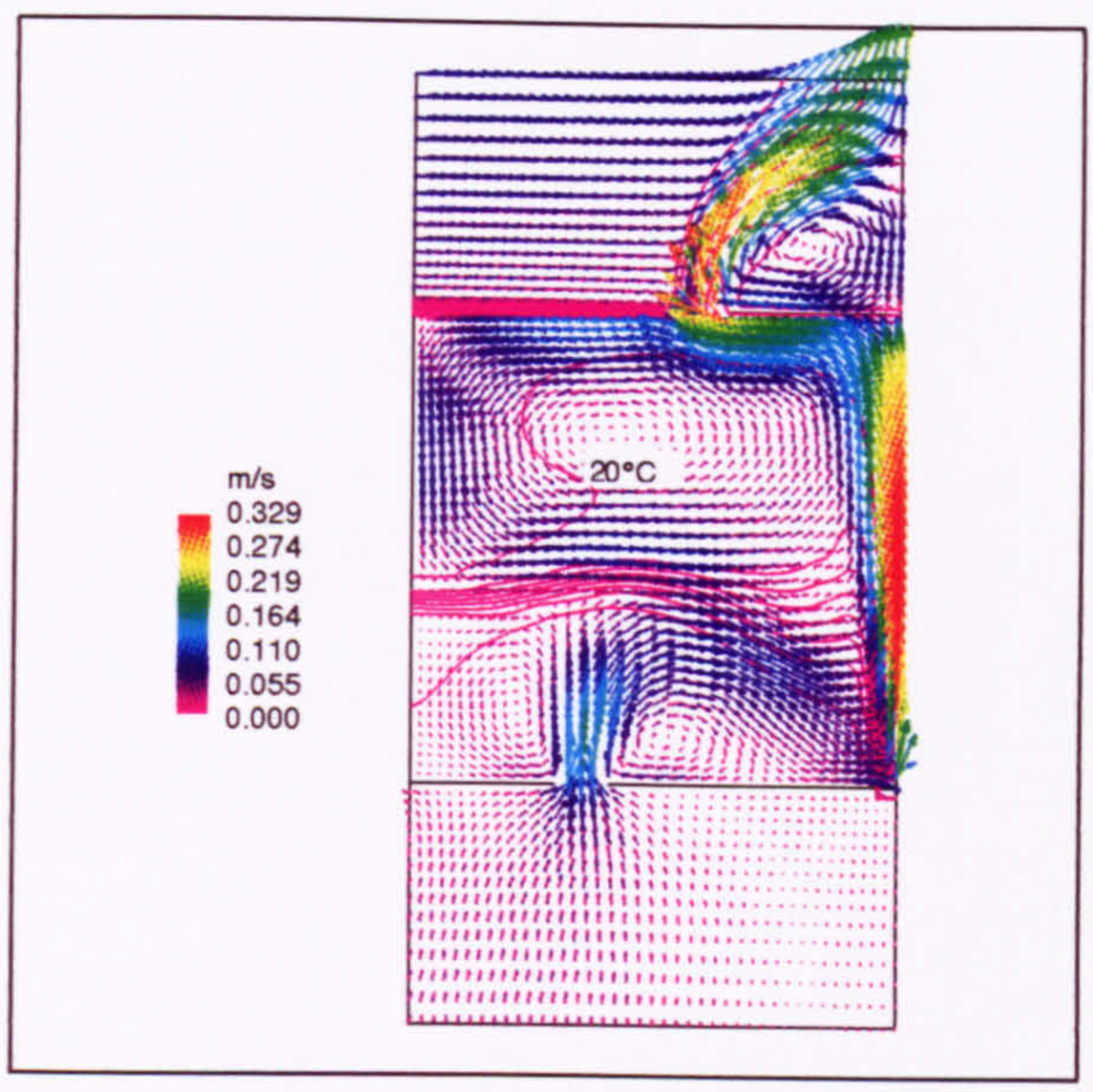

Figure 5.47 Exterior Space 4.

5.11 Summary

This chapter has addressed the CFD modelling of a 2D line source of heat in a rectangular space with openings in the top and bottom. All results have been compared with the theory and experimental work of Linden et al. (1990).

A good estimate of the flow was found using the default under-relaxation factors after about 4000 iterations. In order to obtain full convergence (i.e. adherence to the convergence criteria), under-relaxation had to be imposed in the form of false time-steps. This is a particular type of under-relaxation which is closely related to the rate at which variables evolve and the local mesh size. The size of the false time-step was largely found by trial and error, although a good estimate was found by dividing the smallest cell dimension by the largest velocity in the space. These two values could be taken from the initial simulation results in which default under-relaxation was used.

An analysis of the mesh density and structure used to obtain the solution revealed convergence problems when highly non-orthogonal (skewed) meshes were employed. It was concluded that relatively coarse meshes could be used to give a good qualitative picture of the flow pattern, but finer meshes were necessary to enable accurate calculations of plume properties and interface height.

The CFD results offered good qualitative agreement with the theory of Linden et al. (1990). That is:

- h increased as A_L^* was increased;
- h was independent of B_L [1];
- g_h' decreased as A_L^* was increased; and
- g_h' increased as B_L was increased.

Since the plume plays a vital role in determining the flow properties, a detailed analysis of the plume behaviour was conducted and confirmed the following:

---

[1] This considers the slight variations when using the RNG $k-\varepsilon$ model to be negligible.

- $M_L \propto y$;
- $M_L \propto B_L^{1/3}$; and
- $G_T' \propto B_L^{2/3}$.

Plume theory also states that $G_T' \propto y^{-1}$ for a line source, but this was not predicted accurately by the CFD code. Instead, the CFD models predicted relationships of $G_T' \propto y^{-0.6}$ ($k-\varepsilon$ model) and $G_T' \propto y^{-0.57}$ (RNG $k-\varepsilon$ model).

The accuracy of the quantitative predictions of the displacement ventilation flow (interface height and stratification strength) rely on the successful modelling of the plume. One of the most important parameters governing the plume is the plume entrainment. When compared with the value of entrainment used by Linden et al. (1990) and that found experimentally previously (Morton et al. (1956), Rouse et al. (1952), and Baines and Turner (1969)), the RNG $k-\varepsilon$ model agreed favourably, whereas the standard $k-\varepsilon$ model over-predicted the entrainment. This lead to an over-prediction of plume volume flux using the standard $k-\varepsilon$ model which caused the interface to form earlier (lower). The corresponding under-prediction of plume buoyancy did not adversely affect the prediction of buoyancy change across the interface due to a cancelling effect of entrainment and interface height between the two turbulence models.

An investigation of the exterior space used in the CFD model concluded that the same results could be obtained using exterior zones above and below the space only, rather than an exterior domain surrounding the whole box. This enabled substantial reductions in simulation time which would prove invaluable in three dimensional simulations.

Chapter 6

Three Dimensional Modelling of Buoyancy-Driven Displacement Ventilation: Line Source

6. Three Dimensional Modelling of Buoyancy-Driven Displacement Ventilation: Line Source

6.1 Preamble

Having established a successful modelling strategy for simulating two dimensional flows, sufficient knowledge had been acquired to proceed with potentially more realistic, three dimensional simulations. This chapter describes the 3D simulations carried out using CFX to model the flow resulting from a line source of buoyancy. This formed a transition from 2D (line source) simulations to 3D point source simulations, and enabled any inaccuracies in the 2D simulations arising from the inherent 'slot' representation of the openings to be investigated.

Many of the findings resulting from the 2D simulations were used to begin the 3D work. For example, use and choice of under-relaxation parameters, turbulence modelling, exterior modelling, values for enthalpy and buoyancy reference temperatures, etc., were all influenced by the 2D work. Due to the findings of Chapter 5, all simulations were conducted using both the standard and the RNG $k-\varepsilon$ models, and particular attention was given to the value of the entrainment constant α_T predicted in each case. The effects of varying opening sizes and source strength were analysed. The reference case for analysis in this chapter is **Benchmark 2.**

6.2 Definition of Benchmark 2

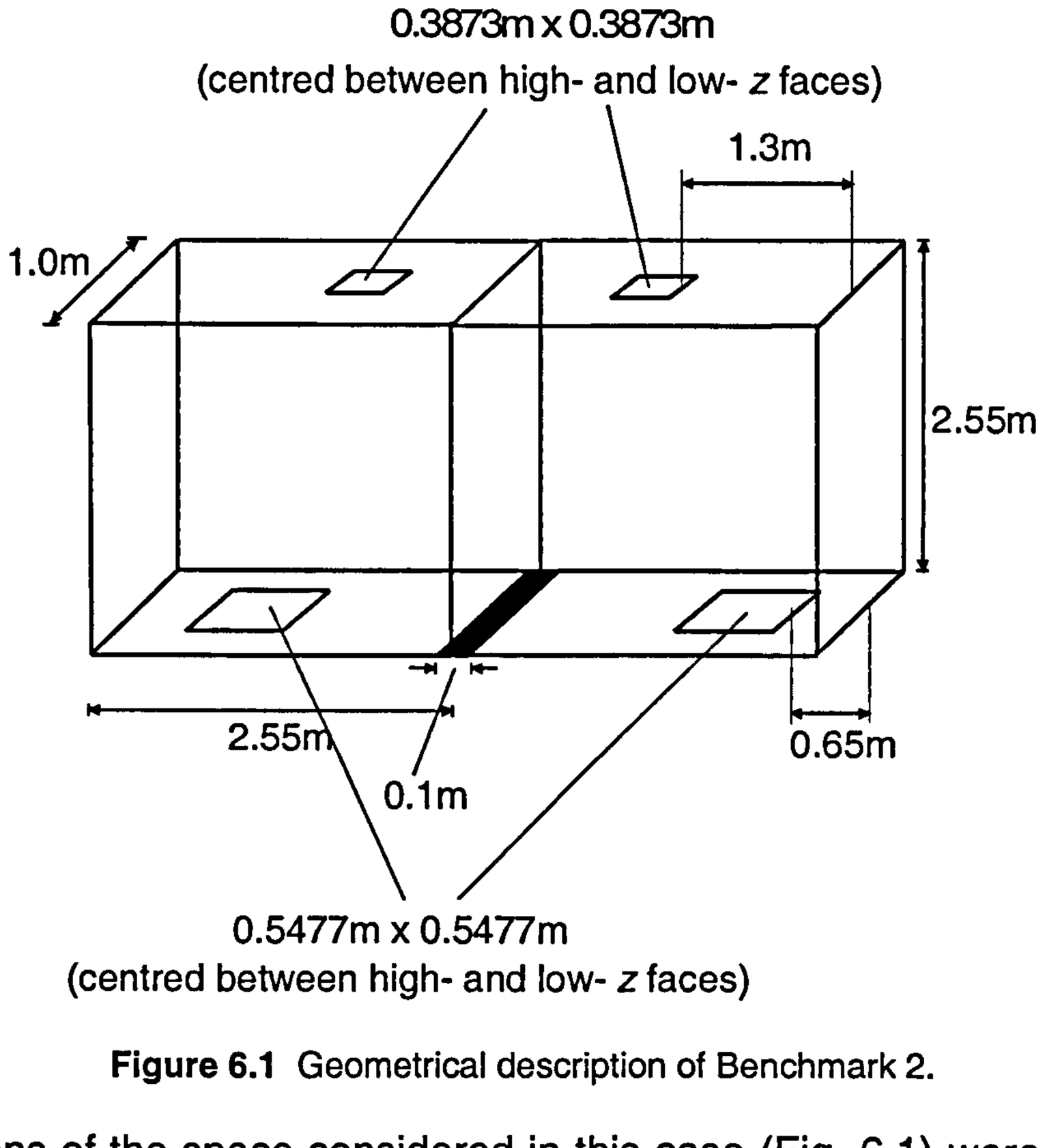

Figure 6.1 Geometrical description of Benchmark 2.

The dimensions of the space considered in this case (Fig. 6.1) were the same as those for Benchmark 1 and the *z* dimension was set equal to 1m for numerical convenience. The source strength was 200W and the ambient temperature set to 18°C. All fluid properties and reference temperatures were the same as those used for Benchmark 1.

One of the aims of this benchmark was to establish how well a 2D simulation of a line source (Benchmark 1) is able to represent a 3D simulation. Consequently, the opening areas (per unit length in the *z*-direction) in Benchmark 2 were the same as those for Benchmark 1, the only difference being that the holes in this benchmark were rectangular compared with the 'long slots' inherent in using a 2D model.

6.3 Representing Benchmark 2 in CFX

Once again, the technique of modelling some of the exterior space to account for the effects of flow through the openings was adopted. Based on the sensitivity analysis carried out in §5.10, only exterior spaces above and below the space were defined (Fig. 6.2). A symmetry plane was again used to reduce computation. The WALL boundary shading on the high-z face of the box is omitted in Figure 6.2 for clarity.

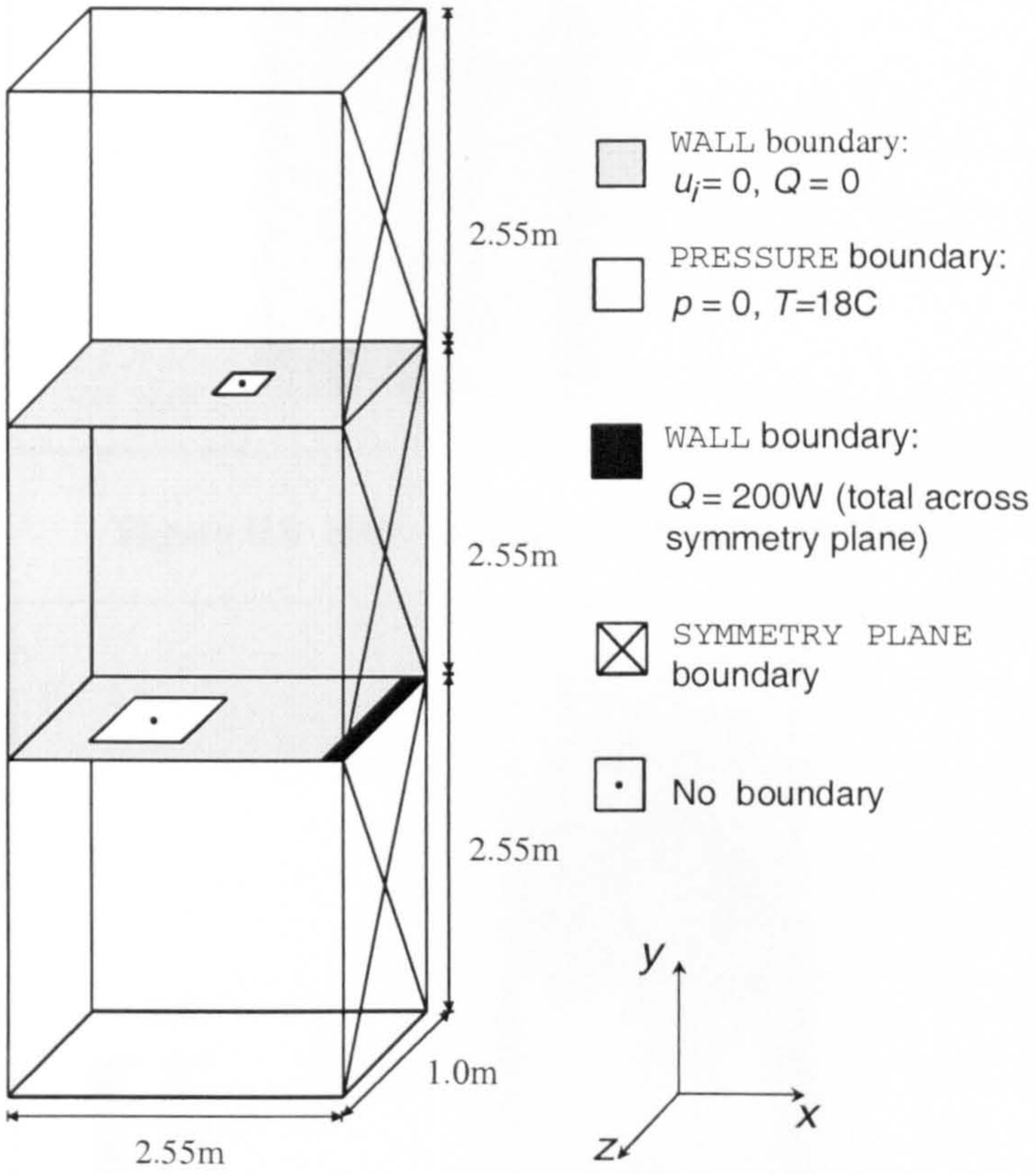

Figure 6.2 Representation of Benchmark 2 in CFX.

To enable reliable comparisons with the 2D results, a similar mesh structure was used in the x-y plane as in Benchmark 1 - 46×40 in the room and 46×25 in each of the exterior spaces (Fig. 6.3). 21 cells were used in the z direction (pro-rata according to length). The appearance of the mesh is slightly different to Benchmark 1 owing to the different block structure required to define the exact opening sizes.

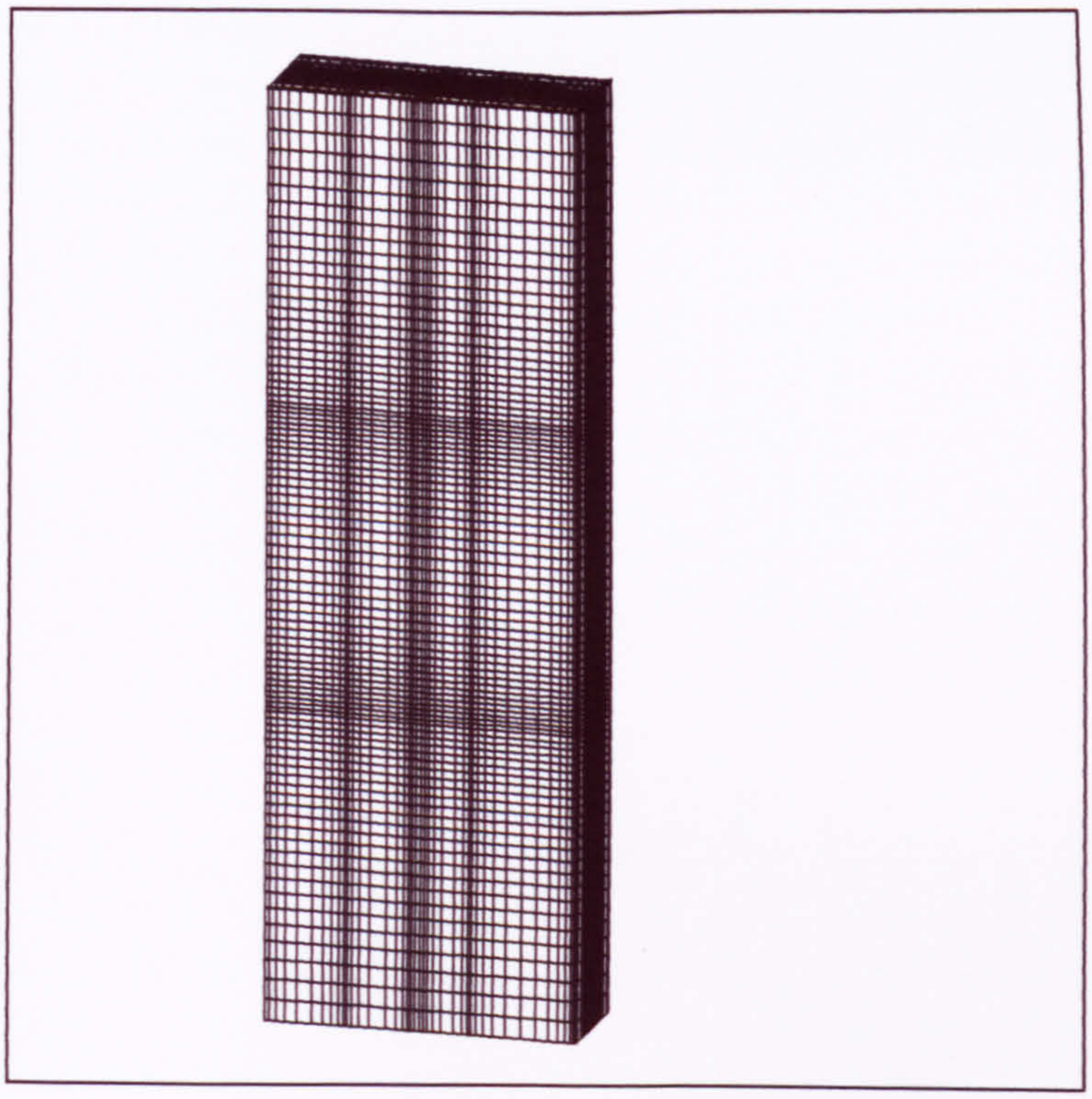

Figure 6.3 Mesh structure used in Benchmark 2.

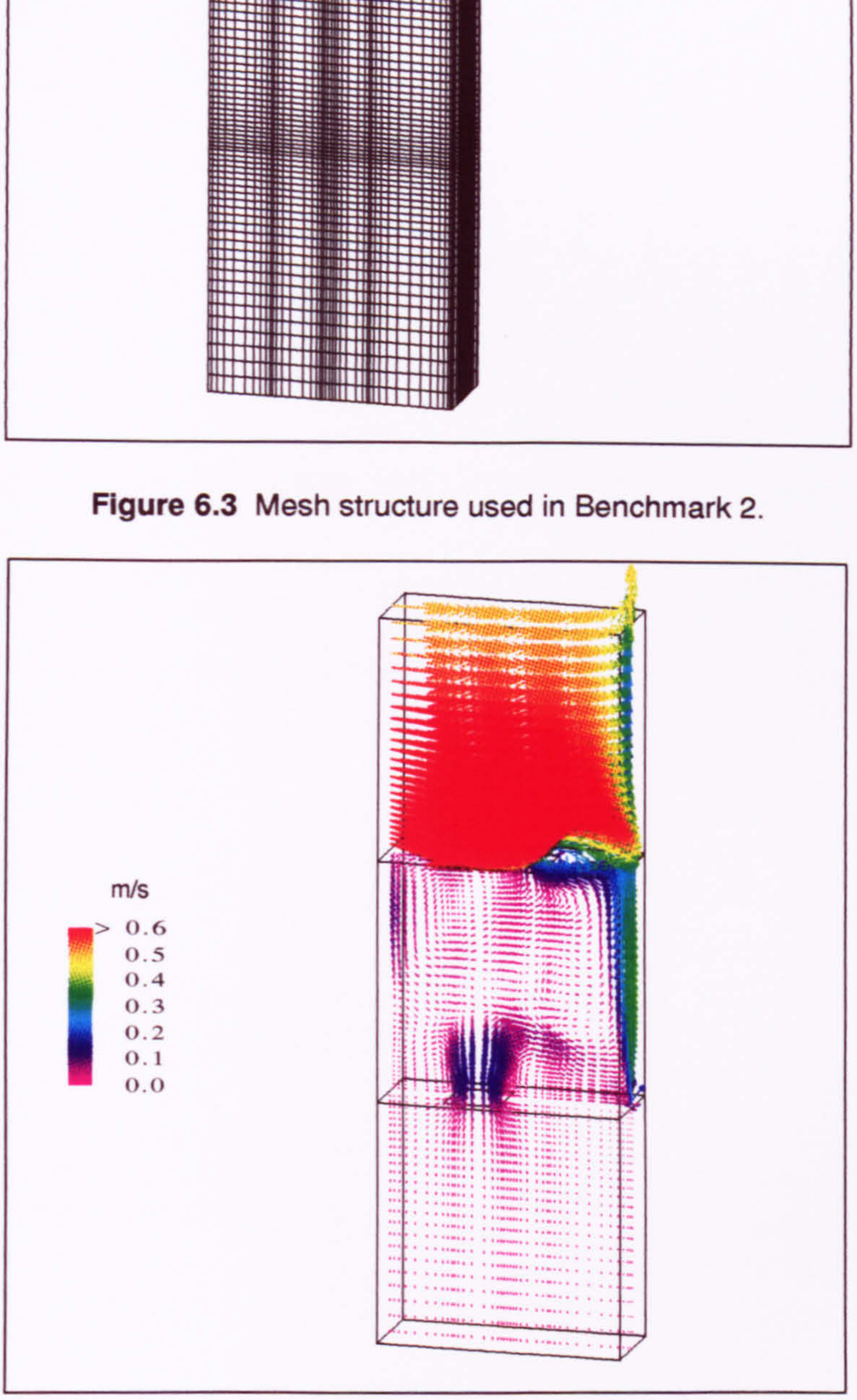

Figure 6.4 Inaccurate velocity field in Benchmark 2 simulation.

6.4 Analysis of Benchmark 2 Results

6.4.1 Initial Simulations

The first simulation, carried out using default under-relaxation factors and no false time-stepping, showed constant absolute values but very high residuals ($He_{res} \approx 150\text{W}$). Analysis of the velocity field revealed unrealistically high air flows in the positive z-direction across the pressure boundaries (Fig. 6.4). This 'artificial entrainment' problem was mentioned and explained in §5.10. In 3D however, its presence appeared to be much more dominant and it was not possible to eliminate the effect using under-relaxation or false time-stepping. `WALL` boundaries were therefore imposed on the high- and low-z faces of the exterior space. A similar problem also occurred in some initial simulations across the low-x face of the lower exterior space, so a `WALL` boundary was imposed here also. Convergence was then obtained after about 1000 iterations using default under-relaxation factors and no false time-stepping, followed by about 2000 iterations using false time-steps of 0.1s on all three momentum equations (absolute values were constant and $He_{res} \cong 0.08\text{W}$). Table 6.1 shows the key numerical parameters and techniques used to obtain the result.

Table 6.1 Summary of numerical parameters and techniques used to obtain a solution for Benchmark 2.

Parameter/Technique	Details
Solution procedure	Hybrid differencing was used on all convection terms except in the mass conservation equation where central differencing was used. Pressure correction was carried out using the SIMPLEC algorithm. For further details see §§D.3.3 and D.4.2).
Turbulence	Standard k-ε (§4.5.4).
Enthalpy reference temperature	Ambient (= 18°C).
Buoyancy reference temperature	Ambient (= 18°C).
Under-relaxation factors	Default (momentum: 0.65, mass: 1.0, turbulent kinetic energy and dissipation: 0.7, energy: 0.7).
False time-steps	0.1s on u, v and w momentum equations in restart simulations.
Mesh	$46 \times 90 \times 21$ (see Fig. 6.3).
Boundary conditions	The domain boundary is made up of: SYMMETRY PLANE boundaries (§4.6.3); PRESSURE boundaries (§4.6.2) where $p = 0$ and $T = 18°C$; and WALL boundaries. WALL boundaries were required on some domain boundaries in the exterior to prevent 'artificial entrainment'. All WALL boundaries are adiabatic ($Q = 0$) except the source ($Q = 200W$) and posses the no-slip condition ($u_i = 0$) and wall functions described in §4.6.1.

6.4.2 Analysis of the Displacement Flow Pattern in Benchmark 2

The predicted flow patterns of this benchmark were very similar to its 2D counterpart (Benchmark 1), demonstrating the now familiar buoyancy-driven displacement ventilation flow pattern (Fig. 6.5). An important difference however, was the more random nature of the flow direction exhibited in the 3D case (c.f. Figs. 5.9 and 6.5). This is due to the freedom of motion now available in the z-direction. This also results in lower speeds due to the three dimensional dissipation of the available energy. This slow, random motion is particularly noticeable in the region above the interface, which supports the theory of Linden et al. (1990) who predicted a well-mixed upper layer. Another reason for the more random flow is the square openings which enable different flow patterns to establish in different z planes along the box (Figs. 6.5 - 6.7). Notice the higher

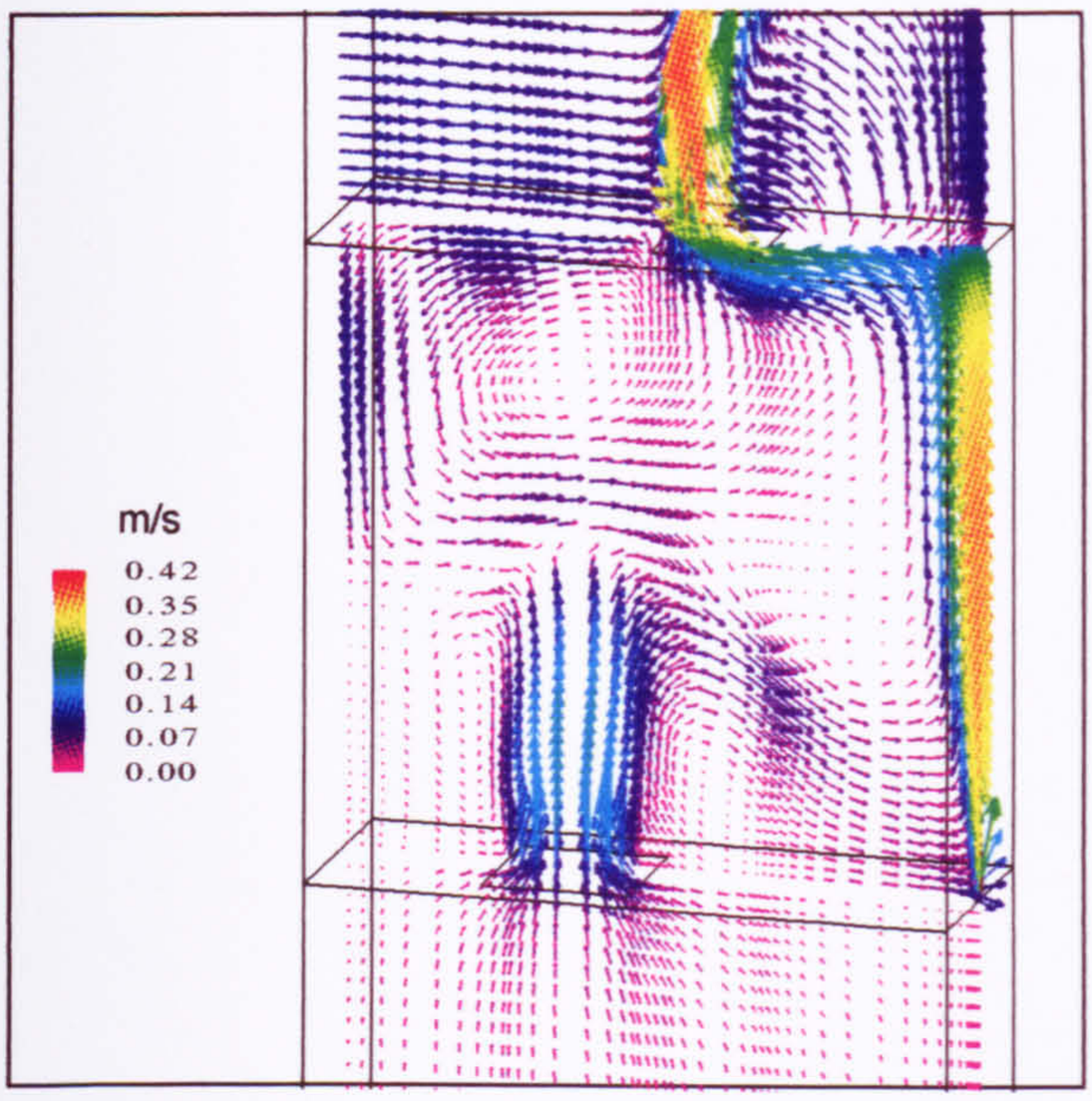

Figure 6.5 Velocity vectors in plane $z = 0.5$m.

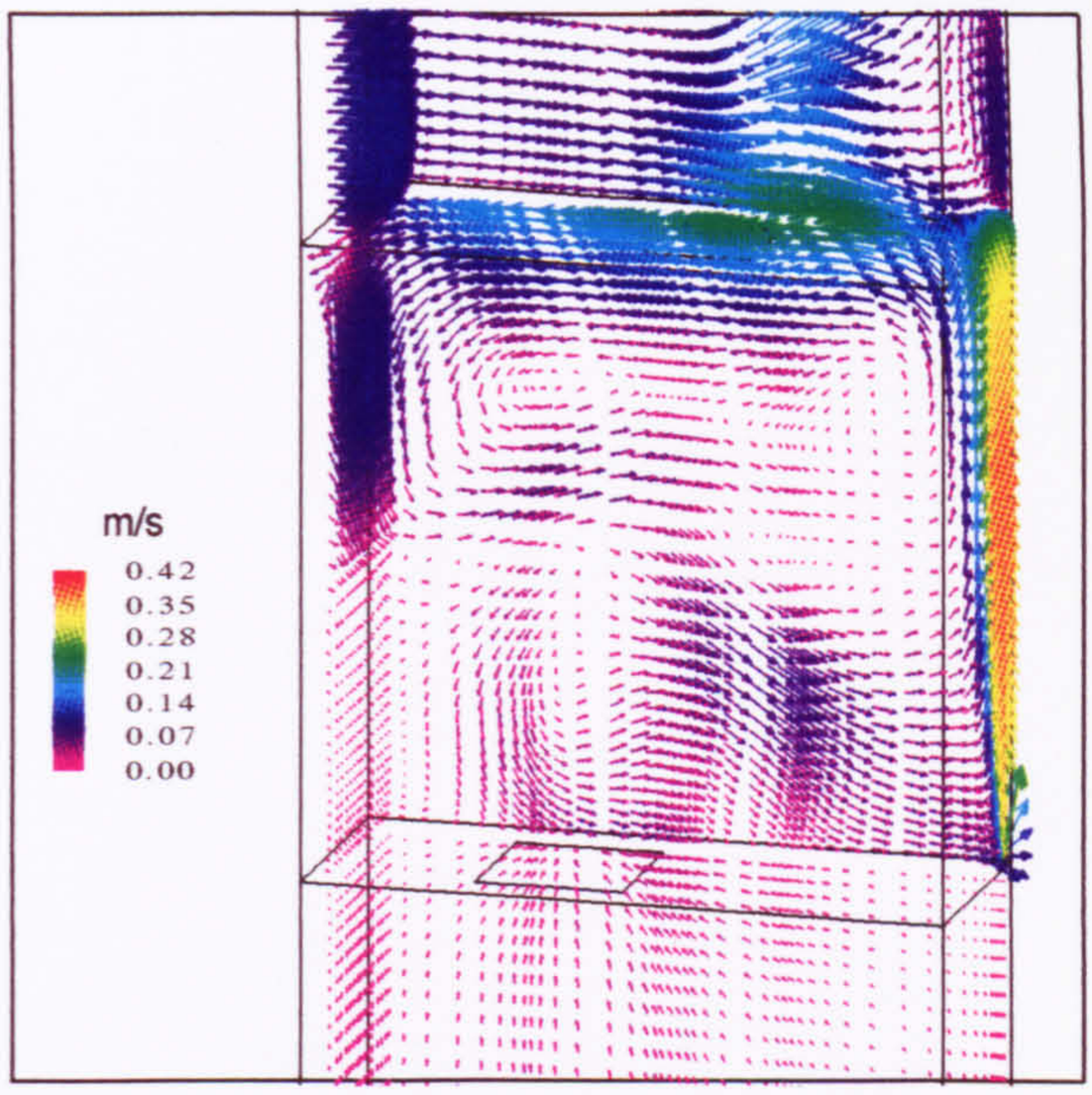

Figure 6.6 Velocity vectors in planes $z = 0.1$m and $x = 0.1$m.

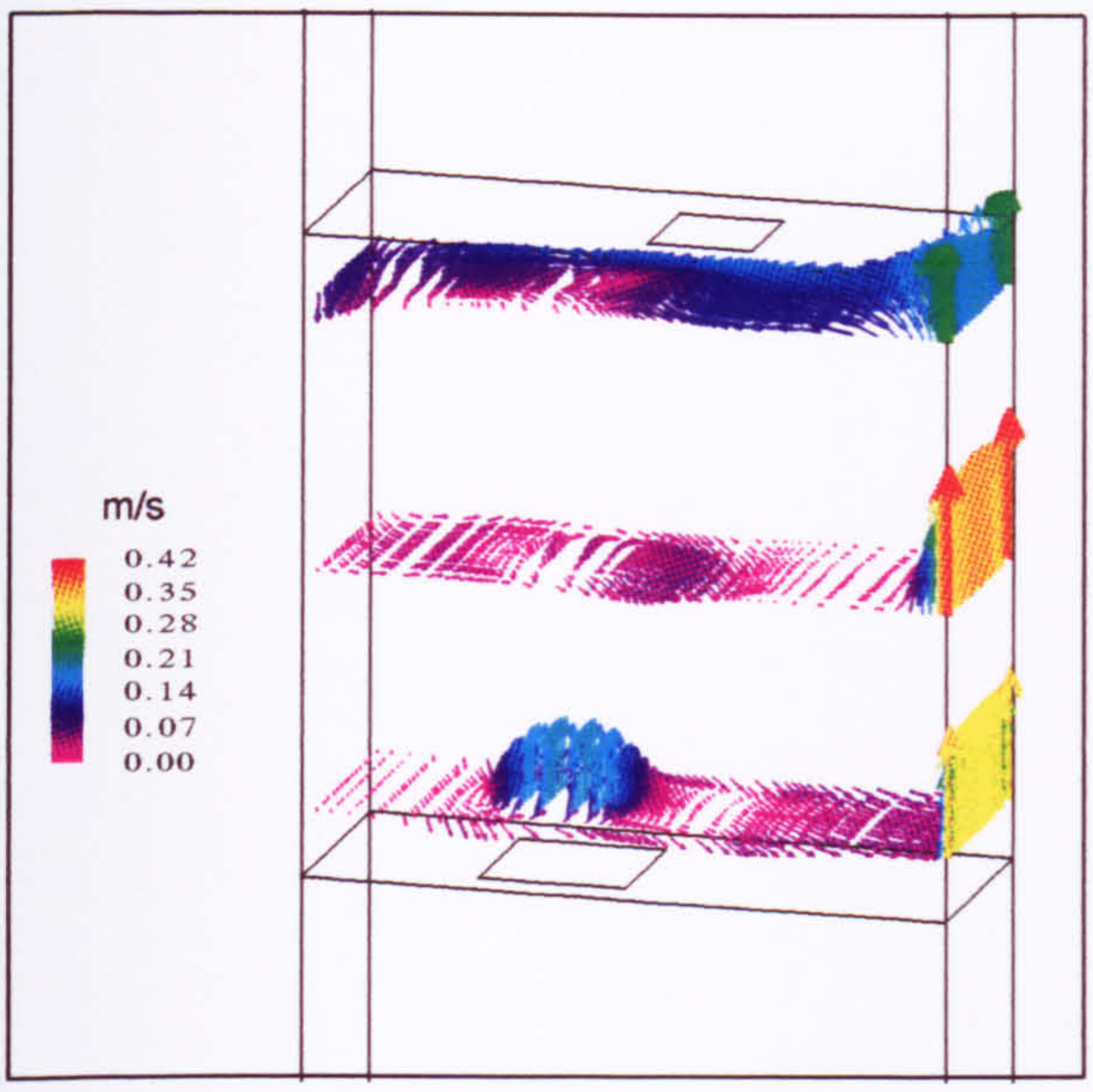

Figure 6.7 Velocity vectors in planes $y = 0.25$m, y = 1.2m and $y = 2.3$m.

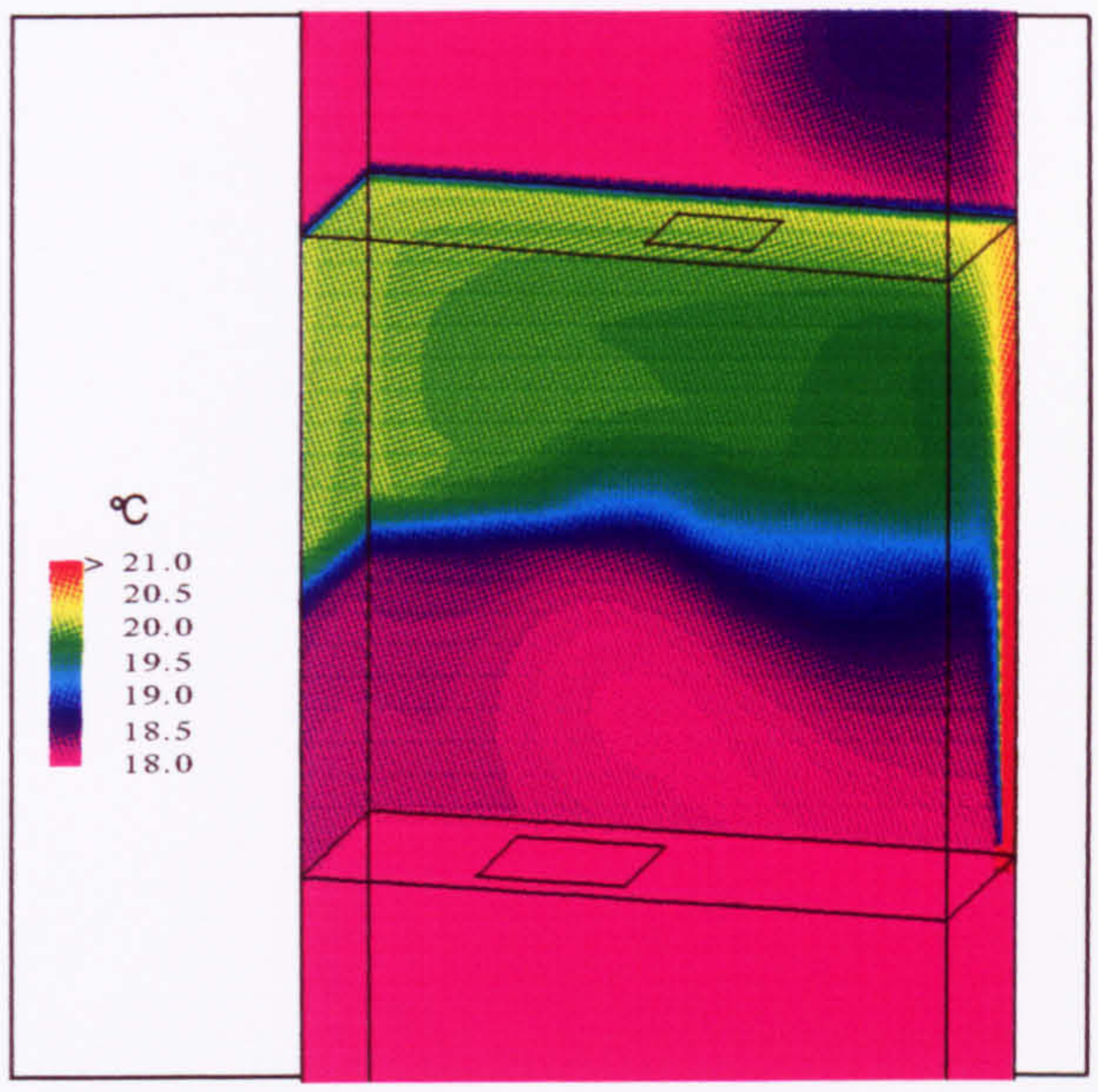

Figure 6.8 Temperature prediction in planes $z = 0.01$m and $x = 0.01$m.

velocities predicted at each end of the plume in Figure 6.7 due to the presence of the solid boundary on the high- and low-z faces causing less entrainment in this region. As predicted, a clearly defined interface is established, not only in the *x-y* plane, but also in the *y-z* plane (Fig. 6.8). This is also illustrated by the vertical temperature profiles shown in Figure 6.9, which also depicts a difference in interface height predicted by the 2D and 3D simulations.

A restart of Benchmark 2 using the RNG $k-\varepsilon$ model revealed a similar flow pattern with a slightly higher interface (Fig. 6.10). The interface properties predicted by Benchmark 2 for the two turbulence models (Table 6.2) show the same characteristic behaviour that was found in Benchmark 1, i.e. the RNG $k-\varepsilon$ model predicts a higher interface than the standard $k-\varepsilon$ model, but a similar stratification strength due to the cancelling effect of entrainment and interface height (§5.7). A more detailed comparison of benchmarks 1 and 2 is given in §6.5.

Table 6.2 Displacement ventilation flow properties predicted by Benchmark 2.

	CFD		Theory
	$k-\varepsilon$	RNG	(Linden et al. (1990))
h/H	0.457	0.544	0.603
g'/G'_H	1.92	1.99	1.66
ach^{-1}	22.42	21.81	25.66[1]

[1] This value is calculated using the theoretical value of M_L (Eq. 3-25) at $y = h$ where h is the interface height predicted by Linden et al. (1990).

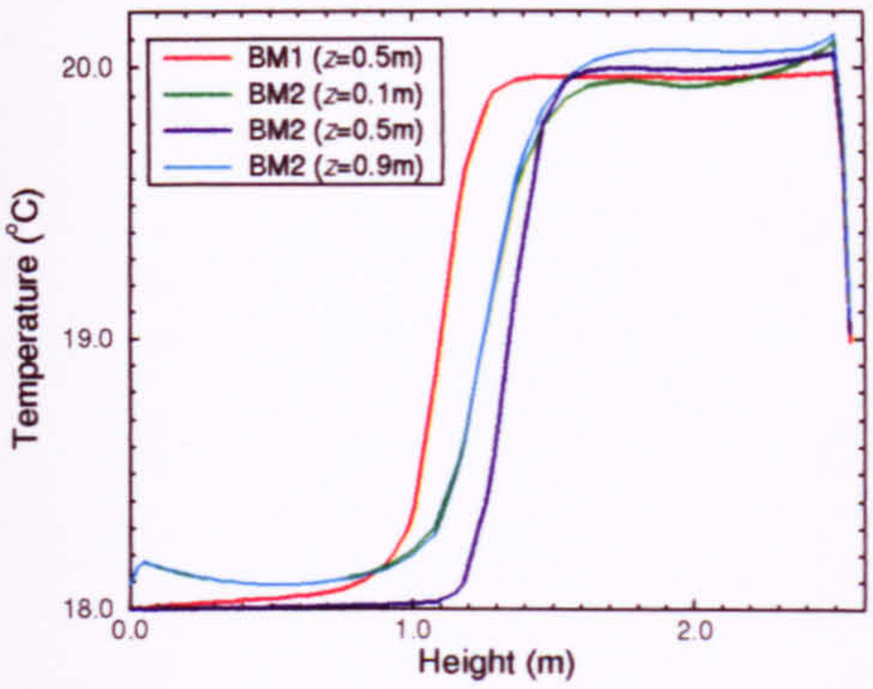

BM1 - Benchmark 1, BM2 - Benchmark 2

Figure 6.9 Vertical temperature profiles for benchmarks 1 and 2 at a distance of 0.2m from the left-hand wall of the space.

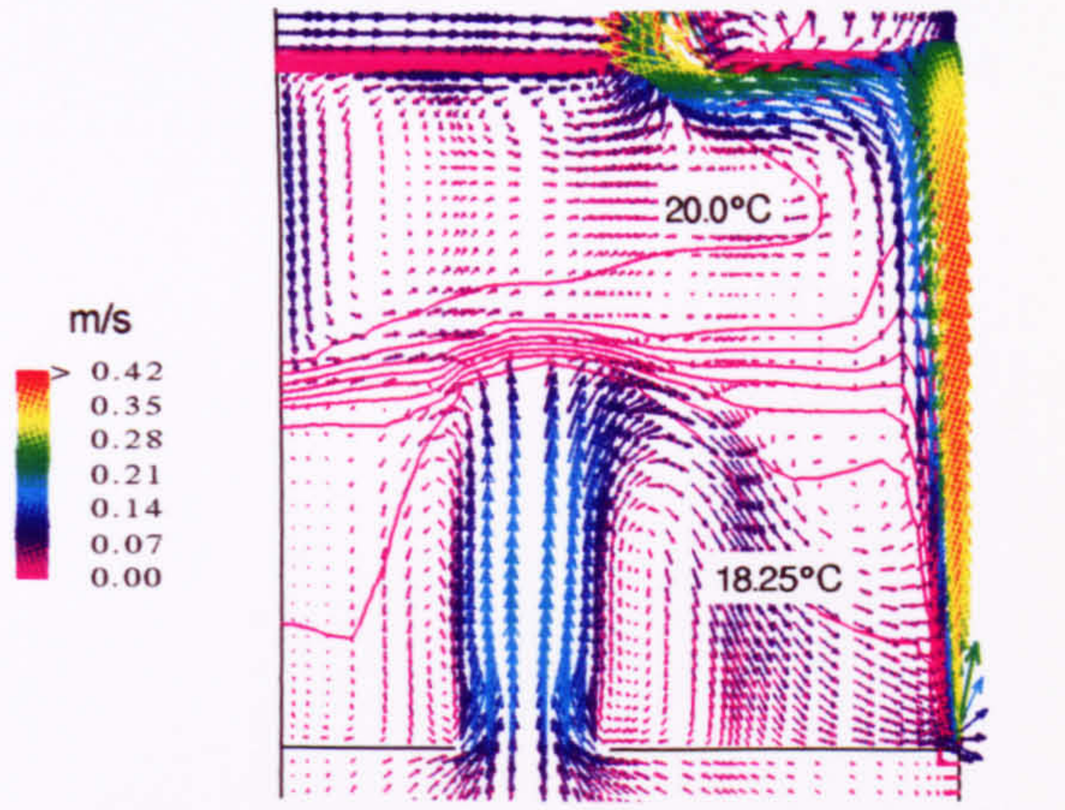

Figure 6.10 Velocity vectors and temperature contours in the plane $z = 0.5$m when using the RNG $k-\varepsilon$ model for Benchmark 2.

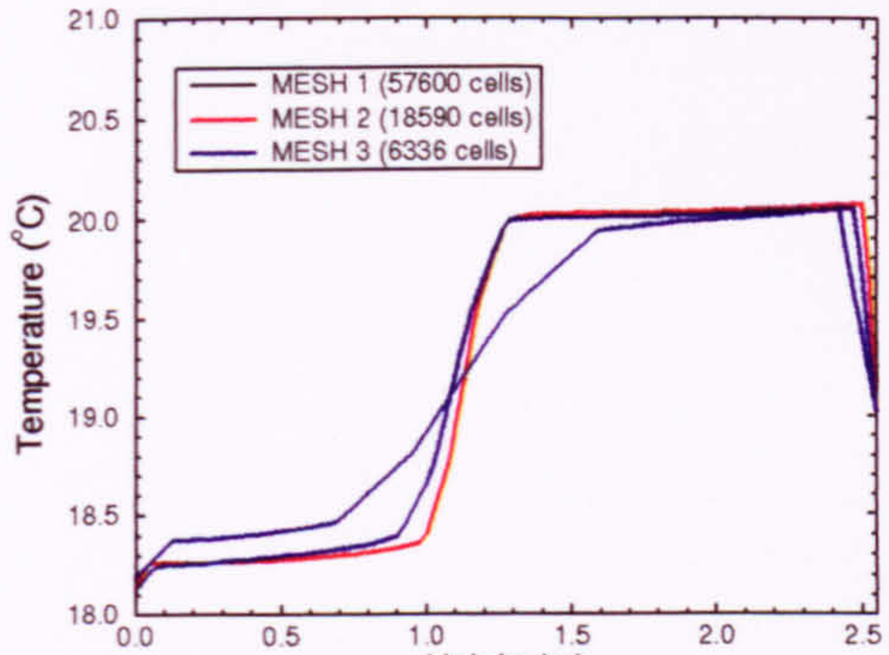

Figure 6.11 Comparison of vertical temperature profiles for different mesh densities at 0.2m from the left-hand wall.

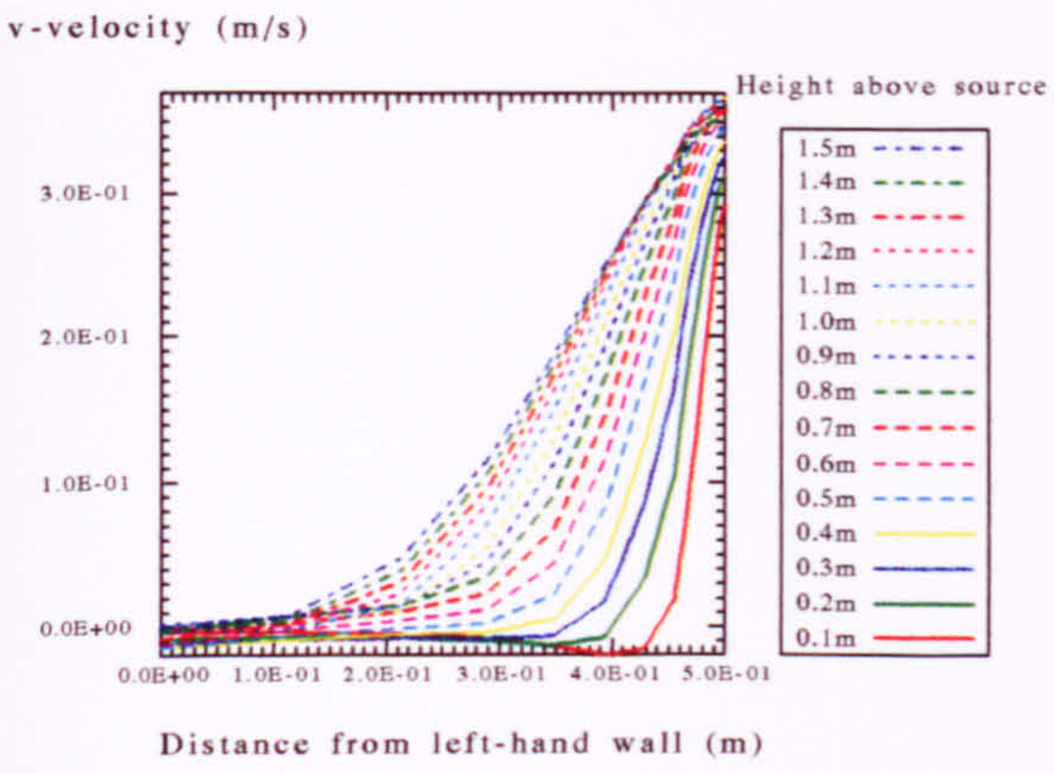

(a)

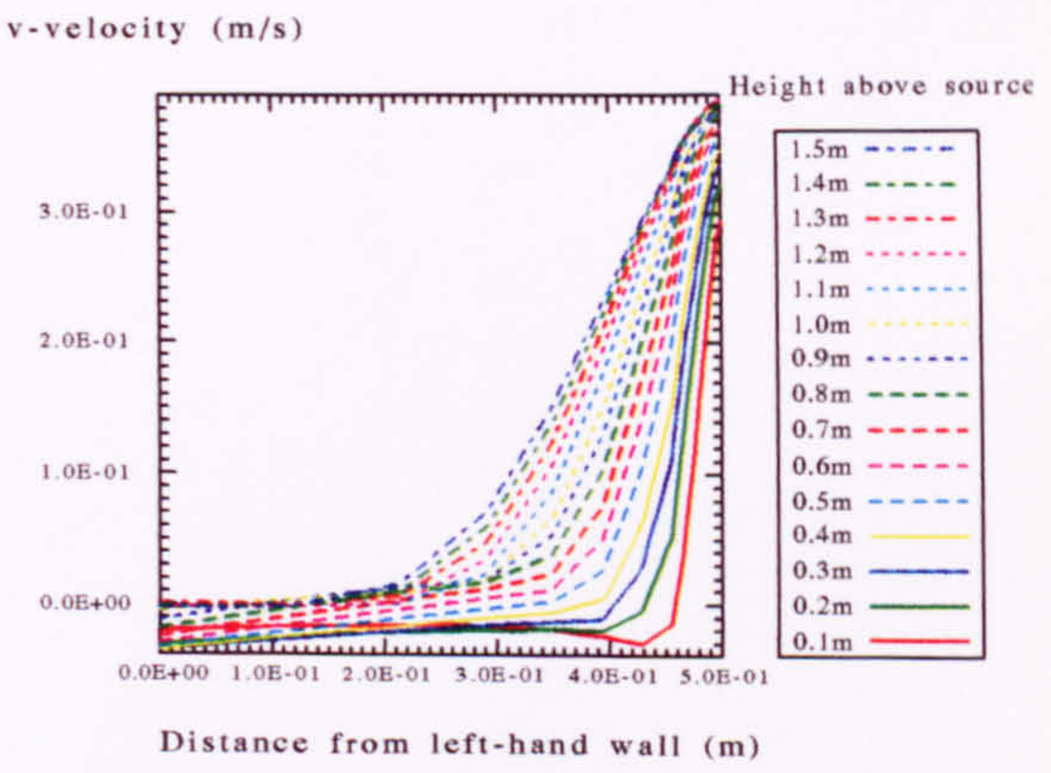

(b)

Figure 6.12 Vertical velocities in plane $z = 0.5$m at 10cm vertical intervals for (a) standard $k-\varepsilon$ model, and (b) RNG $k-\varepsilon$ model.

6.4.3 Mesh Investigation

To ensure that inaccuracies due to mesh resolution were small, two coarser meshes were investigated (Table 6.3). The results confirmed the same findings as Benchmark 1, i.e. a coarser mesh could have been adopted if only a qualitative prediction of the flow field was required, but the fine mesh (MESH 1) was needed in order to accurately calculate the plume properties and measure the interface height (note the more diffuse interface predicted using MESH 3 (Fig. 6.11).

Table 6.3 Effect of mesh density on displacement ventilation flow properties (standard $k-\varepsilon$ model).

Case	Number of cells	h/H	g'_h / G'_H	Air change rate (ach^{-1})
MESH 1 (Benchmark 2)	86940	0.457	1.92	22.42
MESH 2	18590	0.448	1.88	22.12
MESH 3	6336	0.438	1.85	22.84

6.4.4 Plume Properties

6.4.4.1 Plume Entrainment

Given the findings from the 2D simulations, it was important to calculate the ('top-hat') entrainment constant, α_T. Therefore, vertical velocity profiles were measured in the plane containing the upper and lower openings ($z = 0.5$m) (Figs. 6.12a and 6.12b) - this location enabled reliable comparisons with those measured in Benchmark 1. Comparison of Figures 6.12a and b already suggests that the RNG model has again predicted a narrower plume than the standard $k-\varepsilon$ model.

Using the same technique adopted in Chapter 5, the Gaussian plume width, b_G, and axial velocity, v_G, were used to calculate the 'top-hat' properties b_T and v_T. These properties, along with the corresponding value for enthalpy, are given in Table 6.4.

Table 6.4 Comparison of plume data obtained from Figures 6.12(a) and (b) for the standard and RNG $k-\varepsilon$ turbulence models.

Height above source (m)	$v_T = \frac{v_G}{\sqrt{2}}$ (*)		$b_T = \sqrt{\frac{\pi}{2}} b_G$ (*)		$He_T = \frac{He_G}{2}$ (*)	
	$k-\varepsilon$	RNG	$k-\varepsilon$	RNG	$k-\varepsilon$	RNG
0.1	0.206	0.208	0.042	0.038	8143.0	5838.9
0.2	0.221	0.227	0.061	0.052	4240.35	4417.5
0.3	0.230	0.238	0.083	0.061	3369.1	3559.9
0.4	0.238	0.245	0.099	0.074	2815.3	2992.2
0.5	0.244	0.252	0.117	0.088	2429.5	2587.2
0.6	0.249	0.257	0.132	0.099	2148.6	2287.4
0.7	0.253	0.262	0.148	0.112	1936.1	2057.3
0.8	0.257	0.265	0.165	0.126	1772.0	1876.6
0.9	0.259	0.268	0.181	0.136	1640.8	1729.9
1.0	0.260	0.271	0.192	0.148	1535.6	1610.0
1.1	0.259	0.272	0.209	0.161	1451.2	1512.7
1.2	0.257	0.272	0.225	0.173	1381.5	1430.9
1.3		0.272		0.185		1264.0
1.4		0.270		0.194		1305.9
1.5		0.267		0.208		1257.0

(*) See Appendix B for derivation of these formulae.

The gradient of the graphs in Figure 6.13 were used to determine the entrainment constant, α_T, predicted by each turbulence model:

$$\text{gradient} = \alpha_T \qquad \text{(Eq. (B-29))}$$

$$\Rightarrow \quad \alpha_T^{k-\varepsilon} = 0.16 \text{ and } \alpha_T^{RNG} = 0.12$$

6.4.4.2 Volume Flux in the Plume

Using the 'top-hat' values calculated in Table 6.4, the variation of volume flux in the plume, M_L, with height was plotted (Fig. 6.14) using the expression $M_L = 2b_T v_T$.

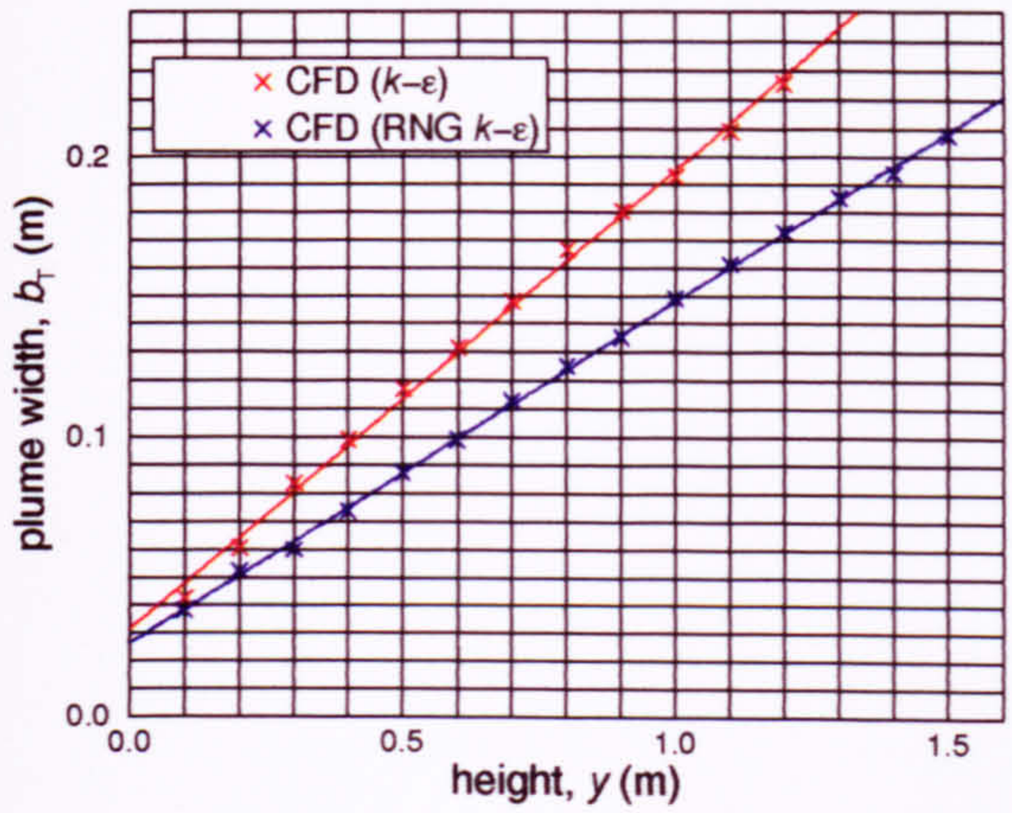

Figure 6.13 Variation of plume width with height above the source for both turbulence models.

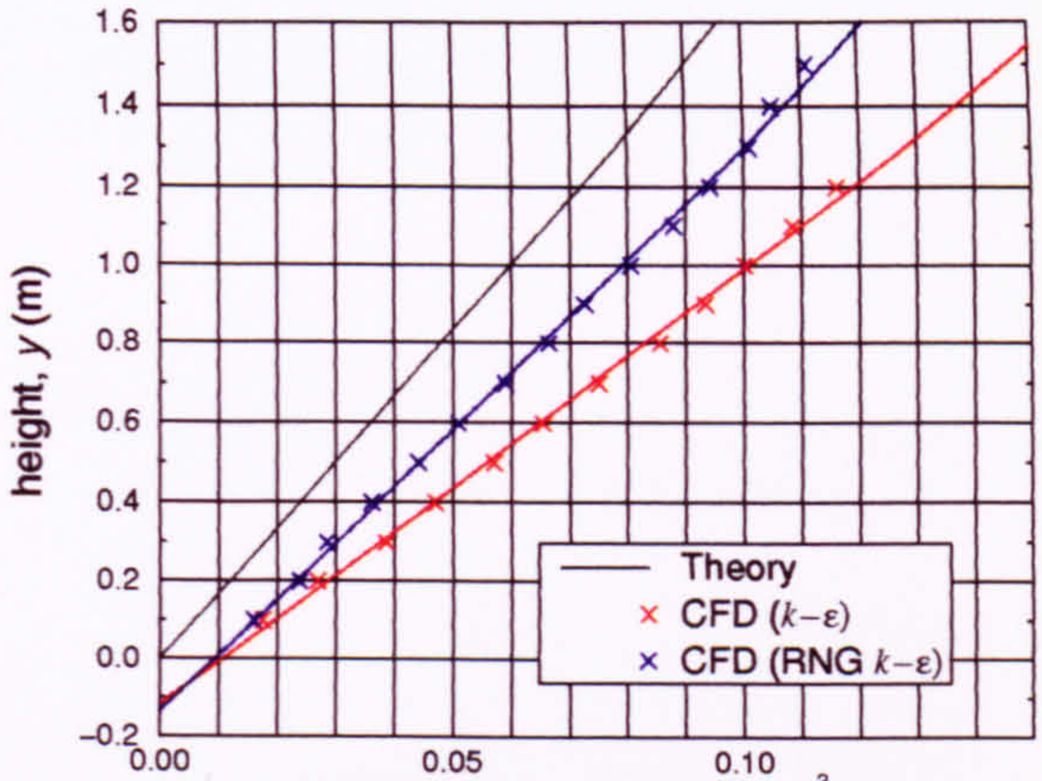

Figure 6.14 Variation of plume volume flux with height above the source.

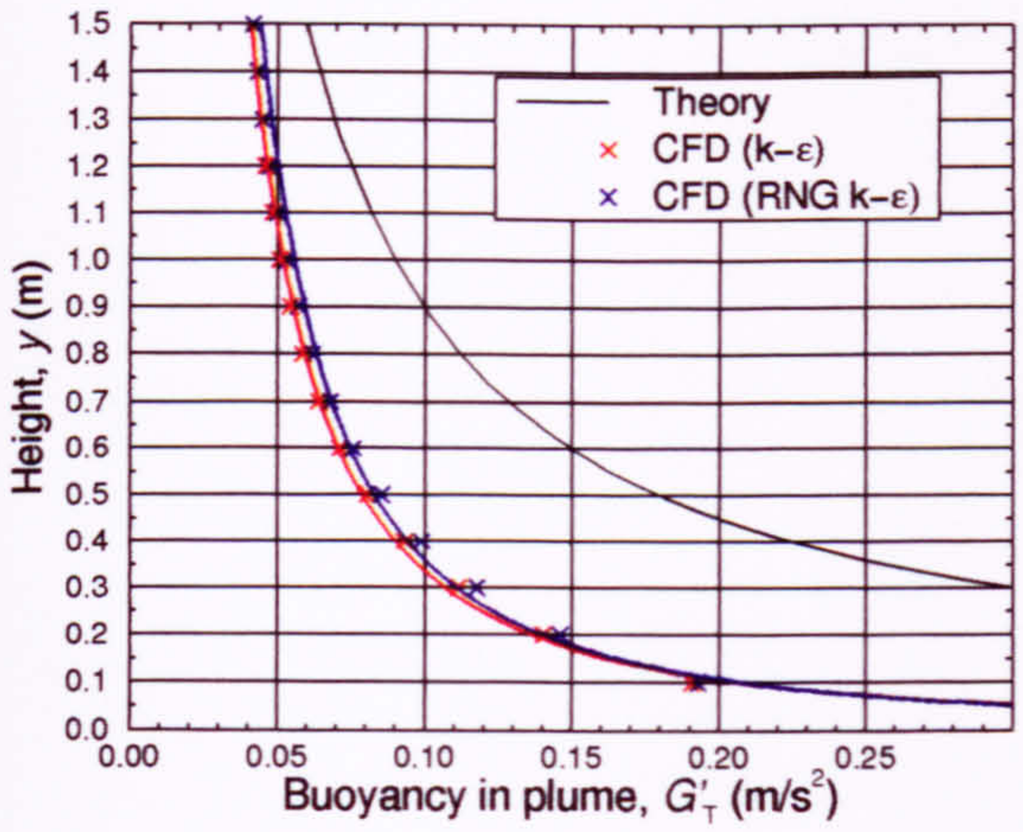

Figure 6.15 Variation of plume buoyancy with height above the source.

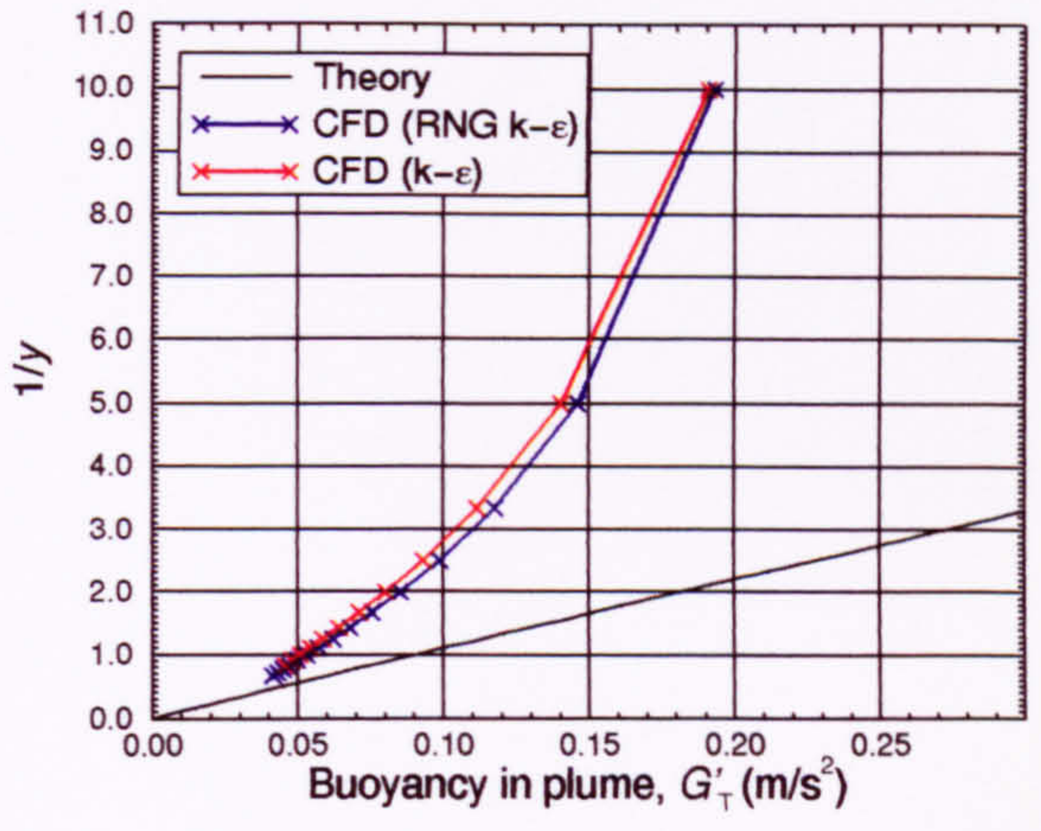

Figure 6.16 Variation of plume buoyancy with y^{-1}.

The volume flux in the plume is given in the theory by Eq. (3-25): $M_L = DB_L^{1/3} y$. According to this equation, the volume flux varies linearly with height above the source. This is demonstrated by the CFD results for both turbulence models (Fig. 6.14). The gradient of these graphs is given by $1/DB_L^{1/3}$. It therefore follows from the entrainment constants calculated in §6.4.4.1 that the $k-\varepsilon$ line should posses a smaller gradient than the RNG line whose gradient should be closer to that of the theoretical line, which was indeed the case. The differences in the *y*-axis intercept are due to the existence of the virtual origin discussed in section 5.4.4. It is seen from Figure 6.14 that the standard $k-\varepsilon$ model predicts a virtual origin at $y \approx -0.1\text{m}$ and the RNG $k-\varepsilon$ model at $y \approx -0.12\text{m}$. The graphs in Figure 6.14 give volume fluxes of $M_L^{k-\varepsilon} = 0.115\,\text{m}^3/\text{s}$ and $M_L^{\text{RNG}} = 0.106\,\text{m}^3/\text{s}$ at the interface heights $y = 1.17\,\text{m}$ and $y = 1.39\,\text{m}$ respectively, which are larger than the volume fluxes through the space predicted by the CFD simulations (Table 6.2). This may be due to the entrainment of air across the interface caused by momentum forces of the incoming air on the interface (see Fig. 6.5).

6.4.4.3 Buoyancy in the Plume

The buoyancy in the plume, G'_T, was calculated from the plume data in Table 6.4 using the expression

$$G'_T = \frac{g\beta(He_T - He_{ref})}{C_p} \tag{6-1}$$

where the reference value He_{ref} was taken to be the ambient value (=0). The CFD results are compared with the theory in Figures 6.15 and 6.16.

Due to the over-prediction of the volume flux in the plume (Fig. 6.14), caused by an over-prediction of entrainment, it follows from Equation (3-16) ($B = G'_T M$), that the buoyancy in the plume should be *under*-predicted (Fig. 6.15). However, as was observed in Benchmark 1, the CFD simulations predicted a different *shape* to this graph suggesting that the buoyancy in the CFD plumes does not reduce with

height in the same manner as predicted by the theory. This is again substantiated by the non-linear relationship in Figure 6.16 (recall Eq. (3-26): $G' = B_L^{2/3}/yD$).

6.4.5 Effect of Changes in Source Strength

6.4.5.1 Flow Pattern

The CFD results for the standard $k-\varepsilon$ model confirmed the theoretical predictions that although a larger source strength induces higher velocities and a larger temperature change across the interface, the height of the interface remains constant (Table 6.5 and Figs. 6.17 and 6.18). The flow patterns predicted using the RNG $k-\varepsilon$ model show small discrepancies in the interface height (Figs. 6.19 and 6.20 and Table 6.5), namely, an increase in source strength raises the interface slightly. This effect was also observed in Benchmark 1 (Table 5.8) and is discussed in Chapter 8. However, the effect seems larger in Benchmark 2 (variations of about 6.7%) than in Benchmark 1 (variations of about 1%).

Table 6.5 Effect of source strength on displacement ventilation flow parameters.

Source strength (W)	h/H		g'_h / G'_H		ach^{-1}	
	$k-\varepsilon$	RNG	$k-\varepsilon$	RNG	$k-\varepsilon$	RNG
50	0.457	0.533	1.93	2.00	14.12	13.84
200	0.457	0.544	1.92	1.99	22.42	21.87
500	0.457	0.570	1.99	2.03	30.17	29.34
1000	0.457	0.571	1.98	2.04	38.20	36.82

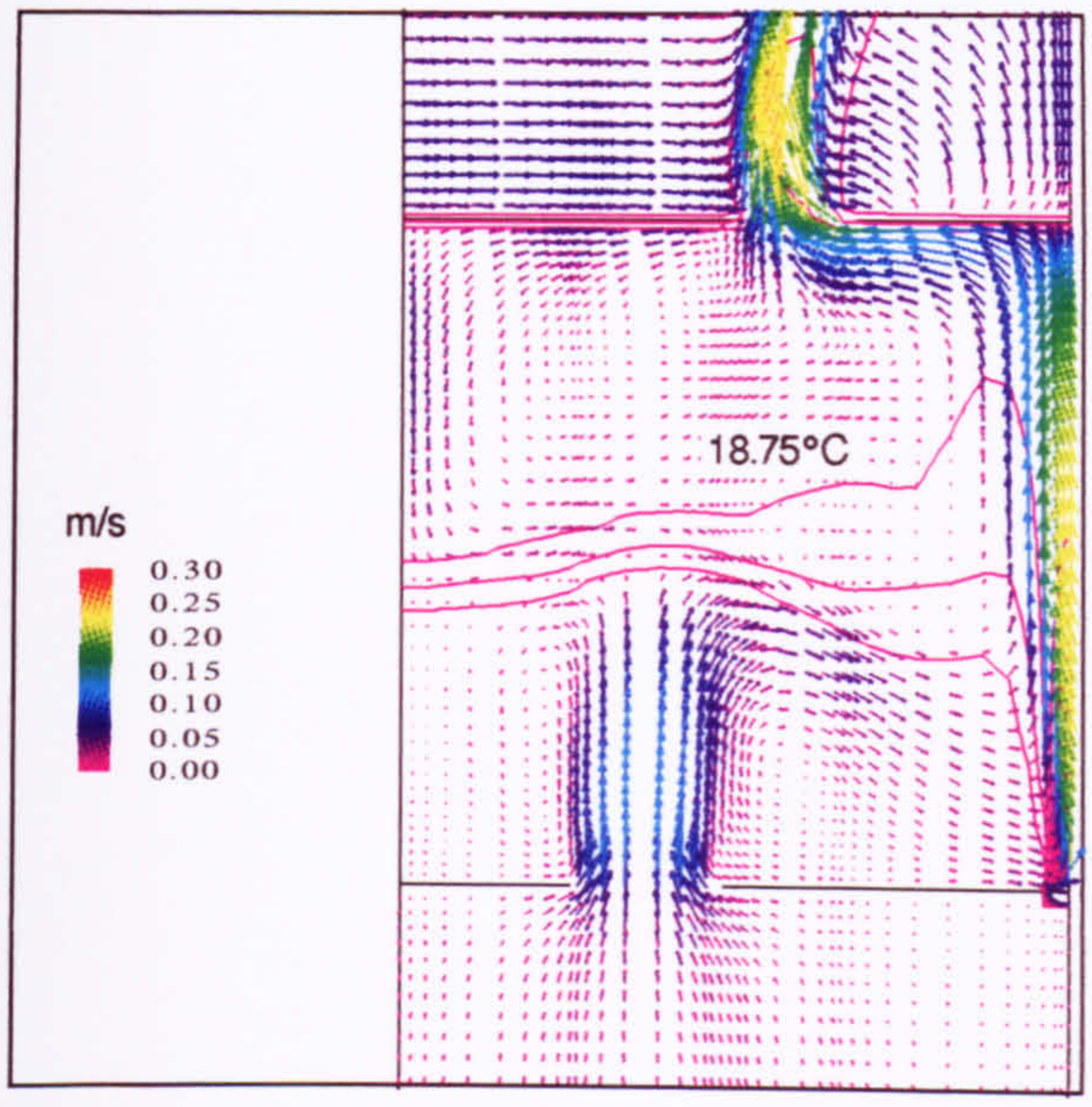

Figure 6.17 Flow pattern for Q = 50W using the standard $k-\varepsilon$ model.

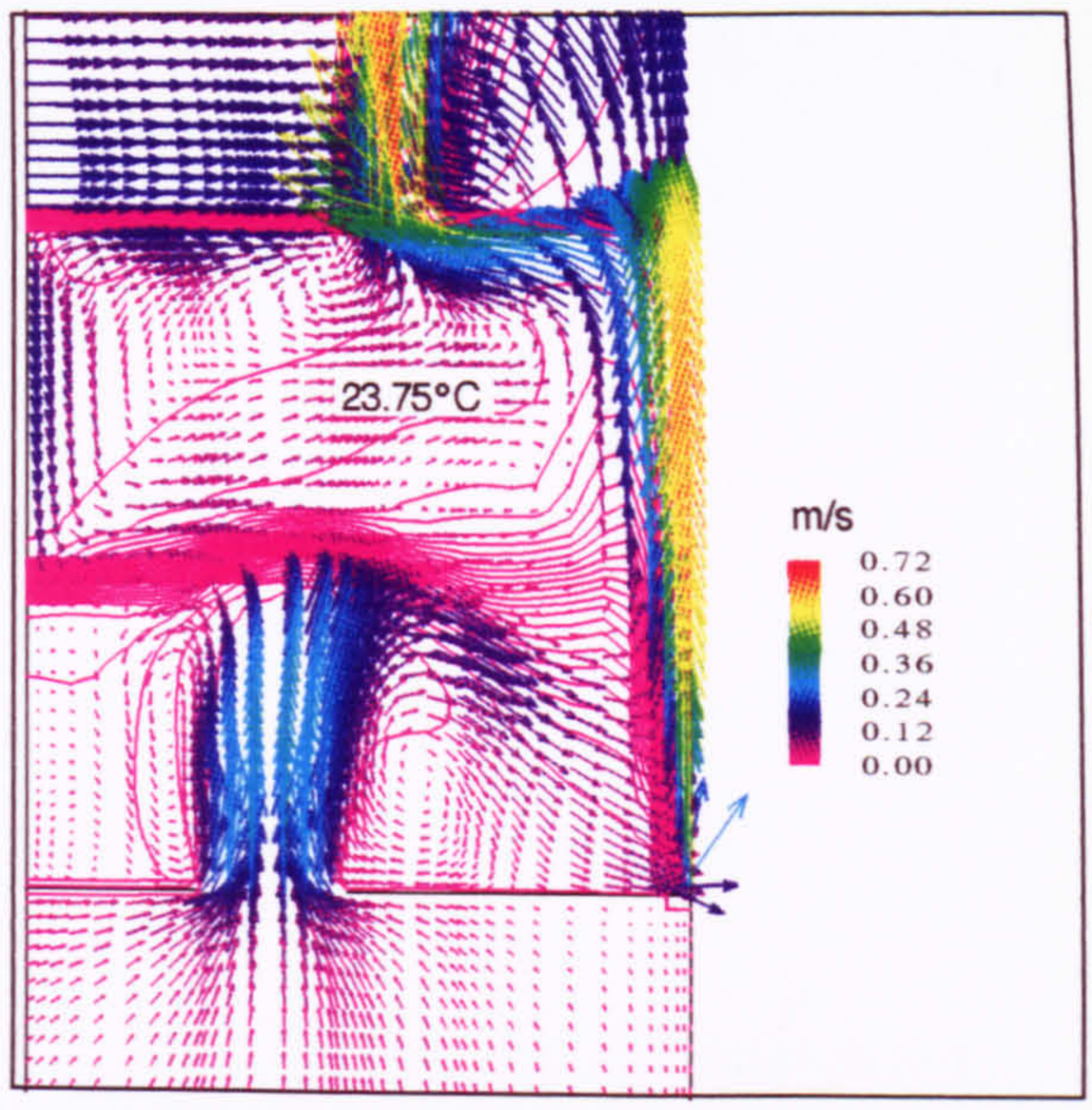

Figure 6.18 Flow pattern for Q = 1000W using the standard $k-\varepsilon$ model.

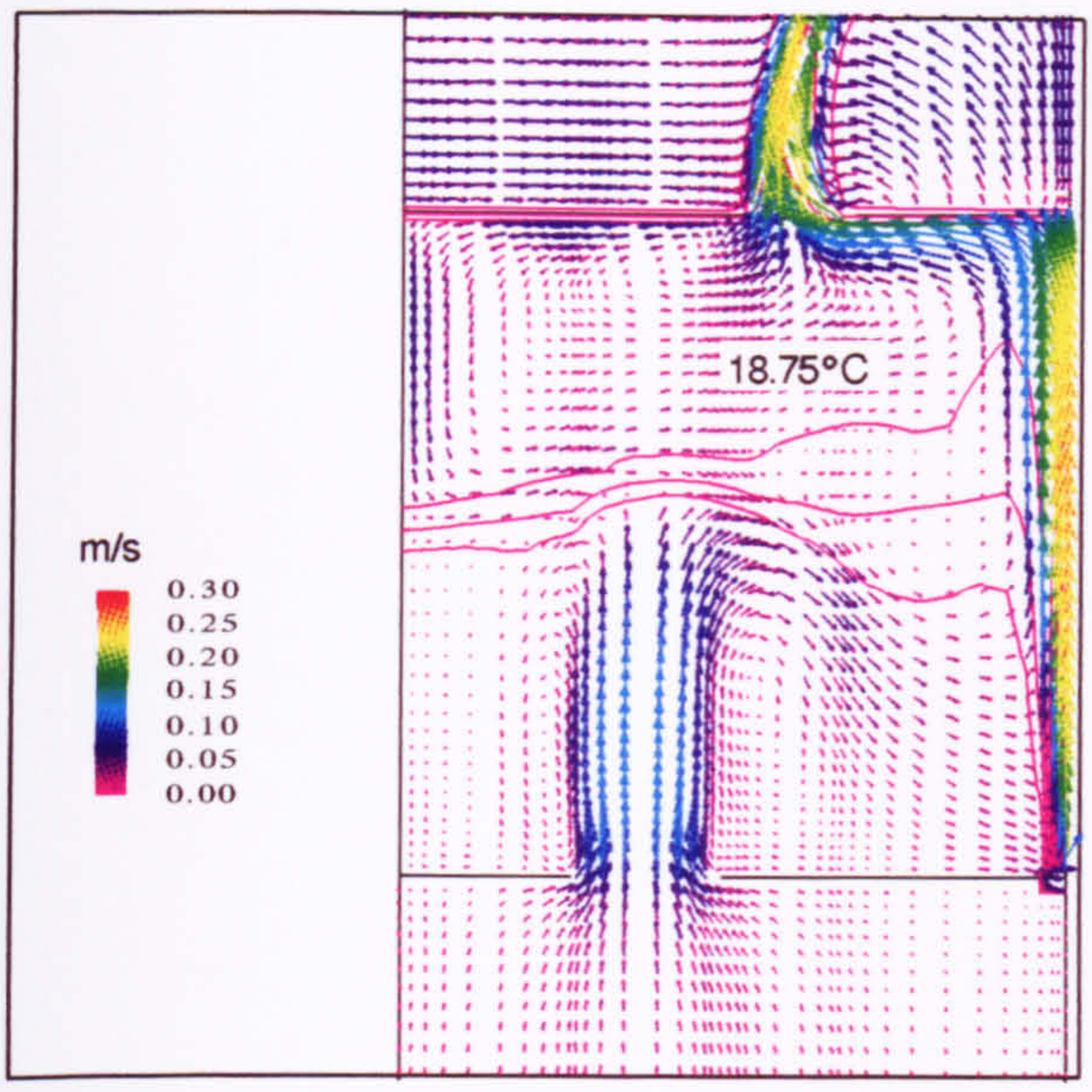

Figure 6.19 Flow pattern for Q = 50W using RNG $k-\varepsilon$ model.

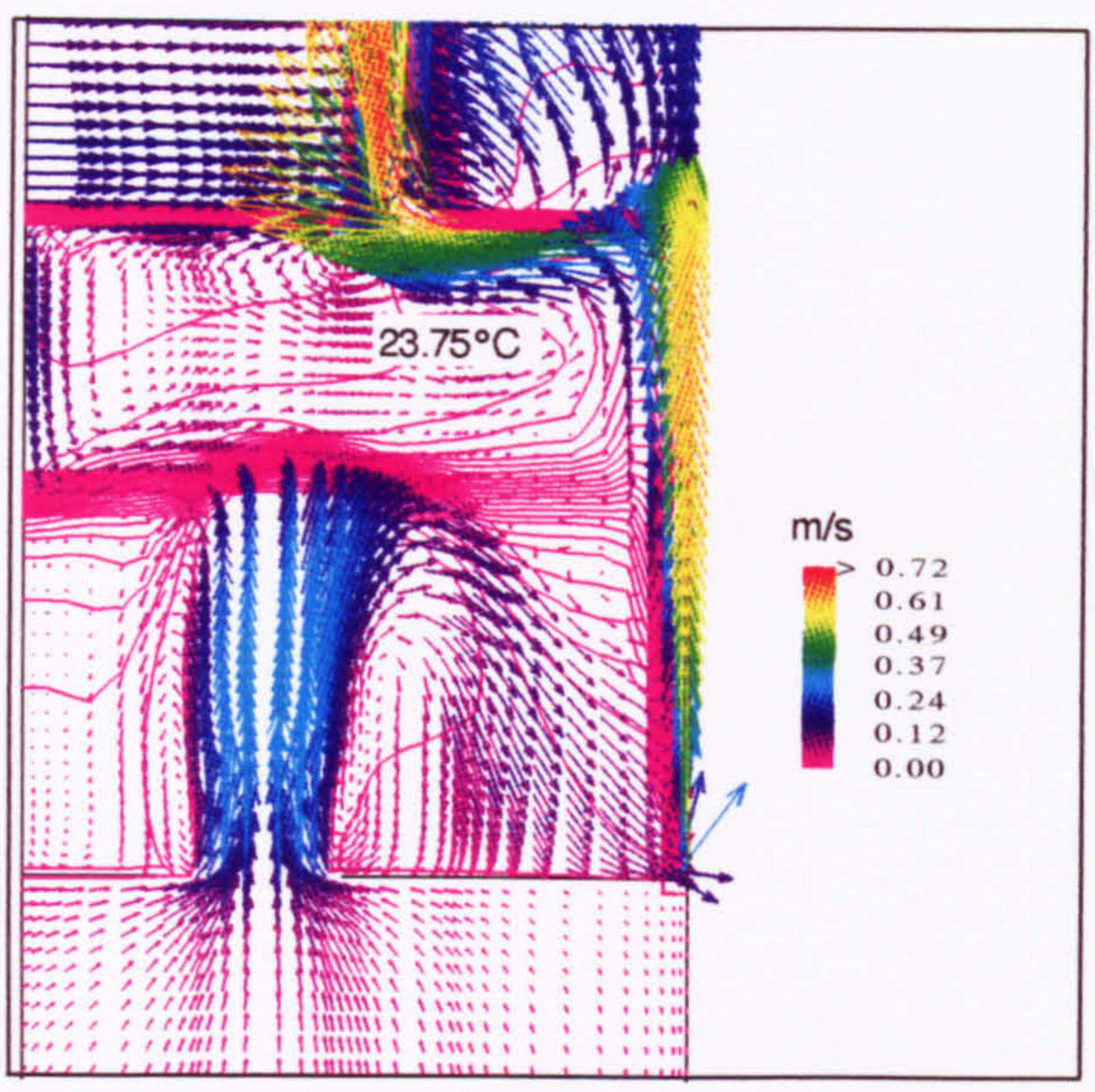

Figure 6.20 Flow pattern for Q = 1000W using RNG $k-\varepsilon$ model.

6.4.5.2 Volume Flux in the Plume

The standard $k-\varepsilon$ model successfully predicted the linear relationship between M_L and $B_L^{1/3}$ (Fig. 6.21). The slight non-linearities when using the RNG model are considered negligible but may be caused by a poorly mixed plume. This is discussed further in Chapter 8 (§8.3.5).

The difference in entrainment prediction is reflected in Figure 6.22 where the RNG model results show much more favourable agreement with the theory than those obtained using the standard $k-\varepsilon$ model.

6.4.5.3 Buoyancy in the Plume

Following the discrepancies reflected in Figures 6.15 and 6.16, it is not surprising to observe substantial discrepancies in the variation of plume buoyancy with source strength (Figs. 6.23 and 6.24). Although G_T' seems to be varying linearly with $B_L^{2/3}$ (Fig. 6.23), it does so at a different rate to that predicted by the theory (Eq. (3-26)).

6.4.6 Effect of Changes in Opening Area

Opening sizes were varied such that the lower opening was always larger than the upper to reduce impingement of momentum forces on the interface as much as possible (recall Fig. 5.30), while the heat source was kept constant at 200W. The CFD results showed excellent qualitative behaviour for both turbulence models, i.e. as the effective area of the openings was increased, the interface rose and the change in temperature across the interface decreased (Figs. 6.25 and 6.26).

The quantitative variation of opening area with interface height and stratification strength compare favourably with the theoretical predictions (Figs. 6.27 and 6.28). The reason for the CFD predictions of h/H not following a perfect curve could be due to measurement errors caused by some impingement of the incoming air on the interface. In all cases the RNG $k-\varepsilon$ model produced a higher interface than the standard $k-\varepsilon$ model due to its lower prediction of entrainment into the plume.

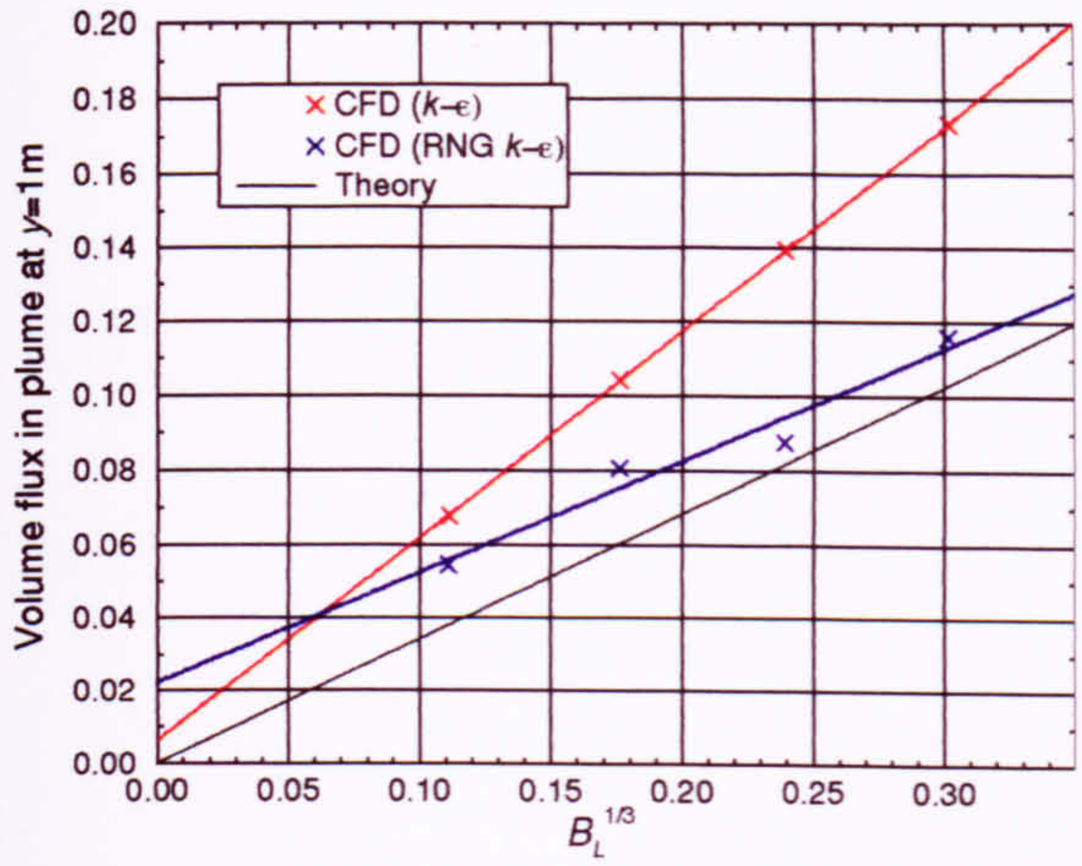

Figure 6.21 Variation of volume flux in the plume with $B_L^{1/3}$.

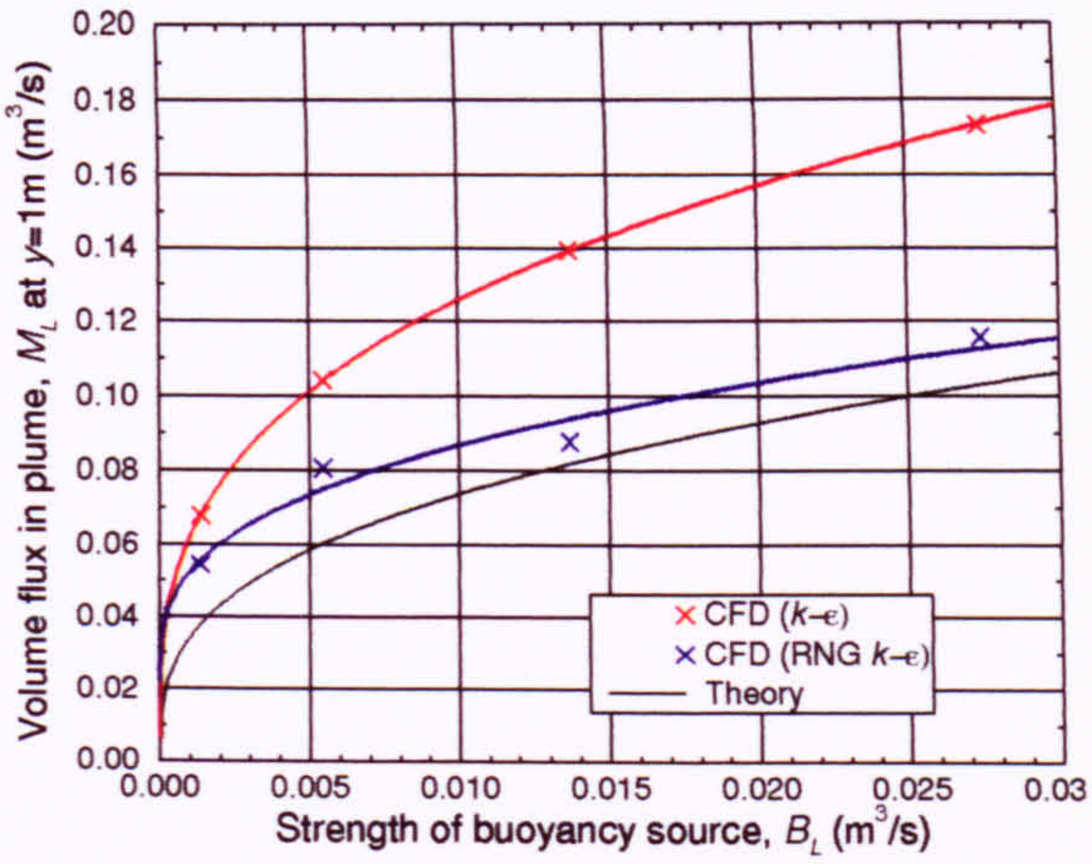

Figure 6.22 Variation of volume flux in the plume with source strength.

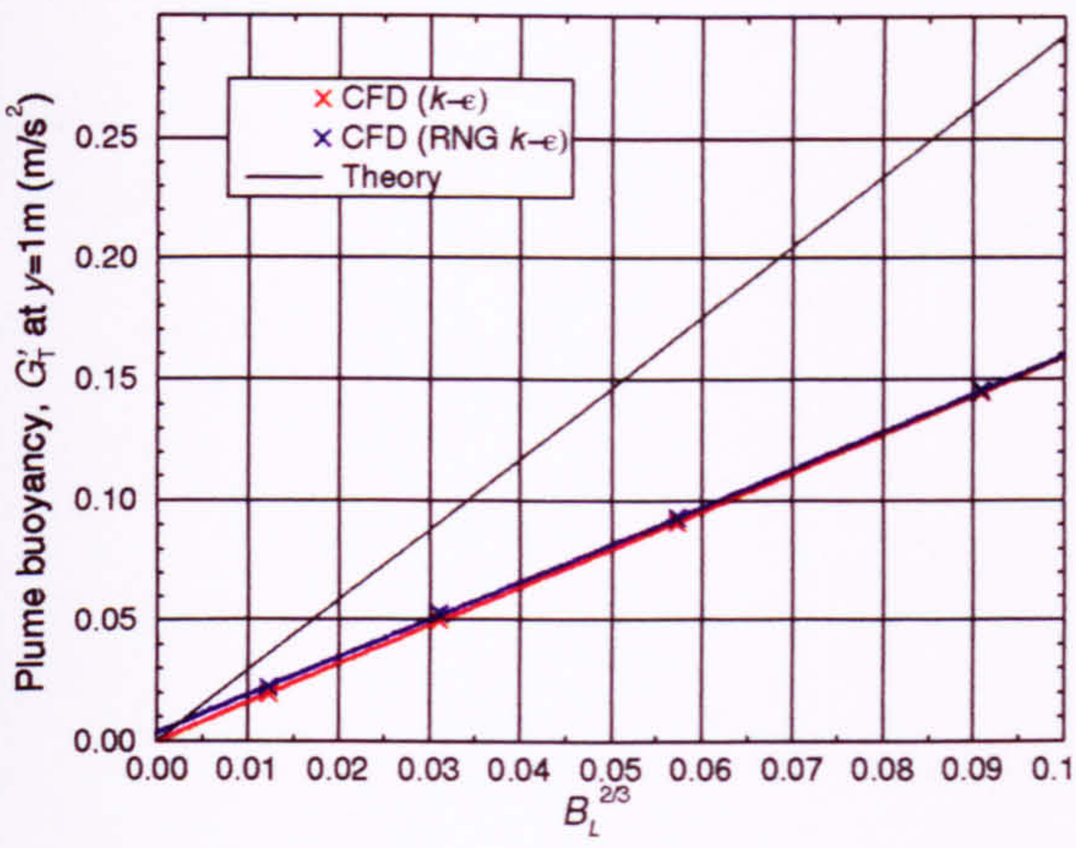

Figure 6.23 Variation of plume buoyancy with $B_L^{2/3}$.

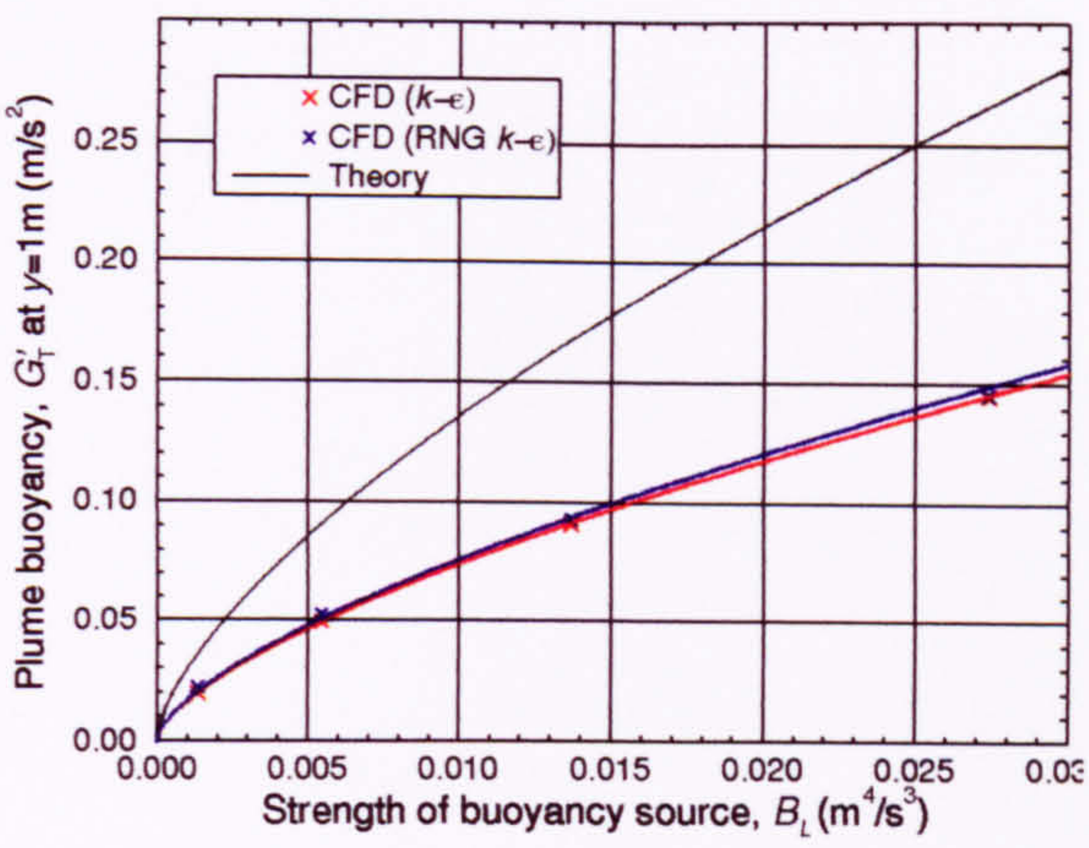

Figure 6.24 Variation of plume buoyancy with source strength.

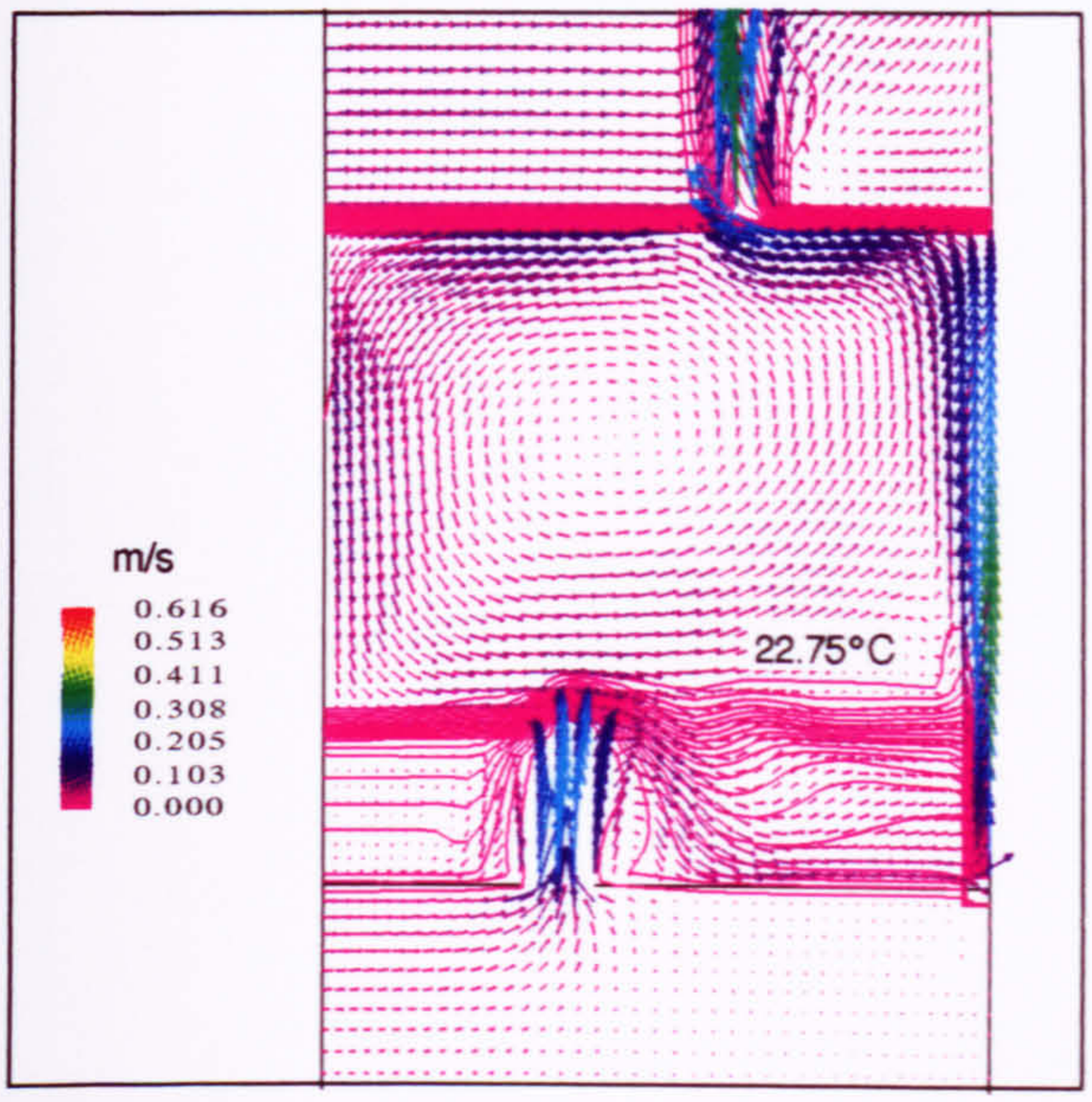

Figure 6.25 Flow pattern predicted by the RNG $k-\varepsilon$ model for $A_L^* / H = 0.034$ ($Q = 200\text{W}$).

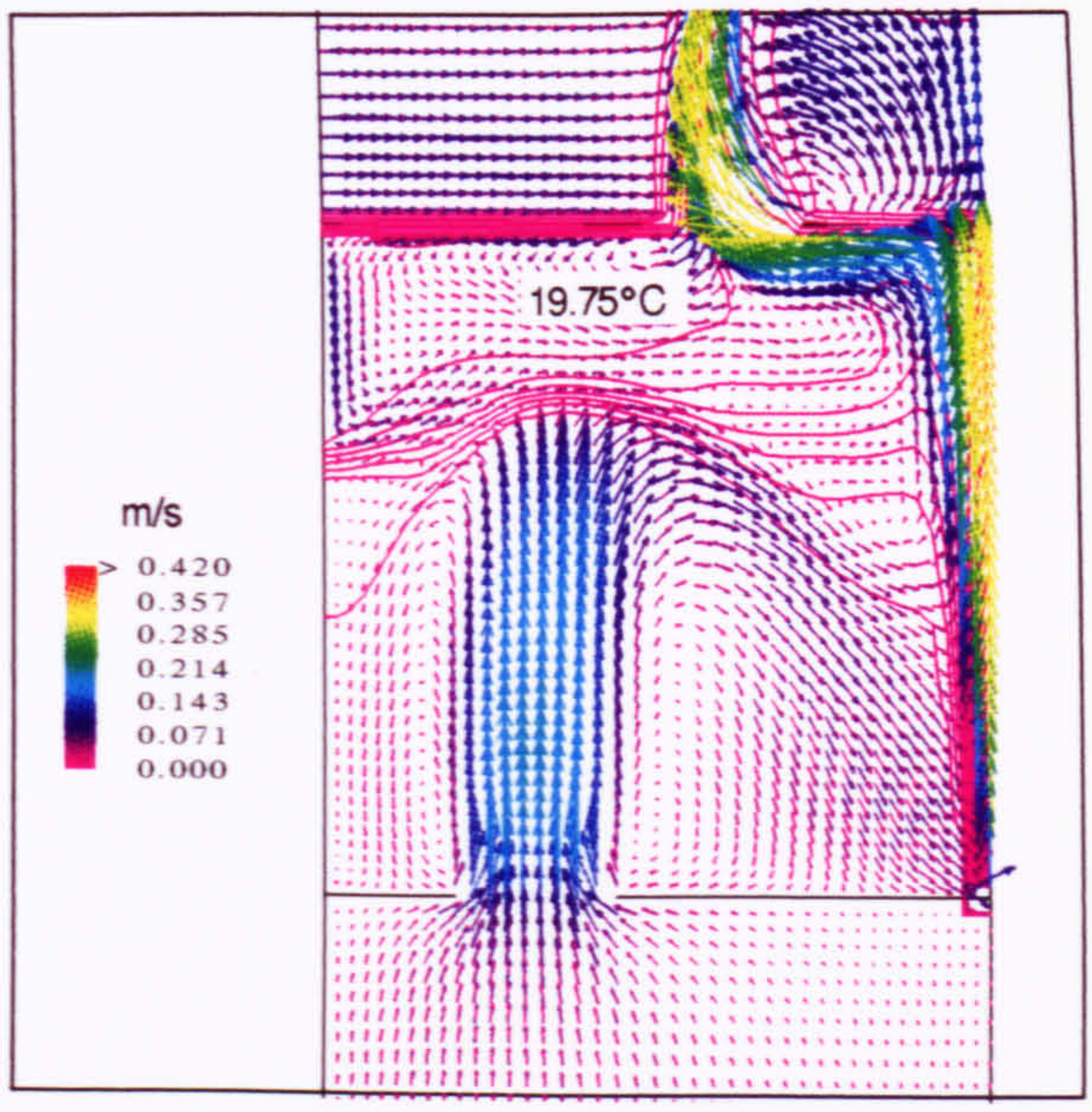

Figure 6.26 Flow pattern predicted by the RNG $k-\varepsilon$ model for $A_L^* / H = 0.198$ ($Q = 200\text{W}$).

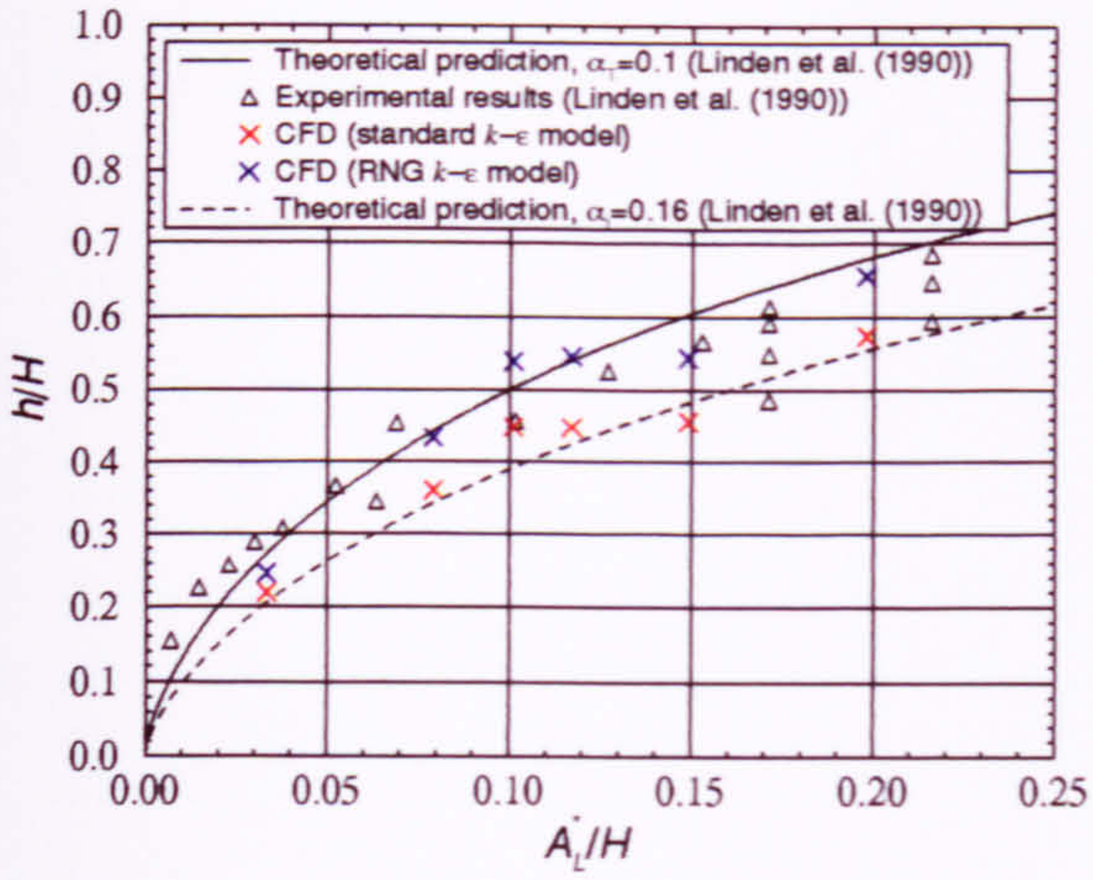

Figure 6.27 Variation of interface height with effective opening area.

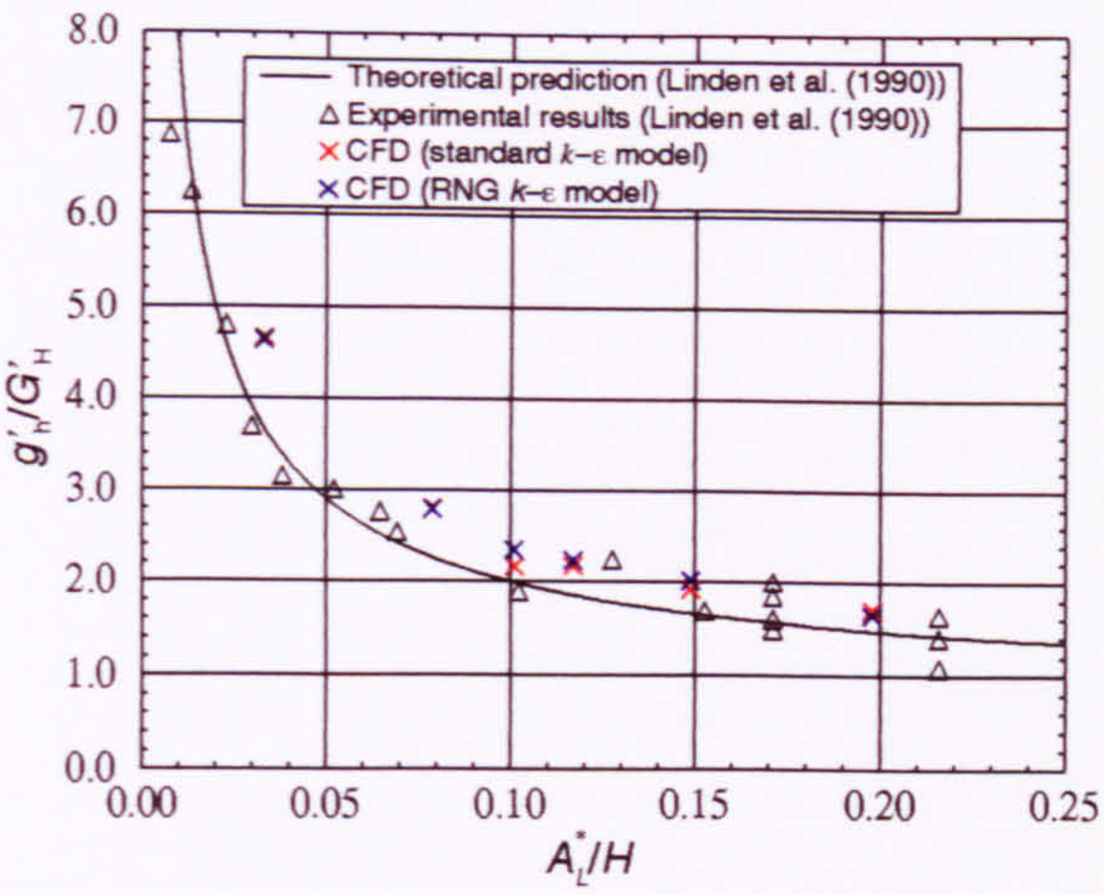

Figure 6.28 Variation of buoyancy change across the interface with effective opening area.

Since the CFD results generally predicted lower interface heights than the analytical solutions, it follows from Equation (3-29) ($g'_h / G'_H = H / h$) that the CFD values for g'_h / G'_H should lie *above* the analytical line, which is confirmed by Figure 6.28. However, the two turbulence models differed much less in their predictions of g'_h, than they did for interface height due to the cancelling effect of entrainment and interface height explained in section 5.7

6.5 Comparison of Benchmarks 1 and 2

Benchmarks 1 and 2 enable an evaluation of how well 2D simulations represent a 3D line source. The key properties of the flows for benchmarks 1 and 2 are compared in Table 6.6.

Table 6.6 Comparison of flow properties for 2D and 3D representations of a line source of buoyancy (standard $k-\varepsilon$ model only).

Case description		h/H (m)		g'_h / G'_H		α_T		ach^{-1}	
A_L^*/H	Q	BM1	BM2	BM1	BM2	BM1	BM2	BM1	BM2
0.148	50W	0.390	0.457	1.86	1.93	N/C	N/C	14.12	13.84
0.148	200W	0.390	0.457	1.84	1.92	0.17	0.16	22.42	21.87
0.148	1000W	0.390	0.457	1.84	1.98	N/C	N/C	38.48	38.20

BM1 - Benchmark 1, BM2 - Benchmark 2, N/C - not calculated.

The main differences between the results for benchmarks 1 and 2 were the slightly higher interface in Benchmark 2 (Fig. 6.29) and slightly larger buoyancy change across the interface (Fig. 6.30). These were thought to be due partly to the use of `WALL` boundaries at the high- and low- z faces of the room in Benchmark 2 (rather than `SYMMETRY PLANE` boundaries used in Benchmark 1). This reduced the potential for entrainment in the vicinity of these solid boundaries and thus reduced the net entrainment per unit length in Benchmark 2 compared with that of Benchmark 1. This reduced entrainment lead to a lower volume flux in the plume and therefore a higher interface height and also a greater buoyancy

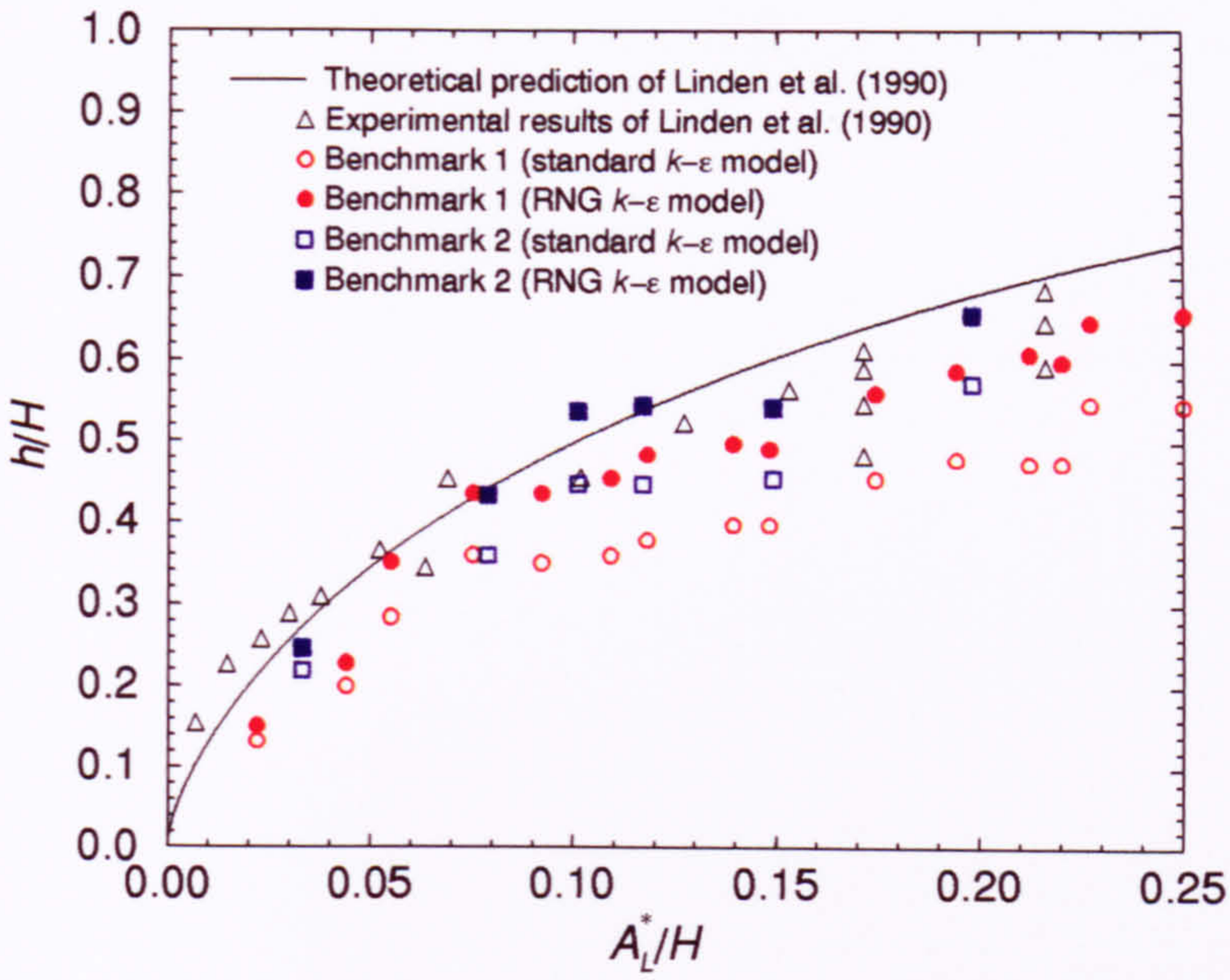

Figure 6.29 Variation of interface height with opening area: comparison of benchmarks 1 and 2.

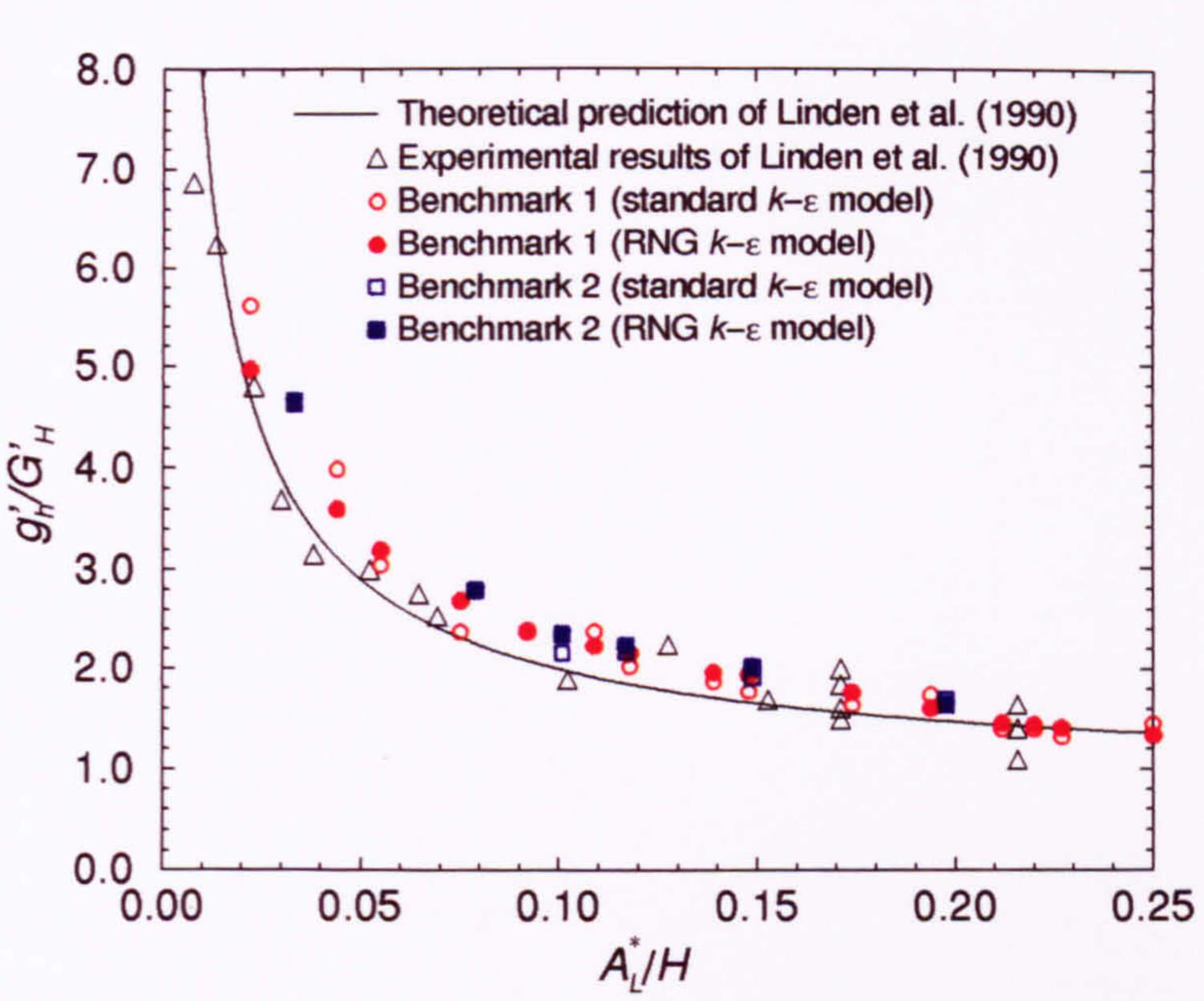

Figure 6.30 Variation of buoyancy across the interface with opening area: comparison of benchmarks 1 and 2.

in the plume which yielded a greater buoyancy change across the interface. There is also some evidence in the predicted flow patterns to suggest that the interface height was forced upwards by the momentum of the incoming air. This effect is greater in Benchmark 2 due to the larger momentum per unit volume of ambient air entering through the square opening compared to the slot in Benchmark 1.

6.6 Summary

This chapter has concentrated on Benchmark 2 - three dimensional modelling of the displacement ventilation flow resulting from a line source of buoyancy using both the standard and the RNG $k-\varepsilon$ turbulence models.

The results showed similar trends to those observed in Benchmark 1 - i.e. the RNG model predicted a smaller value of plume entrainment than the standard $k-\varepsilon$ model which lead to more favourable agreement with the theoretical predictions of Linden et al. (1990), based on $\alpha_T = 0.1$. The RNG-prediction of the interface height again demonstrated some slight dependence on the source strength. The buoyancy variation in the plume again exhibited discrepancies in its variation with height above the source.

The incoming air in Benchmark 2 appeared to posses greater momentum now that square openings had replaced the long slots of Benchmark 1, due to a larger mass flow per unit volume. This effect makes accurate measurement of the interface height difficult.

It is concluded that the 2D simulations of Benchmark 1 provided a very good approximation to the 3D flows modelled in Benchmark 2. The only limitations of the 2D model appeared to be the inherent 'slot' representation of the openings and the failure to model wall effects at each end of the plume. It is thought that the latter gave rise to the prediction of a slightly reduced entrainment and therefore higher interface height and larger buoyancy change across the interface.

Chapter 7

Three Dimensional Modelling of Buoyancy-Driven Displacement Ventilation: Point Source

7. Three Dimensional Modelling of Buoyancy-Driven Displacement Ventilation: Point Source

7.1 Preamble

This chapter presents the results of the CFD modelling of a *point* source of buoyancy and draws on the point source theory of Chapter 3 for comparison. The work is laid out in the same order as the previous chapter to enable easy comparison between the point and line source results.

The reference case defined for this chapter is **Benchmark 3.**

7.2 Definition of Benchmark 3

The same size room was used here as Benchmark 2, with the line source replaced by a square (point) source measuring 0.1m×0.1m (total) in the centre of the floor. The ambient temperature was 18°C and the source strength 200W. All fluid properties and reference temperatures were the same as those used for benchmarks 1 and 2.

Opening sizes were defined such that the resulting interface height predicted by the analytical work of Linden et al. (1990), was the same as that for Benchmark 2. This was achieved by using lower openings of area $a_l = 0.316\text{m} \times 0.316\text{m}$ and upper openings of area $a_u = 0.21\text{m} \times 0.21\text{m}$, giving a total effective opening area of $A^* = 0.114\text{m}^2$. According to the theory of Chapter 3 this should produce a larger value of g'_h/G'_H because the constant C in Equation (3-14) is smaller than D (Eq. (3-25)) which is used for plumes produced by line sources.

7.3 Representing Benchmark 3 in CFX

This benchmark uses the same computational domain as Benchmark 2.

Following the 'artificial entrainment' problem observed across the low-*x* face of the lower exterior space in Benchmark 2, it was decided to run two initial simulations to investigate both PRESSURE and WALL boundaries at this location. WALL boundaries were still required at the high- and low-*z* faces of the exterior zones.

Based on the mesh investigation conducted in the previous chapter, it was decided to employ the same mesh density used in Benchmark 2 but with local refinement in the vicinity of the source, giving a mesh density of $46 \times 90 \times 21$.

7.4 Analysis of Benchmark 3 Results

7.4.1 Initial Simulations

The same strategy for obtaining convergence was used here as in the previous two chapters. Satisfactory convergence was obtained after 1000 iterations using default under-relaxation factors and no false time-stepping, followed by a restart for 4000 iterations using false time-steps of 0.1s on all three momentum equations. Once again, 'artificial entrainment' was observed across the PRESSURE boundary on the low-*x* face of the lower exterior space. This caused the incoming air to issue into the space obliquely (Fig. 7.1) compared with the flow pattern when a WALL boundary was used (Fig. 7.2). All subsequent simulations were conducted using a WALL boundary at this location.

7.4.2 Analysis of the Displacement Flow Pattern in Benchmark 3

The steady displacement flow predicted by Linden et al. (1990) was successfully reproduced by the CFD model (Figs. 7.2 and 7.3). The main difference between this result and that for the line source is the higher plume velocities produced by the point source, even though the same source strength had been used. This is because the input of heat energy is concentrated over a much smaller area leading to higher local air temperatures and hence a greater buoyancy force. Since the source in this benchmark does not extend the full length of the space, there is not a distinctive circulation flow pattern above the interface. Instead, the

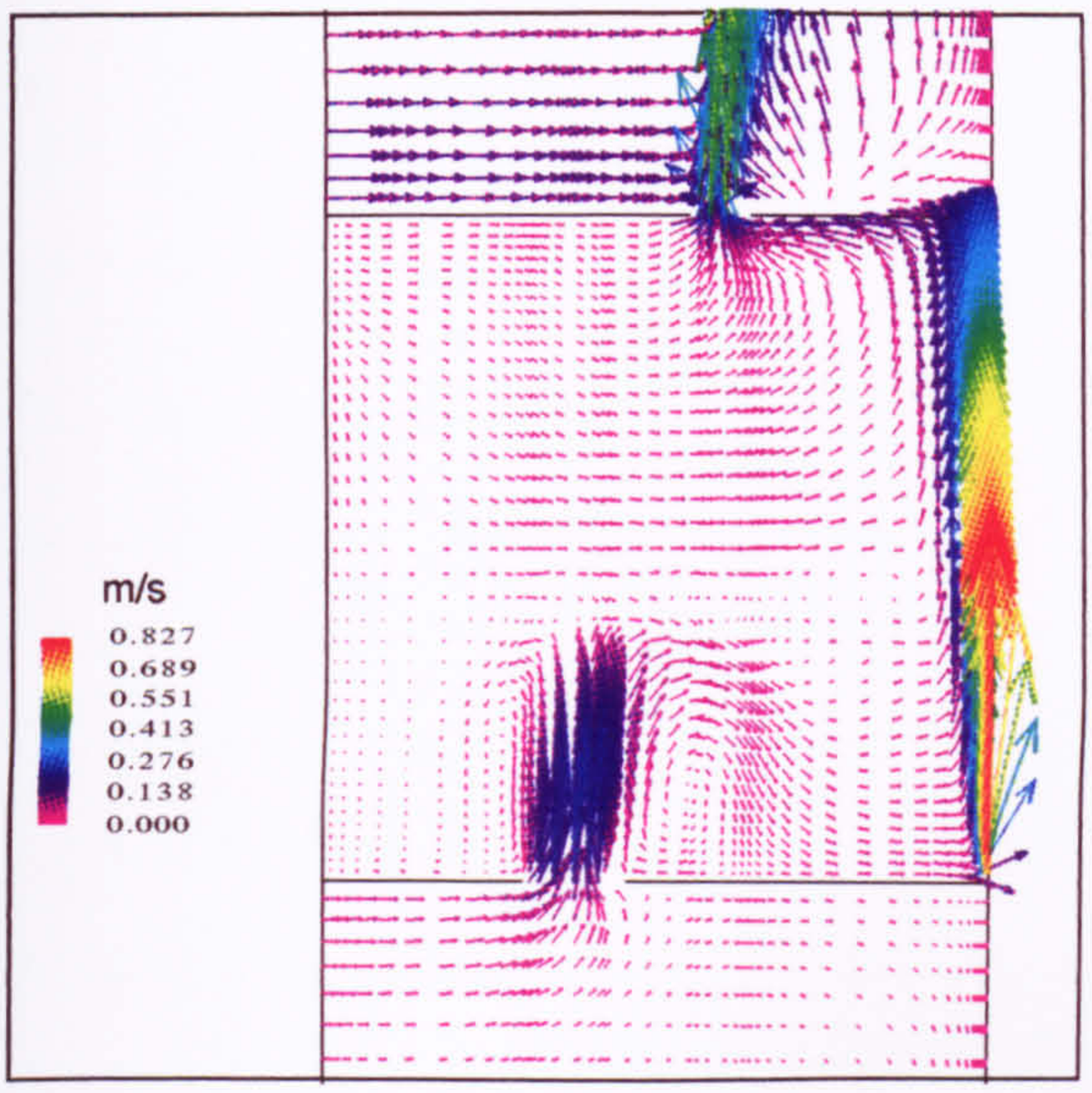

Figure 7.1 Flow pattern predicted in plane $z = 0.5$m when using a PRESSURE boundary at low-x face in lower exterior.

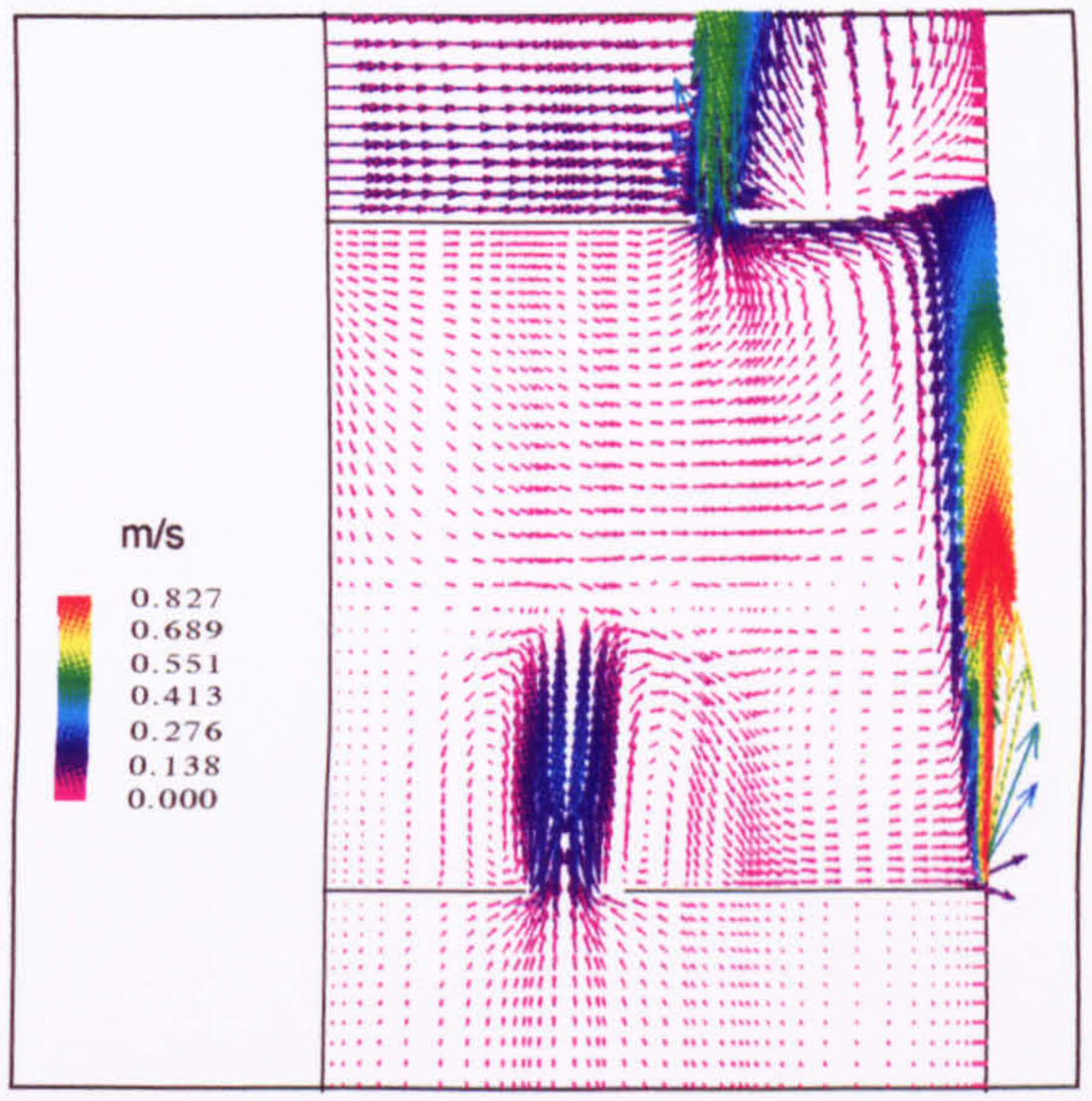

Figure 7.2 Flow pattern predicted in plane $z = 0.5$m when using a WALL boundary at low-x face in lower exterior.

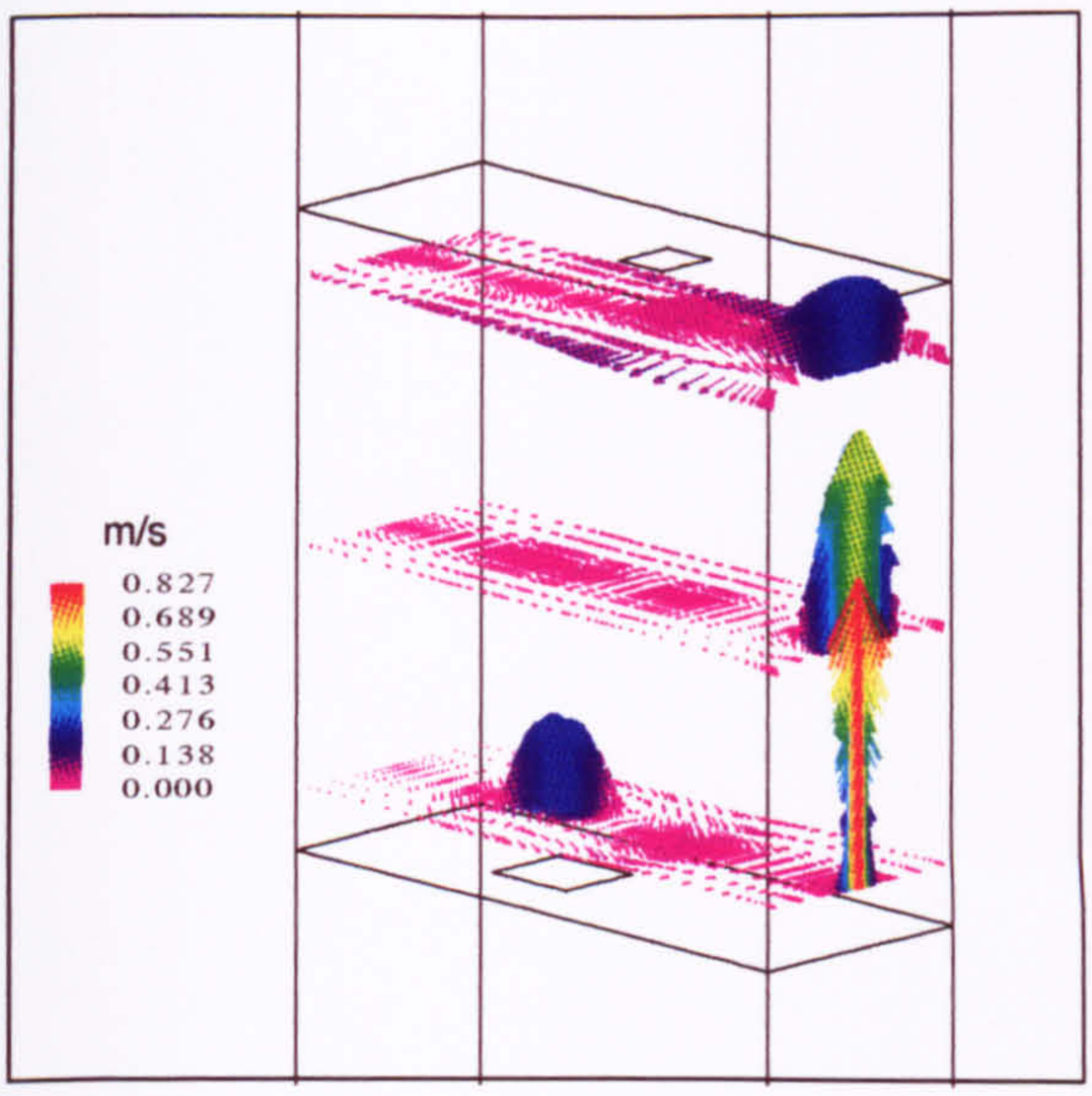

Figure 7.3 Velocity vectors in the planes $y = 0.25$m, $y = 1.2$m and $y = 2.3$m .

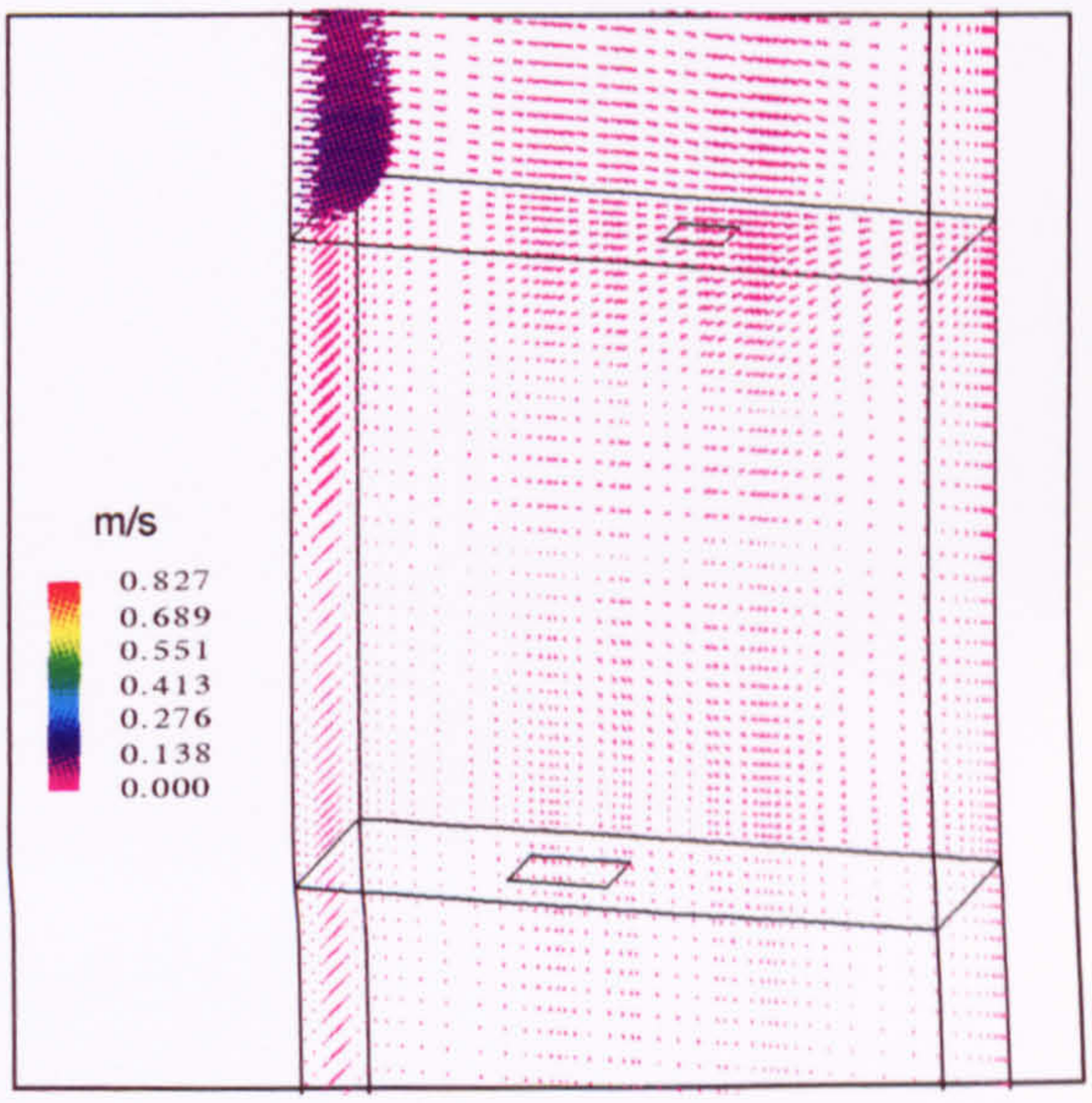

Figure 7.4 Velocity vectors in the planes $z = 0.01$m and $x = 0.01$m .

air speeds are slower and the flow appears to be more random (Figs. 7.2 and 7.4). This is also true of the air in the region between the inlet and the plume (Fig. 7.2).

The clear definition of the interface and the uniformity of the temperature above are depicted in Figures 7.5 - 7.7. Note that the interface is virtually horizontal whereas in Benchmark 2 the height varied a little across the box (c.f. Figs. 7.5 and 6.8). This is thought to be due to the stronger stratification strength in Benchmark 3 and the smaller volume flux impinging on the interface. The vertical temperature profiles for benchmarks 2 and 3 are compared in Figure 7.8. Note the similarity in interface height (as expected), but the larger change in temperature across the interface in Benchmark 3. Also notice the slightly warmer-than-ambient air below the interface caused by some mixing across the interface from the upper to the lower region. The simulation using the RNG $k-\varepsilon$ turbulence model gave very similar results, but again predicted a higher interface (Fig. 7.9). This figure also illustrates some mixing across the interface.

The displacement ventilation flow properties for benchmarks 2 and 3 are summarised in Table 7.1 for both turbulence models.

Table 7.1 Comparison of displacement ventilation flow properties predicted by Benchmark 2 and 3.

	CFD				Theory (Linden et al. (1990))	
	$k-\varepsilon$		RNG			
	BM2	BM3	BM2	BM3	BM2	BM3
h/H	0.457	0.426	0.544	0.472	0.603	0.603
g'_h/G'_H	1.92	2.72	1.99	2.75	1.66	2.32
ach^{-1}	22.42	9.97	21.81	9.69	25.66	11.53

BM2 - Benchmark 2 BM3 - Benchmark 3

In line with the results from both previous benchmarks, the predicted interface height in Benchmark 3 showed closer agreement with the theory when modelled using the RNG $k-\varepsilon$ model. The reasons for the small differences in interface heights predicted by benchmarks 2 and 3 can be attributed either to the reduced

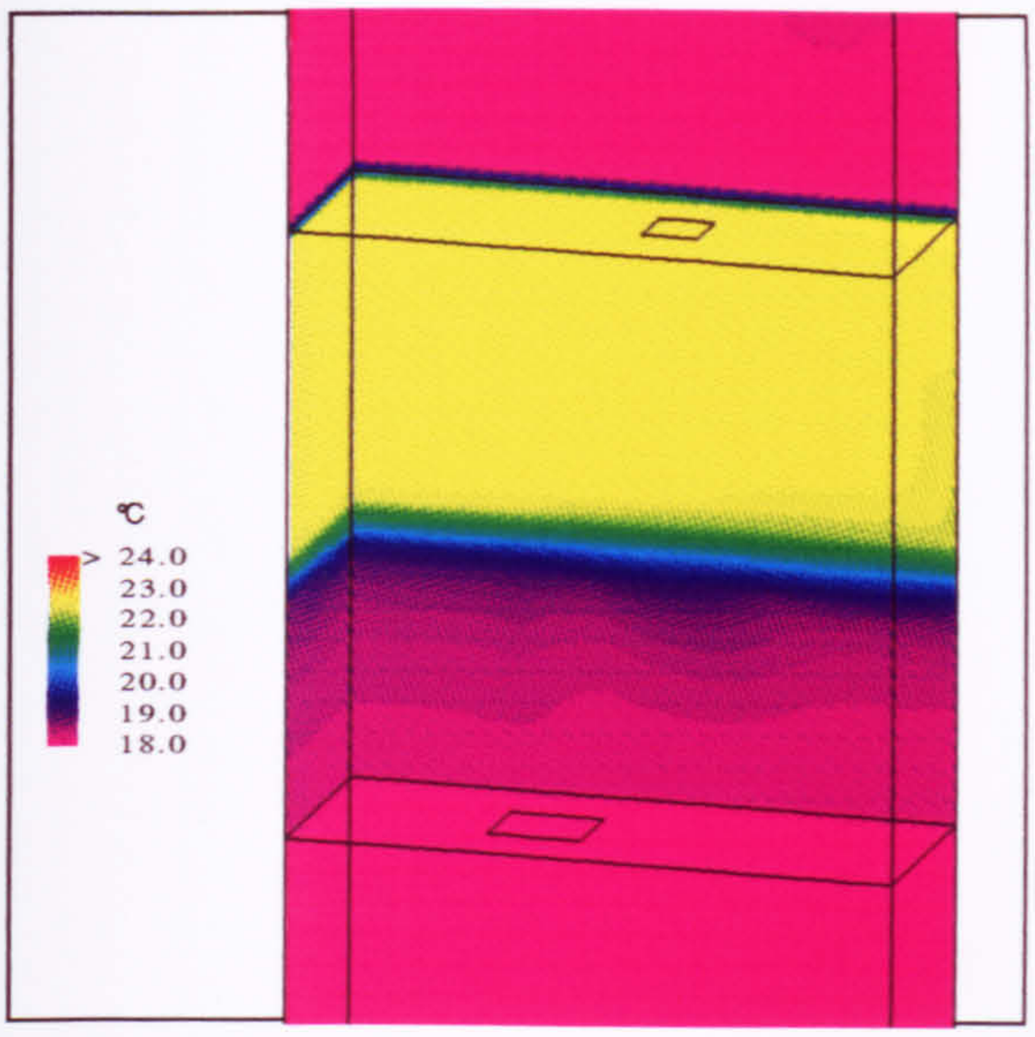

Figure 7.5 Predicted temperature field in planes $z = 0.01$m and $x = 0.01$m .

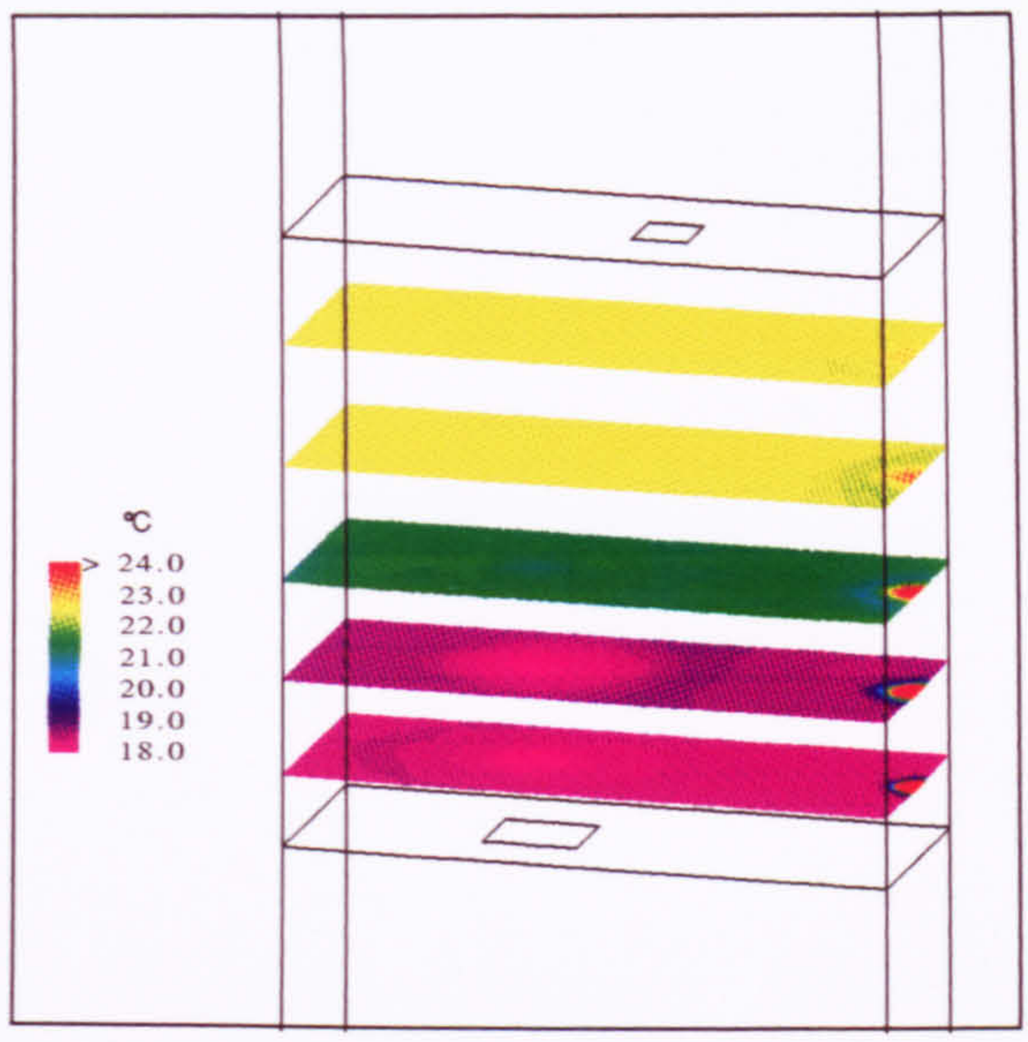

Figure 7.6 Predicted temperature fields across various horizontal planes within the box.

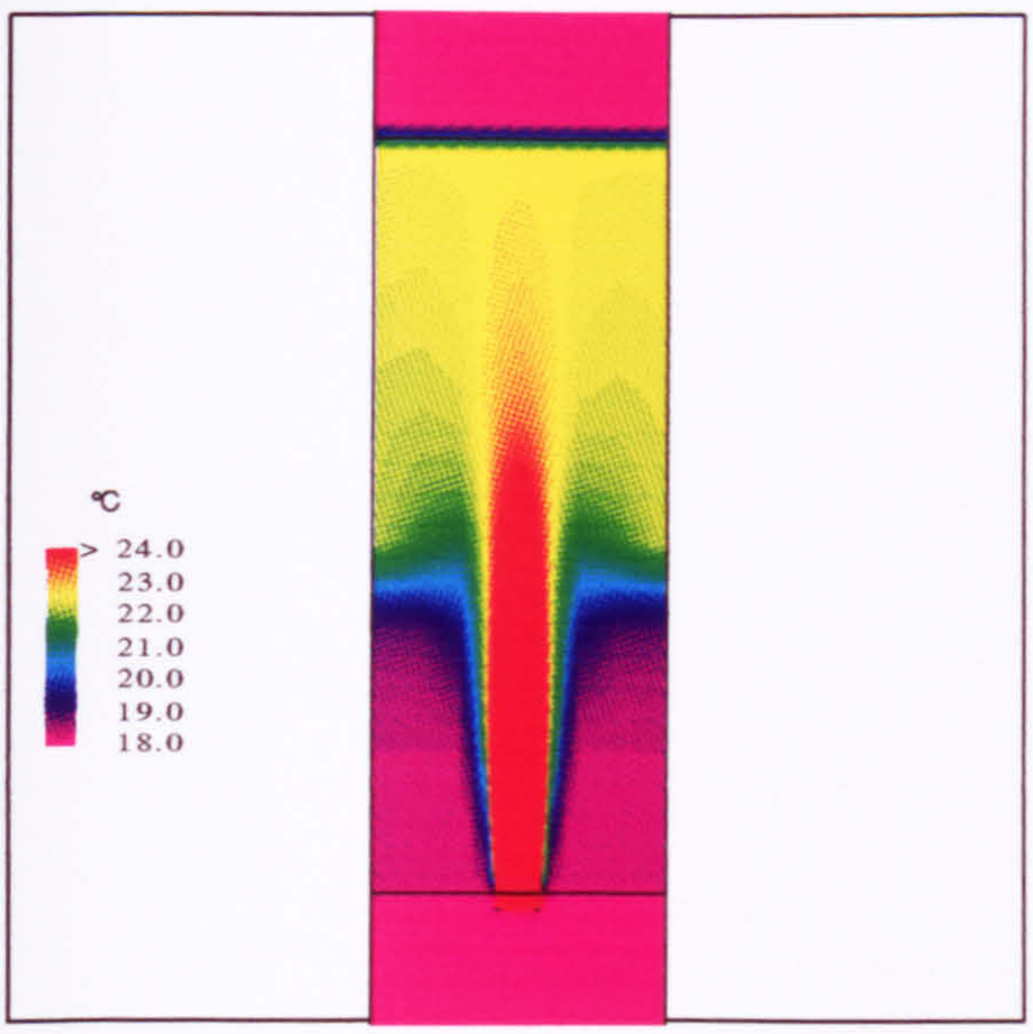

Figure 7.7 Predicted temperature field in the *y-z* plane containing the source.

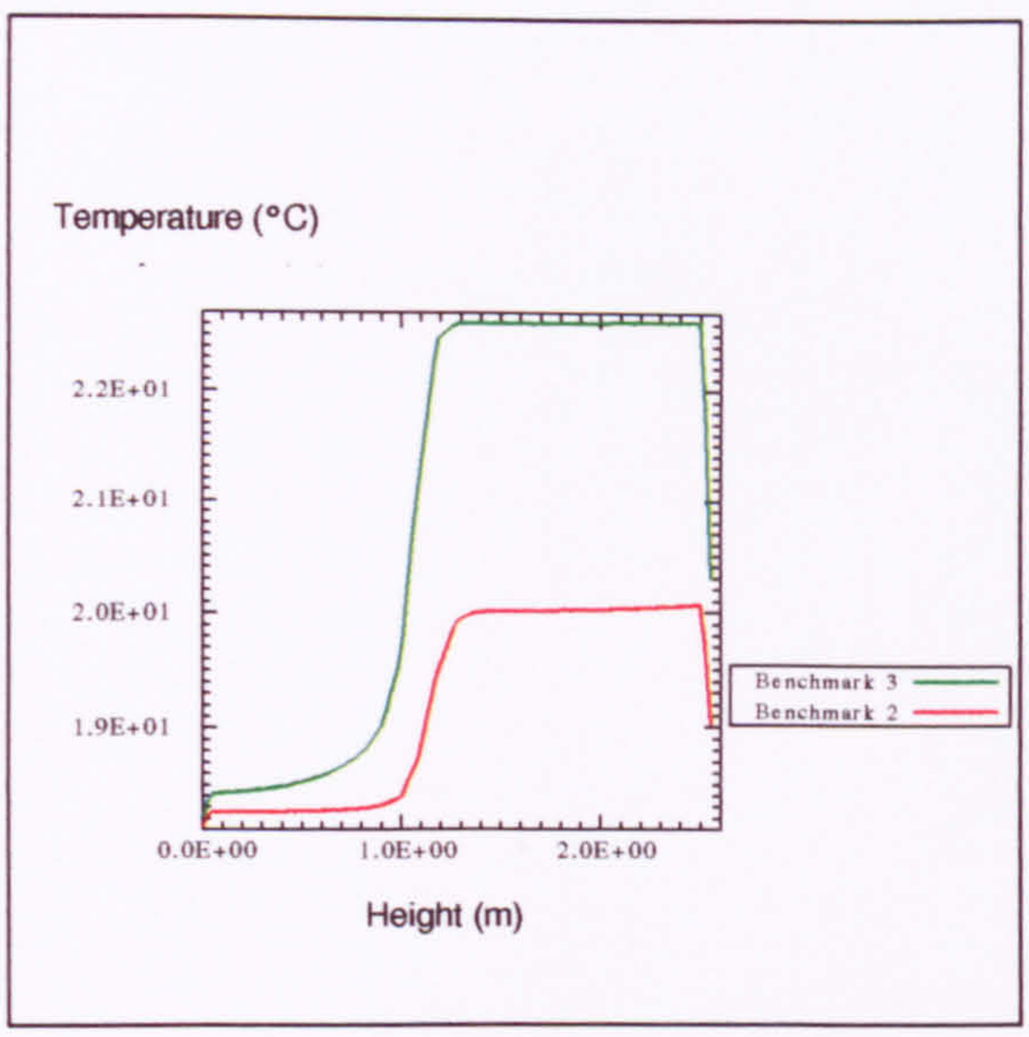

Figure 7.8 Vertical temperature profiles for benchmarks 2 and 3 at ($z = 0.5$m, $x = 0.2$m).

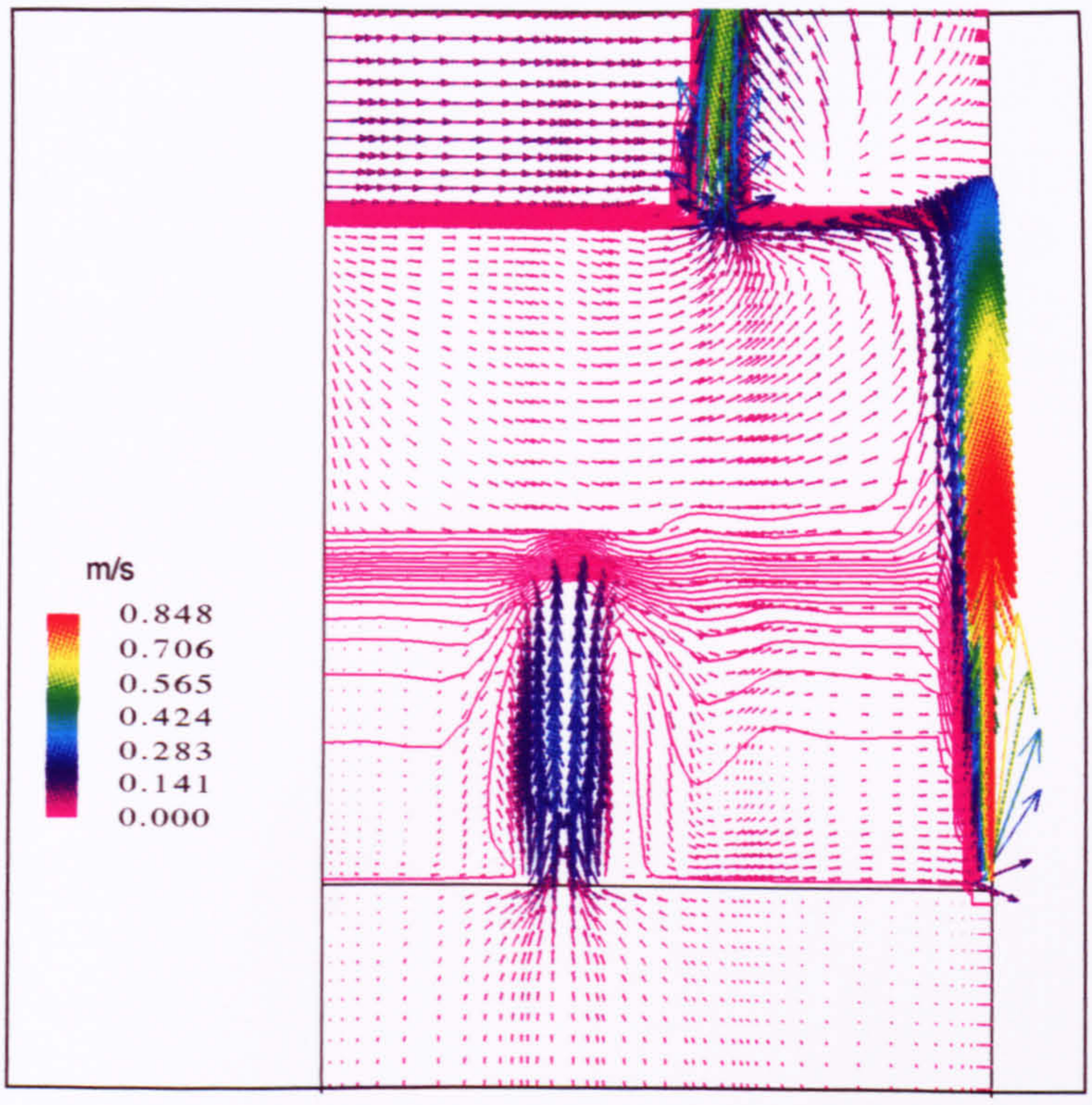

Figure 7.9 Flow pattern and temperature distribution for Benchmark 3 when using the RNG $k-\varepsilon$ turbulence model.

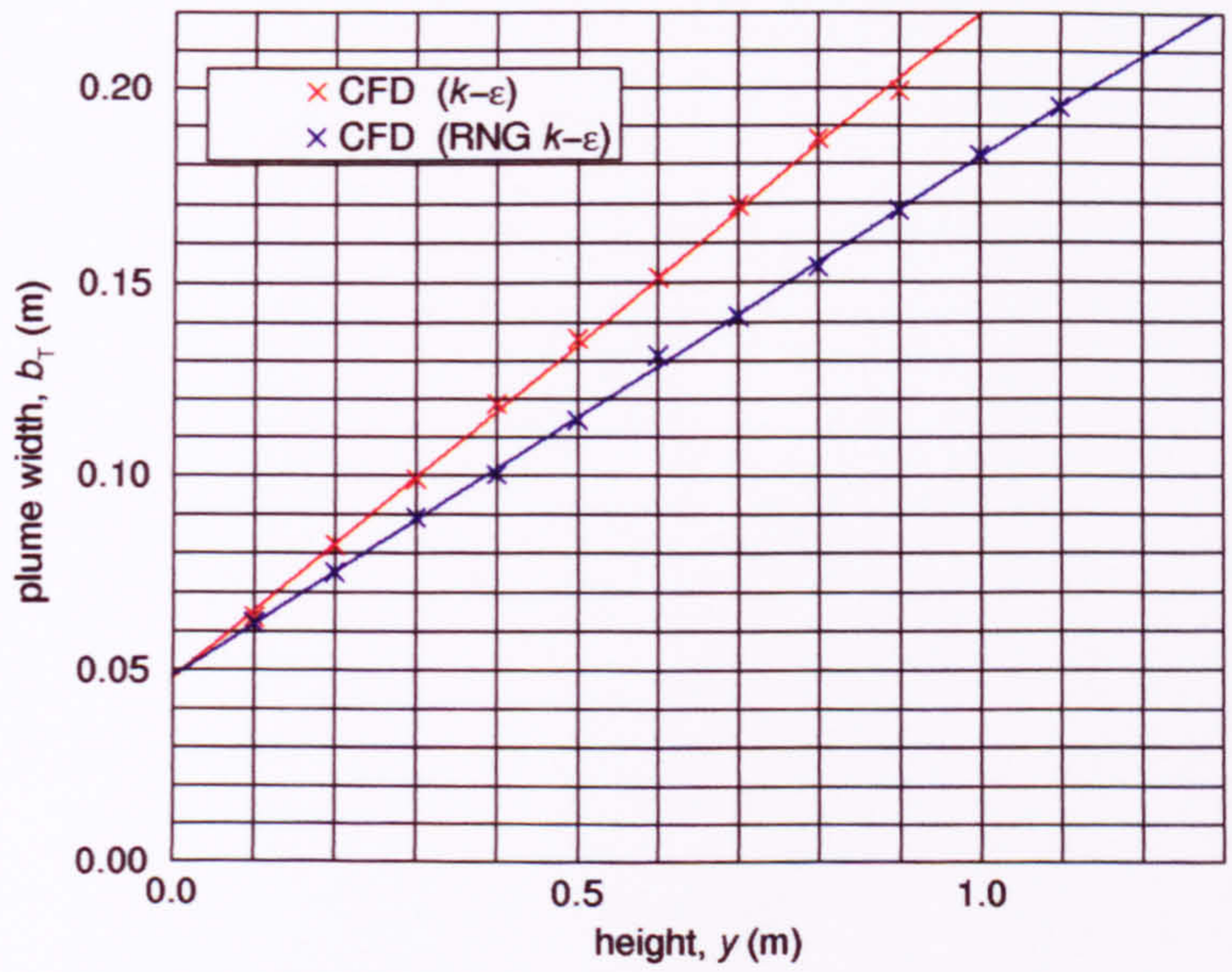

Figure 7.10 Variation of plume width with height above the source for both turbulence models.

effect of the incoming air on the interface in Benchmark 3, caused by a stronger stratification and less momentum entering the lower opening, or to different entrainment values (see §7.4.3.1). The similarity in stratification strength predicted by the two turbulence models for benchmarks 1 and 2 is replicated here (Table 7.1) and is due to the cancelling effect between the higher interface and the lower entrainment. The CFD simulations for this benchmark successfully predicted a larger buoyancy change across the interface than for Benchmark 2 (recall Fig. 7.8).

7.4.3 Plume Properties

7.4.3.1 Plume Entrainment

Using vertical velocity profiles in the plume, a measure of the Gaussian plume width, b_G, at various heights was determined. This was then converted to a 'top-hat' quantity using Equation B-4. The results are shown, along with the corresponding values for enthalpy and *v*-velocity, in Table 7.2.

The rate of change of plume width b_T with height above the source, *y*, (Fig. 7.10) was used to calculate the predicted values of entrainment, α_T, for both turbulence models as follows:

$$\text{gradient} = \frac{6}{5}\alpha_T \qquad \text{(Eq.(3-11)}$$

$$\Rightarrow \qquad \alpha_T^{k-\varepsilon} = 0.14 \quad \text{and} \quad \alpha_T^{RNG} = 0.11$$

Table 7.2 Comparison of plume data for the standard and RNG $k-\varepsilon$ turbulence models.

Height above source (m)	$v_T = \frac{v_G}{2}$ (*)		$b_T = \sqrt{2}b_G$ (*)		$He_T = \frac{He_G}{2}$ (*)	
	$k-\varepsilon$	RNG	$k-\varepsilon$	RNG	$k-\varepsilon$	RNG
0.1	0.391	0.394	0.064	0.062	29537.5	29713.0
0.2	0.402	0.416	0.082	0.075	21413.0	22439.0
0.3	0.390	0.417	0.099	0.089	15924.5	17512.5
0.4	0.376	0.412	0.119	0.100	12291.0	14012.5
0.5	0.364	0.402	0.136	0.115	9803.0	11436.0
0.6	0.353	0.391	0.151	0.132	8052.5	9511.5
0.7	0.343	0.380	0.170	0.141	6769.0	8041.0
0.8	0.335	0.369	0.187	0.154	5802.0	6900.0
0.9	0.324	0.358	0.199	0.168	5043.0	5986.5
1.0	0.314	0.348	0.212	0.182	4446.6	5256.5
1.1	0.302	0.337	0.226	0.195	3979.0	4675.0
1.2	0.289	0.315	0.235	0.208	3602.1	4199.3
1.3	0.275	0.312	0.238	0.218	3301.1	3814.0
1.4		0.298		0.231		3497.2
1.5		0.283		0.240		3232.2

(*) See Appendix B for derivation of these formulae.

7.4.3.2 Volume Flux in the Plume

The values in Table 7.2 were used to calculate volume flux using the formula $M = \pi b_T^2 v_T$. As expected, due to its lower prediction of entrainment, the RNG curve is closer to the theoretical curve (Fig. 7.11).

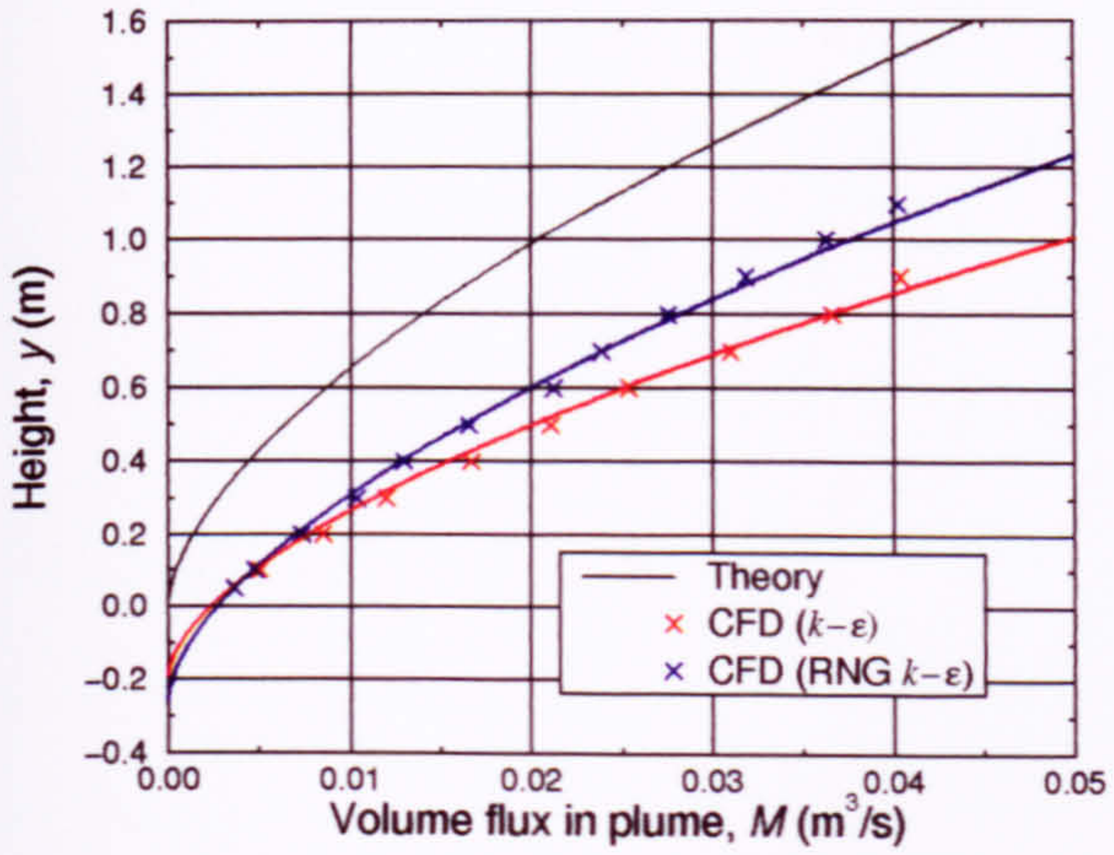

Figure 7.11 Variation of plume volume flux with height.

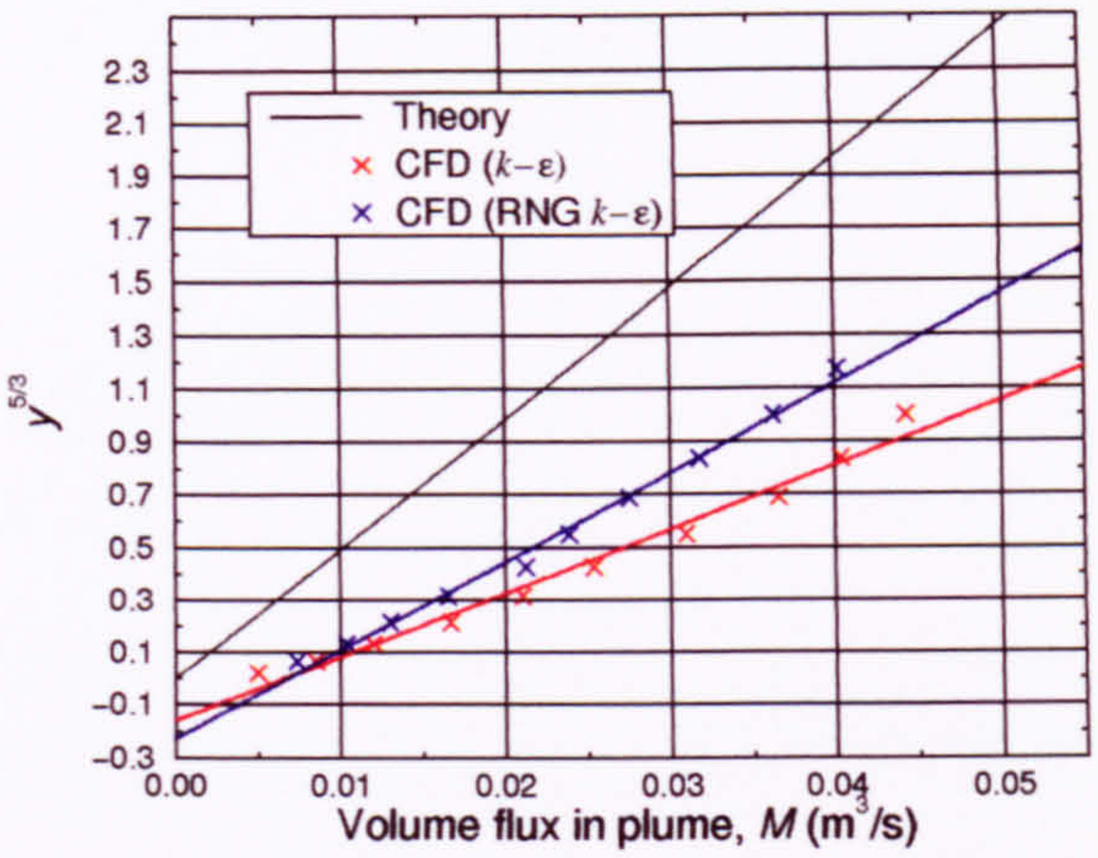

Figure 7.12 Variation of plume volume flux with $y^{5/3}$.

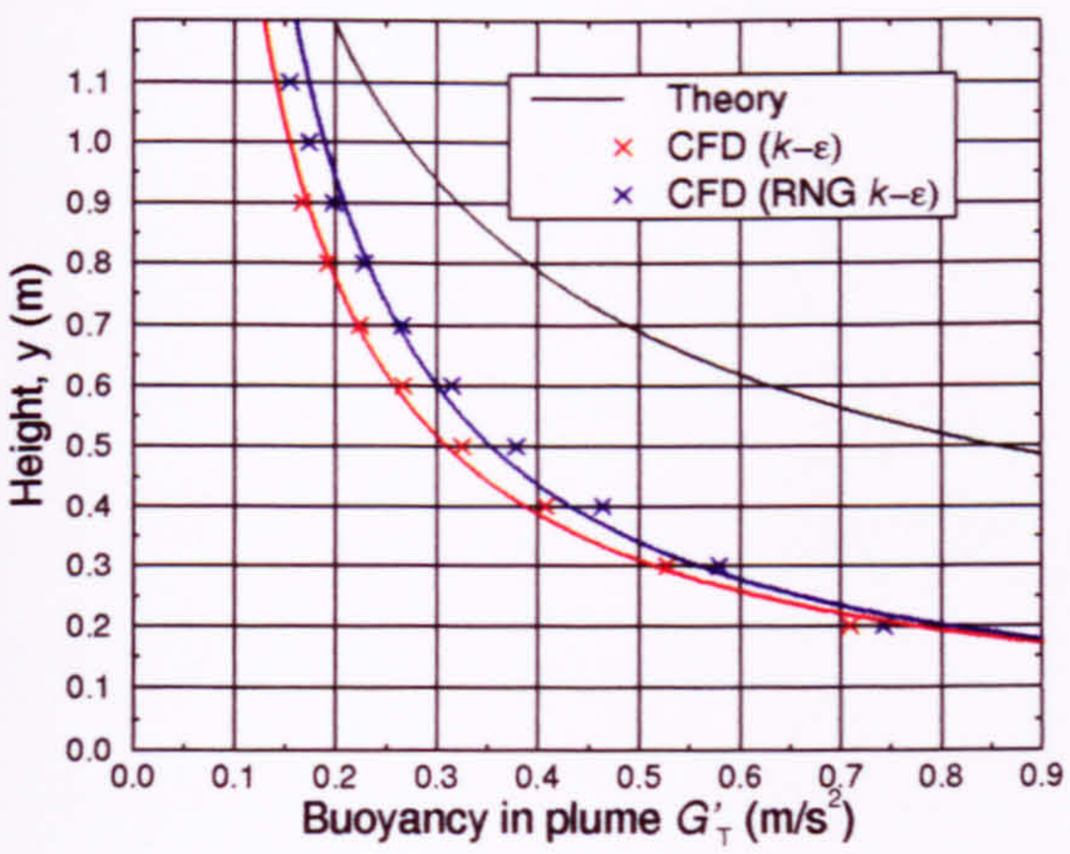

Figure 7.13 Variation of plume buoyancy with height.

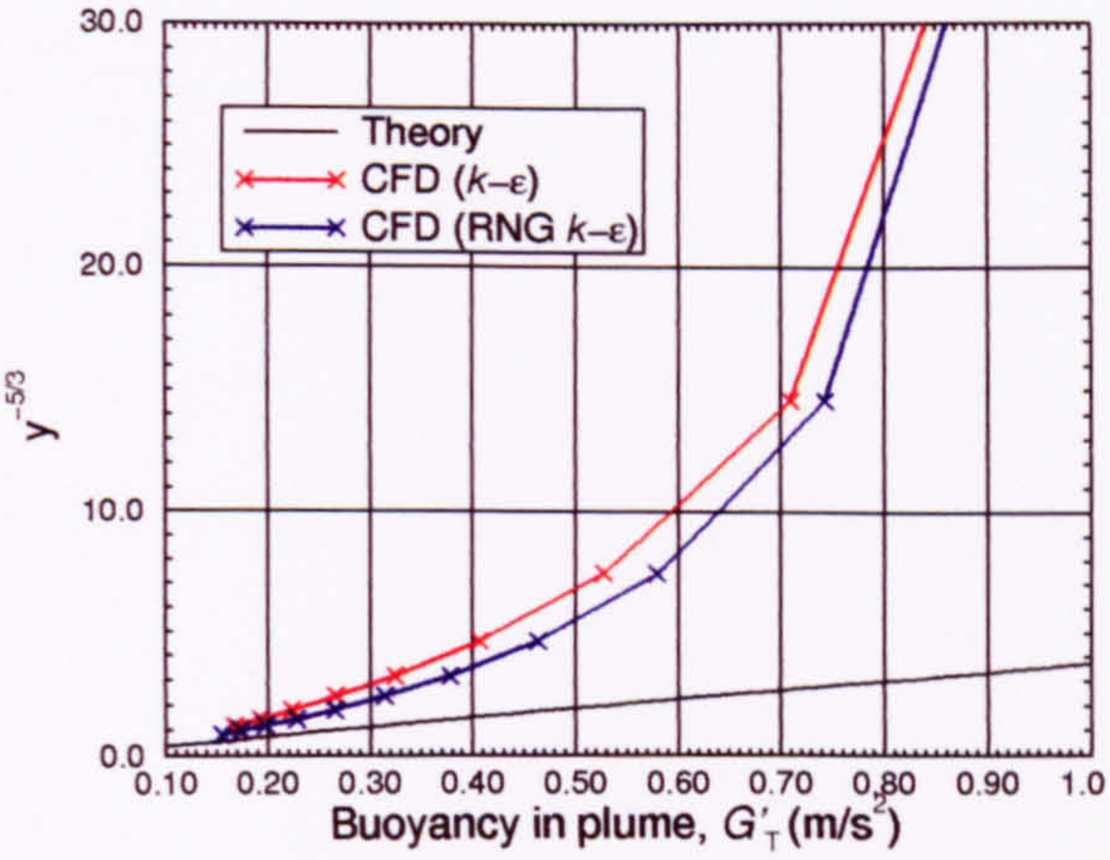

Figure 7.14 Variation of plume buoyancy with $y^{-5/3}$.

This is substantiated by the linear plot of M versus $y^{5/3}$ (Fig. 7.12) in which the gradient of the lines should be directly proportional to $\alpha_T^{4/3}$ (Eq. 3-14). The y-intercept discrepancy can again be attributed to the existence of a virtual origin below the real source origin as explained in section 5.4.4. By extending the lines in Figure 7.12 it was found that virtual origins for the standard and RNG $k-\varepsilon$ plumes lie at approximately $y = -0.15$m and $y = -0.22$m respectively. The plume volume fluxes at the interface height for each case were $M^{k-\varepsilon} = 0.05\,m^3/s$ and $M^{RNG} = 0.048\,m^3/s$. These are again higher than the fluxes through the openings which is thought to be caused by downwards entrainment of air across the interface (see Fig. 7.2).

7.4.3.3 Buoyancy in the Plume

The values of enthalpy shown in Table 7.2 were used to plot the variation of plume buoyancy with height (Figs. 7.13 and 7.14), using Equation (6-1). These figures resemble the findings of the previous chapters very closely. Although a lower plume buoyancy is indicative of a higher entrainment, the variation of G'_T with $y^{-5/3}$ is not linear suggesting inaccuracies in the CFD model when using either turbulence model.

7.4.4 Effect of Changes in Source Strength

7.4.4.1 Flow Pattern

The effect on the flow of increasing the source strength was to increase the induced velocities and hence the volume flux through the space and also the stratification strength (Table 7.3 and Figs. 7.15 - 7.18). The theory of Linden et al. (1990) predicts no change in interface height with source strength. However, both line source and point source simulations predicted *small* changes when using the RNG $k-\varepsilon$ model (Table 7.3). Benchmark 3 simulations also predicted very slight changes in interface height when using the standard $k-\varepsilon$ turbulence model

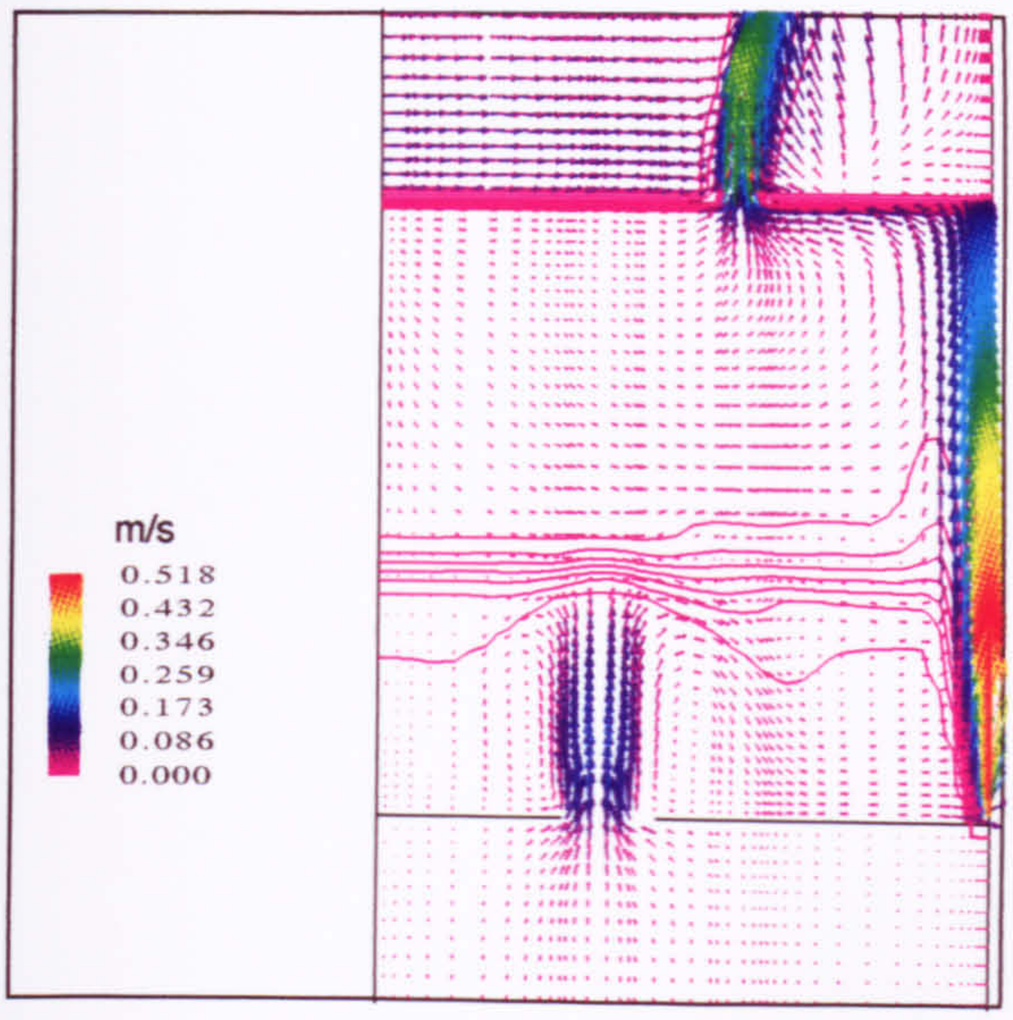

Figure 7.15 Predicted flow pattern using the standard $k-\varepsilon$ model with a heat source of 50W.

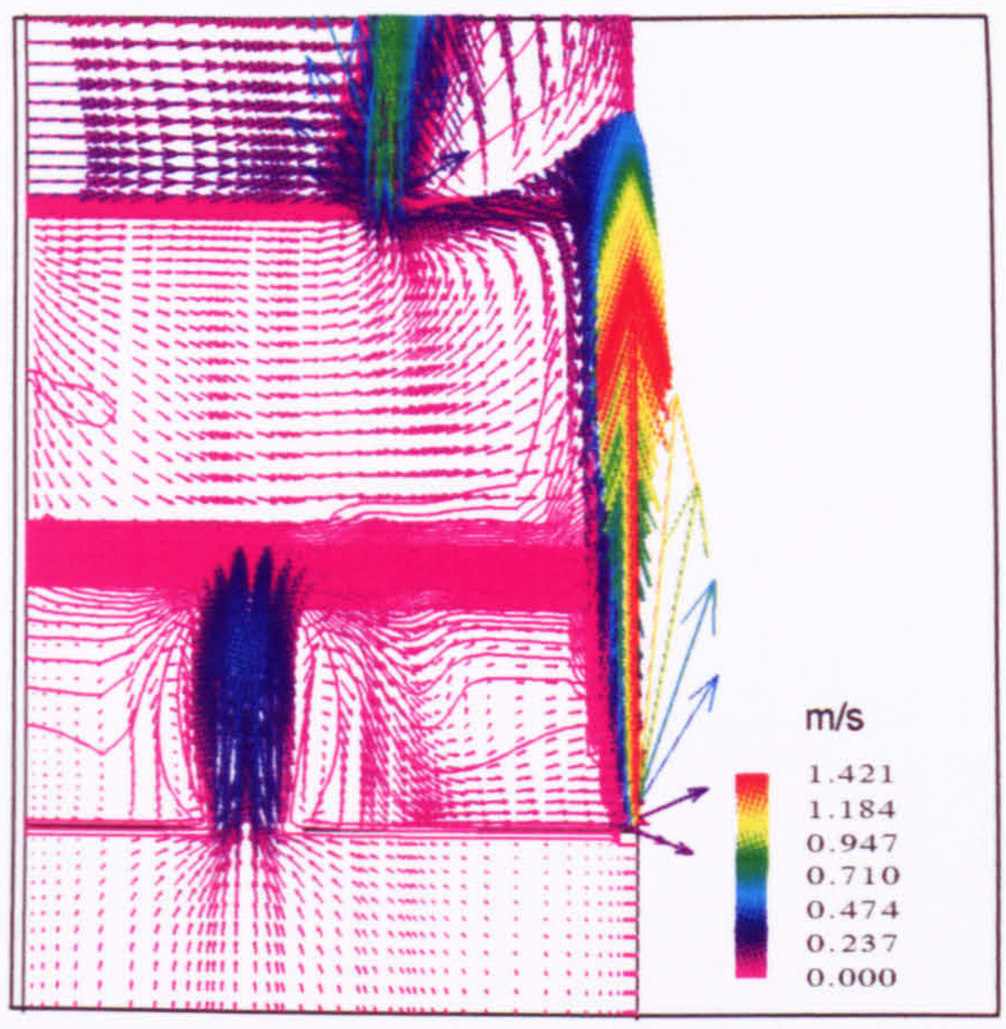

Figure 7.16 Predicted flow pattern using the standard $k-\varepsilon$ model with a heat source of 1000W.

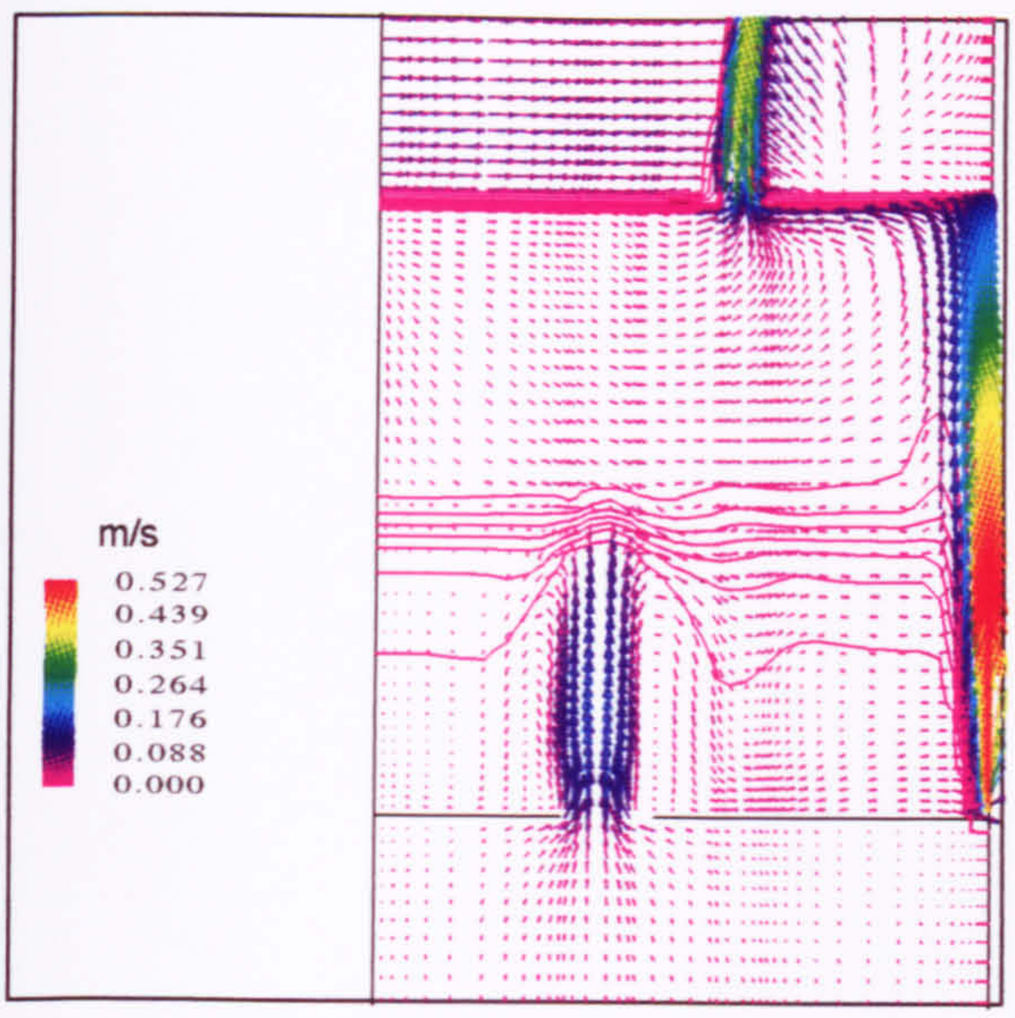

Figure 7.17 Predicted flow pattern using the RNG $k-\varepsilon$ model with a heat source of 50W.

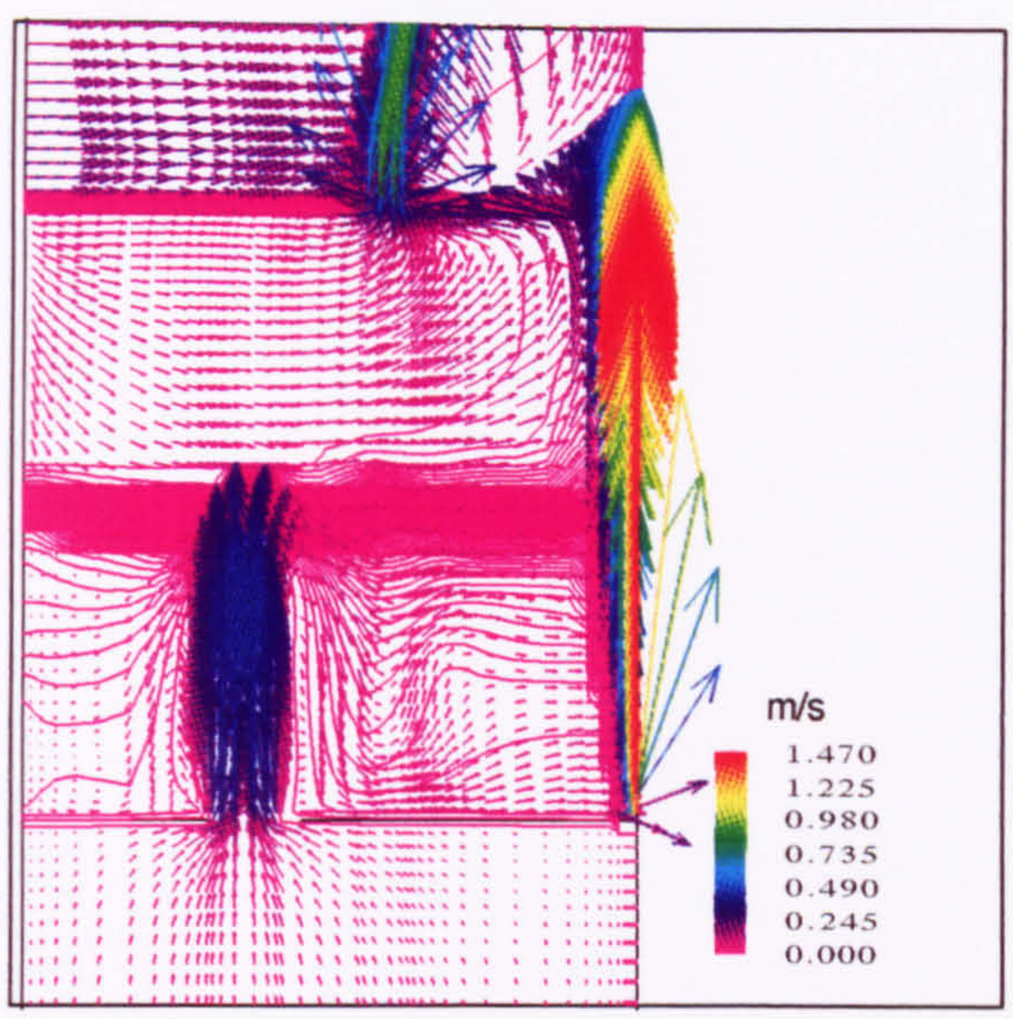

Figure 7.18 Predicted flow pattern using the RNG $k-\varepsilon$ model with a heat source of 1000W.

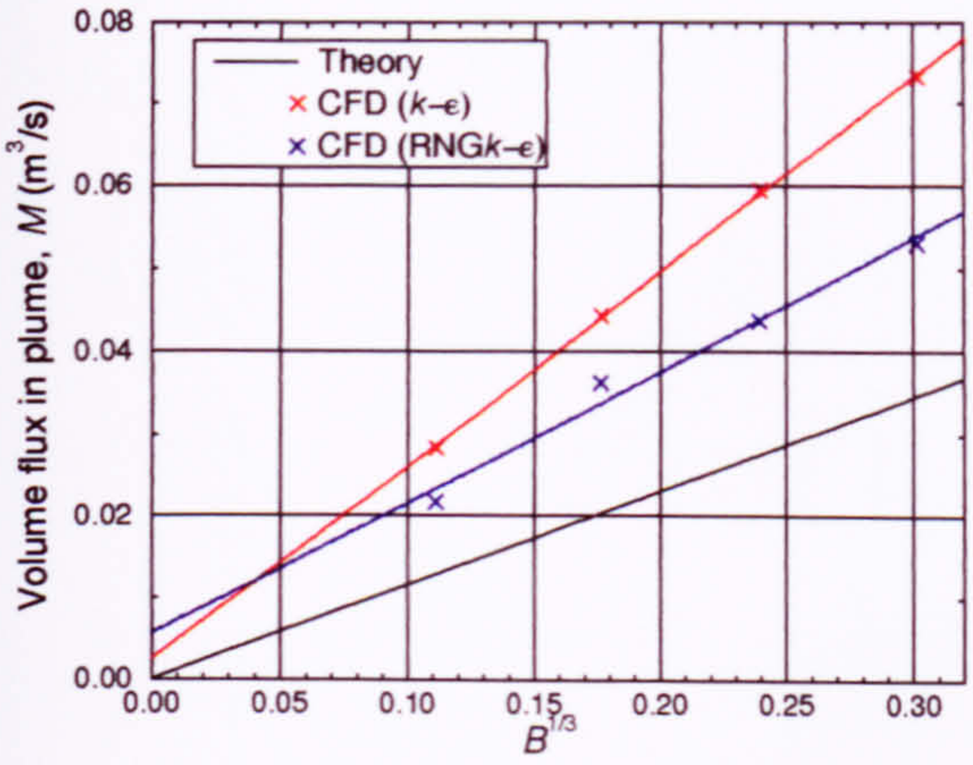

Figure 7.19 Variation of plume volume flux with $B^{1/3}$.

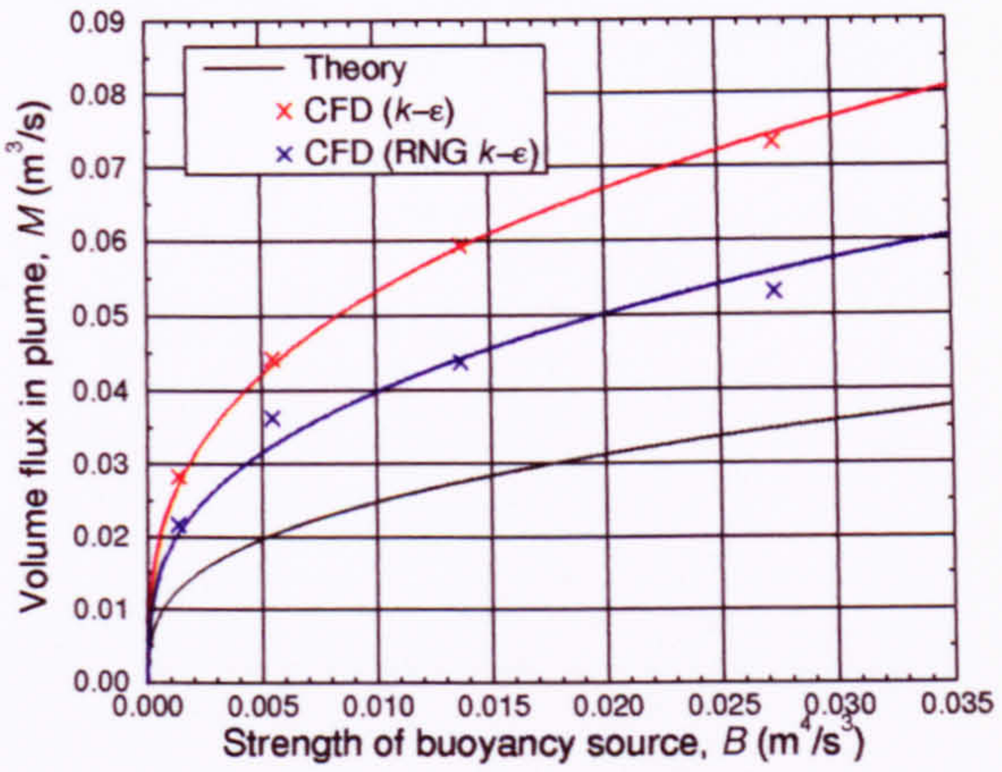

Figure 7.20 Variation of plume volume flux with source strength.

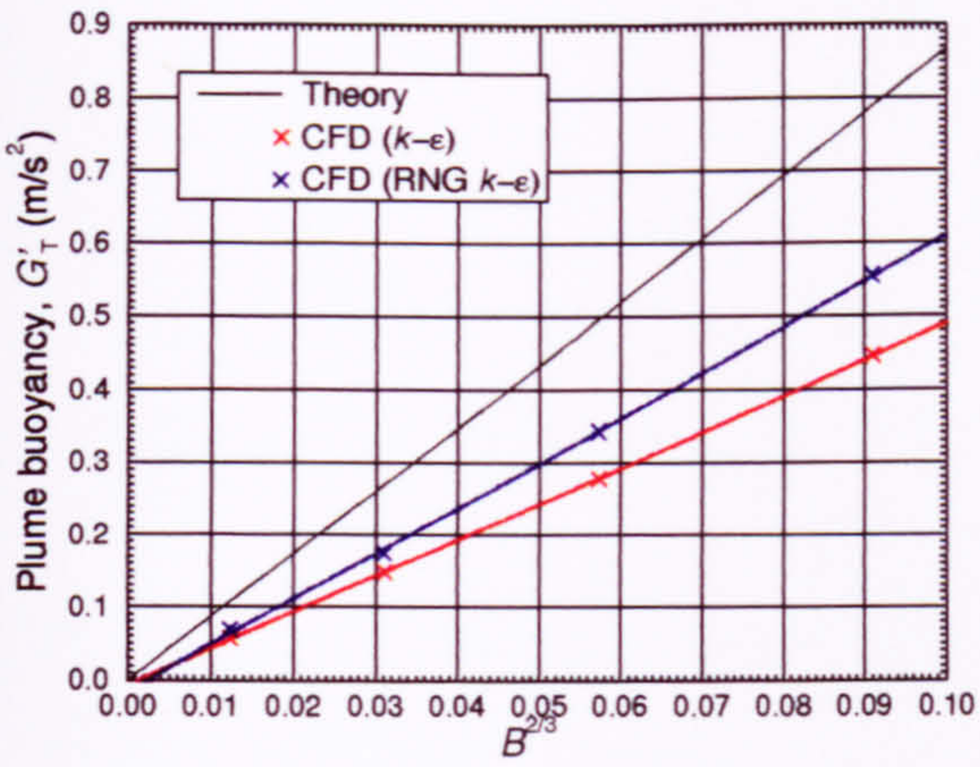

Figure 7.21 Variation of plume buoyancy with $B^{2/3}$.

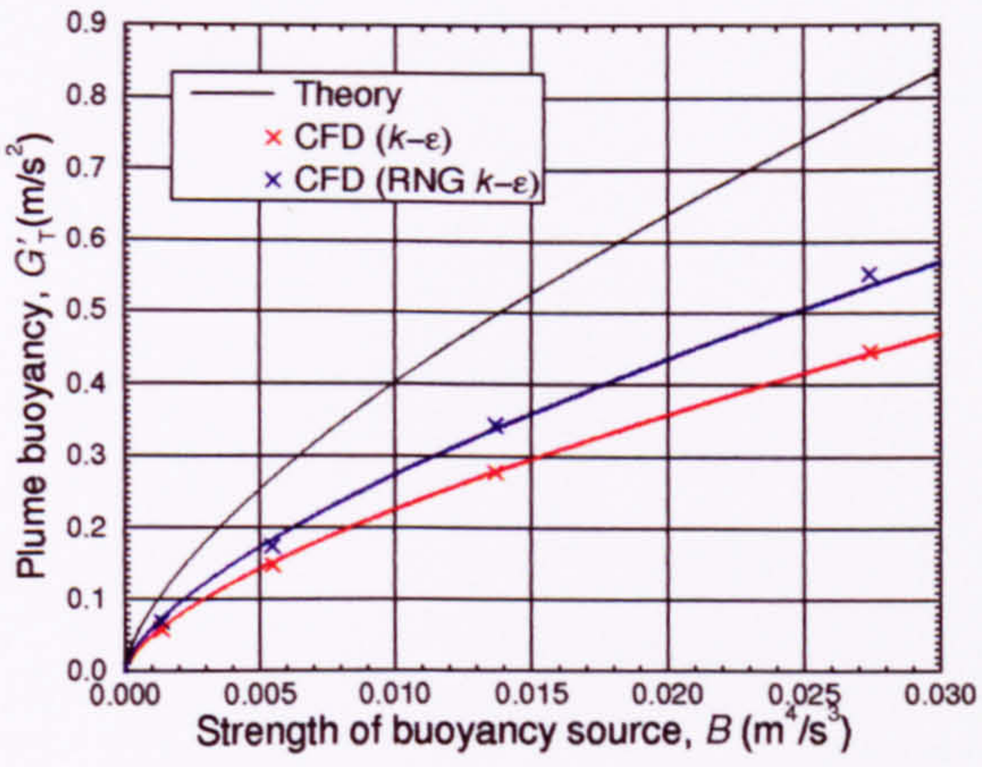

Figure 7.22 Variation of plume buoyancy with source strength.

which is thought to be caused by the circular plume in this benchmark being less stable than the line plumes in benchmarks 1 and 2.

Table 7.3 Effect of source strength on displacement ventilation flow parameters.

Source strength (W)	h/H				g'_h / G'_H		ach^{-1}	
	$k-\varepsilon$		RNG		$k-\varepsilon$	RNG	$k-\varepsilon$	RNG
	BM2	BM3	BM2	BM3	BM3	BM3	BM3	BM3
50	0.457	0.400	0.533	0.472	2.72	2.75	6.22	6.16
200	0.457	0.426	0.544	0.472	2.72	2.75	9.91	9.74
500	0.457	0.426	0.570	0.495	2.71	2.75	13.46	13.28
1000	0.457	0.444	0.571	0.509	2.71	2.73	16.99	16.77
variation (%)	0	4	7	4				

BM2 - Benchmark 2, BM3 - Benchmark 3.

7.4.4.2 Volume Flux in the Plume

Both turbulence models successfully predicted the linear relationship between volume flux M, and $B^{1/3}$ (Fig. 7.19). As expected, the gradient of the RNG line was closer to the theory than the standard $k-\varepsilon$ model due to its lower prediction of plume entrainment. The y-intercept discrepancy can be attributed to the non-zero volume flux predicted at $y = 0$ due to the virtual origin. The qualitative variation of volume flux with source strength is good (Fig. 7.20), although the actual values show discrepancies due to the virtual origin effect and higher prediction of entrainment, particularly when using the standard $k-\varepsilon$ model.

7.4.4.3 Buoyancy in the Plume

The over-prediction of entrainment by both turbulence models caused an under-prediction of plume buoyancy (Fig. 7.21) which follows from Equation (3-15). It is also thought that the presence of a virtual origin contributes to a lower prediction of buoyancy. This is explained in more detail in Chapter 8 (§8.3.3).

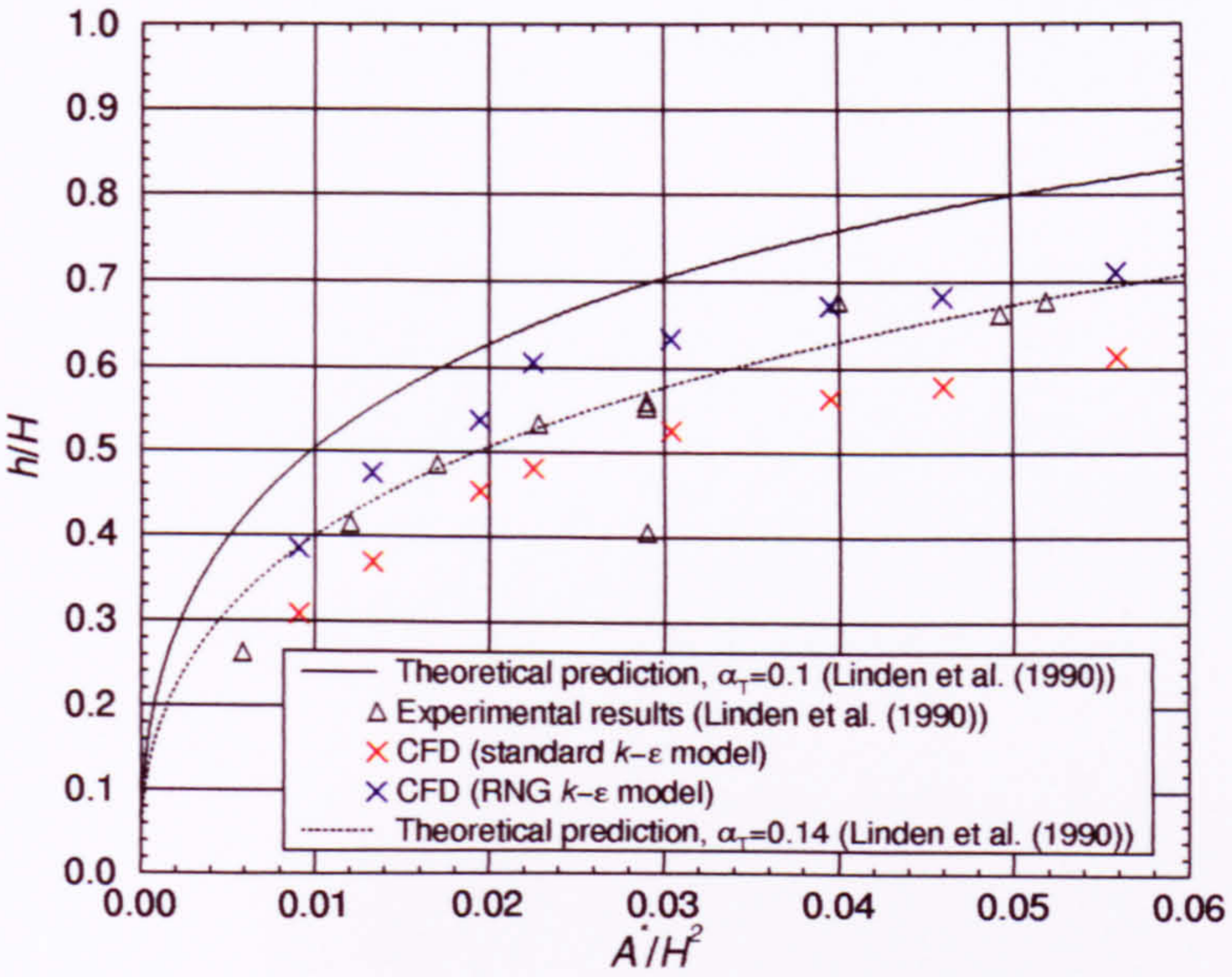

Figure 7.23 Variation of interface height with effective opening area.

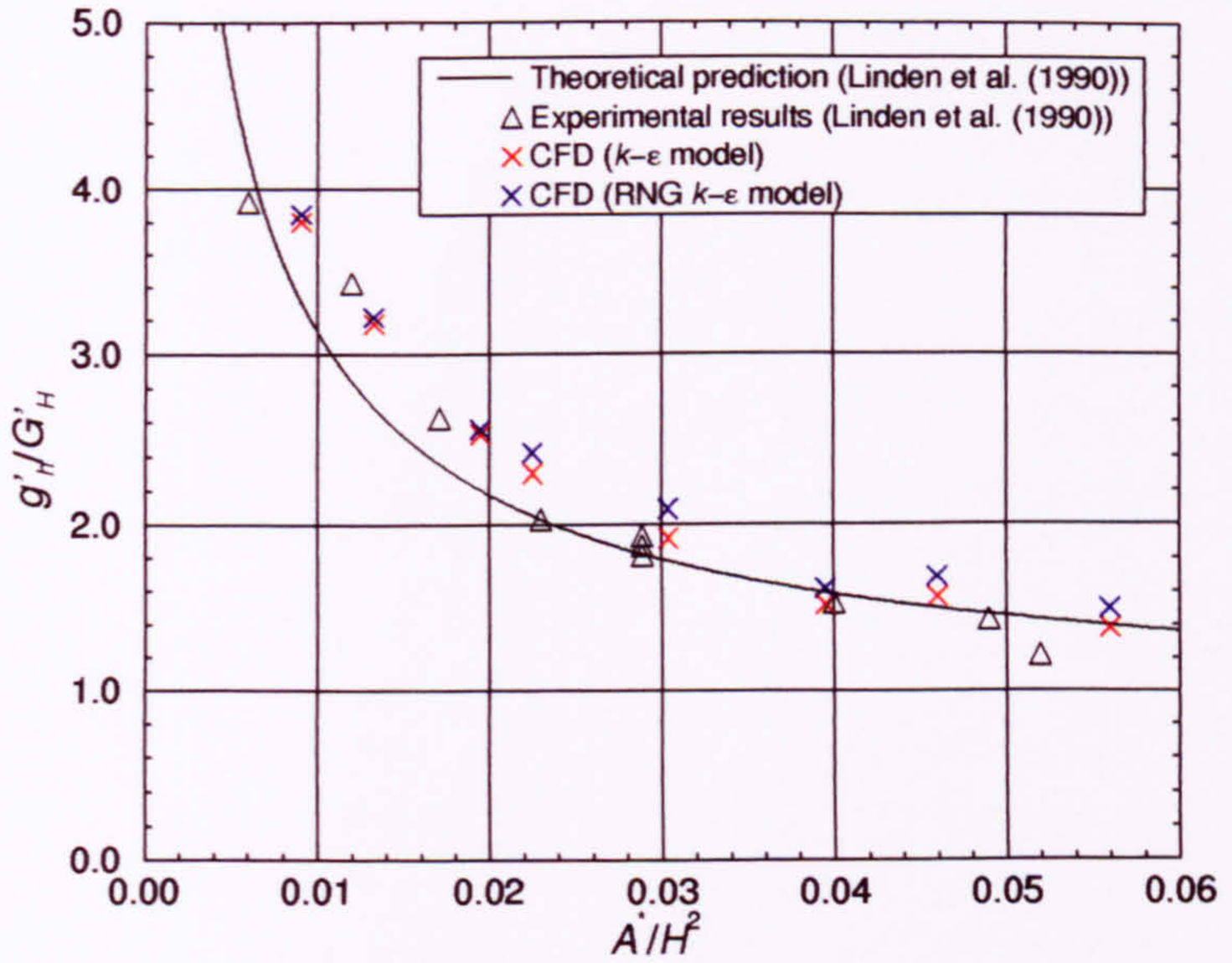

Figure 7.24 Variation of buoyancy change across the interface with effective opening area.

7.4.5 Effect of Changes in Opening Area

As predicted by Linden et al. (1990), an increase in effective opening area A^*, caused an increase in interface height (Fig. 7.23) and a decrease in buoyancy change across the interface (Fig. 7.24) for a constant heat source. Like the previous two chapters, the Benchmark 3 set of simulations has consistently predicted higher interfaces when using the RNG $k-\varepsilon$ model rather than the standard $k-\varepsilon$ model. Once again both turbulence models predict similar values for g'_h / G'_H due to the cancelling effect of the different interface heights and entrainment values between the two turbulence models (Fig. 7.24).

7.5 Summary

This chapter has addressed the ability of CFD to model buoyancy-driven displacement ventilation resulting from a (3D) point source of buoyancy in a simple space with upper and lower openings. The opening sizes were defined such that the resulting interface height predicted by the analytical work of Linden et al. (1990) was the same as that for benchmarks 1 and 2 where a 2D line source of buoyancy was considered. However, this benchmark predicted an interface height between that of benchmarks 1 and 2. The reasons for a lower interface height in Benchmark 3 than Benchmark 2 are thought to be because, in Benchmark 3, there is stronger stratification and less momentum in the entering air. The differences between benchmarks 1 and 3 are small but could be attributable to instabilities in the 3D plume modelled in Benchmark 3. This is discussed further in Chapter 8 (§8.3.3).

The simulations in this chapter accurately predicted the displacement ventilation flow pattern demonstrated by Linden et al. (1990) and showed the same trends as benchmarks 1 and 2. That is, the RNG $k-\varepsilon$ turbulence model predicted a lower value of entrainment than the standard $k-\varepsilon$ model, which resulted in closer quantitative agreement with the theory for plume volume flux and hence interface height.

The existence of a virtual origin of the heat source caused a larger volume flux in the plume than predicted by the theory, which contributed to the under-prediction of the interface height in all cases. The use of an infinitesimally small point source in the theory is thought to be the cause of the variation of plume buoyancy with height above the source being poorly predicted by the CFD model. However, the variation was such that the error diminished as distance from the source increased. Consequently, the change in buoyancy across the interface was only subject to a small error.

Slight variations in interface height for different source strengths were predicted by both turbulence models. This may be caused by the circular plume being less stable than the line plume.

Chapter 8

Discussion of Results and Suggestions for Further Work

8. Discussion of Results and Suggestions for Further Work

8.1 Preamble

The aims of this research were: to evaluate the accuracy with which CFD is able to model buoyancy-driven displacement ventilation; and to offer guidance on its reliability and how it should be used for modelling such flows. This chapter addresses these issues by first suggesting optimal techniques for modelling the three benchmark cases, and then discussing the key results and how they compare with those predicted by Linden et al. (1990). From the points raised in these two sections, suggestions are made as to how CFD might be applied to real buildings and the accuracy which could be expected. An example application is then given.

Following the findings discussed in this chapter, the last section outlines areas which would benefit from further research. A summary has not been used at the end of this chapter since this forms the conclusions in Chapter 9.

8.2 Guidance on How to Model the Benchmark Cases

8.2.1 Boundary Conditions

It is common amongst CFD practitioners to experience difficulty in modelling airflows in which there is exchange of air between the interior and exterior of a space driven by natural forces. The difficulty lies in deciding what boundary conditions to impose at such interfaces, in particular conditions on turbulence parameters. One way of eliminating this difficulty is to extend the computational domain to include some of the air outside of the space of interest. A sensitivity analysis carried out using Benchmark 1 concluded that exterior zones only on façades with openings were sufficient. The extent of such zones is largely dependent upon available computing power, but was extended by 2.55m (i.e. the

height of the space) above and below the space in all three benchmarks considered in this research. The conditions imposed on the boundaries of the exterior zones should reflect, as close as possible, an infinite exterior domain, or at least, behave such that their existence has no effect on the flow entering or leaving the ventilated space. One may imagine the flow at an infinite distance away from the space (in the absence of wind) having zero velocity. This could be achieved by specifying solid surfaces at these domain boundaries. However, this would require knowledge of the rate of heat loss at all points on the solid boundary, so instead, boundaries across which there is zero normal gradient on velocities and turbulence quantities were imposed. These are known as PRESSURE boundaries in CFX, where constant values of pressure and temperature are specified. The value of temperature imposed is the ambient temperature. Pressure needs to be imposed such that its value, in the absence of all other driving forces, produces no net flow. In an attempt to achieve this, a value of $p = 0$ was imposed on all domain boundaries surrounding the exterior zones, (except the SYMMETRY PLANE boundaries). However, for flows between two PRESSURE boundaries facing each other, there exist an infinite number of solutions. Recall from Newton's first law of motion *that a body moving through space continues to do so at a constant velocity unless acted upon by an external force.* That is, no net force is required to maintain a body's motion - whatever its speed. This effect was observed in the 3D simulations in which two facing PRESSURE boundaries, with no net force between them, yielded an unrealistically high-velocity flow. To avoid this problem, the PRESSURE boundaries on the high- and low-*z* faces of the exterior zones were replaced with WALL boundaries. This 'false entrainment' effect was also observed, but to a lesser extent, across *adjacent* PRESSURE boundaries, particularly in the lower exterior space where buoyancy-driven air movement was minimal.

In geometries possessing symmetry it is common practice to reduce computational time by use of SYMMETRY PLANE boundaries. Symmetry was therefore assumed in each benchmark along the line bisecting the buoyancy

source. This made a pre-simulation assumption that the plume would not meander from side-to-side. In fact, plumes often do behave in this manner (McGuirk and Whittle 1991) and this may have been the cause of non-convergence in the simulations without false time-steps (see also §8.2.4). However, since the oscillations on the flow variables in the non-converged solution were small and the simulations of the complete geometry (with no SYMMETRY PLANE) presented no serious convergence problems, it was assumed that any asymmetric behaviour would be small. It was also constructive to produce a perfectly symmetric plume to enable detailed and accurate analysis of the plume.

All solid surfaces were adiabatic and employed conventional wall function conditions that model the steep gradient in flow variables close to solid surfaces. The details of these functions were given in §4.6.1.

The source of buoyancy, also defined using a solid surface, modelled a steady input of heat across the face of the computational cell.

8.2.2 Mesh Definition

The purpose of the computational mesh is two-fold. Firstly, and most importantly, it enables solution of the flow variables by tracking transport of mass, momentum and enthalpy. To do this accurately, it is important to place more grid nodes in areas where there may be large gradients in the flow variables, such as solid boundaries and openings, relative to other areas where the flow is largely unchanging. Secondly, the mesh is used to provide a picture of the resulting flow field by plotting velocity vectors, temperature contours and pressure contours, etc., which use (and interpolate) values from each cell centre. Consequently, the greater the number of cells, the more detailed the qualitative picture of the flow becomes.

When defining the initial simulation of Benchmark 1, an estimate was made of the mesh density whereby the smallest cell dimension was set equal to half that of the source width (5cm). In the mesh investigation sections of chapters 5 and 6,

different densities were considered to ensure a *grid-independent-solution* had been achieved. This was done by analysing the results from coarser and finer meshes in an attempt to identify the optimum mesh density and structure such that results, which did not depend significantly on further mesh refinement, could be obtained within an acceptable simulation time. The parameters used to determine whether or not a grid-independent-solution had been achieved were interface height, buoyancy change across the interface, air change rate and velocity in the vicinity of the plume.

The mesh investigation exercises showed that very good approximations to the flow field could be obtained using a relatively coarse mesh, for example 17×17 cells in Benchmark 1 over an area of $2.55\text{m} \times 2.55\text{m}$. However, a finer mesh was needed to enable accurate predictions of quantitative parameters such as interface height. In particular, for this research it was necessary to accurately predict plume properties which necessitated a finer mesh within the plume (Fig. 8.1).

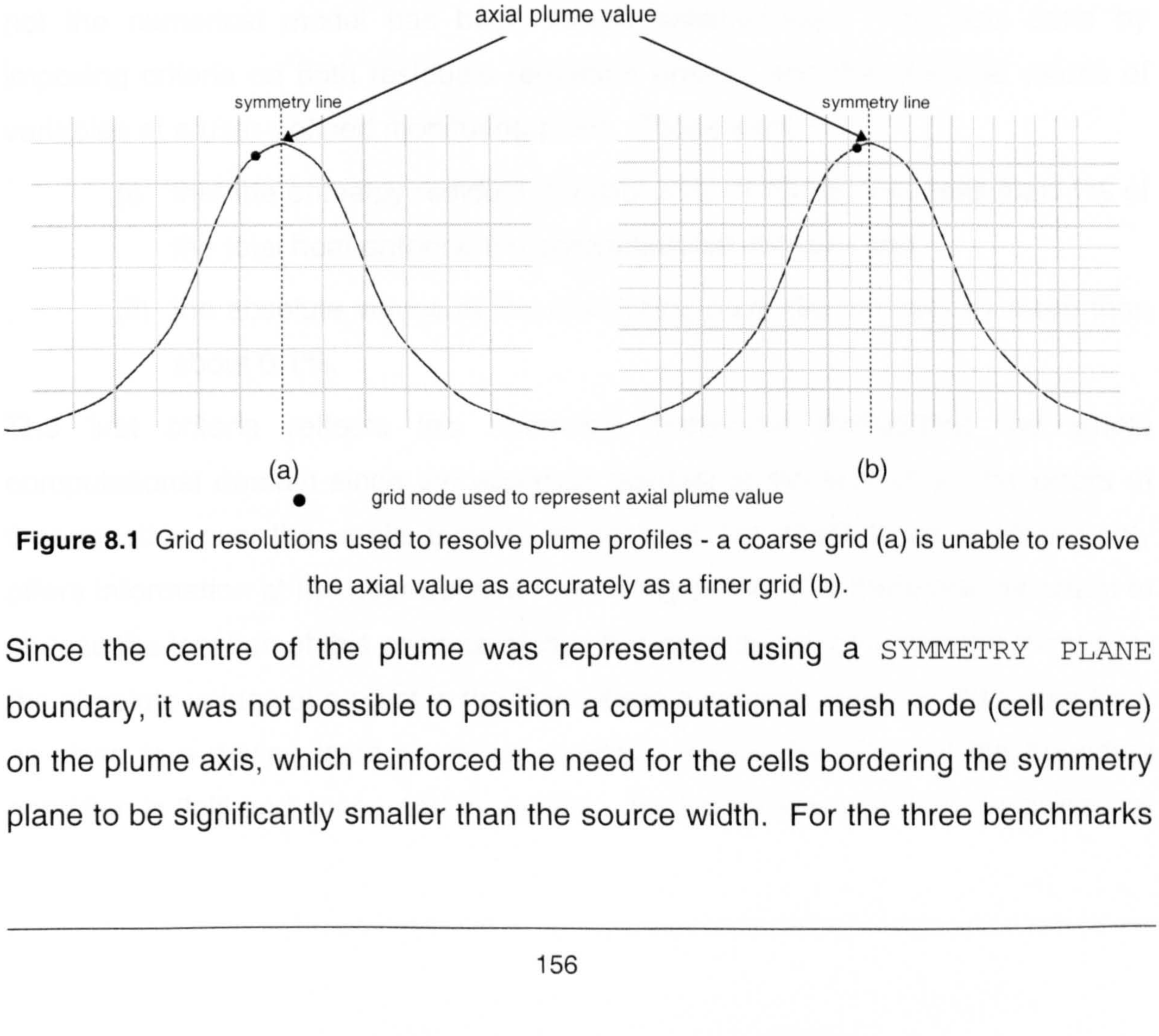

Figure 8.1 Grid resolutions used to resolve plume profiles - a coarse grid (a) is unable to resolve the axial value as accurately as a finer grid (b).

Since the centre of the plume was represented using a `SYMMETRY PLANE` boundary, it was not possible to position a computational mesh node (cell centre) on the plume axis, which reinforced the need for the cells bordering the symmetry plane to be significantly smaller than the source width. For the three benchmarks

described in this research, a (half) source width of 5cm was modelled using cells of width 1cm.

Convergence difficulties were encountered when using grid layouts with highly skewed (non-orthogonal) cells. This is thought to be due to the deferred correction approach adopted by CFX in which the off-diagonal diffusion terms in the solution matrix are absorbed into the source term (see §D.9). This can cause degradation of convergence due to the lack of diagonal-dominance in the matrix equation (Eq. (D-20)). By way of offering user-control over this problem in CFX, opportunity is given for these terms to be omitted for some of the iterations (say for half of the maximum number of iterations) and then included when the flow solution has begun to establish itself. This can be thought of as a type of under-relaxation technique.

8.2.3 Convergence Criteria

When using CFD it is necessary to establish criteria which determine whether or not the numerical model has been solved satisfactorily. This was done by imposing criteria on both residuals (equation errors), and the absolute values of variables at a user-defined monitoring point. These were:

(i) that the enthalpy residual (having units of Watts) was less than 1% of the total heat entering the computational domain; and

(ii) the absolute values at the monitoring point did not vary by more than about 0.1%.

The first criteria reflects the numerical behaviour throughout the whole computational domain since the equation residual is the *sum* of *all* the errors of that equation over the whole domain. In contrast, the absolute value criteria only offers information at the user-defined monitoring point. It is therefore important to choose the location of this point carefully. It is considered inappropriate to monitor the absolute values at a point in the flow where a solution is easily attainable such as close to a driving force boundary condition where the effect of the boundary condition is 'felt' and accounted for quickly. Similarly there is little to be gained by

monitoring the solution at the core of a recirculation zone, for example, where the flow may never become perfectly steady and does not offer the user much useful information. It is therefore recommended that for the benchmarks analysed here, the monitoring point be placed either in the centre of the outlet or high up in the plume. The flow variables at both of these locations are closely related to important flow parameters such as air change rate and plume buoyancy and will not settle down completely until the flow pattern in the whole space is well established.

8.2.4 Obtaining a Solution

The benchmark results confirmed the findings of previous researchers (e.g. Ideriah (1980), Fraikin et al. (1982) and Thompson et al. (1985)) that buoyancy-driven flows are difficult to solve using CFD techniques. This is thought to be due largely to the decoupled way in which the equations are solved. That is, since there is no separate conservation equation for pressure, the relationship between the pressure and the velocity field is realised by the need for the velocity components, calculated using the momentum equations and a guessed pressure field, to also satisfy the continuity equation. This coupling is difficult to resolve in buoyancy-driven flows because the velocities are not specified prior to the commencement of the solution process at any point in the domain. Instead, the process relies on the generation of an accurate pressure field to drive the flow. Since the driving forces (governed by the temperature differences) and the resulting velocities are small, this makes the solution procedure prone to instabilities.

Such instabilities were observed in the solution process when using the default under-relaxation factors to control the iteration procedure. Tightening of these factors (decreasing their value) did not improve convergence. A more physical method of under-relaxation is false time-stepping whereby the evolution of the solution is controlled by a time-scale which more accurately reflects the rate at which the variables are changing, and the computational cell volumes based on which the flow variables are being solved.

The drawback of using false time-stepping is knowing what values to use such that the instabilities in the variables can be resolved. By expressing the time scale as a length scale divided by a velocity scale: $t_f = d_f / v_f$, this difficulty is eased slightly provided a suitable length scale and velocity scale can be found. In order to reflect the numerical procedure, d_f should reflect the length scale of the computational mesh. A suitable velocity scale was found by realising that the default under-relaxation techniques (with no false time-stepping) were able to produce a good approximation to the flow field, and therefore yielded typical velocities which could be used to represent v_f. This realisation was supported by observing that the absolute values were oscillatory only within a narrow band of values and that the enthalpy residual was within one order of magnitude of the required criteria.

Satisfactory convergence, i.e. adherence to both criteria, was achieved by restarting the approximate solution (which adopted the default under-relaxation factors) using false time-steps of 0.1s on all momentum equations. This value was arrived at largely by trial and error, but is approximately equal to the smallest cell size in the domain divided by the largest calculated velocity. The need for false time-stepping specifically on the momentum equations reflects the poor coupling between pressure and velocity in buoyancy-driven flows. With the advent of *coupled* solution algorithms such as CFX 5 recently developed by Computational Fluid Dynamics Services (1997) at AEA, Harwell, it is anticipated that many convergence difficulties of this type could disappear.

Under-relaxation techniques are able to enhance convergence by making the solution matrix more diagonally dominant and hence more stable, thereby increasing the likelihood of convergence (§D.7). However, the *rate* of convergence is reduced meaning that more iterations are needed before convergence is reached.

The numerical parameters and solution techniques used to obtain solutions for all three benchmarks are summarised in Table 8.1.

Table 8.1 Numerical parameters and solution techniques used in all three benchmarks.

Parameter/Technique	Details
Solution Procedure	Hybrid differencing was used on all convection terms except in the mass conservation equation where central differencing is used. This is to enable accurate application of the pressure correction algorithm in which central differences are used on the pressure gradient terms. Pressure correction was carried out using the SIMPLEC algorithm with the Rhie and Chow (1983) interpolation algorithm to prevent pressure velocity decoupling due to the non-staggered (co-located) grid. Details of the linear equation solvers used can be found in Table D.2.
Under-relaxation factors	Mass equation: 1.0, momentum equations: 0.65, k, ε and enthalpy equations: 0.7.
False Time-Steps	Initial simulations used no false time-stepping to obtain an approximation to the flow. These were then restarted using false time-steps of 0.1s on each momentum equation to establish a more accurate solution. The number of iterations in each stage of the solution process was typically about 2000.
Enthalpy Reference Temperature	Ambient.
Buoyancy Reference Temperature	This reference temperature had to equal that set at the PRESSURE boundary (i.e. ambient) in order to prevent a net pressure being established due to a numerical (unphysical) buoyancy force.
Turbulence	Standard $k-\varepsilon$ model (§4.5.4) and Renormalisation Group (RNG) theory $k-\varepsilon$ model (§4.5.5).

8.3 Accuracy of the Benchmark Results

Tables 8.2 and 8.3, which provide a summary of all three benchmark results, are referred to throughout this section.

In an attempt to offer the reader a more practical insight into the stratification strength g'_h, this parameter is also represented by ΔT_h, the change in temperature across the interface, using the expression

$$\Delta T_h = \frac{\Delta He_h}{C_P} = \frac{g'_h}{g\beta} \tag{8-1}$$

where ΔHe_h = change in enthalpy across the interface.

Table 8.2 Results for all three benchmarks using the standard $k-\varepsilon$ turbulence model.

Benchmark 1:

$h/H = 0.390$, $g'_h / G'_H = 1.84$, $\Delta T_h = 1.97$, $\alpha_T = 0.17$

Axial plume velocity at $y = 1$m above the source = 0.339m/s

Volume flow in the plume at $y = 1$m above the source = 0.094m^3/s

Buoyancy in the plume at $y = 1$m above the source = 0.047m/s^2

Volume flux through space = 0.081m^3/s

ach^{-1} = 22.42

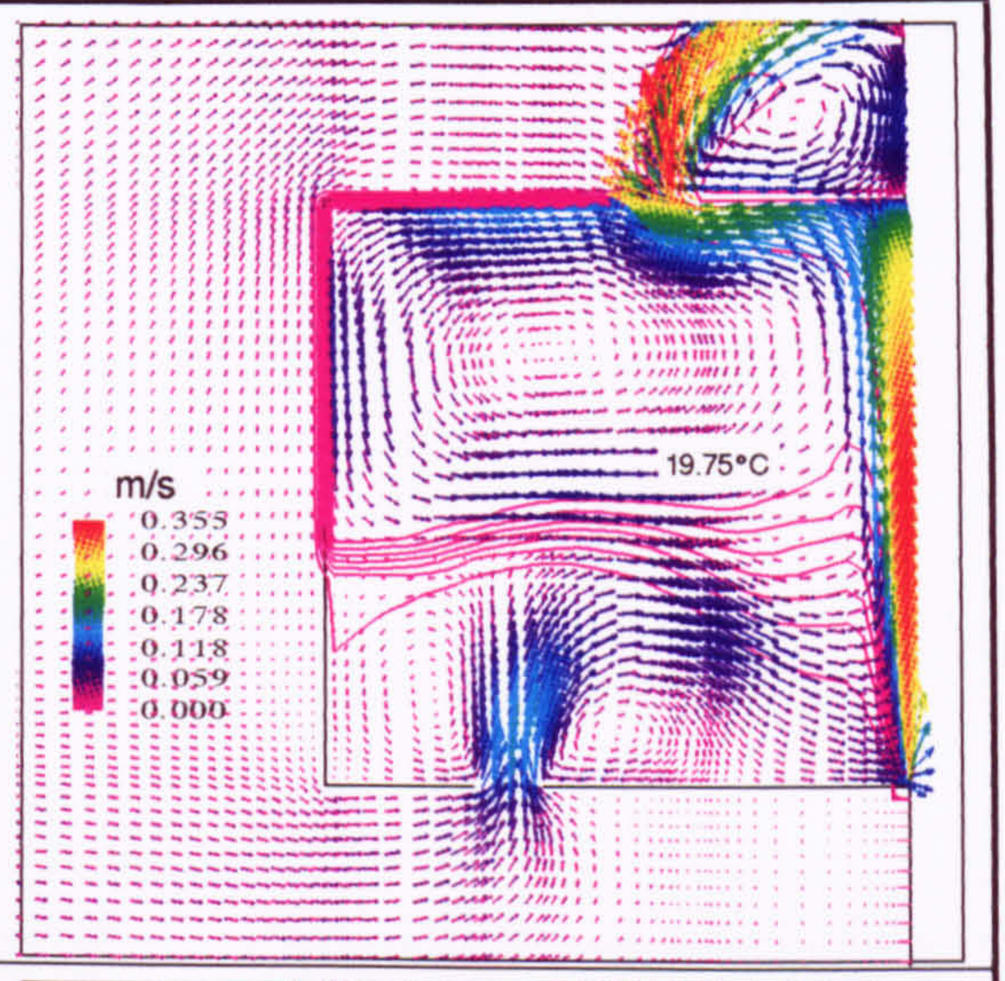

Benchmark 2:

$h/H = 0.457$, $g'_h / G'_H = 1.92$, $\Delta T_h = 2.06$, $\alpha_T = 0.16$

Axial plume velocity at $y = 1$m above the source = 0.368m/s

Volume flow in the plume at $y = 1$m above the source = 0.100m/s

Buoyancy in the plume at $y = 1$m above the source = 0.05m/s^2

Volume flux through space = 0.081m^3/s

ach^{-1} = 22.42

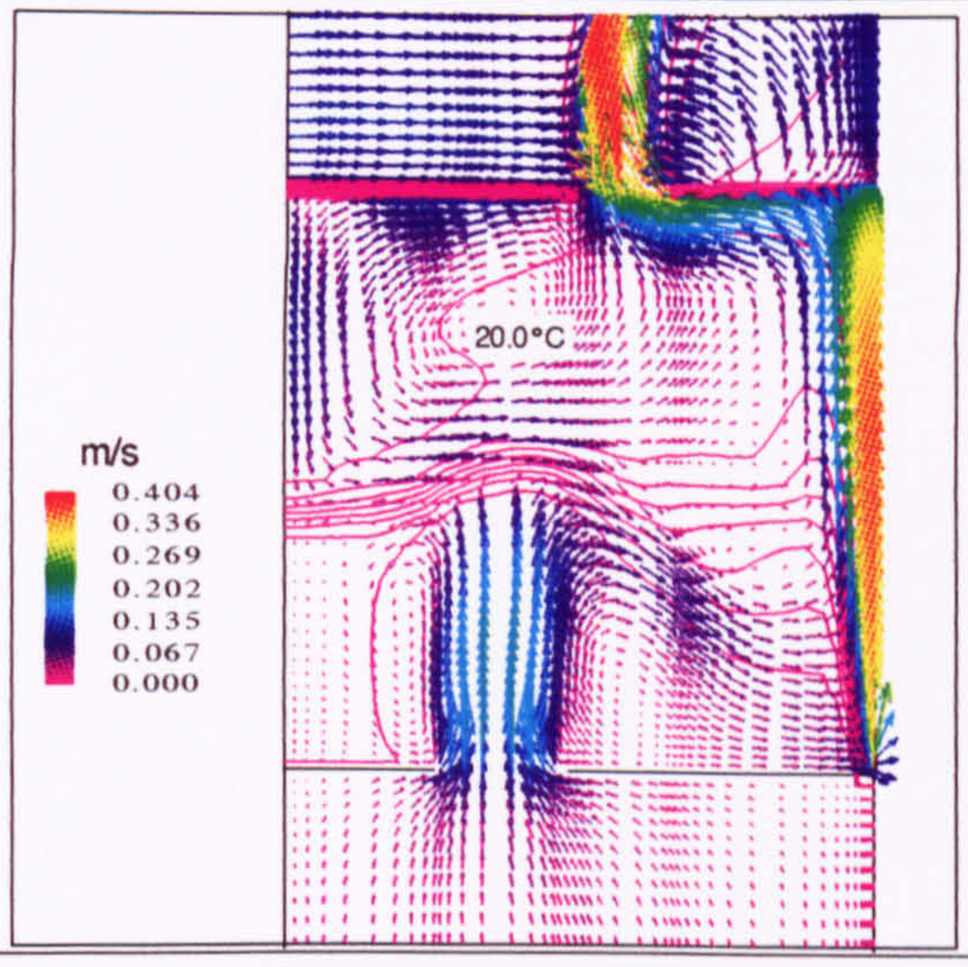

Benchmark 3:

$h/H = 0.426$, $g'_h / G'_H = 2.72$, $\Delta T_h = 4.63$, $\alpha_T = 0.14$

Axial plume velocity at $y = 1$m above the source = 0.628m/s

Volume flow in the plume at $y = 1$m above the source = 0.044m^3/s

Buoyancy in the plume at $y = 1$m above the source = 0.147m/s^2

Volume flux through space = 0.036m^3/s

ach^{-1} = 9.97

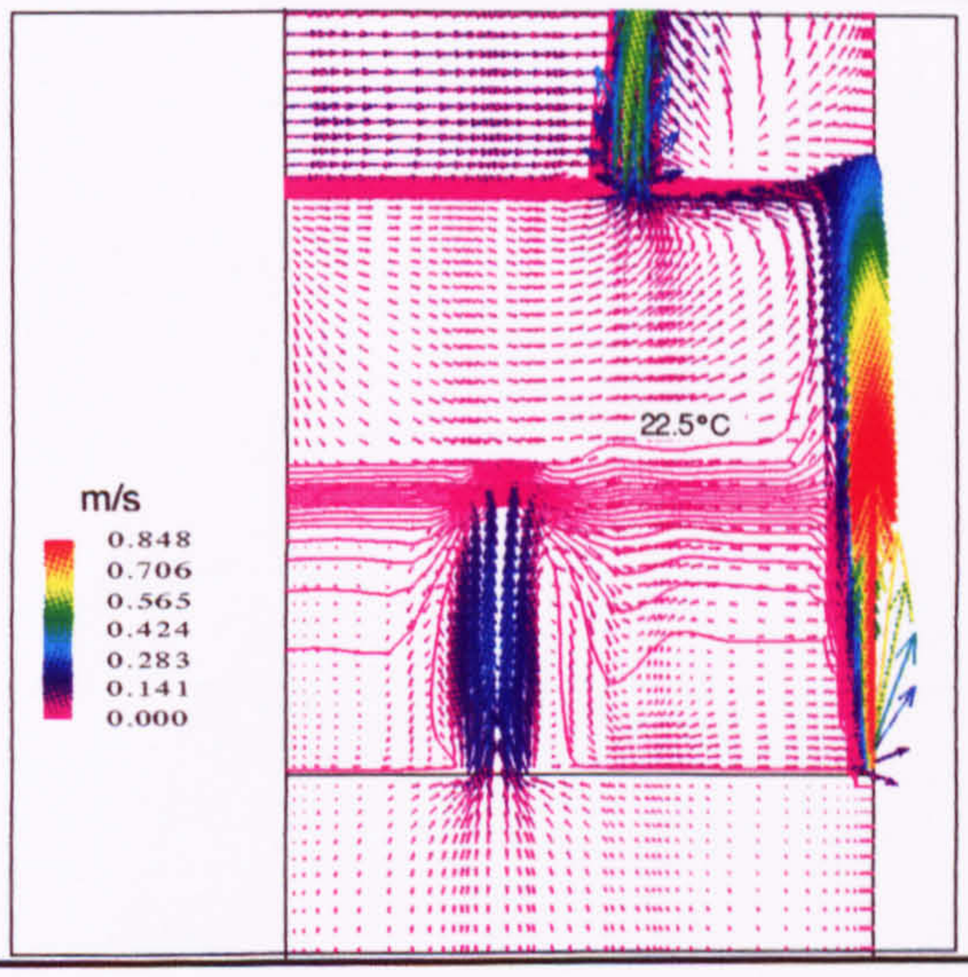

Table 8.3 Results for all three benchmarks using the RNG $k-\varepsilon$ turbulence model.

Benchmark 1:

$h/H = 0.490$, $g'_h/G'_H = 1.88$, $\Delta T_h = 2.01$, $\alpha_T = 0.12$

Axial plume velocity at $y = 1$m above the source = 0.387m/s

Volume flow in the plume at $y = 1$m above the source = 0.082m^3/s

Buoyancy in the plume at $y = 1$m above the source = 0.055m/s^2

Volume flux through space = 0.079m^3/s

ach^{-1} = 21.90

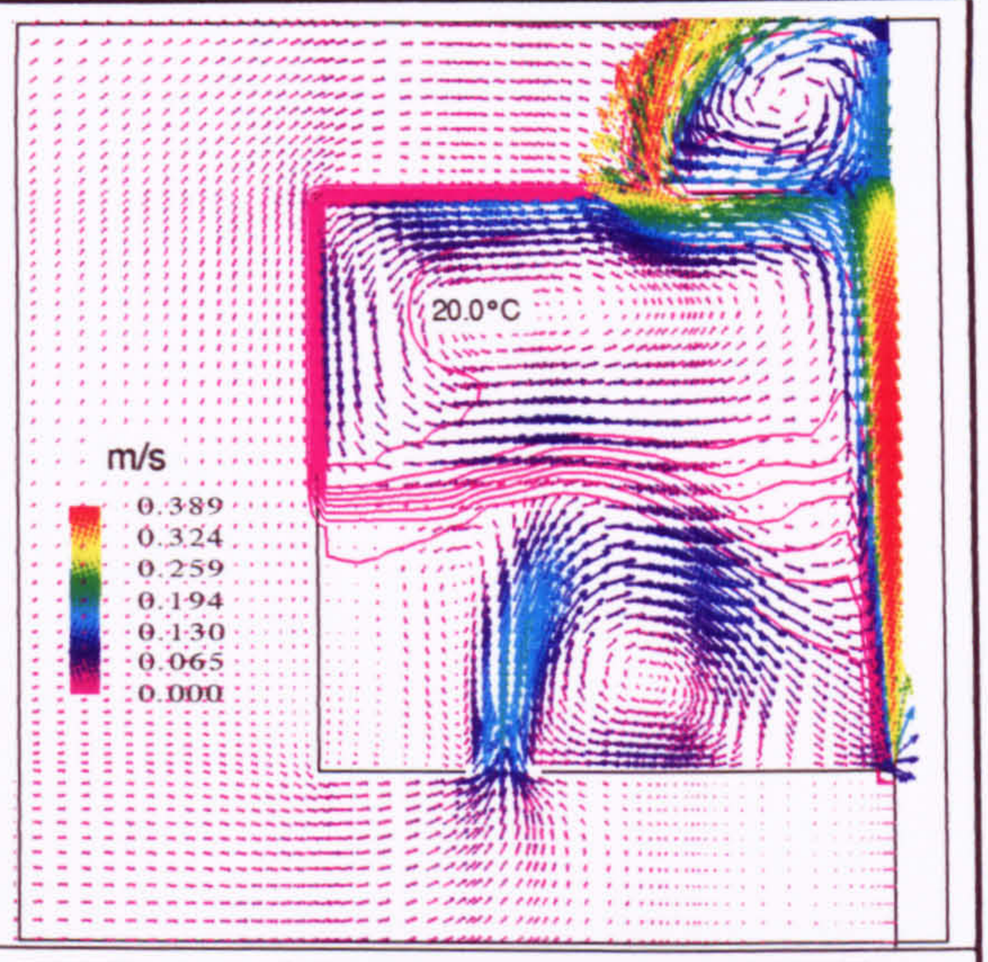

Benchmark 2:

$h/H = 0.544$, $g'_h/G'_H = 1.99$, $\Delta T_h = 2.13$, $\alpha_T = 0.12$

Axial plume velocity at $y = 1$m above the source = 0.383m/s

Volume flow in the plume at $y = 1$m above the source = 0.080m^3/s

Buoyancy in the plume at $y = 1$m above the source = 0.053m/s^2

Volume flux through space = 0.079m^3/s

ach^{-1} = 21.81

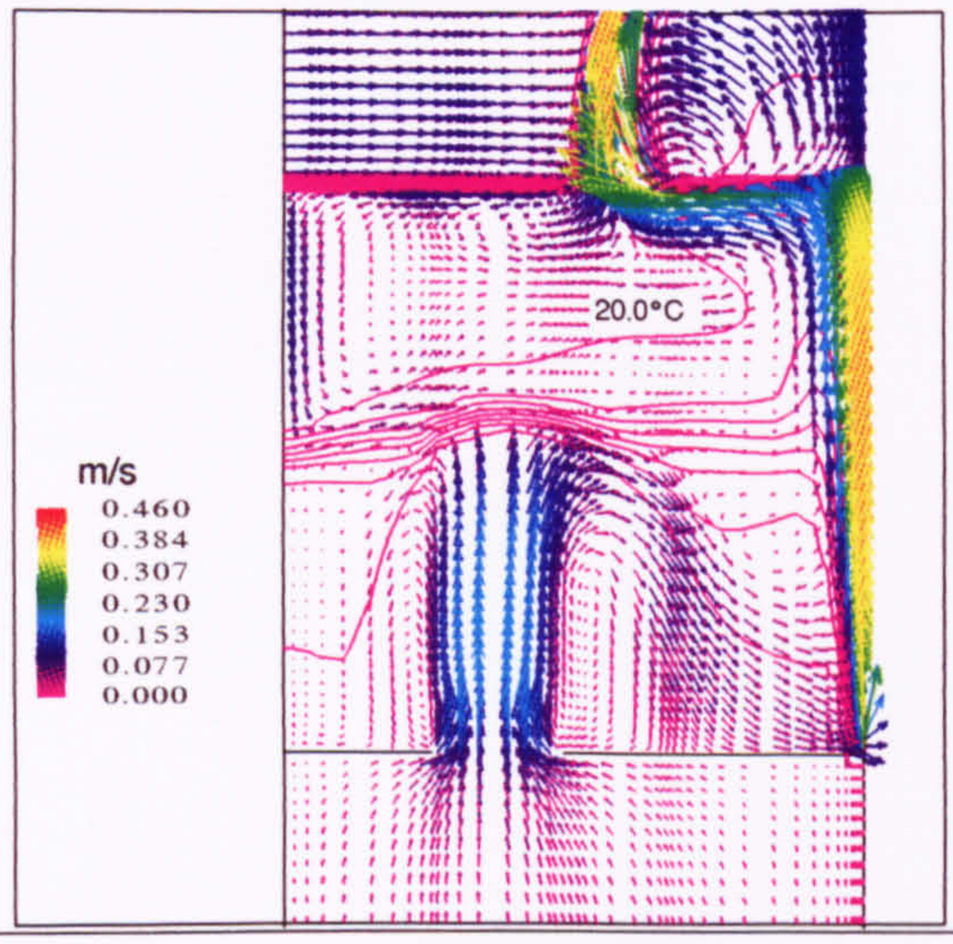

Benchmark 3:

$h/H = 0.472$, $g'_h/G'_H = 2.75$, $\Delta T_h = 4.68$ $\alpha_T = 0.11$

Axial plume velocity at $y = 1$m above the source = 0.696m/s

Volume flow in the plume at $y = 1$m above the source = 0.036m^3/s

Buoyancy in the plume at $y = 1$m above the source = 0.174m/s^2

Volume flux through space = 0.035m^3/s

ach^{-1} = 9.69

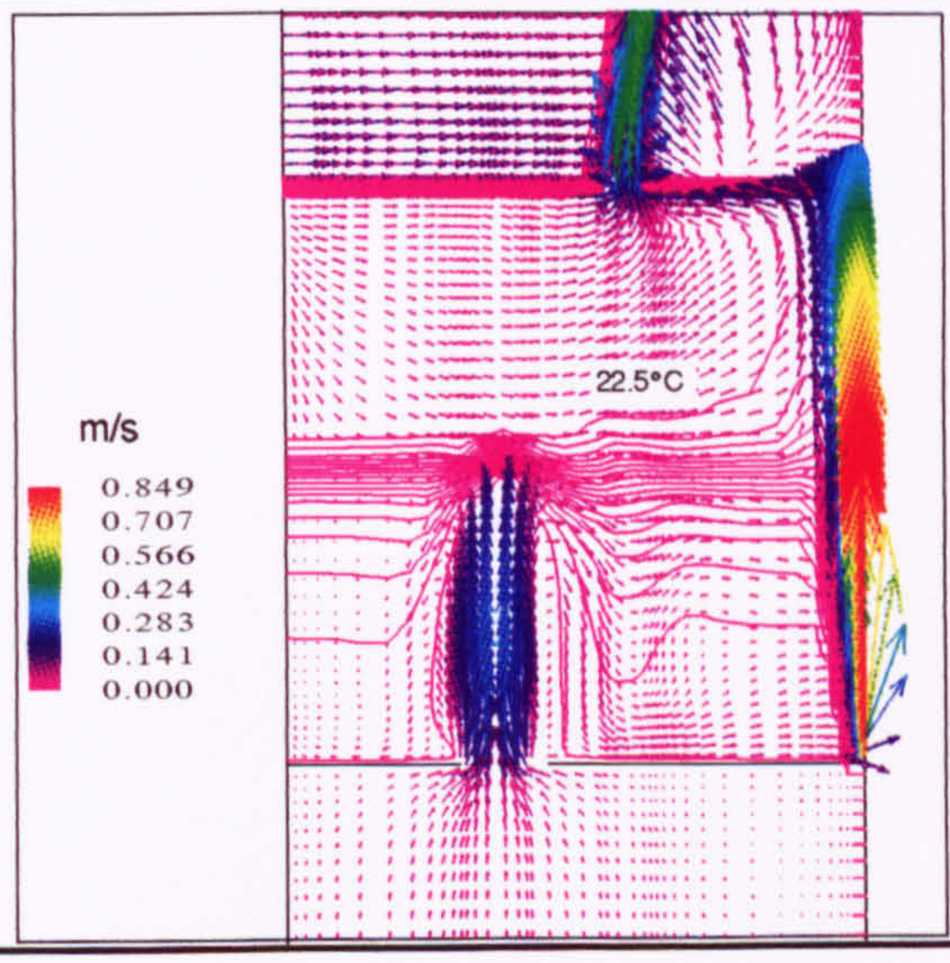

8.3.1 Two Dimensional Modelling

Benchmark 1 provided a 2D preliminary study to the 3D case investigated in Benchmark 2. The only differences between the 2D and 3D simulation results were the slightly higher values for interface height and stratification strength which were thought to be caused by a combination of lower entrainment prediction in Benchmark 2, and larger momentum forces acting on the interface, pushing it upwards, also in Benchmark 2. Possible causes for these discrepancies are as follows.

2D simulations are conducted by taking a slice in the *x*-y plane through a geometry that is assumed to be infinite and unchanging in the z direction. The main misrepresentation in the 2D model was therefore the definition of openings, which appeared as square openings in the 3D simulations but had to be represented as infinitely long slots in the 2D model (still retaining the same area per metre length of the geometry normal to the slice). This gave rise to a higher momentum force per unit volume in Benchmark 2 than Benchmark 1. The second 2D modelling limitation was the inability to represent the walls of the room at the high- and low-*z* faces, which caused a reduction in entrainment in this region and therefore a higher interface.

It was concluded that these modelling limitations were an acceptable trade-off against the short running time as a means of obtaining a good approximation to the flow, and learning much about how to model buoyancy-driven flows.

8.3.2 Flow Pattern

All three benchmarks produced the overall flow pattern observed by Linden et al. (1990). That is, a buoyant plume formed above the heat source which caused a layer of warm air to accumulate in the upper region of the space. This layer drove a flow out through the upper openings since the hydrostatic pressure difference between the top and bottom of the layer inside the space was smaller than that between the same levels outside the space. The buoyancy force driving this flow can be thought of as a *reduced gravity* force, g', where

$$g' = g\beta(T_u - T_a) \tag{8-2}$$

where: T_u = temperature of air in the upper region of the box, and

T_a = ambient (outside) air temperature.

As the air leaves the space through the upper openings, cooler, ambient air enters via the lower openings and is entrained into the plume. It was shown by Linden et al. (1990), that as the plume entrained the lighter, warmer air that was being recirculated in the upper part of the space, a *steady-state* was produced. This was verified by the CFD simulations since a *converged* solution was successfully found when solving the steady-state equations. The steady-state result successfully predicted a clear interface separating the well mixed, warm buoyant air above from the cooler, ambient air below.

The main discrepancy in the qualitative flow pattern between the work of Linden et al. (1990) and the three CFD benchmarks is the orderly (less random) nature of the flow below the interface in the CFD predictions compared with the more random appearance observed in the salt bath experiments. One of the aspects of this is a dominant incoming flow of ambient air which impinges on the interface potentially causing it to rise in that region, resulting in a non-horizontal interface. These momentum forces are also thought to be responsible for encouraging some entrainment of warmer air across the interface from the upper to the lower region. These effects are more noticeable in Benchmark 2, which is probably due to the larger momentum flux per unit volume entering the space in this case compared with benchmarks 1 and 3. This less random flow prediction should not be unexpected, since the random effects observed in the salt bath experiments are thought to be time-dependent and so will not be accurately modelled by the steady-state form of the governing flow equations used in this research. It is possible that any short-term transient effects that occurred in the salt bath modelling experiments could be 'hidden' in the CFD simulations by the use of false time-stepping. Recall that without imposing false time-stepping, a good approximation to the flow was obtained with *oscillations on the absolute values*. Such oscillations may be a manifestation of these short-term transient effects.

There is also concern that the incoming air is impinging on the buoyant plume close to its base which may affect its development in terms of volume and buoyancy flux. In benchmarks 1 and 2 there is slight concern over the large recirculation flow above the interface, caused by the line plume, which impinges on the interface close to the left-hand wall which may be forcing it downwards in that region. A simulation in Chapter 5 of a wider space eliminated both the momentum impingement above the interface and the impingement of incoming air at the base of the plume. The results predicted a slightly higher interface which could be attributed to either of these effects, although the more likely cause is the reduction in impingement on the upper side of the interface close to the left-hand wall since the interface had become more horizontal in this region.

8.3.3 Plume Modelling

Fundamental to the successful prediction of buoyancy-driven displacement ventilation flows is the accurate modelling of the plume. Consequently much time was devoted to analysing the accuracy with which the CFD model was able to predict the various aspects of a buoyant plume. The two main properties governing a plume are its volume flux, $M_{(L)}$, and its reduced gravity, or buoyancy, G'. Both these properties are functions of the plume entrainment $\alpha_{G,T}$ which relates the velocity into a plume with the velocity on the plume axis at that height, thus it determines the rate of spread of the plume. For mathematical ease, 'top-hat' profiles were assumed for the velocity and buoyancy in the plume with which has been associated a 'top-hat entrainment' α_T such that $\alpha_T = b_T/y$ (2D) (Eq. B-29), and $\alpha_T = 5b_T/6y$ (3D) (Eq. 3-11).

The value used for α_T by Linden et al. (1990) in their analytical work was 0.1. It should be noted that this is an empirical value which is very difficult to measure and various values have been found by others. For example, Morton et al. (1956) measured $\alpha_T = 0.13$, Rouse et al. (1952) measured $\alpha_T = 0.12$, and Baines and Turner (1969) measured $\alpha_T = 0.14$. There is also no evidence to suggest that entrainment should be the same for point and line source plumes.

For all three benchmarks, the RNG $k-\varepsilon$ model predicted a lower rate of entrainment, closer to that assumed in the theory, than the standard $k-\varepsilon$ model (c.f. tables 8.1 and 8.2). This resulted in a smaller value of plume volume flux and a larger value of plume buoyancy. All the CFD simulations predicted larger entrainment values than that used by Linden et al. (1990).

The linear variation of plume volume flux with height, indicated by the governing equations for a line plume, was accurately reproduced by the CFD simulations of benchmarks 1 and 2. The differences in gradient between the theoretical and the CFD lines are caused by the different predictions of entrainment, and the horizontal 'shift' in the graphs is thought to be caused by the virtual origin effect which predicts a non-zero volume flux at $y = 0$. All benchmarks predicted virtual origins in the range $-0.15 < y^{k-\varepsilon} < -0.1$ and $-0.22 < y^{RNG} < -0.12$, for the standard and RNG $k-\varepsilon$ models respectively.

The governing equations for a plume emanating from a point source predict a linear variation between volume flux and $(\text{height})^{5/3}$. Although not as robust as the linear relationships in benchmarks 1 and 2, this was modelled well by the simulation results of Benchmark 3. The slight non-linearities in Benchmark 3 (Fig. 7.12) are thought to be due to small instabilities in the plume caused by the 'three-sided entrainment', rather than the 'single-sided entrainment' in benchmarks 1 and 2 (Fig. 8.2).

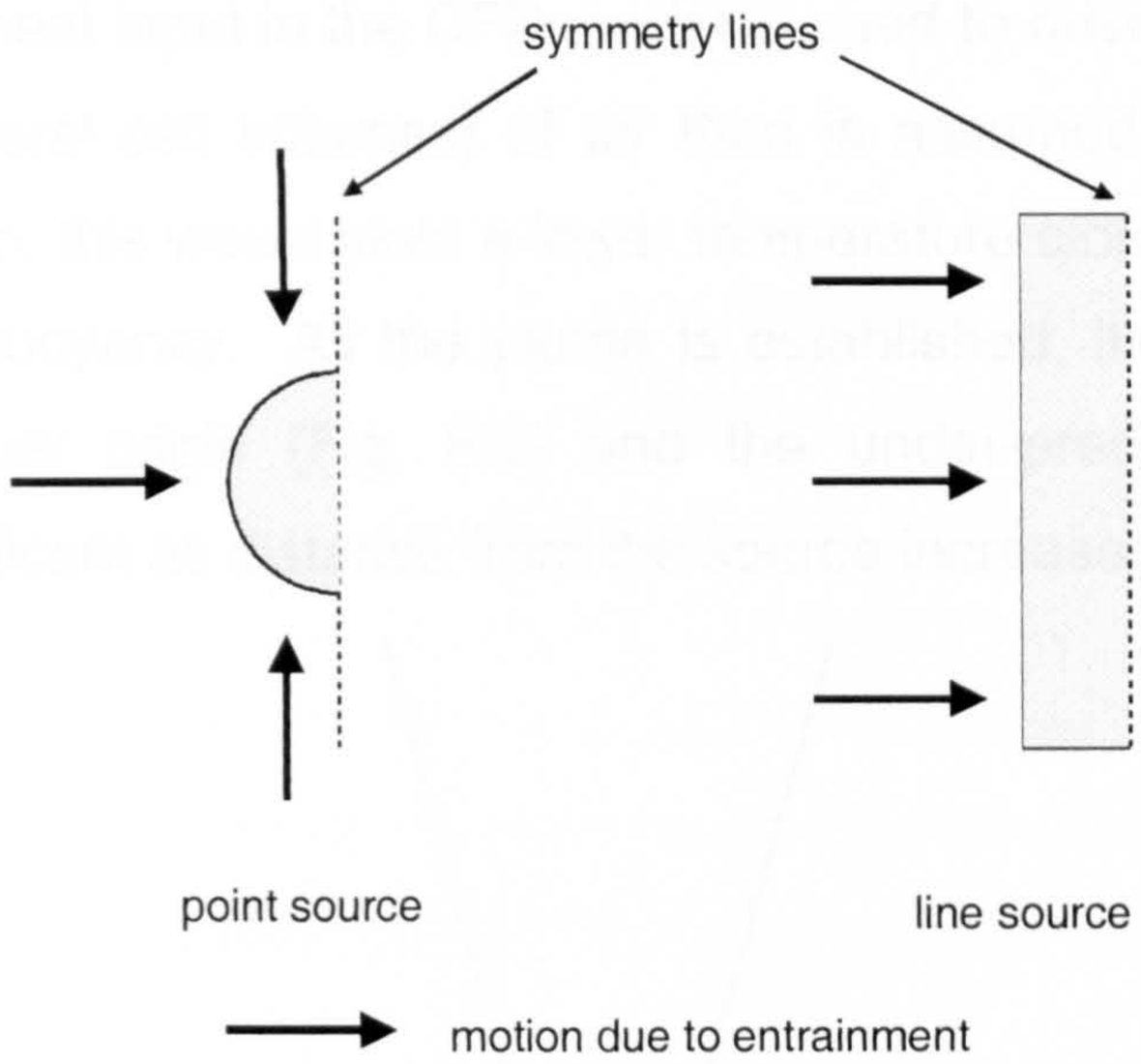

Figure 8.2 Plume entrainment viewed from above.

The variation of plume buoyancy with height is poorly predicted by all three benchmarks. Table 8.4 shows the predicted theoretical relationship between G'_T and height above the source, y, for plumes from line and point sources, and the equations of the curves fitted to the CFD predictions.

Table 8.4 Predicted variations of plume buoyancy with height above the source.

	Line source	Point source
Theory (Linden et al. (1990)	$G'_T = 0.09y^{-1}$	$G'_T = 0.269y^{-5/3}$
CFD ($k-\varepsilon$)	$G'_T = 0.050y^{-0.6}$ (*)	$G'_T = 0.155y^{-1}$
CFD (RNG)	$G'_T = 0.056y^{-0.57}$ (*)	$G'_T = 0.190y^{-0.9}$

(*) Separate expressions for benchmarks 1 and 2 have not been included as the fitted curves were almost identical.

The discrepancies in the coefficient values can mainly be attributed to the different predictions of entrainment. The major cause for concern lies in the 'shape' of the variation of G'_T with y, given by the index of y. Although further investigation is needed, it is thought that these discrepancies could be caused by the virtual origin effect. All of the plume equations presented in Chapter 3 assume either an infinitesimally narrow line source or an infinitesimally small point source. This was not possible in a CFD model due to the finite nature of the computational mesh.

Consequently, the heat input in the CFD model is used to raise the buoyancy of a larger volume (several cell volumes) of air than is assumed in the theory. By energy conservation, this would yield a lower temperature close to the source and therefore a lower buoyancy. As the plume is established, its shape assumes a source at the virtual origin (Fig. 8.3) and the under-prediction of buoyancy becomes less significant as distance from the source increases.

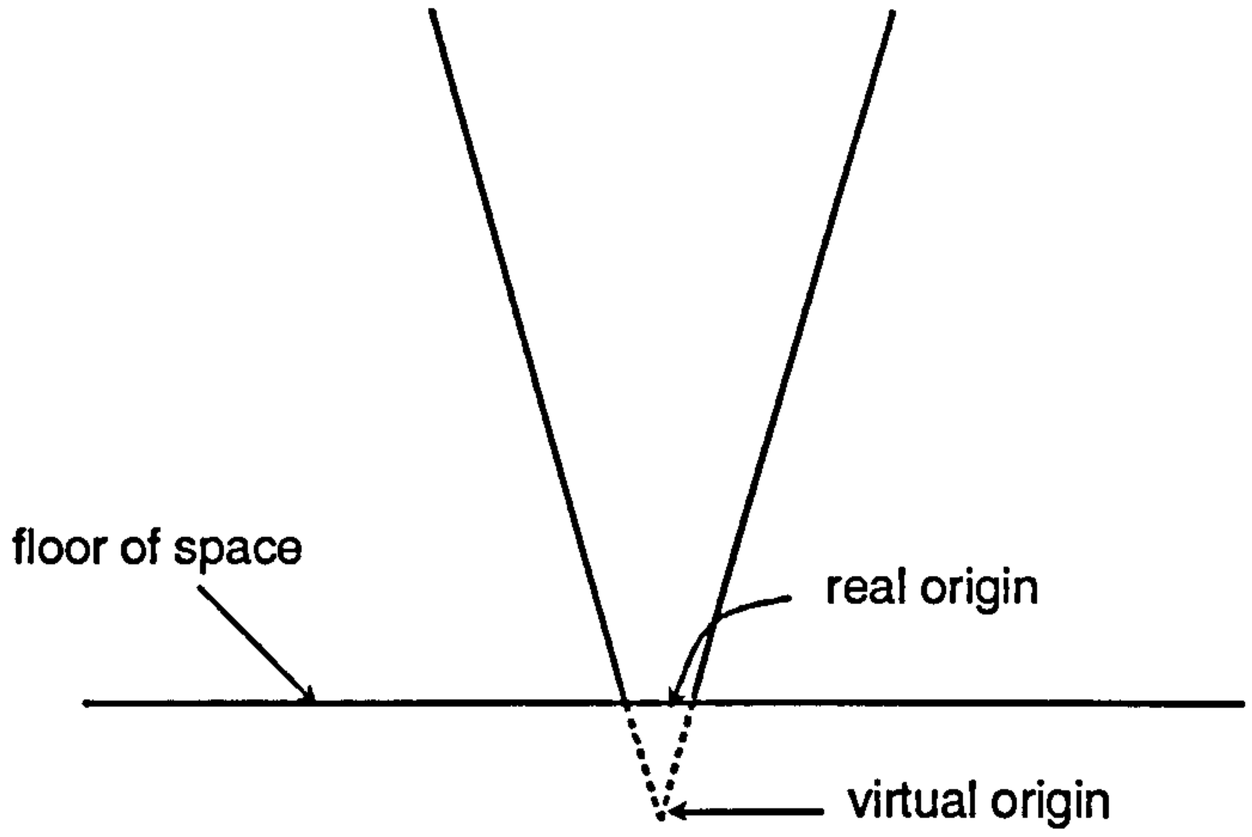

Figure 8.3 Shape of buoyant plume.

This would result in a different gradient function ($\partial G'_T / \partial y$) than that predicted, but nevertheless produces favourable agreement with the theoretical solution for g'_h since this is equal to $G'_T(y = h)$ which is the largest vertical distance from the source in the buoyant plume where the under-prediction of buoyancy is thought to be least significant.

8.3.4 Interface Parameters and Effect of Opening Size

The parameters used to define the interface produced by the displacement flow are the interface height, h, and the change in buoyancy across the interface, g'_h, also referred to as the strength of the stratification. Throughout this work, to enable comparisons with the work of Linden et al. (1990), these parameters have been normalised with respect to the height of the space, H, and the plume buoyancy, G'_H, at (the hypothetical) height $y = H$.

All but three simulations predicted *lower* interface heights and higher stratification strengths than the theory. These two findings are self-consistent with the

relationship $g'_h / G'_H = H / h$ (2D, Eq. (3-29)) and $g'_h / G'_H = (H / h)^{5/3}$ (3D, Eq. (3-24)).

The interface is formed when a steady-state flow has established in which the volume flux in the plume is equal to that leaving or entering the space. The interface height can therefore be thought of as that height at which there is least vertical motion *outside the plume*. In the flow patterns predicted by the CFD results, there was evidence of motion across the interface from the upper to the lower zone, thought to be caused by momentum impingement of the incoming air on the interface which entrained some of the air above the interface into the lower zone.

Since a lower entrainment rate was predicted by the RNG $k-\varepsilon$ model than by the standard $k-\varepsilon$ model, it took a longer vertical distance for the plume modelled using the RNG model to attain the volume flux of that passing through the space, consequently the interface predicted by the RNG turbulence model is higher. A corresponding effect is not observed in the stratification strength due to the cancelling effect between the interface heights and entrainment values predicted by the two turbulence models. This phenomenon was explained in detail in section 5.7.

The main factor thought to be responsible for the discrepancies between the CFD results and the theoretical line is an inaccuracy in the definition of the effective opening area $A^*_{(L)}$ established by Linden et al. (1990) which has also been used when calculating the effective opening area used in the CFD simulations. This could be the cause of discrepancies between the theoretical predictions and the salt bath model results. It is therefore interesting to note the similarity in predictions between the CFD and the experimental results (Figs. 5.28, 6.27 and 7.23).

The formula used to calculate $A^*_{(L)}$ incorporated the drop in pressure head as fluid *enters* the space (variable *c* in Eq. (3-19)), but neglected the effect as the fluid *leaves* the space through the upper openings. The modified expression ($A^{**}_{(L)}$)

was included in a more recent paper by Linden and Cooper (1996) and takes the form

$$A_{(L)}^{\bullet\bullet} = \frac{C_d a_u a_l}{\left[\frac{1}{2}\left(\frac{C_d^2}{c} a_u^2 + a_l^2\right)\right]^{1/2}} \tag{8-3}$$

where: a_u = total area of upper openings;

a_l = total area of lower openings;

C_d = discharge coefficient at the upper openings; and

c = discharge coefficient at the lower openings.

When assuming values of 0.61 for both discharge coefficients (see Awbi (1994), §3.1) the modified results for the salt bath experiments and CFD simulations agree more favourably with the theory (Figs. 8.4 - 8.9).

However, the interface height is still under-predicted in many of the cases where the standard $k-\varepsilon$ model is used, particularly in Benchmark 3. Two possible factors contributing to this discrepancy lie in the area of plume modelling. Firstly the theory with which the experimental and CFD results are compared assumes an infinitesimally small point, or narrow line source as the origin of the plumes. Since the source bath experiments and CFD simulations possess virtual origins reflecting their finite source area, the interface height in the theoretical solution is effectively measured from a level *below* that used for measuring the CFD and experimental interface predictions. For the CFD model, this will result in an under-prediction of interface height in the range 0.1m to 0.22m ($0.039 < h/H < 0.086$).

The second issue lies in the value of plume entrainment. The reason for the standard $k-\varepsilon$ model predicting a lower interface height than the theory and the RNG $k-\varepsilon$ model is almost certainly due to its higher prediction of entrainment.

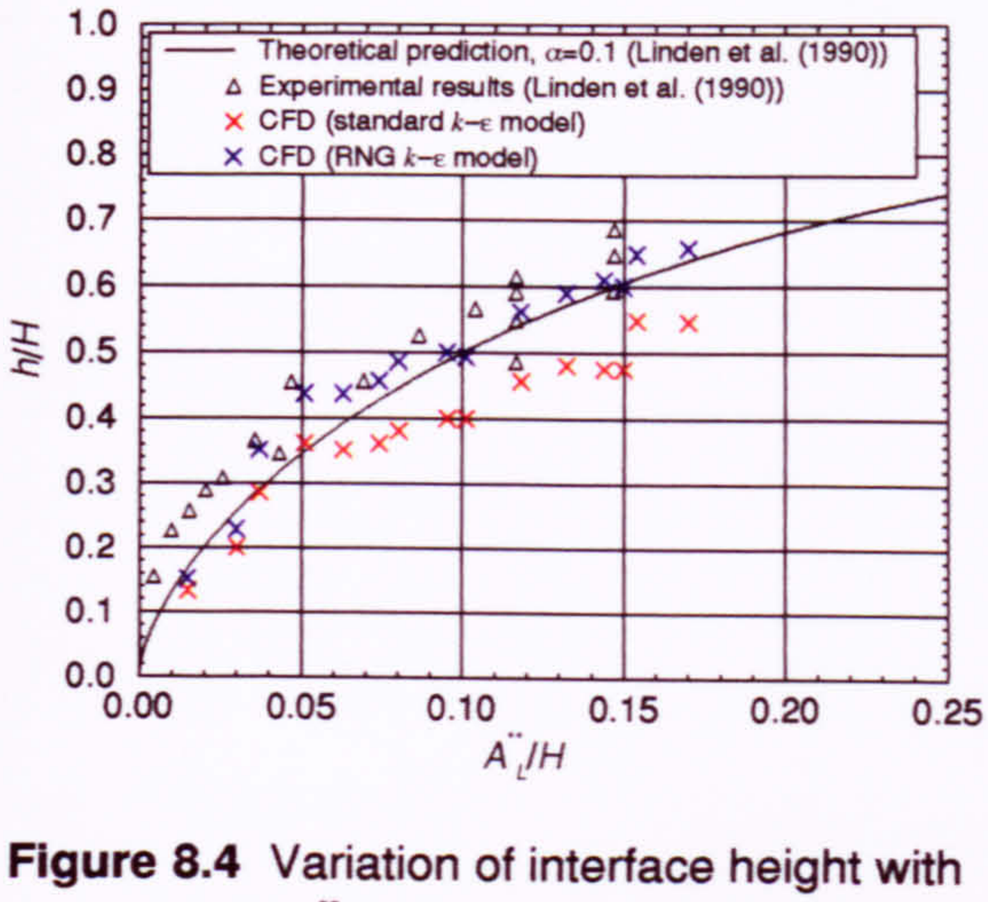

Figure 8.4 Variation of interface height with A_L^{**} (Benchmark 1).

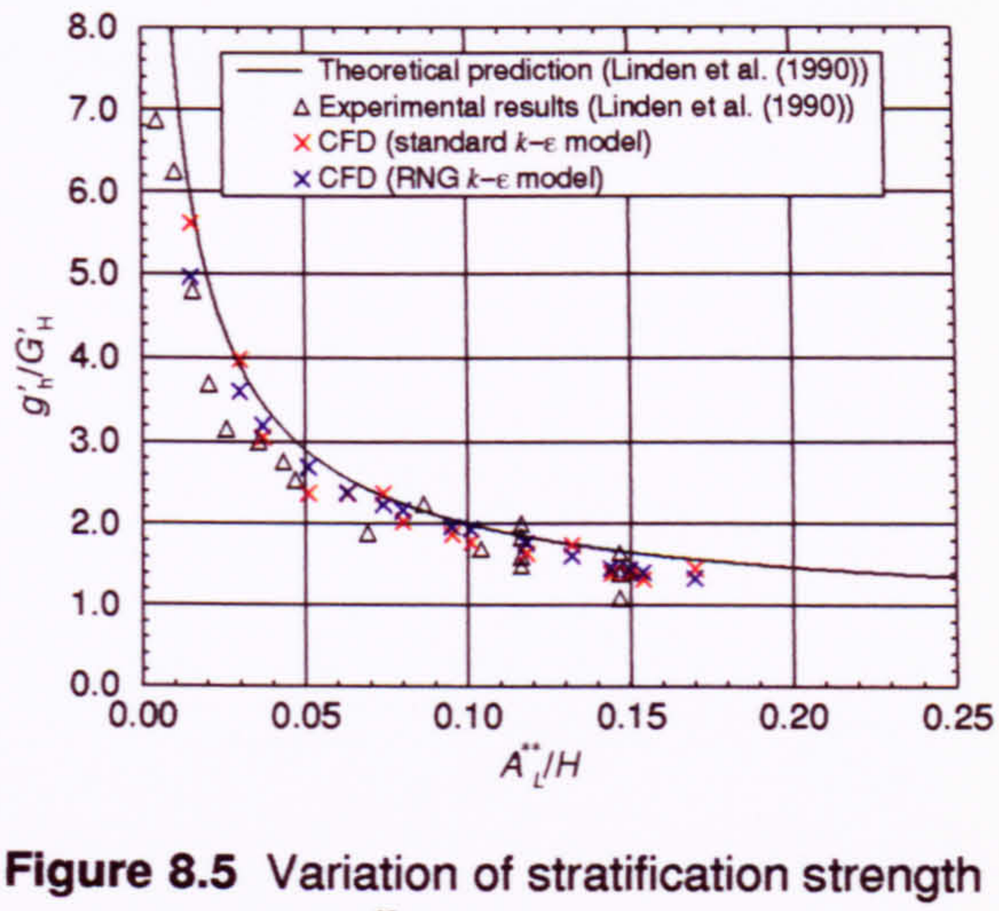

Figure 8.5 Variation of stratification strength with A_L^{**} (Benchmark 1).

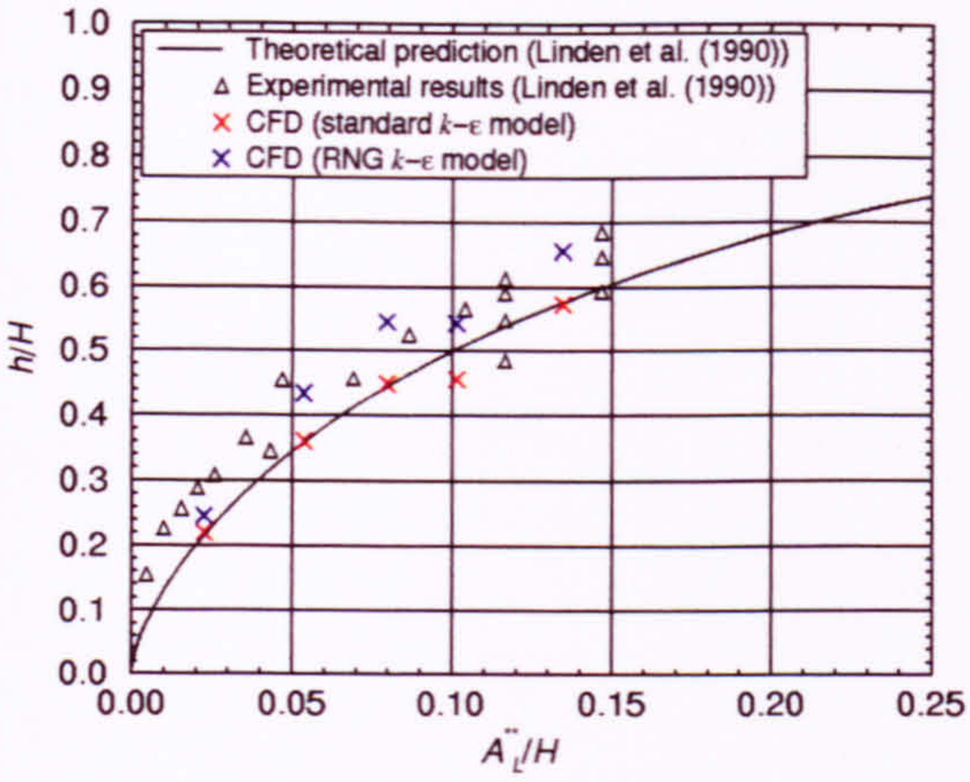

Figure 8.6 Variation of interface height with A_L^{**} (Benchmark 2).

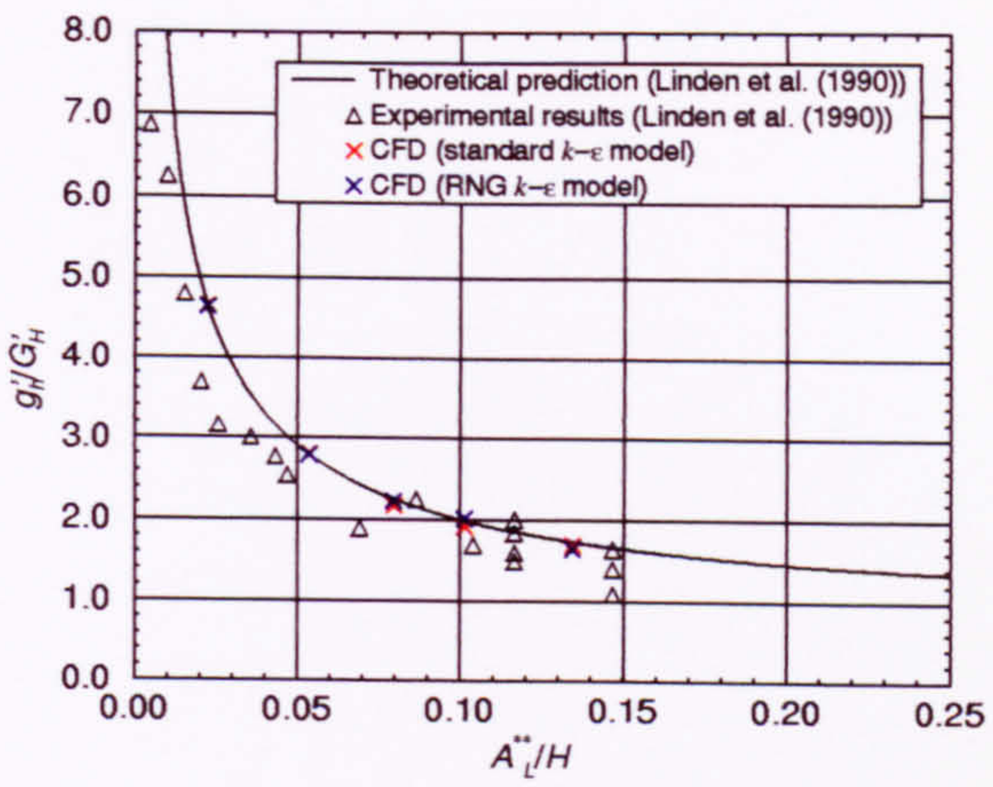

Figure 8.7 Variation of stratification strength with A_L^{**} (Benchmark 2).

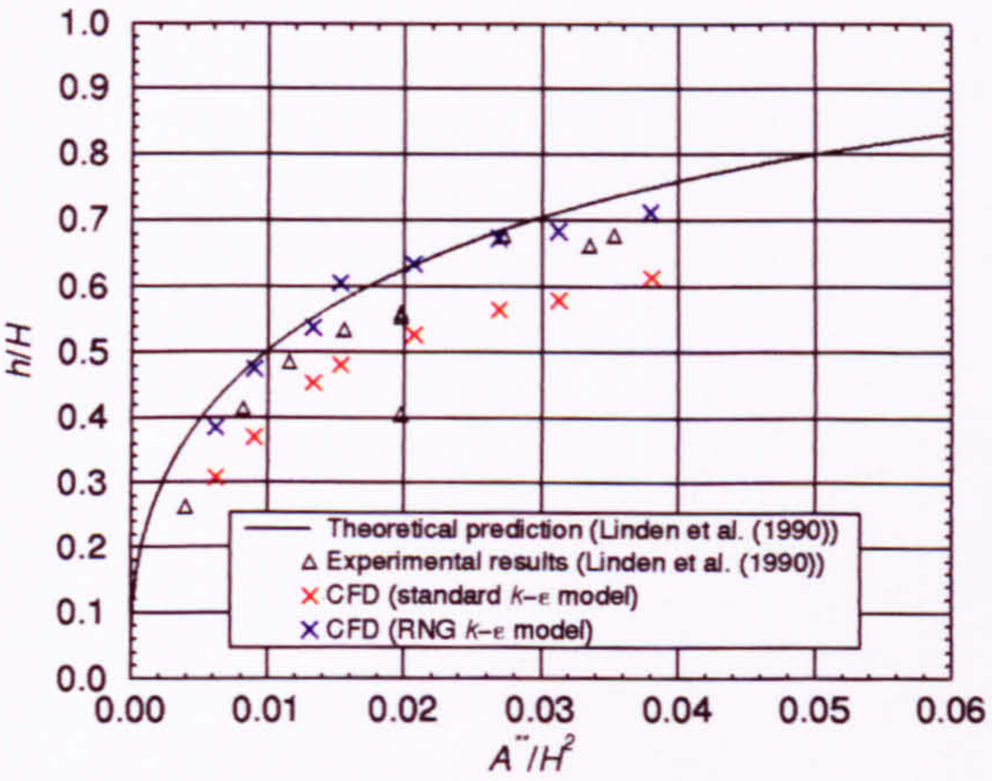

Figure 8.8 Variation of interface height with A^{**} (Benchmark 3).

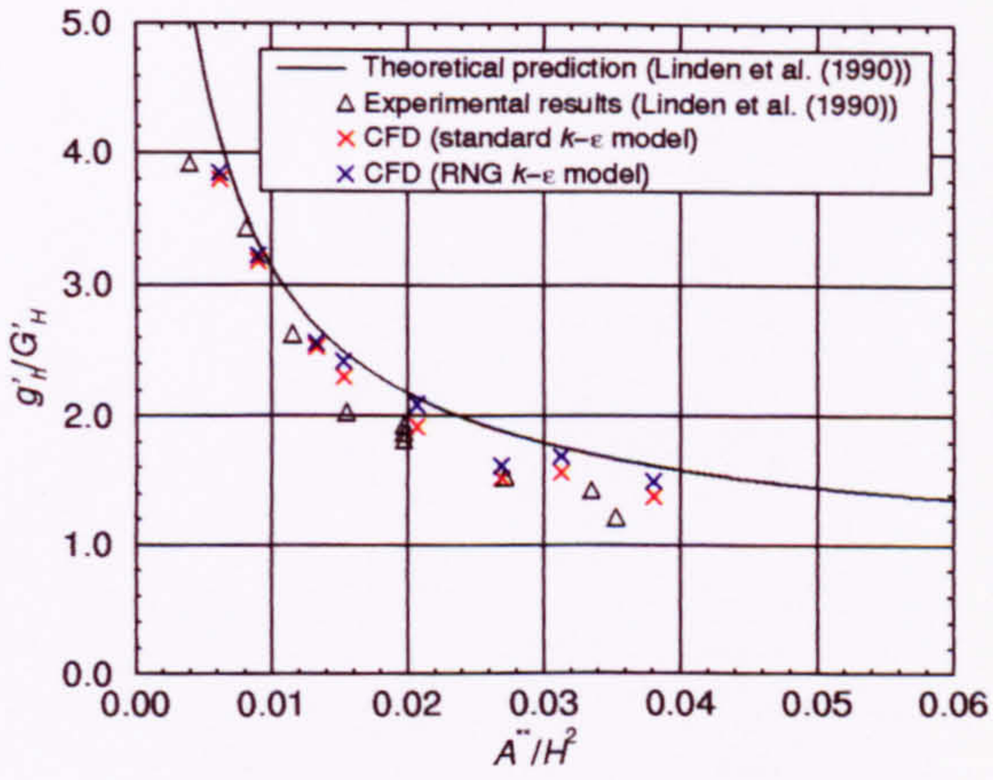

Figure 8.9 Variation of stratification strength with A^{**} (Benchmark 3).

The qualitative agreement between interface height and effective opening area, and between stratification strength and effective opening area is good. The slight non-'linearities' in the interface height predictions, (i.e. points that do not lie close to the curve of best fit), are thought to be caused by errors in identifying the interface height which was made difficult by the impingement on the interface of the incoming air momentum. This was less noticeable in Benchmark 3 in which there was a lower air change rate and therefore smaller momentum force impinging on the interface, and a stronger stratification, possibly able to withstand these momentum forces.

It is expected that the variations in plume entrainment will not cause dramatic changes in the predictions of ΔT_h due to the cancelling effect of the entrainment and interface height described in section 5.7.

8.3.5 Turbulence Modelling

The results have shown that different values for plume entrainment have been predicted by the two turbulence models. This is thought to cause different interface heights and air change rates (c.f. tables 8.2 and 8.3). Both turbulence models used employ the *eddy viscosity* concept whereby an enhancement to the laminar viscosity (μ_l) is used, known as the turbulent or eddy viscosity μ_t, resulting in an effective viscosity μ_{eff} :

$$\mu_{eff} = \mu_l + \mu_t \qquad \text{(Eq. 4-38).}$$

The sole purpose of the turbulence models is then to find a value for μ_t by solving conservation equations for k and ε for use in the equation

$$\mu_t = \rho C_\mu \frac{k^2}{\varepsilon}. \qquad \text{(Eq. 4-44)}$$

It is therefore instructive to investigate the values of μ_t, k and ε predicted by the two turbulence models in order to establish the possible causes for the different predictions

It is evident from contour plots of μ_t for Benchmark 1 that the standard $k-\varepsilon$ model generally predicts larger values for the eddy viscosity than the RNG model (c.f. Figs. 8.10 and 8.11). By considering turbulence quantities along a vertical line in the plume (Figs. 8.12 and 8.13), it is observed that throughout most of the plume and after the plume has settled down (above $y \approx 0.4\text{m}$), the RNG model predicts a lower value for k and a higher value for ε. Coupled with a lower value for C_μ, this yields a lower value for the eddy viscosity (Fig. 8.14 and Eq. (4-44) above). Similar behaviour is observed along a horizontal line at $y = 0.65\text{m}$ above the floor of the space (Figs. 8.15 - 8.17).

One manifestation of the smaller viscosity predicted by the RNG model is that more energy is available to bring about a higher mean flow velocity (c.f. tables 8.2 and 8.3), since less is being dissipated into viscosity.

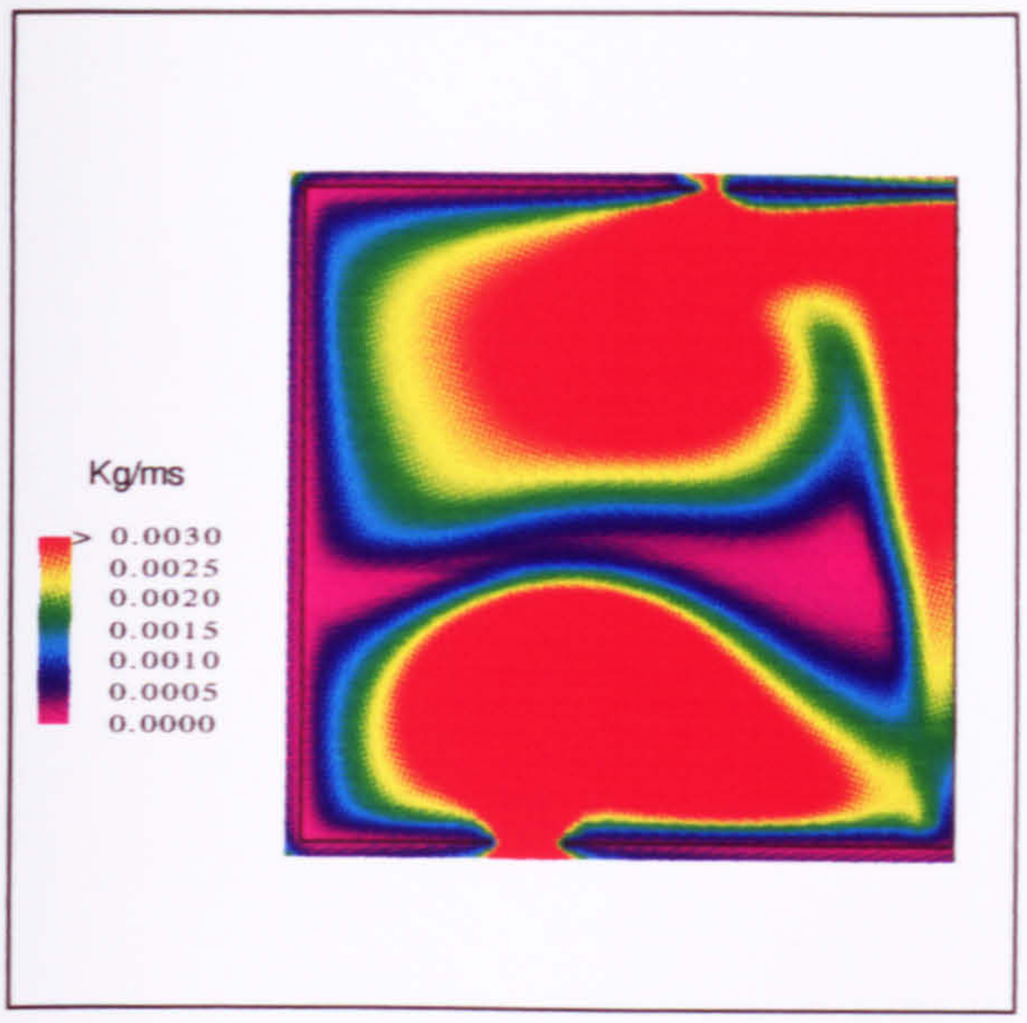

Figure 8.10 Eddy viscosity predicted by the standard $k-\varepsilon$ model (Benchmark 1).

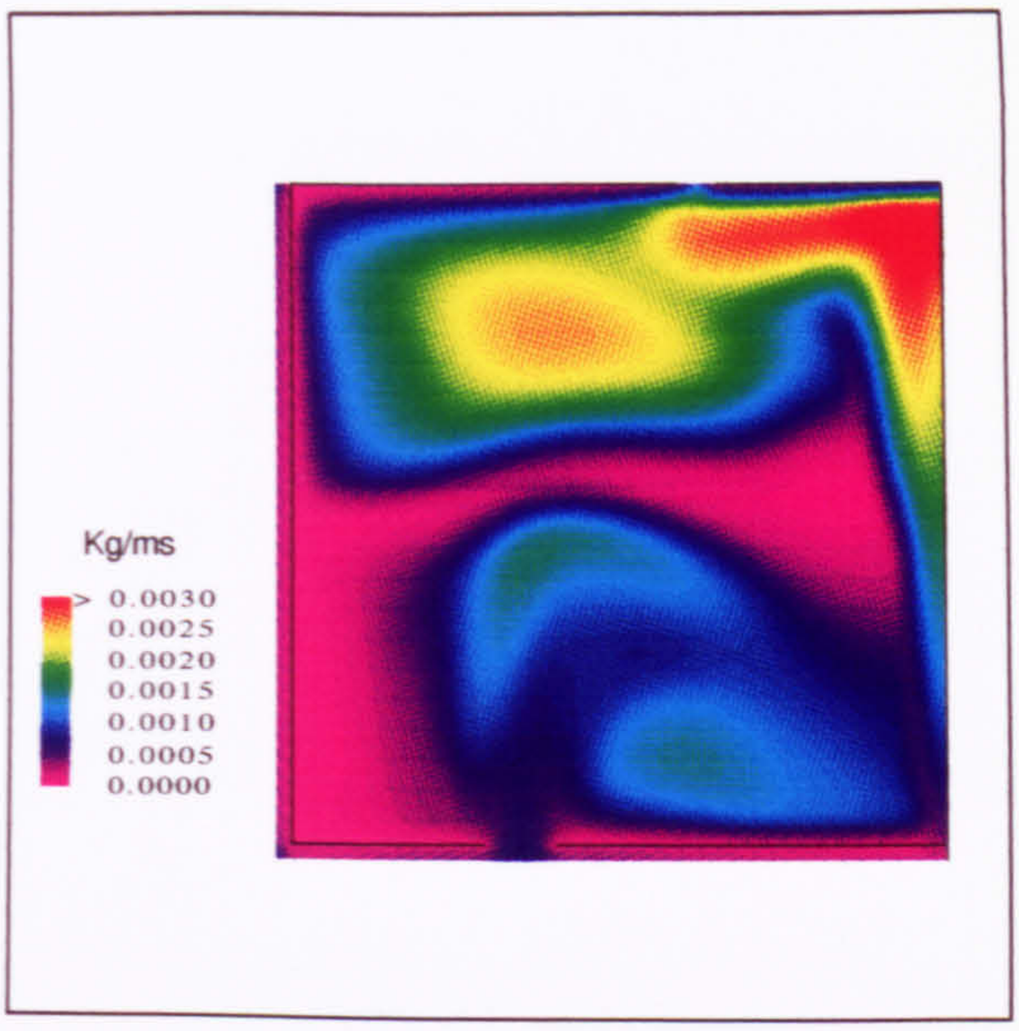

Figure 8.11 Eddy viscosity predicted by the RNG $k-\varepsilon$ model (Benchmark 1).

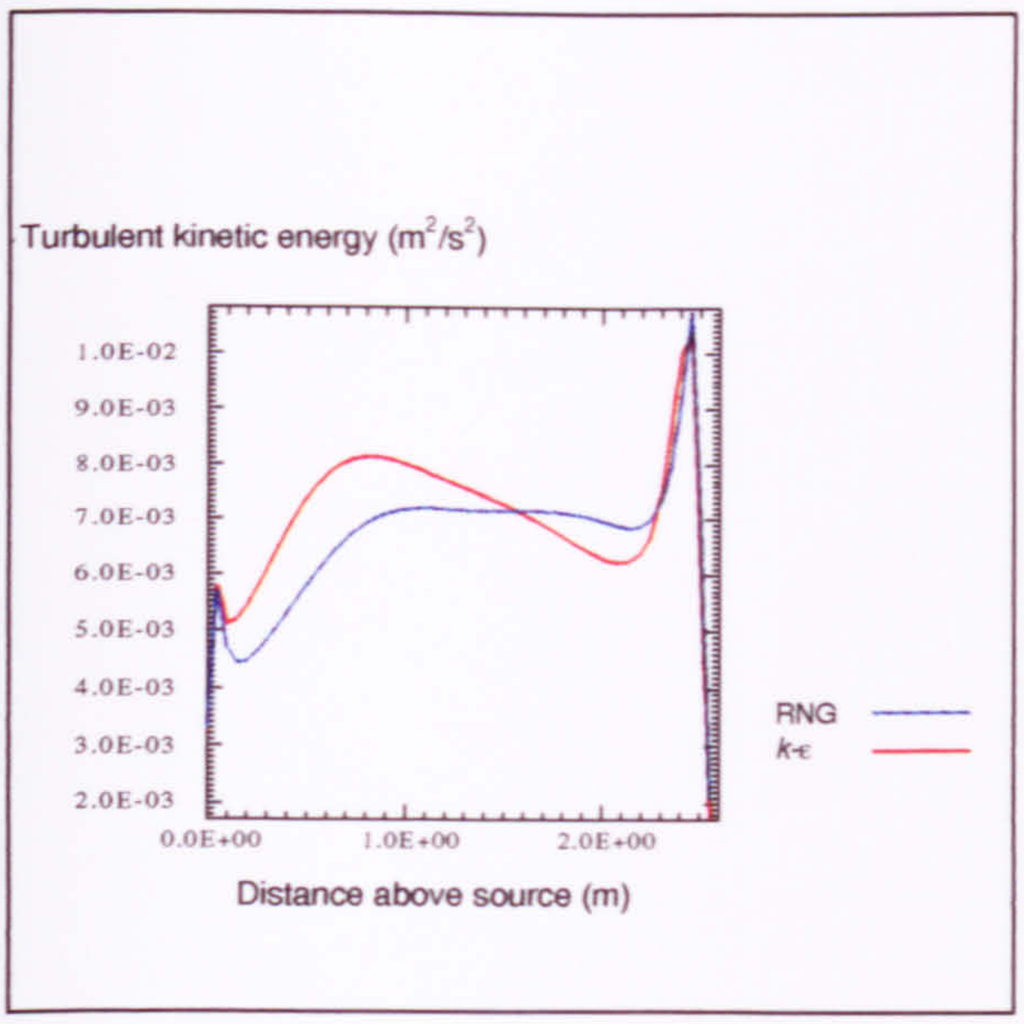

Figure 8.12 Predictions of turbulent kinetic energy along the plume axis (Benchmark 1).

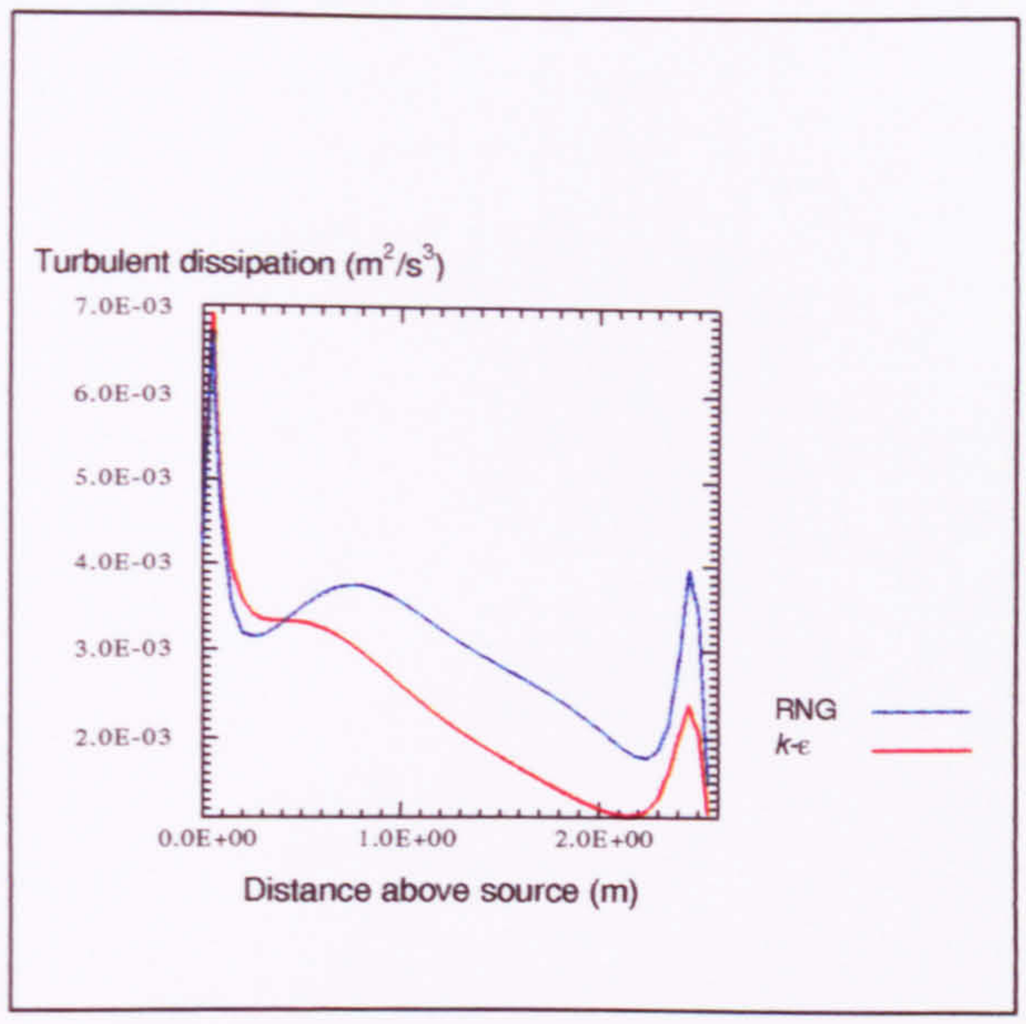

Figure 8.13 Predictions of turbulent dissipation along the plume axis (Benchmark 1).

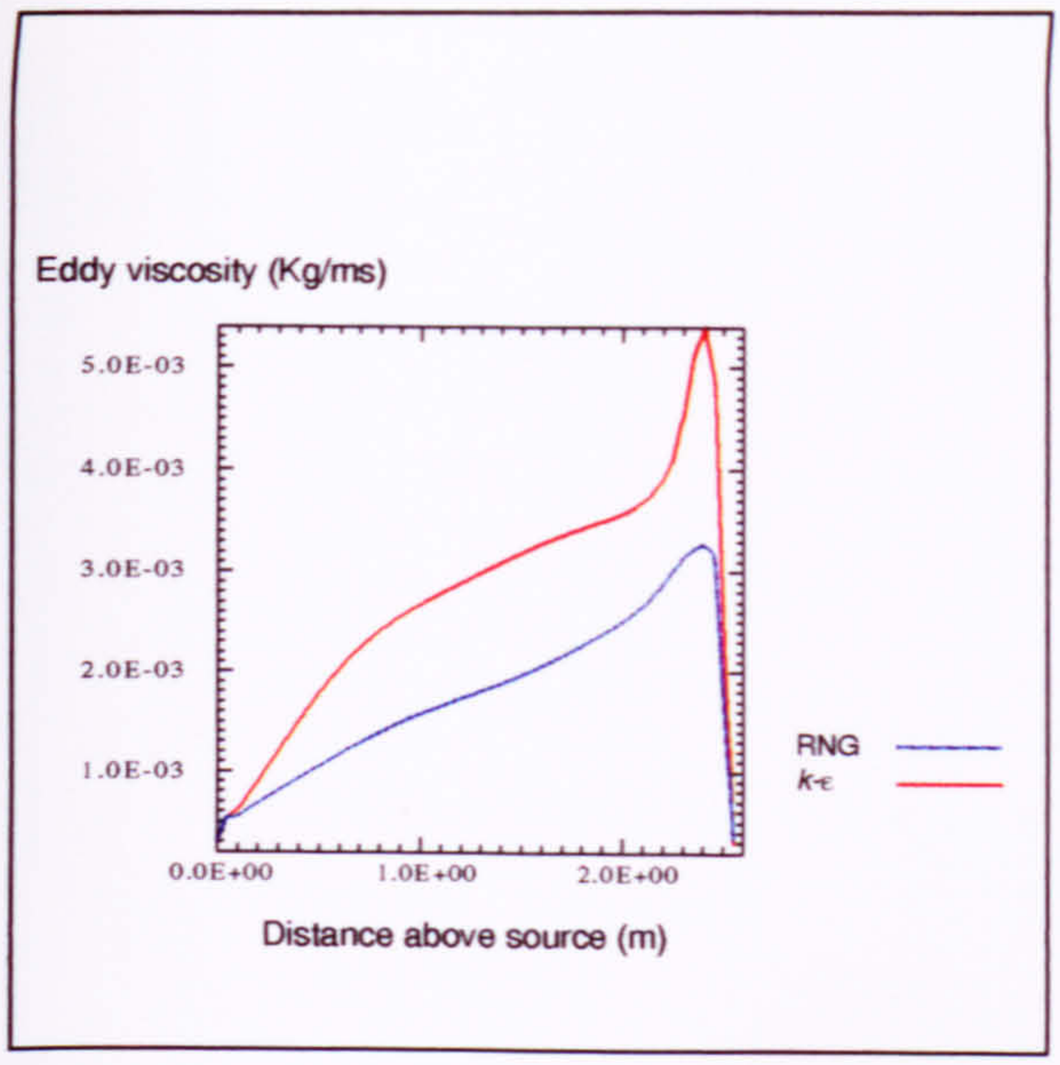

Figure 8.14 Predictions of eddy viscosity along the plume axis (Benchmark 1).

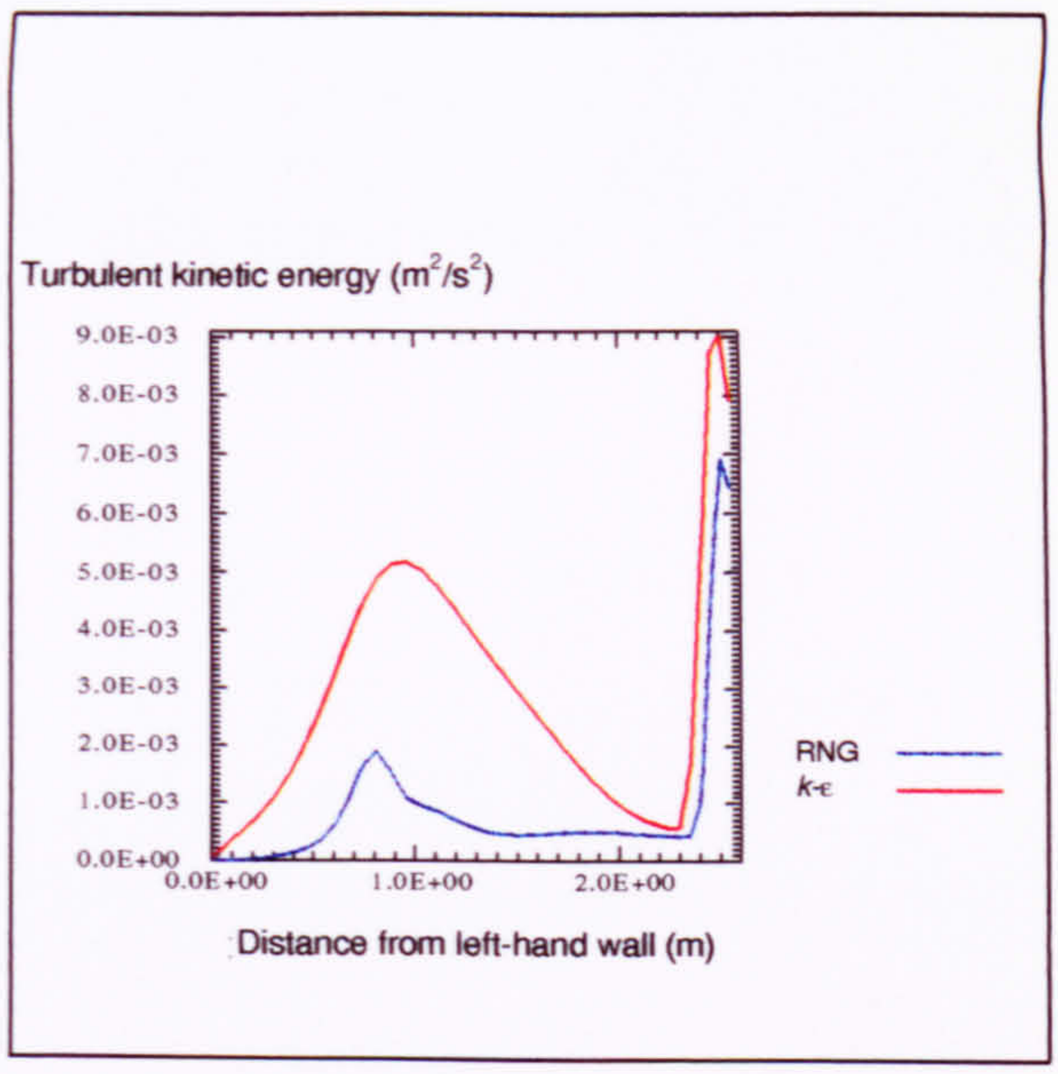

Figure 8.15 Predictions of turbulent kinetic energy along a horizontal line at 0.65m above the floor (Benchmark 1).

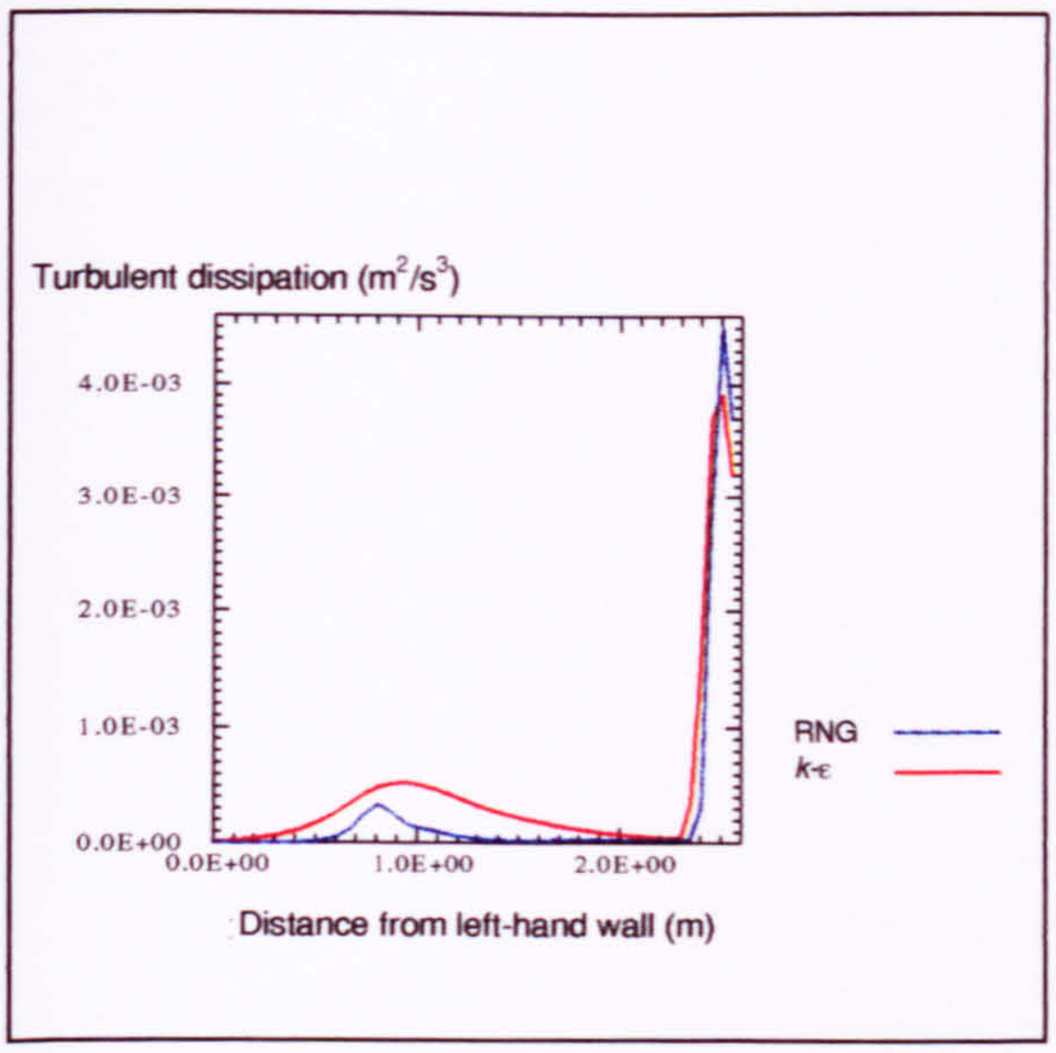

Figure 8.16 Predictions of turbulent dissipation along a horizontal line at 0.65m above the floor (Benchmark 1).

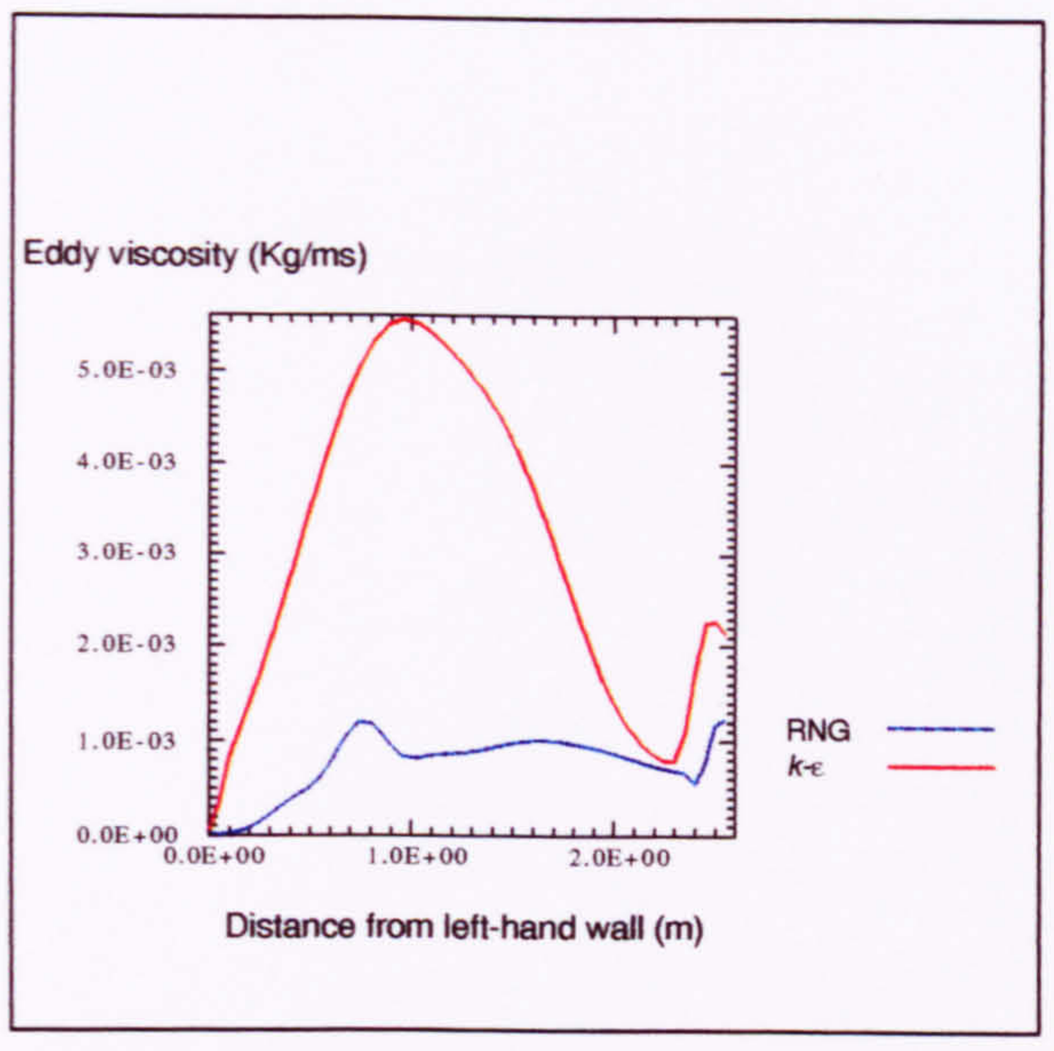

Figure 8.17 Predictions of eddy viscosity along a horizontal line at 0.65m above the floor (Benchmark 1).

An immediate consequence of the lower plume entrainment predicted by the RNG model is the narrower plume. This can be thought of as a lower transfer of energy normal to the flow direction (Fig. 8.18).

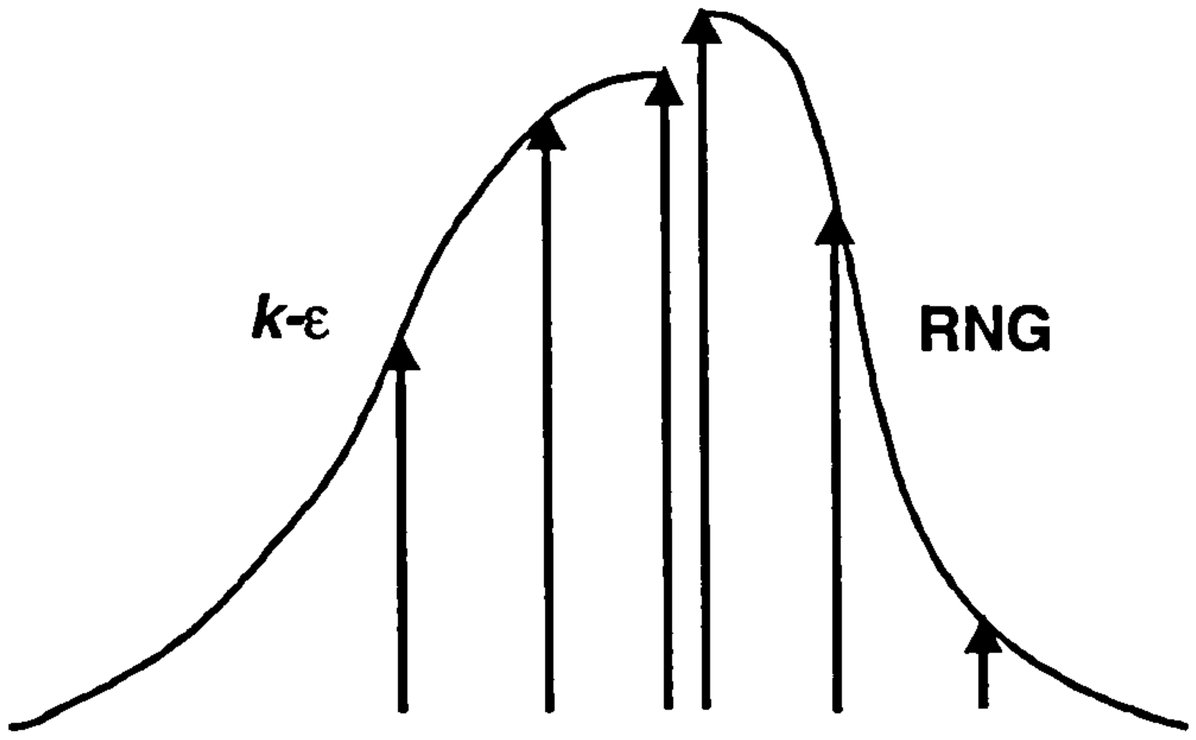

Figure 8.18 Comparison of vertical velocity profiles predicted by both turbulence models.

Transfer of energy in this way is the responsibility of the stress tensor σ_{ij} given by

$$\sigma_{ij} = -p\delta_{ij} + \mu_{eff}\left(\frac{\partial u_i}{\partial x_j} + \frac{\partial u_j}{\partial x_i}\right) \qquad \text{(Eq. 4-1).}$$

Since this is directly proportional to the effective viscosity, μ_{eff}, it follows that the RNG model should also predict a lower value of shear which would account for the narrower plume and the reduced entrainment.

As the source strength was increased, α_T reduced very slightly, causing a small rise in the interface. This could be due to a poorly mixed plume in which air on the axis of the plume is warmer that at its edge. More work is needed to investigate this.

Simulations were conducted for both turbulence models in which the additional buoyancy term in the ε equation was used ($C_3 = 1.0$ in equations 4-46 and 4-51), but the results produced negligible differences. The C_3 term takes the form

$$C_3 \max(G,0),$$

where

$$G = \frac{\mu_{eff}}{\sigma_{He_t}} \beta g \frac{\partial T}{\partial y}. \qquad \text{(Eq. (4-48))}$$

The term becomes non-zero when $G > 0$. For the latter to occur, $\partial T / \partial y$ must be negative, i.e. warm air must occur below cool air (thereby increasing turbulence dissipation as the warm air rises). Outside the plume, the vertical temperature gradient is positive which nullifies the C_3 term. However, where warm air occurs below cooler air in the plume, the term is invoked. Since the results showed only very small changes in the axial plume properties, it is concluded that this term is small relative to the other production terms in the ε equations (Eqs. (4-46) and (4-51)) and is not significant in determining a buoyancy-driven displacement ventilation flow pattern.

8.3.6 Effect of Source Strength

Linden et al. (1990) predicted that the interface height is independent of the source strength used. The CFD simulations showed that for source strengths between 50W and 1000W, the interface height varied slightly in some cases, namely 3D simulations, and those incorporating the RNG $k-\varepsilon$ model. The marginal discrepancies when using the RNG model were discussed briefly in §8.3.5. Other discrepancies may be due to instabilities in the 3D plume (§8.3.3).

From the theory it is seen that $g'_h / G'_H = (H/h)^{5/3}$ (point source) and $g'_h / G'_H = H/h$ (line source), (Eqs. (3-24) and (3-29)), i.e. the *normalised* stratification does not depend on the source strength. This was successfully predicted by the CFD simulations with only small perturbations. However, the value is not equal to $(H/h_{CFD})^{5/3}$ (point source) or H/h_{CFD} (line source) where h_{CFD} is the CFD-predicted interface height. This is caused by the difference between the entrainment predicted by the CFD model and that used in the normalisation. Due to this discrepancy, equations (3-24) and (3-29) should read

$$\left(\frac{g'_h}{G'_H}\right) = \left(\frac{H}{h_{CFD}}\right)^{5/3} \left(\frac{C_{Linden}}{C_{CFD}}\right)^{5/3} \tag{8-4}$$

and

$$\left(\frac{g'_h}{G'_H}\right) = \left(\frac{H}{h_{CFD}}\right) \left(\frac{D_{Linden}}{D_{CFD}}\right) \tag{8-5}$$

respectively, where the subscript Linden assumes the entrainment constant $\alpha_T = 0.1$ and subscript CFD assumes the entrainment constant predicted by the CFD model. Since the CFD model predicts a value of α_T greater than 0.1 in all cases, it follows from equations (8-4) and (8-5) that the CFD values calculated for g'_h / G'_H (tables 8.2 and 8.3) should be less than the values given by equations (3-24) and (3-29) when using the *CFD-predicted value* of interface height for *h*. This is indeed the case for all benchmarks except in Benchmark 2 when the RNG $k-\varepsilon$ model is used. The cause for this is thought to be due to impingement of incoming air on the interface causing a higher interface height.

The variation of plume volume flux with source strength is modelled well in the CFD simulations in all three benchmarks. The discrepancies in each case are readily attributable to the virtual origin issue and the difference in entrainment. The slight non-linearities in benchmarks 2 and 3 when using the RNG $k-\varepsilon$ model are thought to be caused by the lower predictions of eddy viscosity (§8.3.5) which produce less mixing - an effect which is amplified in three dimensions due to three-sided entrainment.

The relationship of plume buoyancy with source strength is also very well predicted subject to the discrepancies caused by the virtual origin and entrainment. This suggests that the inaccurate modelling of G'_T observed in the CFD simulations is an inability to accurately reproduce the G'_T vs. y relationship. This was discussed in section 8.3.3 where it was also attributed to the existence of the virtual origin.

In summary, the qualitative effects of increasing the source strength were accurately modelled in all benchmarks. That is, the interface remains largely unchanged, and the temperature change across the interface increases causing a higher air change rate through the space.

8.4 Application to Real Buildings

Using the knowledge gained by modelling the three benchmark cases, the following points are made concerning guidance on how to model buoyancy-driven flows in real buildings and the reliability of the results. It is not possible to give step-by-step guidance on how to model all applications of buoyancy-driven flows in buildings, as all cases are different. The points restate the lessons learned throughout this research in a more generic manner.

8.4.1 Guidance

a) Simplifying the Geometry

It is invaluable when using CFD to model building airflows to first run a 2D simulation of the flow. This may be inappropriate for complex, asymmetric geometries, but in simpler cases such as the benchmarks investigated in this research, it can provide a good approximation to the flow pattern and air change rates. However, care must be taken to ensure that opening sizes *per metre* in the direction normal to the 2D slice correspond to the available opening sizes in the real case.

Alternatively, it is often possible to model only a small zone of the geometry under consideration and use symmetry planes to represent adjoining zones. This is particularly useful when a steady-state solution is sought as it enforces symmetry where there may otherwise be small, but negligible, transient effects.

b) Boundary Conditions

In contrast to mechanically-driven ventilation, when flows are driven by natural forces, there is no explicit information available regarding air speeds and flow direction at inlets and outlets. Consequently it is difficult to select with confidence, the most suitable boundary conditions at openings that accurately account for the effects of stack (inside/outside temperature difference) and wind. One way of overcoming this is to extend the computational domain beyond these openings by modelling some of the

external air. In doing this, the user allows the CFD code to model the complex flow as air is contracted and then expanded when it passes either way through an opening. The amount of exterior modelled will normally be determined by available hardware, however, an extent of about 3m has been found sufficient by the author in many cases (see §8.4.3, for example). This leaves the user to specify the boundary conditions around the extended domain. Such boundaries can, for example, be used to specify a constant wind and its associated turbulence, or still conditions. The latter can be achieved by specifying a constant pressure around the entire boundary (provided the program's governing equations of momentum account for the pressure differences due to stack effect - $\Delta p = \rho g h$). However, in the absence of significant momentum forces, artificially high air speeds are likely to occur when two such pressure boundaries are located opposite one another, and to a lesser extent when they are adjacent. This phenomenon, explained in more detail in section 8.2.1, can be overcome by imposing zero velocity conditions at such boundaries. This is not thought to adversely affect the prediction of the flow inside the building itself.

c) Mesh Structure

This research has shown that in a space measuring $2.55\text{m} \times 2.55\text{m} \times 1\text{m}$, accurate results can be obtained using cell sizes of the order of $15\text{cm} \times 15\text{cm} \times 15\text{cm}$. Since flow predictions of real buildings are unlikely to be concerned with, for example, detailed predictions of plume behaviour and the *precise* location of stratification interfaces, it is felt that sufficiently accurate results could be obtained using larger cells, particularly in areas where the flow is unchanging. The more important parameter determining a mesh is likely to be hardware limitations. However, sufficient hardware power should be available to enable tests to be undertaken to ensure that grid refinement, in areas such as buoyant plumes and openings, does not significantly change the solution.

This research also confirmed the belief that highly skewed (non-orthogonal) cells should be avoided when modelling buoyancy-driven flows as they can cause instabilities in the solution algorithms.

d) Convergence Criteria

In all CFD simulations it is important to impose convergence criteria that ensure the mathematical model defined has been solved accurately. Suggestions for buoyancy-driven flows are that the flow variables being calculated are constant (say to within about 0.1% of some value), and that the equation errors (residuals) are small, for example that the enthalpy residual is less than about 1% of the total heat entering the domain. It is important to select the solution monitoring point such that maximum information can be gleaned from the values obtained. For example, in natural ventilation flows a suitable location would be in an opening where the flow is unlikely to settle until the overall flow has converged. Some CFD codes enable more than one monitoring point to be specified. This option should be exercised when simulating large geometries in which perturbations at one end of the solution domain may take several iterations to propagate throughout the mesh, or in which the CFD model is so large that significantly different flow patterns (and therefore convergence difficulties) may exist at different locations in the domain.

e) Obtaining a Solution

Long simulation times, of the order of several thousand iterations, should be expected when modelling buoyancy-driven flows. One should also anticipate instabilities in the solution when employing 'standard' under-relaxation techniques such as the default under-relaxation factors offered in CFX (mass equation: 1.0, momentum equation: 0.65, turbulence and enthalpy equations: 0.7). It is possible to overcome such problems by ensuring that the under-relaxation technique takes into consideration the time-scale over which the solution evolves. This can be done using a false time-stepping technique which specifies under-relaxation factors derived using a time-scale

(false time-step) and the local cell dimension. The difficulty lies in selecting the size of the false time-step. A sensitivity analysis carried out in this research suggested values of 0.1s on all momentum equations. Such values have been used successfully by the author in other, more complex simulations (see §8.4.3 for example). If convergence cannot be attained using these values, then smaller false time-steps, say 0.01s, should be investigated. However, it should be borne in mind that the use of such severe constraints will significantly increase simulation time. It is therefore more economical to run an initial simulation with no false time-stepping and when the best solution has been attained (no further reduction in residuals), invoke false time-stepping. If convergence cannot be attained using very small false time-steps (say $\leq$ 0.001s), then it is likely that the problem definition is ill-posed, or that there does not exist a steady-state solution.

8.4.2 Reliability of Results

Provided the simulation accurately represents the flow being considered, it is possible to obtain qualitatively accurate flow patterns of steady-state, buoyancy-driven flows. These, of course, do not depict any potential small scale transient effects. For example, incoming air may appear very pronounced, whereas in reality it might meander from side-to-side and periodically break up. This was observed in the three benchmark cases investigated in this research in which the CFD predicted a very dominant inflow of air, which is thought to have influenced stratification properties, whereas in the salt bath experiments the incoming fluid was not as pronounced. Although such effects are likely to be avoided in reality by the use of grilles over the openings, a transient simulation may provide a more detailed insight into the behaviour of the flow in such regions.

A source of error is likely to emanate from inaccuracies in modelling buoyant plumes which influence important flow parameters such as stratification heights and air change rates. This research has shown that plume entrainment, which affects the key properties of a plume, is dependent upon the turbulence model used. Although the differences were small, the RNG $k-\varepsilon$ model of Yakhot and

Orszag (1992) was found to give results closer to experimental measurement and analytical predictions. The standard $k-\varepsilon$ model of Launder and Spalding (1974) was found to over-predict entrainment. This may cause lower predictions of interface heights and higher air change rates. However, the differences are small. For example, in Benchmark 3 of this research (point source of buoyancy), the difference in interface height between the two turbulence models was about 12cm (4.7% of the height of the space), and the differences in air change rate was $0.17ach^{-1}$ (the standard $k-\varepsilon$ model predicted a rate that was 1.7% larger than that of the RNG $k-\varepsilon$ model).

8.4.3 Application Example

During this research, the author has been involved with several consultancy projects which have analysed the suitability of natural ventilation in proposed building designs (see bibliography).

A typical example was the proposal for a naturally ventilated IT centre at De Montfort University, Bedford (architects - Van Heyningen and Haward). CFD results for a section of the building are shown in figures 8.19 - 8.21. The building comprises four storeys of occupied space surrounding a central atrium. Fresh air provision is via an under-floor duct on the ground floor and clerestory level windows on floors 1,2 and 3. Trickle vents are also used on floors 1 to 3 which comprise pre-heating coils for winter ventilation. The flow is driven entirely by buoyancy forces brought about by constant heat sources distributed over each floor.

Due to time constraints and hardware limitations, a CFD simulation of the whole building was not feasible. Consequently a representative section of the building was analysed. In order to accurately reflect the dimensions and shape of the exhaust stack on the third floor, a 3D simulation comprising a 3.6m deep slice of the building was considered. Symmetry planes were then defined on each of the plane faces of the slice to reflect the full depth of the building. A symmetry plane

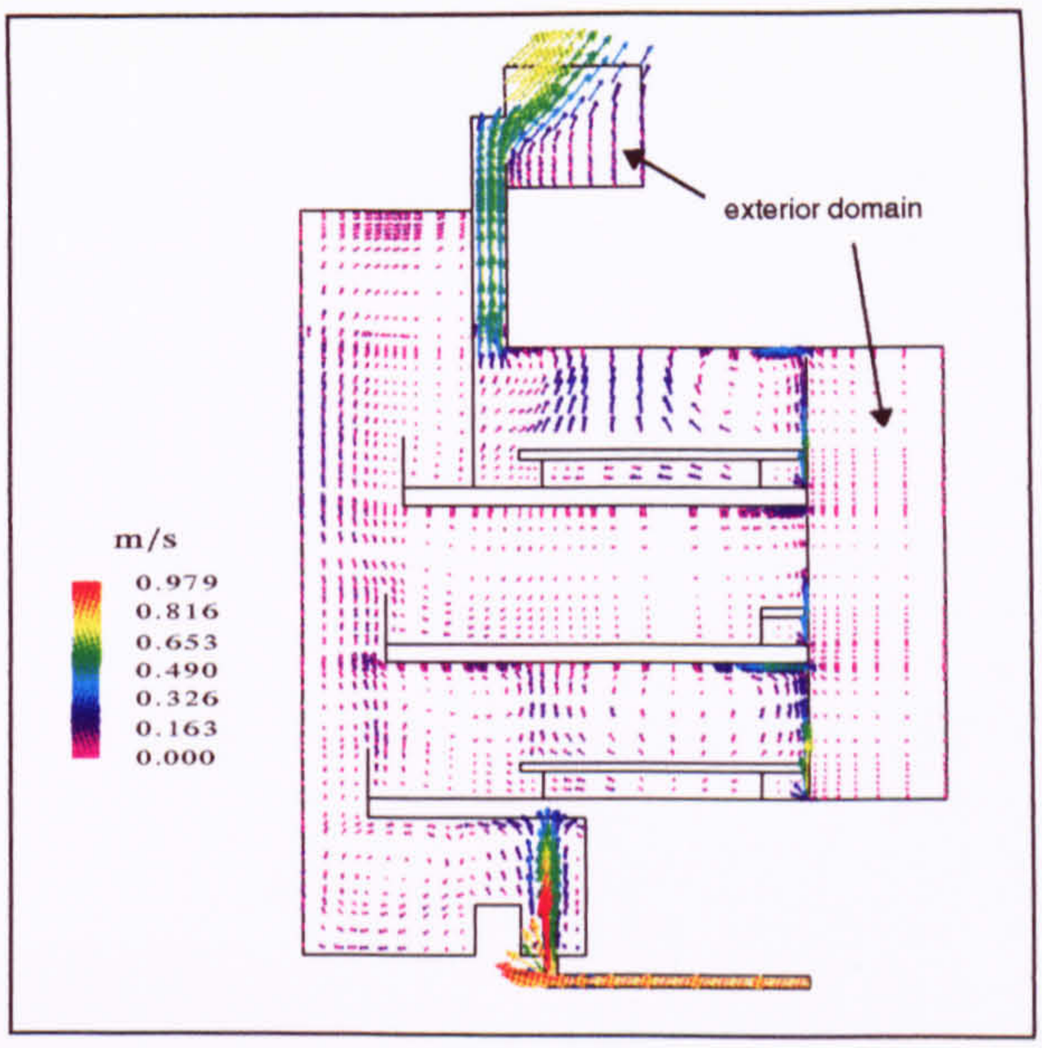

Figure 8.19 Predicted airflow distribution over the height of the building.
(Proposal for IT centre at De Montfort University, Bedford).

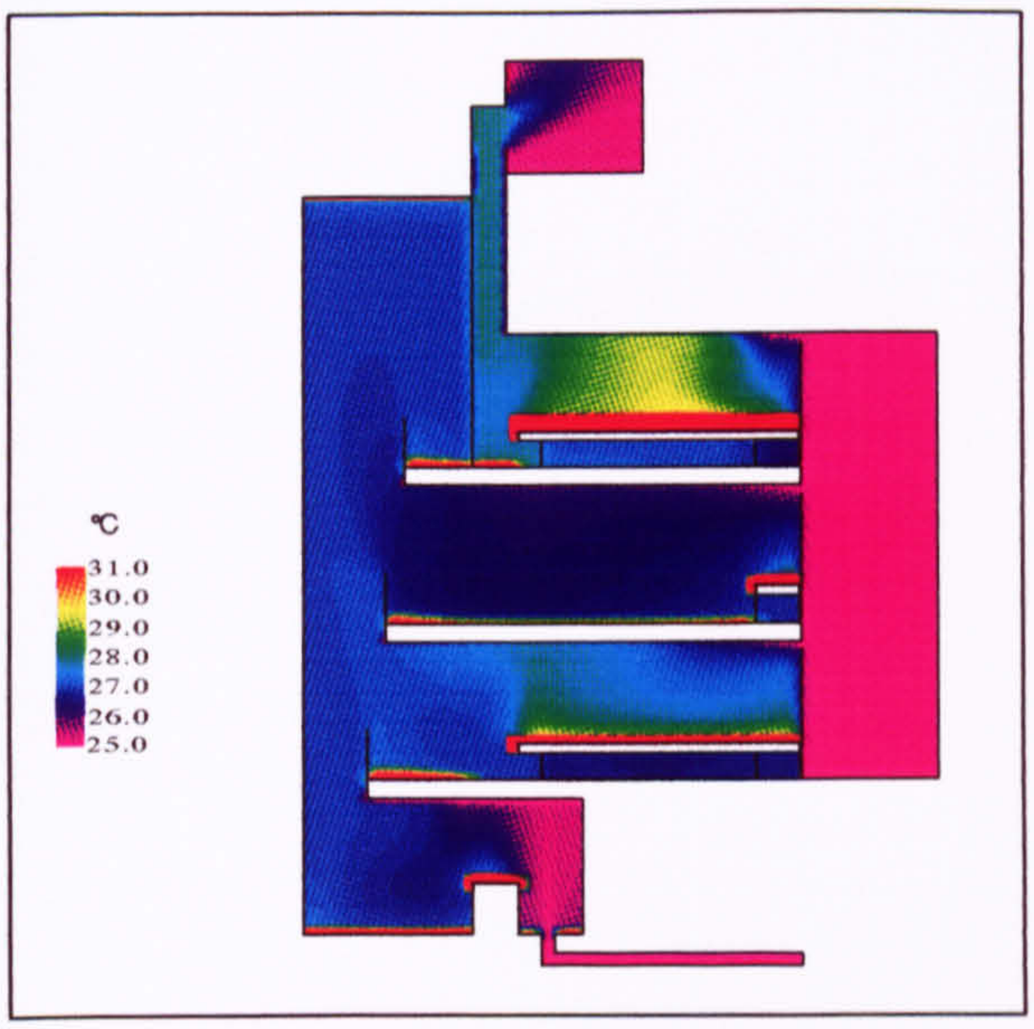

Figure 8.20 Predicted temperature distribution over the height of the building.
(Proposal for IT centre at De Montfort University, Bedford).

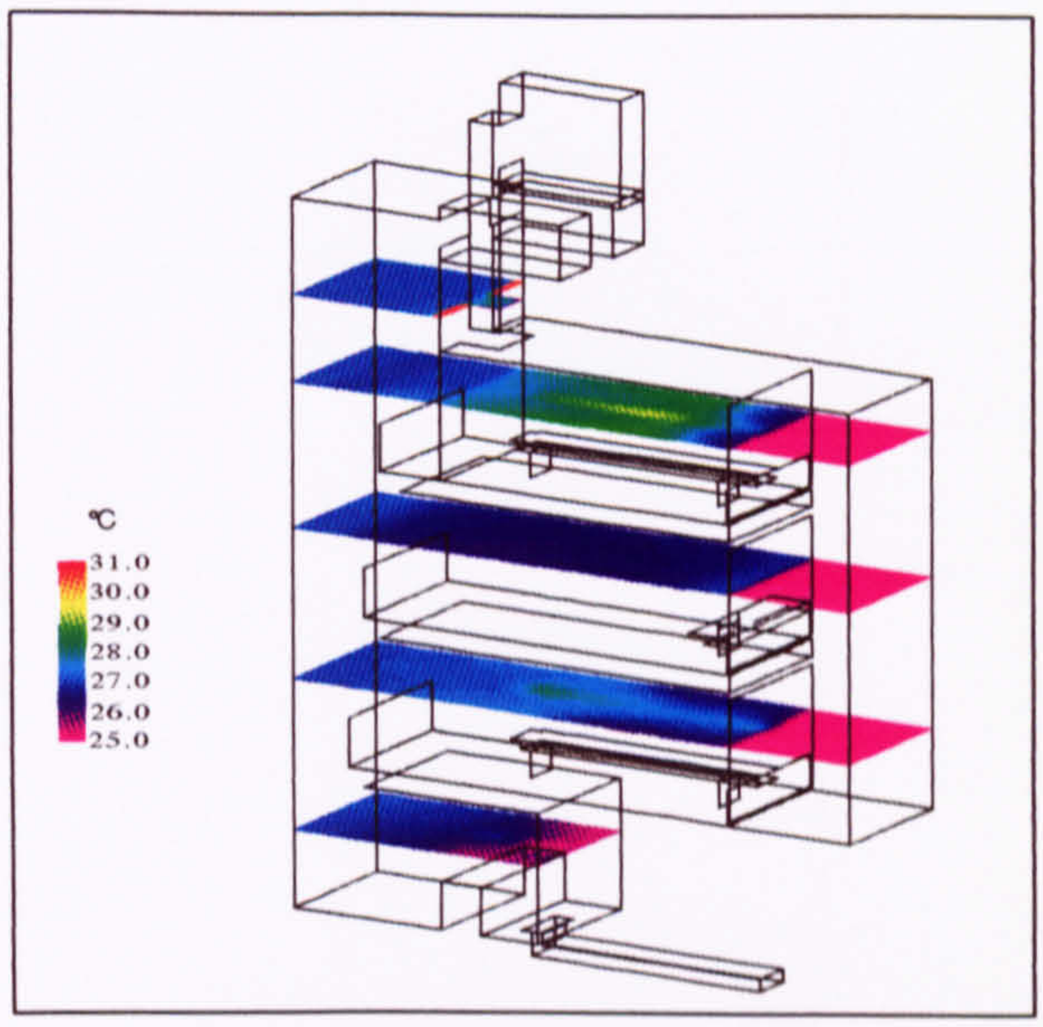

Figure 8.21 Predicted temperature distribution over various horizontal planes.
(Proposal for IT centre at De Montfort University, Bedford).

was also used at the left-hand edge of the domain (in Fig. 8.19) to reflect the opposite half of the atrium and the adjoining, geometrically identical, work areas. Note also that external domains were defined to model airflow as it passes into or out of the building (Fig. 8.19). The simulation shown here was carried out assuming an ambient temperature of 25°C to study summer over-heating risk. Surface temperature boundary conditions on internal structures were obtained using the thermal simulation program ESP (ESRU (1996)). The CFD model incorporated a mesh of approximately 25000 (orthogonal) cells. A converged solution was attained after about 3500 iterations[1] using false time-steps of 0.1s on all three momentum equations.

The CFD results, along with results obtained using the dynamic thermal simulation program, enabled determination of the opening sizes that were necessary to obtain adequate fresh air supply and prevent over-heating. The CFD results in particular emphasised the importance of vertical balancing of the opening sizes at the façade to ensure similar fresh air supply rates on all floors and hence a uniform temperature distribution (Figs. 8.20 and 8.21).

Earlier simulations predicted an undesirable flow from the central atrium space onto the third floor (short circuiting). This was thought to be due to small upward buoyancy forces in the central atrium and was overcome by placing partitions and a door on the third floor. The simulation results also predict a draught risk on the ground floor as air enters via the under-floor plenum (Fig. 8.19). Such problems could be overcome by allowing this air to enter through a wall mounted diffuser.

This application example demonstrates the potential of CFD for informing the design of naturally ventilated buildings by enabling the accurate specification of opening sizes and identifying potential problems such as draughts and short-circuiting of air. Similar techniques have been used by the author for modelling other buoyancy-driven airflows to assist with the design of Coventry University

[1] This required 18.5 hours of CPU time on a Sun SPARC 20 Workstation with 192MB of RAM.

library (CR6) and the Australia 2000 Stadium (CR2, CR3, and Lomas et al. (1997)).

8.5 Suggestions for Further Work

This section is divided into two. The first recommends work that could usefully be undertaken to investigate the few remaining uncertainties identified in this research (current benchmarks). The second proposes suggestions for building on the findings of this research to enable further validation and the confident use of CFD for modelling natural ventilation (new benchmarks).

8.5.1 Current Benchmarks

- More detailed work would be useful to determine precisely the limitation of CFD for modelling buoyant plumes. In particular why the variation of plume buoyancy with height is not reproduced accurately. For example, for a 2D line plume, one might postulate a relationship of the form $G_T' = \lambda B_L^{2/3} / y^n D$ and set about establishing values for λ and n, which might vary according to source area.

- Further work is required to ensure that the flow near the source is being modelled accurately. In this region, temperature differences can be large which raises a question over the validity of the Boussinesq approximation which assumes small density differences.

- An important part of this work has been an investigation of different (but similar) models for representing turbulence. Now that it has been shown that turbulence models affect the key parameters of buoyancy-driven displacement ventilation, it would be worthwhile addressing this issue in even more detail. This would involve investigating the influences of the various constants in the turbulence models and the effects of using different types of model, in particular, second order closure models such as Reynolds Stress models which model anisotropic turbulence. There is some evidence that the RNG $k-\varepsilon$ model (and to a lesser extent the standard $k-\varepsilon$ model) caused changes in the

plume behaviour when subjected to different source strengths. More work is needed to determine the nature and severity of these.

- When simulations were carried out to investigate convergence *progress* by treating iterations as a pseudo-time-scale, and analysing the 'partially converged' solution after 50, 100, 200, 1000, 2000, etc. iterations, it was found that the flow inside the space established itself much sooner than the flow in the exterior zones, and that much of the convergence time, say from about 1000 iterations onwards, was used in resolving the exterior flow. Large savings in computation time would therefore be possible if the exterior zones could be replaced with accurate boundary conditions at the openings. Work to achieve this should be undertaken.

8.5.2 New Benchmarks

- Work to investigate the accuracy of CFD for modelling buoyancy-driven flows in more complex spaces should be undertaken. This could include spaces with openings in the sides rather than top and bottom, and buildings comprising several floors.

- In almost all natural ventilation regimes, wind plays an important role. Hunt and Linden (1997) have investigated these flows using salt bath experiments. It would be a natural progression of this work to use these experimental results for further CFD validation.

- Cooper and Linden (1996) have investigated salt bath and analytical modelling of a naturally ventilated enclosure containing two point sources of buoyancy. Modelling these flows using CFD would enable the interaction behaviour of adjacent plumes to be modelled, and would represent a step closer to modelling densely occupied spaces.

- Throughout this research, heat sources have been modelled idealistically, using a two dimensional 'patch' in the plane of the floor. In practice, sources of heat are produced by bodies possessing volume in three dimensional space. This will almost certainly affect the entrainment and virtual origin issues, and the flow

around the body. Work to investigate the effects of using 'volume sources' could be undertaken.

- The CFD simulations in this research have modelled heat transfer by convection (and diffusion). It would be beneficial to conduct a short investigation on the effects of radiation for a simple case such as that used in Benchmark 3.

Chapter 9

Conclusions

9. Conclusions

9.1 General Conclusions

In this research, steady-state buoyancy-driven displacement ventilation was modelled successfully using Computational Fluid Dynamics (CFD) techniques. The results compare favourably with the flows predicted by the analytical work and salt bath experiments carried out at Cambridge University by Linden et al. (1990). The heat source produces a buoyant plume which entrains the surrounding ambient, cool air. This causes a layer of warm air to form below the ceiling of the space. As the plume entrains this warmer-than-ambient air, a *steady-state* is reached in which a constant-depth layer of well-mixed warm air in the upper part of the space drives a flow through the upper openings. This causes fresh, ambient air to be drawn in through the lower openings which is then entrained into the plume. The interface is robust, and the flow direction at the interface level is predominantly towards the plume.

9.2 The Benchmarks

The work has produced three clearly defined benchmarks for use when evaluating CFD models for predicting buoyancy-driven displacement ventilation:

Benchmark 1 two dimensional modelling of the flow resulting from an *infinite line source* of buoyancy;

Benchmark 2 three dimensional modelling of the flow resulting from a *line source* of buoyancy; and

Benchmark 3 three dimensional modelling of the flow resulting from a *point source* of buoyancy.

All cases considered a simple rectangular space (5.1m wide × 2.55 high ×1m deep) with upper and lower openings and a constant heat source in the centre of the floor.

These benchmarks are simple, easy to implement and posses robust steady-state solutions, thereby enabling new models and algorithms can be tested, new CFD users to gain confidence by comparing output against the expected results, and users to establish techniques for obtaining convergence when modelling buoyancy-driven flows using CFD.

9.3 Modelling Buoyancy-Driven Flows

An objective of this research was to offer guidance on the use of CFD for modelling buoyancy-driven flows.

The work confirmed that buoyancy-driven flows are difficult and time consuming to model. Two key areas of difficulty were identified: (i) specification of accurate boundary conditions at openings, and (ii) controlling convergence due to the weakly coupled set of governing equations. The first difficulty was overcome by modelling some of the exterior air which obviated the need to impose boundary conditions at the openings. However, this generated further difficulties due to opposite pressure boundaries which were overcome by using solid surfaces on some of these boundaries. The second difficulty was eliminated by employing specific *under-relaxation* techniques (control of the solution process), known as false time-stepping, which reflected the time-scale over which the solution evolved. The research has also identified suitable criteria for determining whether or not convergence has been obtained.

Mesh investigation studies showed that a fine mesh was required to accurately resolve plume properties and flow parameters such as interface height. However, accurate qualitative predictions could be obtained using a relatively coarser mesh.

The research also showed that 2D simulations can successfully be used to obtain a good prediction of the 3D case, provided, of course, that a representative slice is considered in which the heat input and opening sizes per metre in the direction normal to the slice, have the same value as those in the corresponding 3D case.

9.4 Accuracy and Reliability

Another objective of the research was to evaluate the accuracy and reliability that can be expected from CFD software when modelling buoyancy-driven displacement ventilation.

This research has shown that CFD can predict buoyancy-driven displacement ventilation in simple geometries to a high degree of accuracy. The main cause for concern was modelling of plume entrainment which is fundamental to the accurate modelling of these flows. It was found that this value changed slightly depending upon the turbulence model employed. The standard $k-\varepsilon$ model predicted values in the range $0.14 < \alpha_T^{k-\varepsilon} < 0.17$, whereas the RNG (Renormalisation Group) theory $k-\varepsilon$ model predicted values in the range $0.11 < \alpha_T^{RNG} < 0.12$ which are closer to values measured in salt bath experiments ($0.12 < \alpha_T < 0.14$).

Linden et al. (1990) assumed a value of $\alpha_T = 0.1$ to derive their analytical solutions. The larger values predicted by the CFD simulations gave rise to larger volume fluxes and smaller buoyancy forces in the plume. This caused lower predictions of the interface height (typically 18% lower ($k-\varepsilon$ model) and 11% lower (RNG $k-\varepsilon$ model)) and smaller air change rates (typically 13% smaller ($k-\varepsilon$ model) and 15% smaller (RNG $k-\varepsilon$ model)).

There are two other discrepancies between the CFD predictions and those of Linden et al. (1990) that are noteworthy. Firstly, it was observed in the CFD simulations that the incoming ambient air impinged on the underside of the interface resulting in a non-horizontal flow at some points along the interface level. This was thought to be caused by the prediction of a less random flow below the interface in the CFD results than was observed in the salt bath experiments, brought about by the omission of transient terms in the CFD model. Secondly, the form of the variation of plume buoyancy with height above the source compared poorly with the analytical predictions for both turbulence models. This has been attributed to the existence of a *virtual origin*, but warrants further investigation.

The results obtained using the RNG $k-\varepsilon$ model were particularly encouraging as this is a new turbulence model available to the CFD community which required validation (e.g. for an effective opening area of $A^* = 0.378\text{m}^2$, $(h/H)_{\text{Linden}} = 0.603$, $(h/H)_{\text{RNG}} = 0.49$, and $(h/H)_{k-\varepsilon} = 0.39$). The only cause for concern was the slight dependence of interface height on the source strength, thought to be caused by small changes in the plume entrainment.

9.5 Closing Remarks

This research has analysed, in detail, the flow in a simple box under displacement ventilation conditions driven by a single source of buoyancy.

Topics relating to the three benchmarks defined in this research which would benefit from further detailed study have been identified and include plume modelling, turbulence modelling, and the boundary condition specification at openings. Future work in the more general area of CFD application to natural ventilation which would be useful includes wind effects, modelling of multiple plumes and densely occupied spaces, radiation effects, and application to more complex spaces.

The work in this thesis has made a contribution towards evaluating the accuracy of CFD for modelling buoyancy-driven displacement ventilation, offered guidance on its use for modelling these types of flows, and provided evidence of the high level of accuracy that can be obtained if this guidance is followed.

References and Bibliography

References

Allard F., Dorer V. B., Feustel H. E. et al. *Fundamentals of the Multi-Zone Air Flow Model - COMIS*, Technical Note 29, Air Infiltration and Ventilation Centre, 1990.

Awbi H. B. *Ventilation of Buildings* E & FN Spon, London 1991.

Baines W. D., Turner J. S. *Turbulent Buoyant Convection from a Source in a Confined Region,* J. Fluid Mech. Vol. 37 pp. 51-80, 1969.

Baines W. D., Turner J. S. and Campbell I. H. *Turbulent Fountains in an Open Chamber*, J. Fluid Mech. Vol. 212 pp. 557-592, 1990.

Banham R. *The Architecture of the Well-tempered Environment*, second edition, The University of Chicago Press, 1984.

Batchelor G. K. *An Introduction to Fluid Dynamics*, Cambridge University Press, 1974.

BRECSU *Energy Consumption Guide 19 - Energy use in offices*, 1998.

Building Research Establishment *BRE's Environmental Building* Compact Disc, 1997. Available from the BRE, Garston, Watford, WD2 7JR, UK.

Chen Q. *Comparison of Different $k-\varepsilon$ Models for Indoor Airflow Computations,* Numerical Heat Transfer (B), Vol. 28, pp. 353-369, 1995.

Chen Q., Moser A. and Huber A. *Prediction of buoyant, turbulent flow by a low-Reynolds-number $k-\varepsilon$ model,* ASHRAE Transactions 96(1), pp. 564-573, 1990.

CIBSE *The Quest for Comfort*, CIBSE, 1997.

CIBSE *Natural Ventilation in Non-Domestic Buildings*, CIBSE Application Manual AM10, 1997.

CIBSE *Building Services Journal*, March 1993, p. 6.

CIBSE *Building Services Journal*, October 1993, pp. 20-25.

CIBSE CIBSE Guide Volume A, London, ISBN: 0 900953 292, 1986.

Computational Dynamics Ltd. *STAR-CD User Manual*, London, UK, 1991.

Computational Fluid Dynamics Services *CFX 4.1 Flow Solver User Guide*, 1995.

Computational Fluid Dynamics Services *CFX 5.1 User Guide*, Vol. 1, 1996.

Cooper P. and Linden P. F. *Natural Ventilation of an Enclosure Containing Two Buoyancy Sources*, J. Fluid Mech. Vol. 311 pp. 153-176, 1996.

Davidson L. *Ventilation by Displacement in a Three-Dimensional Room - A Numerical Study*, Building and Environment, Vol. 24, No. 4, pp. 363-372, 1989.

Davidson L. and Hedberg P *A General Computer Program for Transient, Three Dimensional, Turbulent, Recirculating Flows*, Rep. 86/13, Dept of Applied Thermodynamics and Fluid Mechanics, Chalmers University of Technology, Göteberg, Sweden, 1986.

Edwards M., Linden P. F. and Walker R. R. *Theory and Practice - Natural Ventilation Modelling*, CIBSE National Conference, pp. 102-108, 1994.

Energy Systems Research Unit (ESRU) *Data Model Summary ESP-r Version 9 Series*, ESRU report TR96/2, June 1996.

Fawcett N. S. J. *Getting Started with CFD*, IMechE London, pp. 1-4, 1991.

FLUENT Inc. *Introduction to the Renormalisation Group Method and Turbulence Modelling*, Technical Memorandum 107, 1993.

Fraikin M. P., Portier J. J. and Fraikin C. J. *Application of a $k-\varepsilon$ turbulence model to enclosed buoyancy-driven recirculating flow*, Chem. Eng. Comm., Vol. 13, pp. 289-314, 1982.

Gosman A. D., Pun W. K., Runchal A. K., Spalding D. B., Wolfshtein M. *Heat and Mass Transfer in Recirculating Flows*, Academic Press, London, 1969.

Holmes M. J. and Whittle G. E. *How Accurate are the Predictions of Complex Air Movement Models?*, Building Services Engineering Research and Technology, Vol. 8, No. 2, pp. 29-31, 1987.

Hunt G. R. and Linden P. F. *Passive Cooling by Natural Ventilation: Salt Bath Modelling of Combined Wind and Buoyancy Forces*, Proc. AIVC Conference Greece, Vol. 1, pp. 176-183, 1997.

Ideriah F. J. K. *Prediction of Turbulent Cavity Flow Driven by Buoyancy and Shear*, Journal of Mechanical Engineering Science, Vol. 22, No. 6, pp. 287-294, 1980.

Jacobsen T. V. *Airflow and Temperature Distribution in Rooms with Displacement Ventilation - Full Scale Measurements, Analytical Models and Computational Fluid Dynamics*, PhD Thesis, Aalborg University, Denmark, 1993.

Jayatilleke *The Influence of Prandtl Number and Surface Roughness on the Resistance of the Laminar Sublayer to Momentum and Heat Transfer,* Proc. Heat and Mass Transfer, Vol. 1, p. 193, 1969.

Jones I. P. *The Convergence of a Simple Iterative Strategy for Strongly Stratified Flows*, Numerical Methods in Laminar and Turbulent Flow, Proc. Fourth Int. Conf., Swansea, Wales, pp. 733-740, 1985.

Jones P. J. and Whittle G. E. *Computational Fluid Dynamics for Building Air Flow Prediction - Current Status and Capabilities*, Building and Environment Vol. 27, No. 3, pp. 321-338, 1992.

Jones P., Vaughan N., Jones K., O'Sullivan P., Young A., Crosford B., Bowman N., and Patronis J. *Guidelines for the Design of Natural and Mixed-Mode Ventilation Systems in Commercial Buildings* GR/K63891, 1998.

Kofoed *Thermal Plumes in Ventilated Rooms,* PhD Thesis, University of Aalborg, Denmark, 1991.

Jin Y. *Particle Transport in Turbulent Buoyant Plumes Rising in a Stably Stratified Environment*, PhD Thesis, Royal Institute of Technology, Stockholm, Sweden, 1993.

Lane-Serff G. F., Linden P. F., Parker D. J. and Smeed D. A. *Laboratory Modelling of Natural Ventilation Via Chimneys*, Proc. PLEA 91 Architecture and Urban Space, pp. 505-510, 1991.

Launder B. E. and Spalding D. B. *The Numerical Computation of Turbulent Flows*, Computer Methods in Applied Mechanics and Engineering, Vol. 3, pp. 269-289, 1974.

Linden P. F., Lane-Serff G. F., and Smeed D. A. *Emptying Filling Boxes: the fluid mechanics of natural ventilation*, J. Fluid Mechanics, Vol. 212, pp. 309-335, 1990.

Lomas K. J., Eppel H., Cook M. J. and Mardaljevic J. *Ventilation and Thermal Performance of Design Options for Stadium Australia.* Proc. IBPSA '97, Volume 1, pp. 135-142, 1997, ISBN: 80-01-01646-1.

Lonsdale R. D. *An Algebraic Multi-grid Solver for the Navier Stokes Equations on Unstructured Meshes*, Int. Journal on Numerical Methods for Heat and Fluid Flow, Vol. 3, 1993.

Markatos N. C., Malin M. R. and Cox G. *Mathematical Modelling of Buoyancy-Induced Smoke Flow in Enclosures*, Int. Journal Heat and Mass Transfer, Vol. 25, No. 1, pp. 63-75, 1982.

Markatos N. C. and Pericleous K. A. *Laminar and Turbulent Natural Convection in an Enclosed Cavity*, Int. Journal Heat and Mass Transfer, Vol. 27, No. 5, pp. 755-772, 1984.

McGuirk J. J. and Whittle G. E. *Calculation of Buoyant Air Movement in Buildings - Proposals for a Numerical Benchmark Test Case*, Proc. IMechE Seminar in Computational Fluid Dynamics for the Environmental and Building Services Engineer, London, November 1991.

Morton B. R., Taylor G. I. and Turner J. S. *Turbulent Gravitational Convection from Maintained and Instantaneous Sources*, Proc. Royal Soc. London, Vol. 234, pp. 1-23, 1956.

Murakami S., Kato S. and Ooka R *Numerical Simulation of Horizontal Non-isothermal 3-D Jet in a Room by DSM*, Proc. Roomvent, Vol. 1, Aalborg, Denmark, 1992.

Nielsen P. V. *Moisture Transfer in air conditioned rooms and cold stores*, Proc. Second International CIB/RILEM Symposium on Moisture Problems in Buildings, Paper 1.2.1, Rotterdam, Holland, 1974.

Nielsen P. V., Restivo A. and Whitelaw J. H. *Buoyancy-Affected Flows in Ventilated Rooms,* Numerical Heat Transfer, Vol. 2, pp. 115-127, 1979.

Patankar S. V. *Numerical Heat Transfer and Fluid Flow,* Hemisphere publishing corporation, Taylor and Francis group, New York, USA, 1980.

Precision Visuals *PV-WAVE - Technical Reference Manual*, Colorado, USA, 1988.

Raw G., Slater A., Tong D. and Lush D. *Sick Building Syndrome: a Review of the Evidence on Causes and Solutions*, The Building Research Establishment, 1992.

Rhie C. M. and Chow W. L. *Numerical Study of the Flow Past an Airfoil with Trailing Edge Separation*, AIAA J1, Vol. 21, pp. 1527-1532, 1983.

Rouse H., Yih C. S. and Humphreys H. W. *Gravitational Convection from a Boundary Source,* Tellus 3, pp. 201-210, 1952.

Schmidt W. *Turbulente Ausbreitung eines Stromes Erhizter Luft.*, Z. angew. Math. Mech., Vol. 21, pp. 265-278, 1941.

Shaw C. T. *Using Computational Fluid Dynamics*, Prentice Hall International (UK) Ltd. 1992.

Sherman M. H. and Grimsrud D. T. *Measurement of Infiltration Using Fan Pressurisation and Weather Data*, Proc. A.I.C. Conference Instrumentation and Measuring Techniques, 1980.

Smith G. D. *Numerical Solution of Partial Differential Equations: Finite difference methods*, 3rd Edition, Oxford University Press, UK, 1985.

Stone H. L. *Iterative Solution of Implicit Approximations of Multi-Dimensional Partial Differential Equations*, SIAM Journal of Numerical Analysis, Vol. 7, p. 104, 1968.

Thompson J. F., Warsi Z. U. and Mastin C. W. *Boundary-Fitted Coordinate System for Numerical Solution of Partial Differential Equations*, Journal of Computational Physics, Vol. 47, pp. 1-108, 1982.

Thompson C. P., Wilkes N. S. and Jones I. P. *Numerical Studies of buoyancy driven turbulent flow in a rectangular cavity*, Proc. Conf. on Numerical Methods in Thermal Problems, Vol. 4, Swansea, Wales, 1985.

Turner J. S. *Buoyancy Effects in Fluids*, Cambridge University Press, 1973.

Versteeg H. K. and Malalasekera W. *An Introduction to Computational Fluid Dynamics - the finite volume method*, Longman Group Ltd., 1995.

Walton G. N. *CONTAM93 User Manual*, Report NISTIR 5385, National Institute of Standards and Technology, Gaitersburg MD USA, 1994.

Whittle G. E. *Air Flow Modelling in Atria*, IMechE Seminar on 'Atrium Engineering', Nottingham, UK, June 1990.

Wilson S. and Hedge A. *The Office Environment Survey: A Study of Building Sickness*, London: Building Use Studies Limited, 1987.

Yakhot V., Orszag S. A. *Renormalisation Group Analysis of Turbulence*, J. Sci. Computing, Vol. 1, No. 3, 1986.

Yakhot V., Orszag S. A., Thangam S., Gatski T. B. and Speziale C. G. *Development of Turbulence Models for Shear Flows by a Double Expansion Technique*, Phys. Fluids A, Vol. 4, No. 7, pp. 1510-1521, 1992.

Zienkiewicz O. C. and Taylor R. L. *The Finite Element Method*, 4th edition Vol. 1: *Basic Formation and Linear Problems*, McGraw-Hill, New York, USA, 1989.

Bibliography

Book contributions

Cook M. J, Lomas K.J., Howarth A. & Crane M. *Modelling Natural Ventilation Using Computational Fluid Dynamics.* Proc. ICFD Conf. on Numerical Methods for Fluid Dynamics, Oxford, ISBN: 0 19 851480 8, pp. 351-358, ISBN: 0 19 851480 8, 1995.

Refereed Journals

Cook M. J. and Lomas K. J. *Evaluation of Two Eddy Viscosity Turbulence Models for Predicting Buoyancy Driven Displacement Ventilation.* Building Services Engineering Research and Technology, Volume 19, No. 1, pp. 15-21, ISSN: 0143-6244, 1998.

Refereed Conferences

Cook M. J. and Lomas K. J. *Guidance on the Use of Computational Fluid Dynamics for Modelling Buoyancy Driven Flows.* Proc. IBPSA '97, Volume 3, pp. 57-64, ISBN: 80-01-01646-3, 1997.

Lomas K. J., Eppel H., Cook M. J. and Mardaljevic J. *Ventilation and Thermal Performance of Design Options for Stadium Australia.* Proc. IBPSA '97, Volume 1, pp. 135-142, ISBN: 80-01-01646-1, 1997.

Non-Refereed Conferences

Mansour M. A., Cook M. J., Taki A. H. and Lomas K. J. *Use of Computational Fluid Dynamics for Modelling Passive Downdraught Evaporative Cooling.* Proc. 18th Annual AIVC Conference, Volume 2, pp. 603-611, ISBN: 0 946075 96 4, 1997.

Bowman N. T., Lomas K. J., Cook M. J., et al. *Application of Passive Downdraught Evaporative Cooling (PDEC) to Non-Domestic Buildings.* Proc. Renewable Energy, Volume 10, pp. 191-196, 1997.

Miscellaneous

Cook M. J. and Lomas K. J. *Modelling Buoyancy-Driven Displacement Ventilation*, Article in CFX Update, Computational Fluid Dynamics Services, No. 14, Autumn 1997, p. 17, ISSN 0965-1608, 1997.

Consultancy Reports

CR1. Cook M. J. and Lomas K. J. *CFD Analysis of Shopping Centre: Fenix Centre, Belgium*, 1996.

CR2. Lomas K. J., Eppel H., Cook M. J. and Mardaljevic J. *Ventilation and Thermal Performance in the AS2000 Stadium*, 1996.

CR3. Lomas K. J., Eppel H. and Cook M. J. *AS2000, Sydney Natural Ventilation Studies Part 2 - Interim Findings*, 1996.

CR4. Lomas K. J., Cook M. J. and Patronis J. *Ventilation Strategy for the Merchant Taylors' Hall: Displacement Option - Contract report no.1*, 1997.

CR5. Lomas K. J., Cook M. J. and Patronis J. *Ventilation Strategy for the Merchant Taylors' Hall: Displacement Option - Final Contract Report*, 1997.

CR6. Lomas K. J., Cook M. J. and Eppel H. *Environmental Performance Analysis of Proposed Library for Coventry University*, 1997.

CR7. Robinson D., Cook M. J., Mardaljevic J. and Lomas K. J. *Integrated Building Environmental Performance Assessment: Interim Report* (Polhill IT Centre), 1998.

Appendix A

Selecting CFD Software

A. Selecting CFD Software

A.1 Preamble

This appendix outlines the procedure that was undertaken in selecting a suitable CFD package for use in this research.

A.2 Specification of the CFD Package

A list of desired features was compiled after consulting various publications (e.g. Jones and Whittle (1992), Fawcett (1991), and Shaw (1992)) and holding conversations with experienced CFD users. The features were divided into six groups: pre-processing capabilities; physical modelling capabilities; the solver; post-processing capabilities; user friendliness and user support.

A.2.1 Pre-Processing Capabilities

This is the interface through which the user defines the simulation. It includes geometry and mesh generation and enables specification of boundary conditions, physical models, and numerical parameters used in the solution procedure. Features sought in the pre-processor were:

- 2D and 3D modelling;
- cartesian and cylindrical coordinate systems with body-fitted coordinates (this capability enables grids to be distorted to fit the geometry in question);
- large mesh capacity (up to about 100 000 cells) - this upper limit is often dictated by the available hardware;
- specification of complex boundary conditions, such as transient conditions, and pressure boundaries with discharge coefficients; and
- access to 'Fortran User Routines' to add or modify physical models.

A.2.2 Physical Modelling Capabilities

This section identifies the desired numerical methods for representing the various facets of airflow. In addition to mass, momentum and energy transfer, the following capabilities were sought:

- transient and steady state modelling;
- a selection of turbulence models, including the standard $k-\varepsilon$ model of Launder and Spalding (1974);
- particle tracking - smoke particles, dust particles, and 'clouds' of particles (many particles), the latter may be better represented using a *multi-species* model;
- multi-phase modelling, e.g. evaporation of water in air; and
- accurate boundary layer treatment.

A.2.3 The Solver

Once the various physical models have been specified and the boundary conditions defined, it is the job of the solver to 'organise' all of this information and solve the governing flow equations (Eq. (D-1) and Table D.1) to find values for all of the variables in each cell of the user-defined *mesh* (§D.2) such that the physical models and boundary conditions are simultaneously satisfied. In solving the equations it is necessary to reduce them to a numerical form that can be understood by a computer. This technique is called *discretisation*. There are three main methods for doing this: the Finite Difference Method (FDM); the Finite Element Method (FEM); and the Finite Volume Method (FVM).

The FDM uses Taylor series expansions (Smith 1985) to express first and second order derivatives in terms of differences in the dependent variables at spatial positions only a small distance apart. The FEM has its origins in stress and strain analysis of solid structures. In brief, the domain of interest is divided into small

elements and a certain variation for the dependent variable assumed. Various numerical analysis techniques (Zienkiewicz and Taylor (1989)) are then employed to determine expressions for first and second order derivatives of the dependent variable. This is carried out for *every* element of the domain after which all of the equations are collated and solved. Since each element is considered individually, additional computation is necessary in generating a 'look-up' table containing the connectivity information of the elements.

The most popular technique for discretising the governing CFD equations is the FVM. This method represents a more physical approach to transforming the differential equations. The flow domain is divided into *control volumes* (defined using the cells of the mesh) and the governing conservation equations are integrated over each one. In doing this, physical processes such as convection, diffusion and sources/sinks are dealt with explicitly. Inherent in its method, the FVM draws on features taken from both the finite element and finite difference methods.

The FVM is the most favoured discretisation technique for CFD code developers and was the method sought when selecting CFD software. The method is described in more detail in Appendix D, but its origins can be found in Patankar (1980). A good introductory text to its methods and associated algorithms can be found in Versteeg and Malalasekera (1995).

Two mesh types can be used in CFD programs - *structured* and *unstructured.* A structured mesh comprises six-sided cells arranged in a regular topology to form a cuboid. A structured mesh is necessary for implementation of the FDM. In an unstructured mesh, cells do not have to be six-sided and are often tetrahedral in shape. Since the FEM uses a unique variation of the dependent variables for every cell, the method lends itself well to unstructured meshes. The FVM is used mainly with structured meshes, although algorithms are now available that use the FVM with an unstructured mesh (e.g. Lonsdale (1993) and Computational

Dynamics Ltd. (1991)). In this selection process, a code employing the FVM with a structured mesh was deemed appropriate.

When using the FVM, values for pressure are calculated at the cell centres. Velocity components are then calculated either at cell faces (a *staggered grid*) or, along with pressure, at the cell centres (a *co-located grid*). The latter produces a more accurate results field but requires the use of the Rhie and Chow interpolation algorithm (Rhie and Chow (1983)) to prevent pressure and velocity decoupling.

A.2.4 Post-Processing Capabilities

This is the aspect of the CFD package dedicated to results analysis. CFD codes produce large amounts of data in their results files. The quickest and most effective way to view this data is graphically. Most CFD packages can produce contours (line contours and shaded contours), line graphs and vectors. Some packages also enable the superposition of two of these variables, for example, velocity vectors and temperature contours.

Although graphical analysis is probably the most useful method for viewing results, it is important to check whether or not the package gives access to the results in ASCII format. This is very useful for comparing results with experimental data or other CFD codes as it enables exact properties such as flow rates through openings to be found. It may also be helpful if the software can interface with other visualisation packages such as PV-WAVE (Precision Visuals (1988)).

A CFD package with all or most of these capabilities was sought.

A.2.5 User-Friendliness

The ease with which the user is able to operate the software is determined by the design of the *user interface*. The more friendly a package appears, the shorter

the learning curve will be and the quicker users will be able to obtain meaningful results. Ideally, the type of interface sought was that depicted in Figure A.1.

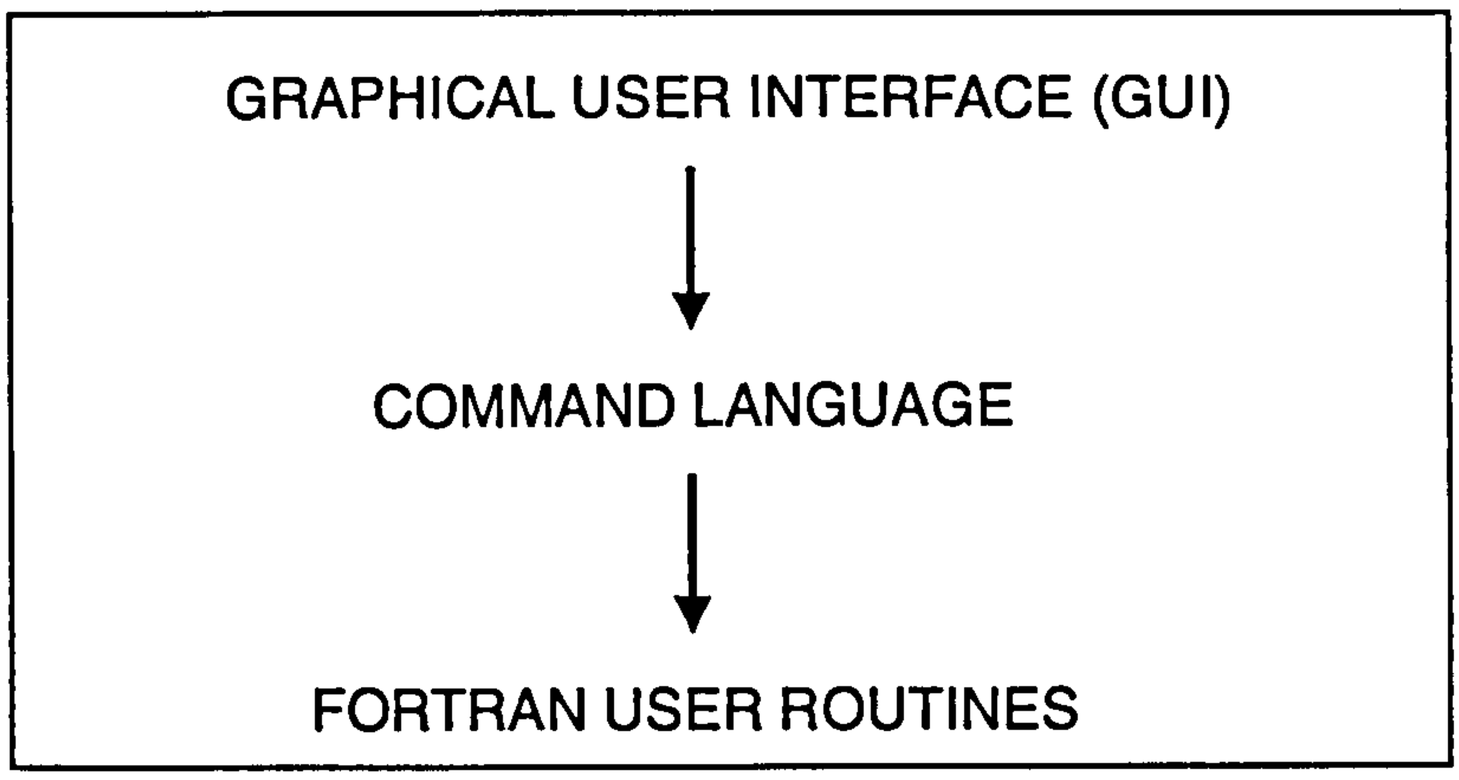

Figure A.1 Structure of a flexible pre-processor.

The GUI provides a very easy introduction to the software and enables basic problems to be set up very quickly using both mouse and keyboard. Less simple problems can be defined using a command language which 'sits beneath' the GUI. This enables files, that are normally produced automatically using the top level menu, to be written (and edited) by the user using a very high level and logical language. The command language offers users much more freedom in defining geometries, meshes, boundary conditions, etc. However, if the command language is still not flexible enough, it is necessary for the user to access *User Fortran Routines*. These are sub-sections of the main CFD code in which users can write Fortran routines to tailor their simulation. For example, to define new physical models, specify complex boundary conditions, define additional output variables, etc.

Two features sought in the solver interface were solution monitoring and the facility to carry out a restart simulation. The first enables users to interactively analyse the solution procedure by viewing, sometimes both graphically and numerically, the equation residuals and the values of the variables at a point. The residuals are the errors between the right-hand and left-hand sides of the discretised governing equations (see Appendix D) and, in a successful solution process, should fall. A restart facility enables the solution from one simulation to

be used as the initial guess for the first iteration of another simulation. This is very useful, for example, if the user wishes to investigate the effects of changes in the operating conditions such as inlet temperatures and occupancy levels.

A.2.6 User-Support

When using CFD software to address difficult problems, it is helpful if good user support is available via an immediate, rapid response method, such as fax, email or telephone. Some vendors also set up email user groups which enable users to send an advice request to all current users of that CFD code. Most companies offer training courses to new and potential users enabling them to overcome some of the initial difficulties and get the most from the software in a shorter period of time. To gain an insight into the quality of user-support, there is much to be gained from visiting potential suppliers *before* selecting a software vendor.

A.3 Evaluating the Available Packages

Seven packages were chosen for investigation. These were considered against a list of 'strongly-desired-features' (Table A.1), following which, it was decided to investigate FLOW3D (now called CFX), FLUENT, and PHOENICS in more detail. This choice was based on elimination of those packages which did not posses one or more of the strongly desired features.

Table A.1 Comparison between CFD codes and the strongly-desired-features.

FEATURE	ARIA	FIDAP	FLOVENT	FLOW3D	FLUENT	PHOENICS	STAR-CD
Discretisation technique	FVM	FEM	FVM	FVM	FVM	FVM	FVM
Mesh type	STR	UNS	STR	STR	STR	STR	UNS
2D *and* 3D	Y	Y	Y	Y	Y	Y	Y
Friendly interface	Y	Y	Y	Y	?	Y	Y
Body-fitted coordinates	N	N/A	N	Y	Y	Y	N/A
Turbulence models: $k-\varepsilon$	Y	Y	Y	Y	Y	Y	Y
Multi-phase/species	N	Y	N	Y	Y	Y	Y
Access to Fortran user-routines	Y	Y	N	Y	Y	Y	Y

FVM - finite volume method, FEM - finite element method,

STR - structured mesh, UNS - unstructured mesh,

Y - features are available, N - features are not available, ? - conflicting views exist.

The three leading packages selected for further investigation were assessed using a concise list of features drawn from section A.2 (Table A.2).

Table A.2 Comparison between CFD codes and the strongly-desired features

FEATURE	FLOW3D (version 3.2)	FLUENT (version 4.11)	PHOENICS (version 1.6 and 'FLAIR')
Solution technique	FVM, co-located grid	FVM, Co-located grid, multi-grid	FVM, staggered grid
Dimensions	2D, 3D	2D, 3D	2D, 3D
Coordinate systems	Cartesian, cylindrical polars, BFC	Cartesian, cylindrical polars, BFC	Cartesian, cylindrical polars, BFC
Mesh type	Structured, multi-block	Structured	Structured
Cell limit	Limited by hardware only	150 000 (hardware limit likely to be reached first)	Limited by hardware only
Geometry and mesh generation	GUI, command language	Menu driven (keyboard)	GUI, PHOENICS Input Language
Flexibility of boundary conditions	Very (command language or Fortran User Routines)	Very (command *interface* or Fortran User Routines)	Very (command language or Fortran User Routines)
Transient/steady	Both	Both	Both
Reynolds number (Re)	Laminar and turbulent (low and high Re. numbers)	Laminar and turbulent (low and high Re. numbers)	Laminar and turbulent
Turbulence models	$k-\varepsilon$, low Re no. $k-\varepsilon$, ASM, RSM, DSM, Reynolds flux model	$k-\varepsilon$, RSM, RNG (*)	$k-\varepsilon$, *k-l*, constant eddy viscosity, RSM (not available with BFCs)
Natural ventilation	Good (1)	Good (4)	Good (4)
Particle tracking	Transport model, multi-phase, scalar	Lagrangian	Separate module GENTRA (*)
Multi-phase	Yes	No	Yes
Multi-species	Yes	Yes	Yes
Boundary layer treatment	Log-layer treatment	Log-layer treatment	Log-layer treatment
Multi-zone regions	Easy via multi-block	Achieved by 'blocking off' cells	Achieved by 'blocking off' cells
Code access	Yes via 'User Fortran Routines'	Yes via 'User Fortran Routines' (*)	Yes via 'User Fortran Routines'
Monitoring of solution (residuals and absolute values)	Yes (graphical using a user-defined monitoring point)	Yes (graphical and numerical)	Yes (graphical and numerical using a user-defined monitoring point)
Restart	Yes	Yes	Yes
Convergence of buoyancy-driven flows	"Can be modelled" (4)	"Can be modelled" (4)	"Can be modelled" (4)
Post-processing	All expected features (#)	All expected features (#)	All expected features (#)
ASCII format results	Yes	Yes	Yes
User friendliness	"Excellent" (1,2)	"Unfriendly, but manuals are good" (1,3)	"Excellent. A very good way to get started" (1)
User support	"Too good!" (1). Excellent" (2)	"Very good" (1)	"Not that good" (1). "Not brilliant" (3).
Cost (•) £ First year: inc. (*) items exc. VAT Second Year: Over three years:	3400 (add 720 if training required) 1200 5800	2500 (add 250 if training required) 2500 7500	2600 (inc. training for 1 person per year) 2600 7800

$k-\varepsilon$ - two-equation model of Launder and Spalding (1974), ASM - algebraic stress model, RSM - Reynolds stress model, DSM - differential stress model, RNG - Renormalisation Group theory $k-\varepsilon$ model.

(1) Present academic users of the code. (2) Present commercial users of the code. (3) Past academic users of the code. (4) Vendors of the code.
Refers to all those capabilities mentioned in §A.2.4. * Extra cost items. • Academic price per user at April 1993.

Following the compilation of Table A.2 and conversations with each vendor and users of each code, it was decided to purchase FLOW3D. This package comprised all of the features sought after including highly commended user-support and a very active team of people working on research and development which is indicative of a commercially stable company. FLOW3D also possessed a *multi-block* technique which enables many individual rectangular meshes to be joined together, enabling complex geometries to be defined with ease. This avoids the computational overhead of 'blocking off' cells which are not part of the flow domain but which are part of the rectangular meshes inherent in other (single block) codes such as FLUENT and PHOENICS.

Appendix B

Additional Plume Theory

B. Additional Plume Theory

B.1 Equating 'Top-Hat' and Gaussian Plume Profiles

B.1.1 Point source of buoyancy

Consider a point source of buoyancy generating an axi-symmetric plume. The velocity and buoyancy profile of such a plume occur in nature as Gaussian. However, for ease of analysis, they can be represented as *'top-hat'* profiles (Fig. B.1).

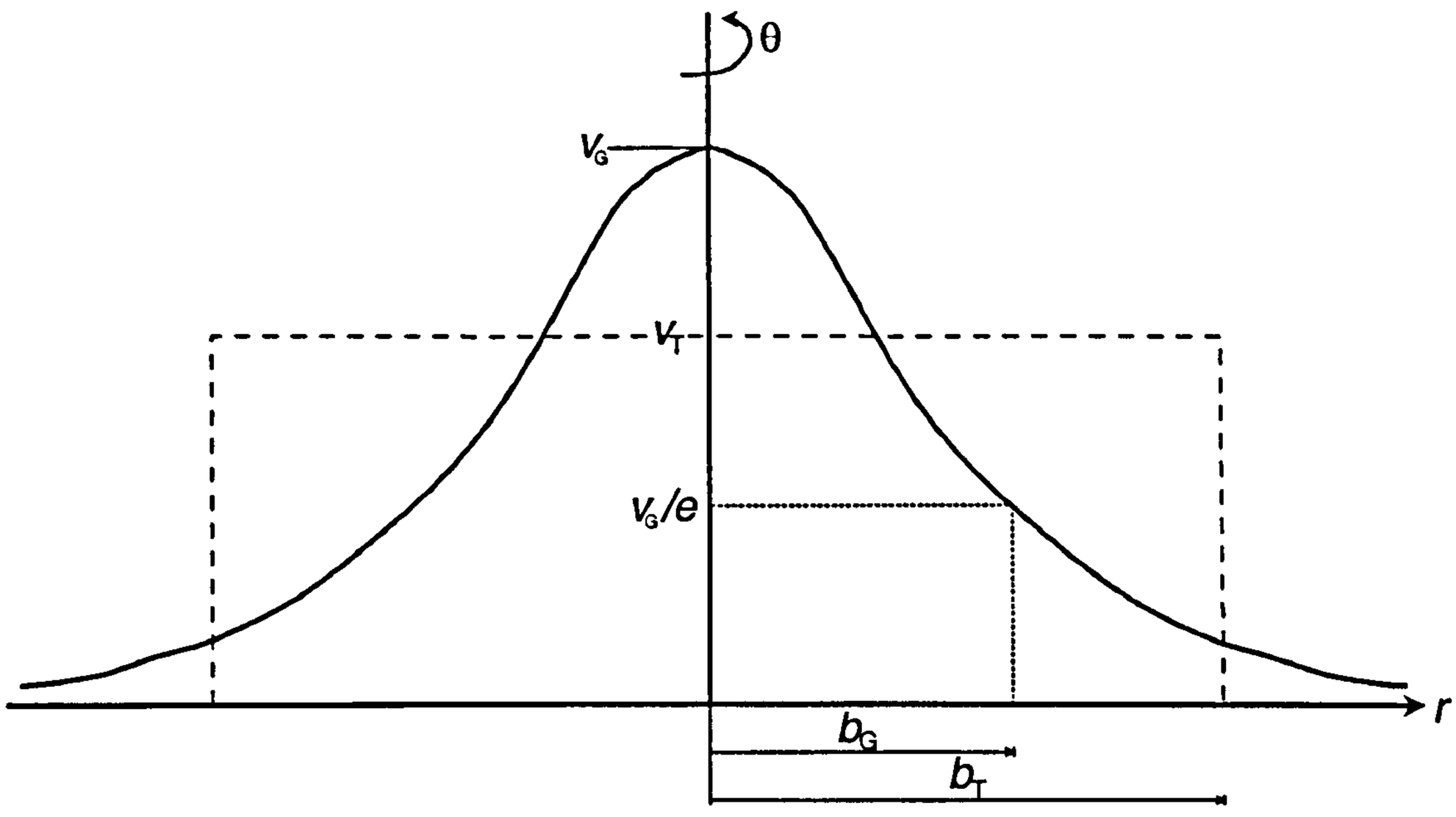

Figure B.1 Cross section of an axi-symmetric plume comparing Gaussian and 'top-hat' profiles.

In order to use the 'top-hat' profile, it is necessary to equate the total volume, momentum and buoyancy fluxes for each profile with one another.

Equating volume fluxes:

$$\pi b_T^2 v_T = \int_{\theta=0}^{2\pi} \int_{r=0}^{\infty} v_G e^{-r^2/b_G^2} r\,dr\,d\theta$$

('Top-Hat') (Gaussian)

$$\Rightarrow \qquad b_T^2 v_T = b_G^2 v_G \,. \tag{B-1}$$

Equating momentum fluxes:

$$\rho\pi b_T^2 v_T^2 = \rho \int_{\theta=0}^{2\pi} \int_{r=0}^{\infty} v_G^2 e^{-2r^2/b_G^2} r\,dr\,d\theta$$

('Top-Hat') (Gaussian)

$$\Rightarrow \qquad b_T^2 v_T^2 = \frac{b_G^2 v_G^2}{2} \,. \tag{B-2}$$

Solving the simultaneous equations (B-1) and (B-2) yields:

$$\boxed{v_T = \frac{v_G}{2}} \tag{B-3}$$

and

$$\boxed{b_T = \sqrt{2} b_G} \tag{B-4}$$

Also equating buoyancy fluxes,

$$\pi b_T^2 v_T G_T' = \int_{\theta=0}^{2\pi} \int_{r=0}^{\infty} v_G e^{-r^2/b_G^2} G_G' e^{-r^2/b_G^2} r\,dr\,d\theta$$

('Top-Hat') (Gaussian)

$$\Rightarrow \qquad b_T^2 v_T G_T' = \frac{b_G^2 v_G G_G'}{2}$$

where G_G' is the buoyancy on the plume axis and G_T' is the corresponding 'top-hat' value.

From Equation (B-1), this gives

$$\boxed{G_T' = \frac{G_G'}{2}} \tag{B-5}$$

B.1.2 Line source of buoyancy

A similar analysis can be conducted for a plume rising from a *line* source of buoyancy of unit length as follows.

Equating volume fluxes:

$$2b_T v_T = 2\int_{r=0}^{\infty} v_G e^{-r^2/b_G^2} dr$$

('Top-Hat') (Gaussian)

$$\Rightarrow \qquad b_T v_T = b_G v_G \frac{\sqrt{\pi}}{2}. \tag{B-6}$$

Equating momentum fluxes:

$$2\rho b_T v_T^2 = 2\rho \int_{r=0}^{\infty} v_G^2 e^{-2r^2/b_G^2} dr$$

('Top-Hat') (Gaussian)

$$\Rightarrow \qquad b_T v_T^2 = \frac{b_G}{\sqrt{2}} v_G^2 \frac{\sqrt{\pi}}{2}. \tag{B-7}$$

Equating buoyancy fluxes:

$$2b_T v_T G_T' = 2\int_{r=0}^{\infty} v_G e^{-r^2/b_G^2} G_G' e^{-r^2/b_G^2} dr$$

$$\Rightarrow \qquad b_T v_T G_T' = \frac{b_G v_G \sqrt{\pi} G_G'}{4}. \tag{B-8}$$

Solving equations (B-6) - (B-8) simultaneously yields:

$$v_T = \frac{v_G}{\sqrt{2}} \tag{B-9}$$

$$b_T = \sqrt{\frac{\pi}{2}} b_G \tag{B-10}$$

$$G_T' = \frac{G_G'}{2} \tag{B-11}$$

B.2 Derivation of the Governing Equations for a Plume Emanating from a Line Source of Buoyancy

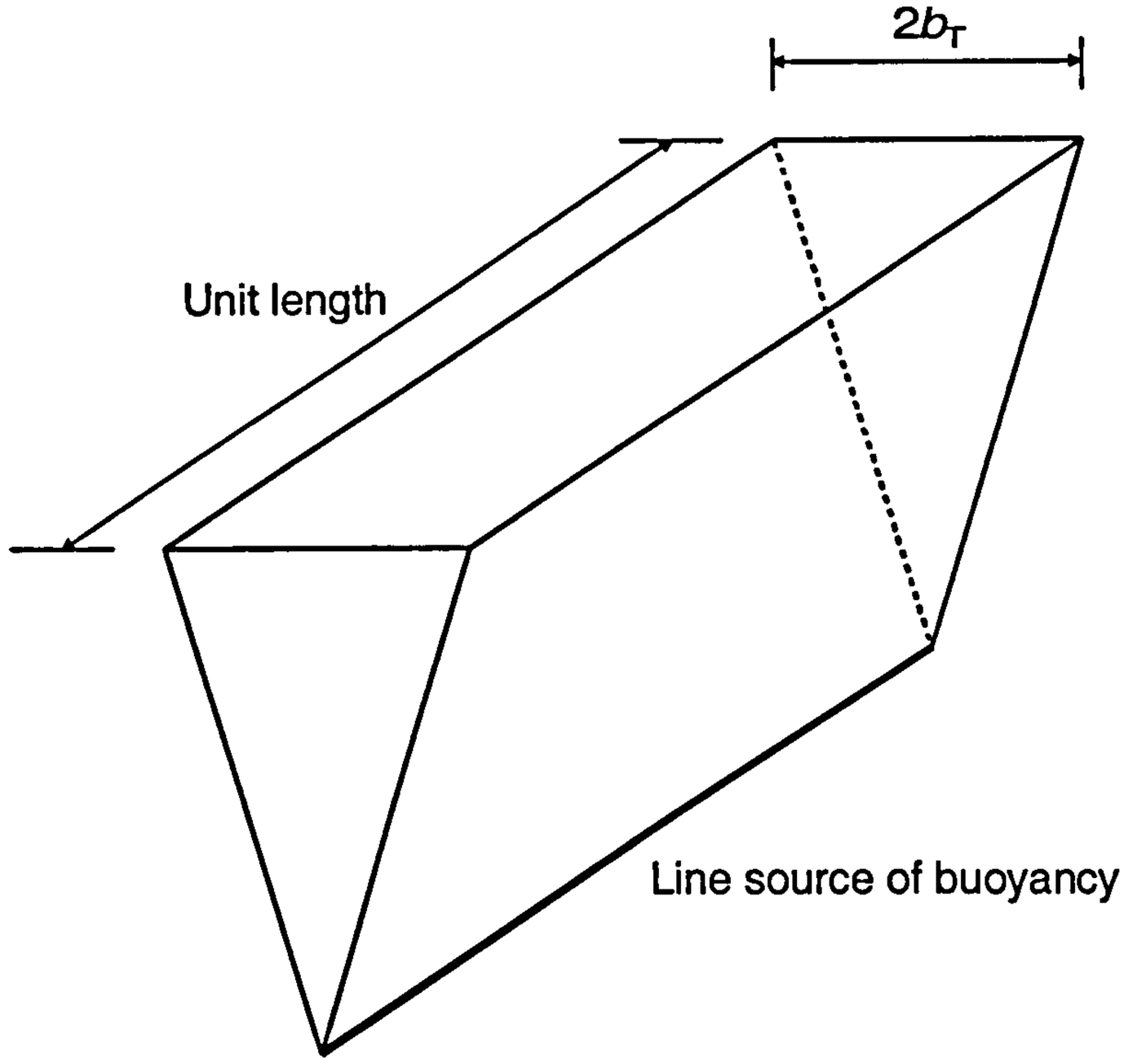

Figure B.2 Plume resulting from a 2D line source of buoyancy.

Consider the unit section of an infinite line plume shown in Figure B.2. Using the 'top-hat' profile assumption introduced in section B.1, conservation equations for volume, momentum and buoyancy can be written as follows:

$$\frac{d}{dy}\left(2b_T v_T\right) = 2\alpha_T v_T \qquad \text{(volume)} \qquad \text{(B-12)}$$

$$\frac{d}{dy}\left(2b_T v_T^2 \rho\right) = 2b_T g\left(\rho_0 - \rho\right) \qquad \text{(momentum)} \qquad \text{(B-13)}$$

$$\frac{d}{dy}\left(2b_T v_T g\left(\rho_1 - \rho\right)\right) = 2\alpha_T v_T g\left(\rho_1 - \rho_0\right) \qquad \text{(buoyancy)} \qquad \text{(B-14)}$$

where: y = vertical height in plume above source;

b_T = width of 'top-hat' profile (Eq. (B-10));

v_T = height of 'top-hat' profile (Eq. (B-9));

α_T = entrainment constant for 'top-hat';

ρ = density in plume;

ρ_0 = density of fluid surrounding plume; and

ρ_1 = some reference density.

Using Equation (B-12), Equation (B-14) can be rewritten as follows:

$$\frac{d}{dy}\left(2b_T v_T(\rho_1-\rho)\right) = (\rho_1-\rho_0)\frac{d}{dy}(2b_T v_T)$$

$$= \frac{d}{dy}\left(2b_T v_T(\rho_1-\rho_0)\right) - 2b_T v_T \frac{d}{dy}(\rho_1-\rho_0)$$

$$\Rightarrow \quad \frac{d}{dy}\left(2b_T v_T(\rho_0-\rho)\right) = 2b_T v_T \frac{d}{dy}\rho_0 \qquad \text{(B-15)}$$

Using the Boussinesq approximation, (chapter 1 of Turner (1973)), the density ρ, occurring on the left hand side of Equation (B-13) can be written as ρ_1. Multiplying Equation (B-15) by $\frac{g}{\rho_1}$ then yields the following set of governing equations:

$$\frac{d}{dy}(b_T v_T) = \alpha_T v_T \qquad \text{(volume)} \qquad \text{(B-16)}$$

$$\frac{d}{dy}(b_T v_T^2) = b_T g\frac{(\rho_0-\rho)}{\rho_1} \qquad \text{(momentum)} \qquad \text{(B-17)}$$

$$\frac{d}{dy}\left[b_T v_T g\frac{(\rho_0-\rho)}{\rho_1}\right] = b_T v_T \frac{g}{\rho_1}\frac{d}{dy}\rho_0 \quad \text{(buoyancy)} \qquad \text{(B-18)}$$

Assuming the ambient fluid to be of uniform density (unstratified), $\rho_1 = \rho_0$, and Equation (B-18) becomes:

$$b_T v_T g\frac{(\rho_0-\rho)}{\rho_0} = \text{ constant, } Q\text{, say.} \qquad \text{(B-19)}$$

Using Equation (3-3) ($B = Mg'$), the buoyancy flux per unit length, B_L is given by $B_L = M_L G'$. Therefore,

$$B_L = M_L G' = 2 b_T v_T g \frac{(\rho_0 - \rho)}{\rho_0} \tag{B-20}$$

$$\Rightarrow \qquad B_L = 2Q\,. \tag{B-21}$$

Equation (B-17) can then be written as

$$\frac{d}{dy}\left(b_T v_T^2\right) = \frac{B_L}{2 v_T}\,. \tag{B-22}$$

The governing equations, (B-16), (B-19) and (B-22) are now solved by defining variables s and t as follows:

$$s = v_T \tag{B-23}$$

$$t = b_T v_T \tag{B-24}$$

Substituting these values into (B-16) and (B-22) yields:

$$\frac{dt}{dy} = \alpha_T s \tag{B-25}$$

$$\text{and} \qquad \frac{d(ts)}{dy} = \frac{Q}{s} \tag{B-26}$$

Putting $t = Ay^a$ and $s = By^b$, where A, B, a, and b are constants, gives:

$$a = 1,\ b = 0,\ A = \left(Q\alpha_T^2\right)^{1/3} \text{ and } B = \left(\frac{Q}{\alpha_T}\right)^{1/3}.$$

Therefore,

$$\boxed{v_T = \left(\frac{B_L}{2\alpha_T}\right)^{1/3}} \tag{B-27}$$

$$\text{and} \qquad b_T v_T = \left(\frac{B_L}{2}\alpha_T^2\right)^{1/3} y\,, \tag{B-28}$$

which implies a rate of spread of the plume given by

$$\boxed{b_T = \alpha_T y\,.} \tag{B-29}$$

(Eq. (B-28) ÷ Eq. (B-27)),

and a reduced gravity in the plume of

$$G'_T = \left(\frac{B_L}{2}\right)^{2/3} \frac{\alpha_T^{1/3}}{b_T} \tag{B-30}$$

(using $B_L = M_L G'$).

Appendix C

Tensor Notation

C. Tensor Notation

This appendix explains the notation of tensors by presenting examples in a cartesian coordinate system.

C.1 First Order Tensors

Eg. 1 - position: $x_i = (x_1, x_2, x_3) = (x, y, z)$

Eg. 2 - velocity: $u_i = (u_1, u_2, u_3) = (u, v, w)$

C.2 Second Order Tensors

Eg. 1 - stress:
$$\tau_{ij} = \begin{bmatrix} \tau_{11} & \tau_{21} & \tau_{31} \\ \tau_{12} & \tau_{22} & \tau_{32} \\ \tau_{13} & \tau_{23} & \tau_{33} \end{bmatrix} = \begin{bmatrix} \tau_{xx} & \tau_{yx} & \tau_{zx} \\ \tau_{xy} & \tau_{yy} & \tau_{zy} \\ \tau_{xz} & \tau_{yz} & \tau_{zz} \end{bmatrix}$$

i.e. τ_{yx} acts in the x direction on a surface whose normal is in the y direction.

Eg. 2 - Kronecka Delta:

$$\delta_{ij} = \begin{bmatrix} 1 & 0 & 0 \\ 0 & 1 & 0 \\ 0 & 0 & 1 \end{bmatrix}$$

C.3 Summation Convention

Eg. 1 $$u_k u_k = u_1 u_1 + u_2 u_2 + u_3 u_3 = uu + vv + ww$$

Eg. 2 $$\frac{\partial u_k}{\partial x_k} = \frac{\partial u}{\partial x} + \frac{\partial v}{\partial y} + \frac{\partial w}{\partial z}$$

Eg. 3 $$\delta_{kk} = \delta_{11} + \delta_{22} + \delta_{33} = 3$$

Appendix D

Solving the Governing Equations in CFX

D. Solving the Governing Equations in CFX

This Appendix describes the solution methods adopted in CFX for solving the governing equations that were presented in Chapter 4. Any new nomenclature used in this appendix is defined locally, and not in the list at the beginning of the thesis.

D.1 The General Form of the Governing Equations

All the governing equations posses the following general *convection-diffusion* form:

$$\underbrace{\frac{\partial}{\partial x_j}\left(\rho\overline{u_j}\,\overline{\phi}\right)}_{\text{Convection term}} - \underbrace{\frac{\partial}{\partial x_j}\left(\Gamma_{\phi_{eff}}\frac{\partial\overline{\phi}}{\partial x_j}\right)}_{\text{Diffusion term}} = \underbrace{S_\phi}_{\text{Source term}} \qquad \text{(D-1)}$$

where ϕ is the variable of interest, $\Gamma_{\phi_{eff}}$ is the relevant effective diffusivity (or viscosity) for ϕ, and S_ϕ is a *source term*. This type of equation is also referred to as a transport equation since it describes the processes by which the dependent variable is transported through the fluid. Each transport equation can then be defined using Table D.1.

Table D.1 Values assigned to $\Gamma_{\phi_{eff}}$ and S_ϕ for the various transport equations when using a *k*-ε turbulence model.

Equation	ϕ	$\Gamma_{\phi_{eff}}$	S_ϕ
Continuity	1	0	0
Momentum	$\overline{u_i}$	$\mu_l + \mu_t$	$\frac{\partial}{\partial x_j}\left(-\overline{p_0}\delta_{ij} + (\mu_l + \mu_t)\frac{\partial \overline{u_i}}{\partial x_j}\right) + \rho g_i$
Enthalpy	$\overline{He}$	$\frac{\lambda}{C_P} + \frac{\mu_t}{\sigma_{Het}}$	0
Turbulent kinetic energy	k	$\mu_l + \frac{\mu_t}{\sigma_k}$	$P + G - \rho\varepsilon$
Dissipation of turbulent kinetic energy	ε	$\mu_l + \frac{\mu_t}{\sigma_\varepsilon}$	$C_1\frac{\varepsilon}{k}(P + C_3\max(G,0)) - C_2\rho\frac{\varepsilon^2}{k}$

From now on, the bars will be omitted from all Reynolds-averaged quantities for brevity.

The three distinct parts of Equation (D-1) account for different aspects of the fluid motion: the convection term represents the flux of ϕ convected by the mass flow rate ρu_i; the diffusion term models the random motion of particles, at a microscopic level due to differences in the density (number) of molecules; and the source term is used for representing the generation and destruction of ϕ. The source term is also used for collecting together terms that do not conveniently fit into the convection or diffusion terms.

It should also be pointed out at this stage that the convection term in the governing equations is *non-linear*, since it comprises *products* of dependent variables. This makes it difficult, if not impossible to solve the equations using a direct method (i.e. as a set of simultaneous equations). Instead, an *iterative* solution method must be used, whereby the equations are successively relinearised and solved until a solution is obtained to within a certain accuracy.

Computers are unable to handle the continuous nature of the partial differential equations that govern fluid flow since they can only produce results at *discrete* points. Therefore, in CFD codes, the governing equations are *discretised*

(linearised) to give algebraic equations which are solved at discrete points throughout the domain. These mechanisms will now be discussed.

D.2 Domain Discretisation

CFD codes divide the domain of interest into *cells* to produce a *mesh*. Early CFD codes, for example PHOENICS, calculated the scalar quantities at the cell centres and the vector quantities, i.e. the velocities, at the cell faces. This methodology was motivated by the idea that differences in the scalar quantities, such as pressure and concentrations, at cell centres, *drive* the flow at the cell faces. This is known as a *staggered grid* approach. More recent codes, such as CFX (CFDS (1996)), use a *co-located grid*. Here, the values of *all* variables are calculated at the cell centres. This has the advantage of only needing one mesh and making it easier to convert to a curvilinear (non-rectangular) mesh since the terms involved are simpler. However, this approach can cause decoupling of the velocity and pressure fields giving a 'chequerboard' effect (§D.4.1). This is overcome by using the Rhie Chow interpolation algorithm (Rhie and Chow (1983), explained in §D.6).

Early CFD codes only permitted cartesian, rectangular grids. However, as computers became more powerful and new algorithms were developed, *body* (*or boundary*) *fitted coordinate* (BFC) systems became available (Thompson et al. (1982)). This meant that although the equations were solved on a regular, rectangular grid in some 'computational space', the grid in the real, 'physical space', could be stretched and bent to fit the domain of interest. This enabled CFD codes to be applied to more complex geometries. CFX also adopts the concept of a local coordinate system to define *multi-block* grids. This enables non-rectangular geometries, such as rooms connected by narrow corridors, to be modelled using a number of *blocks* each comprising a BFC grid. The blocks fit together at whole faces and are arranged so that their interfaces overlap by one cell. These cells, known as dummy cells, are automatically added to the boundaries of blocks and enable (transparent) inter-block data transfer. Such boundaries are known as `INTER BLOCK` boundaries.

D.3 Discretisation of the General Governing Equation for Scalars (*H*, *k*, and ε)

For each of the cells defined using the processes described in §D.2, a *discretised* (linear) equation is produced for each of the governing equations. CFX uses the *finite volume* method to do this. This method draws on ideas from both finite element and the finite difference discretisation techniques, (see Patankar (1980), and Shaw (1992) for more details of these techniques).

D.3.1 The Control Volume Methodology

The finite volume technique is becoming a very popular method for discretising the governing equations in CFD codes. Each cell in the discretised domain is referred to as a *control volume*. For 2D cases (defined in the *x*-*y* plane, say), such control volumes are generated by forcing every cell in the plane to have a finite dimension in the *z* direction (usually of 1m for numerical convenience) and imposing `SYMMETRY PLANE` boundaries on both of the *z* faces. The discretisations carried out in the next few sections are for 2D control volumes. The 3D discretisation follows analogously.

Consider a 2D control volume surrounding the *node P* (Fig. D.1). The neighbouring nodes are denoted by: *N*orth; *S*outh; *E*ast; and *W*est, and the corresponding cell faces by lower case letters: *n*; *s*; *e*; and *w*.

Consider the integration of Equation (D-1) over the control volume in Figure D.1:

$$\int_V \frac{\partial}{\partial x_j}(\rho u_j \phi) dV - \int_V \frac{\partial}{\partial x_j}\left(\Gamma_{\phi_{eff}} \frac{\partial \phi}{\partial x_j}\right) dV = \int_V S_\phi dV \qquad \text{(D-2)}$$

which can be written:

$$\int_S \rho u_j \phi n_j dS - \int_S \Gamma_{\phi_{eff}} \frac{\partial \phi}{\partial x_j} n_j dS = \int_V S_\phi dV \qquad \text{(D-3)}$$

where *S* is the surface comprising all four faces surrounding *P* (*n*, *e*, *s* and *w*).

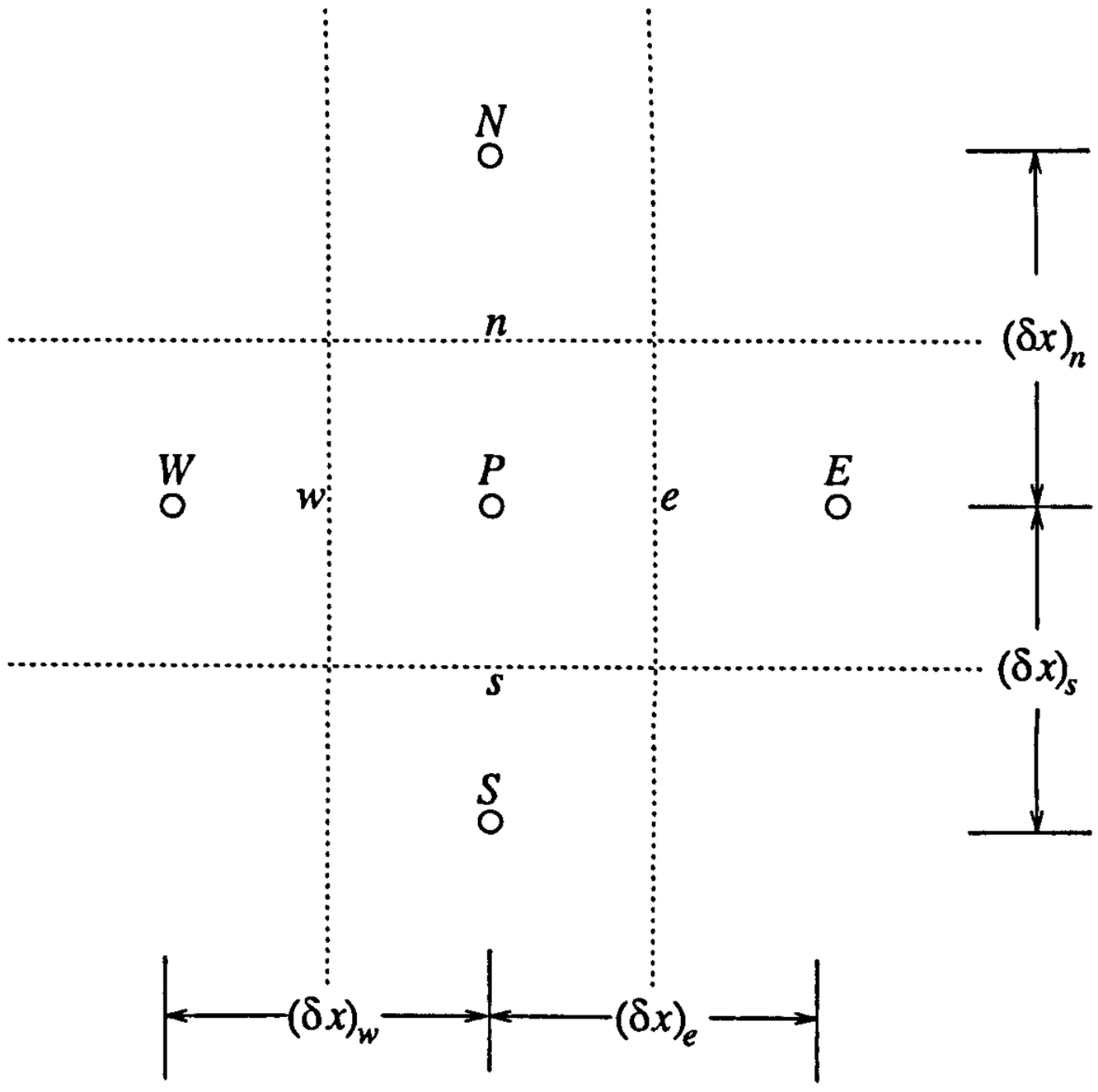

Figure D.1 Control volume around grid node *P*.

D.3.2 The Diffusion Term

This is the most straight forward of the terms to handle, and is discretised as follows:

$$\int_S \Gamma_{\phi_{eff}} \frac{\partial \phi}{\partial x_j} n_j dS = \frac{\Gamma_{\phi_{eff}} A_e}{(\delta x)_e}(\phi_E - \phi_P) - \frac{\Gamma_{\phi_{eff}} A_w}{(\delta x)_w}(\phi_P - \phi_W)$$

$$+ \frac{\Gamma_{\phi_{eff}} A_n}{(\delta x)_n}(\phi_N - \phi_P) - \frac{\Gamma_{\phi_{eff}} A_s}{(\delta x)_s}(\phi_P - \phi_S)$$

$$= D_e(\phi_E - \phi_P) - D_w(\phi_P - \phi_W) + D_n(\phi_N - \phi_P) - D_s(\phi_P - \phi_S) \qquad \text{(D-4)}$$

where:

ϕ_P, ϕ_E, etc. are the values of ϕ at that particular grid node;

A_e, A_w, etc. are the areas of faces *e*, *w*, etc.;

$(\delta x)_e, (\delta x)_w$, etc. are the distances between grid nodes (see Figure D.1);

D_e, D_w, etc. are the diffusion coefficients for the relevant faces given by:

$$D_e = \frac{\Gamma_{\phi_{eff}} A_e}{(\delta x)_e},\ D_w = \frac{\Gamma_{\phi_{eff}} A_w}{(\delta x)_w},\ \text{etc.} \tag{D-5}$$

D.3.3 The Convection Term

Since the convection term is non-linear, it is often responsible for many convergence problems, so its careful discretisation is essential. Integration of the convection term (Eq. (D-6)), yields values of the dependent variable at control volume *faces* (ϕ_e, ϕ_n, etc.).

$$\int_S \rho u_j \phi n_j dS = \rho u_e A_e \phi_e - \rho u_w A_w \phi_w + \rho u_n A_n \phi_n - \rho u_s A_s \phi_s \tag{D-6}$$

where u_e, u_w, etc. are the velocities at the faces *e*, *w*, etc.

These values are expressed in terms of values at grid *nodes* using a *differencing scheme.* Many differencing schemes are available, but the more accurate schemes tend to be less robust or slower. Three of the differencing schemes offered by CFX are described here, of which the third (a combination of the first two) is the one used in this research.

D.3.3.1 Central Differencing

This is probably the most natural approach but is not very robust. The value of ϕ at a face is calculated from the mean of the values at the grid nodes on each side of the face. Equation (D-6) then becomes:

$$\int_S \rho u_j \phi n_j dS = \rho u_e A_e \frac{(\phi_E + \phi_P)}{2} - \rho u_w A_w \frac{(\phi_W + \phi_P)}{2}$$

$$+\rho u_n A_n \frac{(\phi_N + \phi_P)}{2} - \rho u_s A_s \frac{(\phi_S + \phi_P)}{2}$$

$$= \frac{C_e}{2}(\phi_E + \phi_P) - \frac{C_w}{2}(\phi_W + \phi_P) + \frac{C_n}{2}(\phi_N + \phi_P) - \frac{C_s}{2}(\phi_S + \phi_P) \tag{D-7}$$

where C_e, C_w, etc. are the *convection coefficients* for the relevant faces given by

$$C_e = \rho u_e A_e,\ C_w = \rho u_w A_w,\ \text{etc.} \tag{D-8}$$

Note that the expressions $\rho u_e A_e$, $\rho u_w A_w$, etc. represent the mass fluxes across that particular face. Hence in a converged solution, when the continuity equation is satisfied, the sum of these coefficients should equal zero.

D.3.3.2 Upwind Differencing

In this scheme, the value of ϕ at a face takes the value of ϕ at the upstream node. Using the convention that positive velocities are from west to east and south to north in Figure D.1, the following discretised form of the convection term results.

$$\int_S \rho u_j \phi n_j dS = \langle -C_e, 0\rangle \phi_E + \langle -C_e, 0\rangle \phi_P + \langle C_w, 0\rangle \phi_P + \langle C_w, 0\rangle \phi_W$$

$$+\langle -C_n, 0\rangle \phi_N + \langle -C_n, 0\rangle \phi_P + \langle C_s, 0\rangle \phi_P + \langle C_s, 0\rangle \phi_S \qquad \text{(D-9)}$$

where, $\langle a, b\rangle$ denotes the maximum value of a and b.

D.3.3.3 Hybrid Differencing

This is a combination of upwind and central differencing, and is the most robust of the schemes described here. The scheme used depends on the relative magnitudes of convection and diffusion, given by the Peclet number for the face, Pe_f:

$$\mathrm{Pe}_f = \frac{C_f}{D_f} \qquad \text{(D-10)}$$

where: C_f is the convection coefficient at face f;

D_f is the diffusion coefficient at face f; and

$f = n, s, e, w$.

If $|\mathrm{Pe}_f| > 2$, convection dominates diffusion and upwind differencing is used, and when $|\mathrm{Pe}_f| \leq 2$, diffusion becomes important and central differencing is used. This convention gives the following discretisation of the convection term.

$$\int_S \rho u_j \phi n_j dS = \left(\left\langle 0, D_e - \frac{1}{2}C_e \right\rangle + \langle 0, -C_e \rangle\right)\phi_E + \left(\left\langle 0, D_w - \frac{1}{2}C_w \right\rangle + \langle 0, C_w \rangle\right)\phi_W$$

$$+\left(\left\langle 0, D_n - \frac{1}{2}C_n \right\rangle + \langle 0, -C_n \rangle\right)\phi_N + \left(\left\langle 0, D_s - \frac{1}{2}C_s \right\rangle + \langle 0, C_s \rangle\right)\phi_S \qquad \text{(D-11)}$$

Although the hybrid differencing scheme is robust, it can cause *false diffusion* on coarse grids when the Peclet number is high and the flow is oblique to the mesh. This can be illustrated by considering the case in Figure D.2 where two adjacent jets of fluid, one hot and the other cold, enter at 45° to a uniform mesh and the diffusion, Γ_ϕ, *is set to zero.* The resulting flow field should have a temperature of 100 above the diagonal through the bottom left-hand corner, and 0 below, since there should be no diffusion across the interface of the jets. At high Peclet number, upwind differencing is used which gives, $\phi_P = 0.5\phi_W + 0.5\phi_S$. This gives the temperature field shown in Figure D.2, which is clearly not accurate for the zero diffusion case considered. This phenomenon is known as *false diffusion* or *numerical diffusion.*

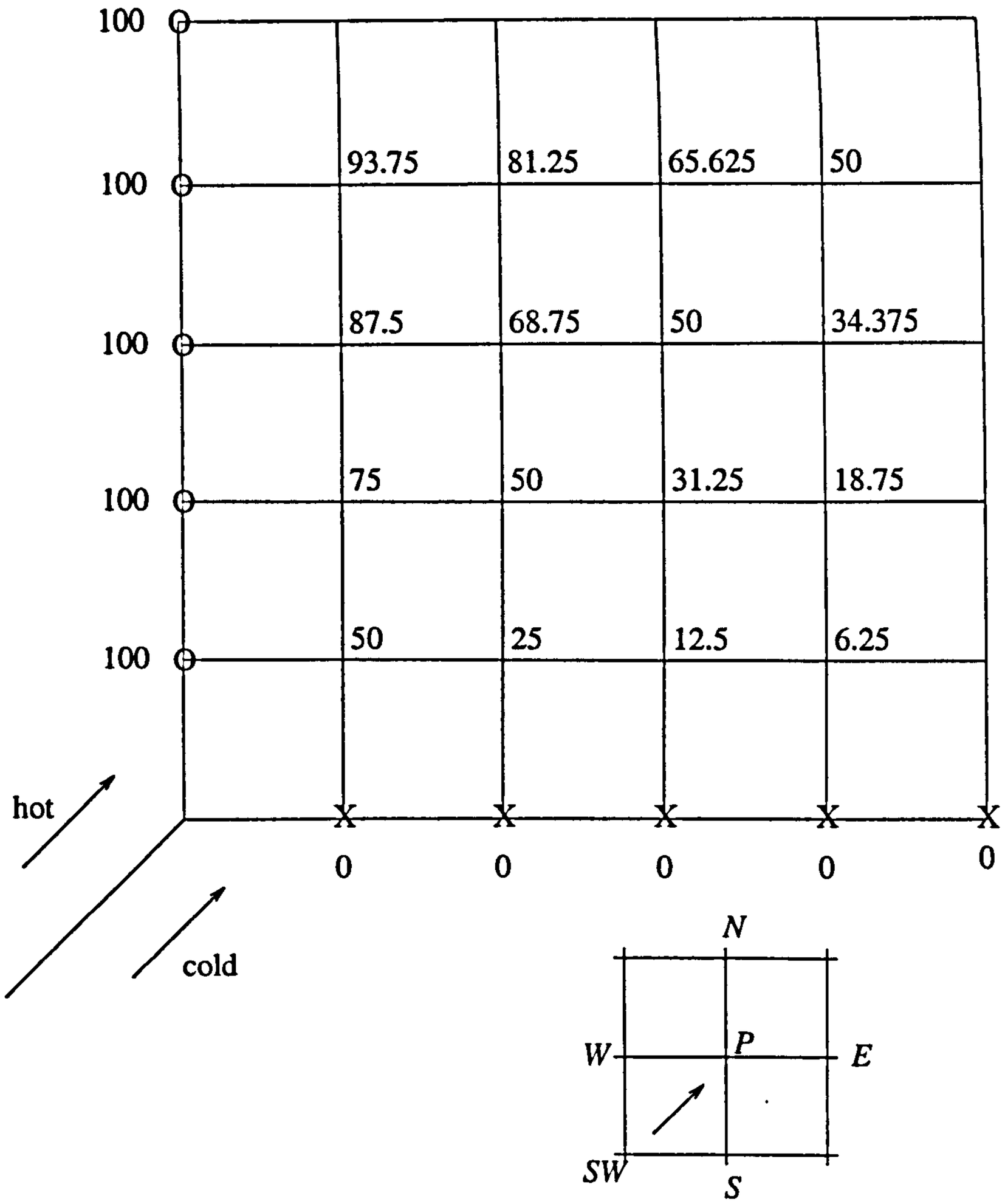

Figure D.2 False diffusion on a uniform mesh at 45° to the flow (after Patankar (1980)).

False diffusion is caused by treating the flow across each control face as locally one-dimensional. For example, in the inset of Figure D.2, the value of ϕ convected by the oblique flow to node *P* actually comes from the *SW* point, but is represented by the two one dimensional components from the *W* and the *S* nodes.

False diffusion is avoided either by aligning the mesh with the flow (often an impractical task), or by making the mesh sufficiently fine so that false diffusion becomes insignificant.

D.3.4 The Source Term

Following Patankar's recommendation (Patankar (1980) and (1981)), the source term is discretised as follows:

$$\int_V S_\phi dV = \overline{S_\phi}\Delta V \tag{D-12}$$

where ΔV is the volume of the control volume and $\overline{S_\phi}$ is the average value of S_ϕ throughout the volume.

This poses no problem provided $\overline{S_\phi}$ is known, however, in many cases, the source term depends on ϕ. It is therefore beneficial to make the term 'at least nominally linear' (Patankar (1980)) by expressing it as:

$$\overline{S_\phi}\Delta V = \left(S_{\phi_C} + S_{\phi_P}\phi_P\right)\Delta V \tag{D-13}$$

The values of S_{ϕ_C} and S_{ϕ_P} should be chosen very carefully if the solution procedure is to succeed (see the four rules of Patankar, (1980)). The most important point to note is that S_{ϕ_P} should be non-positive.

D.3.5 The Final Discretised Equation

Using hybrid differencing for the convection term, the discretised equation for the general differential equation (Eq. (D-1)), can be written as follows:

$$a_P\phi_P = a_E\phi_E + a_W\phi_W + a_N\phi_N + a_S\phi_S + S_{\phi_C}\Delta V \tag{D-14}$$

where: $a_E = \left\langle 0, D_e - \frac{1}{2}|C_e| \right\rangle + \langle 0, -C_e \rangle$;

$$a_W = \left\langle 0, D_w - \frac{1}{2}|C_w| \right\rangle + \langle 0, C_w \rangle;$$

$$a_N = \left\langle 0, D_n - \frac{1}{2}|C_n| \right\rangle + \langle 0, -C_n \rangle;$$

$$a_S = \left\langle 0, D_s - \frac{1}{2}|C_s| \right\rangle + \langle 0, C_s \rangle; \text{ and}$$

$$a_P = a_E + a_W + a_N + a_S - S_{\phi_P}\Delta V \tag{D-15}$$

Equations (D-14) and (D-15) can be written more compactly as:

$$\left(\sum_{nb} a_{nb} - S_{\phi_P}\Delta V\right)\phi_P = \sum_{nb} a_{nb}\phi_{nb} + S_{\phi_C}\Delta V \tag{D-16}$$

and

$$a_P = \sum_{nb} a_{nb} - S_{\phi_P}\Delta V \tag{D-17}$$

respectively, where *nb* sums over all neighbours.

In an attempt to aid convergence, CFX enhances a_P in Equation (D-17) by adding the discretised form of the continuity equation to give:

$$a_P = \sum_{nbi} a_{nb} - S_{\phi_P}\Delta V + C_e - C_w + C_n - C_s \tag{D-18}$$

Recall from section D.3.3.1 that in a converged solution the additional terms in Equation (D-18) should sum to zero yielding Equation (D-17) as originally derived. Arranging a_P in the form of Equation (D-18) has the advantage of enhancing the diagonal of the solution matrix (see §D.7.2) which aids convergence.

It is a simple matter to conduct the above analysis for a three dimensional control volume. This again gives Equation (D-16) but includes the *T*op and the *B*ottom neighbours in the *nb* summation. The extra coefficients are given by:

$$a_T = \left\langle 0, D_t - \frac{1}{2}\left|C_t\right|\right\rangle + \left\langle 0, -C_t\right\rangle$$

$$a_B = \left\langle 0, D_b - \frac{1}{2}\left|C_b\right|\right\rangle + \left\langle 0, C_b\right\rangle$$

and Equation (D-18) becomes:

$$a_P = \sum_{nb} a_{nb} - S_{\phi_P}\Delta V + C_e - C_w + C_n - C_s + C_t - C_b \tag{D-19}$$

This convection coefficient is then used in the general matrix equation (D-20):

$$a_p\phi_p - \sum_{nb} a_{nb}\phi_{nb} = S_{\phi_C}\Delta V \tag{D-20}$$

Discretised equations like Equation (D-16) are formed for each of the scalar transport equations, (*H*, *k*, and ε). Pressure and velocity are treated differently.

D.4 Calculation of Pressure and Velocity

D.4.1 Pressure-Velocity Coupling

Pressure does not satisfy a transport equation and is therefore treated differently to the foregoing explanation. Pressure is given indirectly by the continuity equation in that when the correct pressure is substituted into the momentum equations, the resulting velocity field satisfies mass continuity. Therefore, an algorithm coupling velocity and pressure is employed in which a guessed pressure field is used to give values for the velocity field which when substituted into the continuity equation gives a *pressure correction*. The guessed pressure can then be updated and the process repeated until satisfactory values for pressure and velocity are obtained.

Consider the discretisation of the momentum equation over the control volume shown in Figure D.1.

$$a_P^i u_P^i = \sum_{nb} a_{nb}^i u_{nb}^i + S_c \Delta V \tag{D-21}$$

where $a_P^i = \sum_{nb} a_{nb}^i - S_P \Delta V$

No summation is intended by the repeated *i*, this is simply an indicator of which momentum equation is being considered.

From Table D.1, it is found that the source term S_c is given by:

$$S_c = -\frac{\partial p_0}{\partial x_j}\delta_{ij} + \frac{\partial}{\partial x_j}\left(\mu_{eff}\frac{\partial u_i}{\partial x_j}\right) + \rho g_i \tag{D-22}$$

It is inconvenient to leave the pressure gradient as part of the source term since pressure is one of the variables to be calculated. It is therefore separated out to give

$$a_P^i u_P^i = \sum_{nb} a_{nb}^i u_{nb}^i + S_c' \Delta V - \frac{\partial p_0}{\partial x_i} \Delta V \qquad \text{(D-23)}$$

where $S_c' = S_c + \dfrac{\partial p_0}{\partial x_i}$

The pressure term is discretised using central differencing, i.e.

$$(p_o)_e = \frac{(p_o)_E + (p_o)_P}{2},\ (p_o)_w = \frac{(p_o)_W + (p_o)_P}{2},\ (p_o)_n = \frac{(p_o)_N + (p_o)_P}{2},\ \text{etc.}$$

So the discretised momentum equation becomes:

$$a_P^i u_P^i = \sum_{nb} a_{nb}^i u_{nb}^i + S_c' \Delta V - \left((p_o)_{N_1} - (p_o)_{N_2}\right)\Delta A \qquad \text{(D-24)}$$

where N_1 and N_2 are the nodes either side of P in the direction of the momentum equation being considered, for example, in the *u*-momentum equation, $N_1 = E$, $N_2 = W$, and ΔA is the area of the face perpendicular to the *u* direction.

This formulation of the pressure field can give rise to the 'chequerboard' pressure field effect (Patankar (1980)). This occurs because Equation (D-24) contains the pressures at *alternate* grid nodes rather than *adjacent* grid nodes. This means, a chequerboard pressure field such as that shown in Figure D.3, would be interpreted as a *uniform* field by the discretised momentum equation.

100	300	100	300	100	300
5	27	5	27	5	27
100	300	100	300	100	300
5	27	5	27	5	27
100	300	100	300	100	300

Figure D.3 A 2D chequerboard pressure field (after Patankar (1980)).

A similar problem can occur when discretising the continuity equation as follows:

$$\int_V \frac{\partial}{\partial x_j}(\rho u_j)dV = 0$$

$$\Rightarrow \int_S \rho u_j dA = 0$$

$$\Rightarrow \rho u_e A_e - \rho u_w A_w + \rho u_n A_n - \rho u_s A_s + \rho u_t A_t - \rho u_b A_b = 0$$

$$\Rightarrow C_e - C_w + C_n - C_s + C_t - C_b = 0 \qquad \text{(D-25)}$$

The discretised equation involves velocities at cell faces. If central differencing is used to calculate these, a chequerboard velocity field could result.

These phenomena are clearly unrealistic and must be avoided. Many codes, such as FLUENT and PHOENICS, deal with this problem by using a staggered grid (§D.2). Instead, CFX uses a co-located grid in which all variables are calculated at cell centres, and avoids velocity-pressure decoupling by using the Rhie Chow algorithm (Rhie and Chow (1983)) to interpolate the velocities calculated at the cell centres to the cell faces (§D.6).

D.4.2 Pressure Correction Algorithm

Equation (D-23) will now be written as follows for brevity.

$$a_P^i u_P^i = \sum_{nb} a_{nb}^i u_{nb}^i + S_c' \Delta V - f(p) \tag{D-26}$$

All iterative techniques require variables to have initial values before they can begin. Suppose p^* is the initial guess to the pressure field, then

$$p = p^* + p' \tag{D-27}$$

where p' is the pressure required to correct the guess to the true solution[1], p.

Substituting the guessed pressure field into Equation (D-26) yields the following, in which u^{i*} is the initial guess of the velocity field and has the same form as Equation (D-27).

$$a_P^i u_P^{i*} = \sum_{nb} a_{nb}^i u_{nb}^{i*} + S_c' \Delta V - f(p^*) \tag{D-28}$$

When substituting the guessed velocity field into the discretised continuity equation (Eq. D-25), an error m_P results:

$$m_P = C_e^* - C_w^* + C_n^* - C_s^* + C_t^* - C_b^*. \tag{D-29}$$

m_P can be thought of as a source of mass that must be annihilated.

It is now necessary to improve the guessed pressure field, p^*, so that the velocity field moves closer to the real solution (given by the satisfaction of the continuity equation). This is done using a *pressure correction algorithm* which operates by iteratively updating the guessed pressure and velocity fields as follows.

Consider the difference between equations (D-28) and (D-26):

$$a_P^i u_P^{i'} = \sum_{nb} a_{nb}^i u_{nb}^{i'} - f(p') \tag{D-30}$$

where the primed terms are corrections to the guessed values (see Eq. (D-27)).

---

[1] The true solution refers to the solution of the *discretised* equation.

This is used to give a velocity correction formula:

$$u_P^{i'} = \gamma \frac{\sum_{nb} a_{nb}^i u_{nb}^{i'}}{a_P^i} - \frac{f(p')}{a_P^i} \qquad \text{(D-31)}$$

In this research the SIMPLEC pressure correction algorithm is used in which $\gamma = 1$. SIMPLEC stands for *Semi-Implicit Method for Pressure-Linked Equations (Consistent approximation)*.

By making the assumption that $u_{nb}^{i'} = u_P^{i'}$, Equation (D-31) can be written:

$$u_P^{i'} = -\frac{1}{a_P^i - \gamma \sum_{nb} a_{nb}^i} f(p') \qquad \text{(D-32)}$$

So the new guesses for the pressure and velocity fields, become:

$$p_P^{**} = p_P^{*} + p_P' \qquad \text{(D-33)}$$

and

$$u_P^{i**} = u_P^{i*} + u_P^{i'} = u_P^{i*} - \frac{1}{a_P^i - \gamma \sum_{nb} a_{nb}^i} f(p') \qquad \text{(D-34)}$$

This new guess for the velocity field is now substituted into the continuity equation (Eq. (D-25)). Using central differencing to approximate $f(p')$, and assuming the velocities at the cell faces have been calculated, this yields the following pressure correction equation:

$$b_P p_P' = \sum_{nb} b_{nb} p_{nb}' - m_P \qquad \text{(D-35)}$$

where: $b_P = \sum_{nb} b_{nb}$

and $b_{nb} = \sum_{k=1}^{3} \frac{1}{a_P^k - \gamma \sum_{nb} a_{nb}^k} \qquad (nb = e, w, n, s, t, b)$

The complete iteration process can be summarised as follows.

1. Set (guess) the initial values for all variables at grid nodes

2. Calculate the convection and diffusion coefficients
3. Use the guessed pressure field to calculate values for the velocity components, u^{i*} (Eq. (D-28))
4. Solve pressure correction equation (Eq. (D-35))
5. Set the new guess for pressure to $p^{**}\left(=p^{*}+p'\right)$
6. Calculate updated values for the velocity components from Equation (D-34)
7. Solve all scalar transport equations (e.g. enthalpy, k, and ε)
8. Use p^{**} as new pressure field, return to step 2 and repeat until a converged solution is obtained.

Steps 3 to 6 form the SIMPLEC algorithm stage of the iteration process.

D.5 Linear Solvers

One cycle of the above procedure represents one *outer iteration* in CFX. The outer iterations represent the coupling between the different variables. At various stages of the outer iteration, the linearised equations that have been developed in this appendix have to be solved. This is done by employing a variety of linear solvers, all of which are based around the same algorithm. When forming these linear equations, it is noticed that the matrix of coefficients has a common, simple form - all the non-zero elements fall along the leading, and two adjacent, diagonals. This enables the use of the *Tri-Diagonal Matrix Algorithm (TDMA)* which adopts a recurrence relation to carry out forward-, and back-, substitution (see Patankar (1980) for more details).

In a one-dimensional problem, the TDMA can be used as it stands to solve the linear equations. However, in two and three dimensions, the TDMA would require huge amounts of data storage and is therefore used in combination with other algorithms. For example, the equations for H , k and ε are solved using a line

solver which considers a line of grid nodes (O) and their neighbours (X) as shown in Figure D.4.

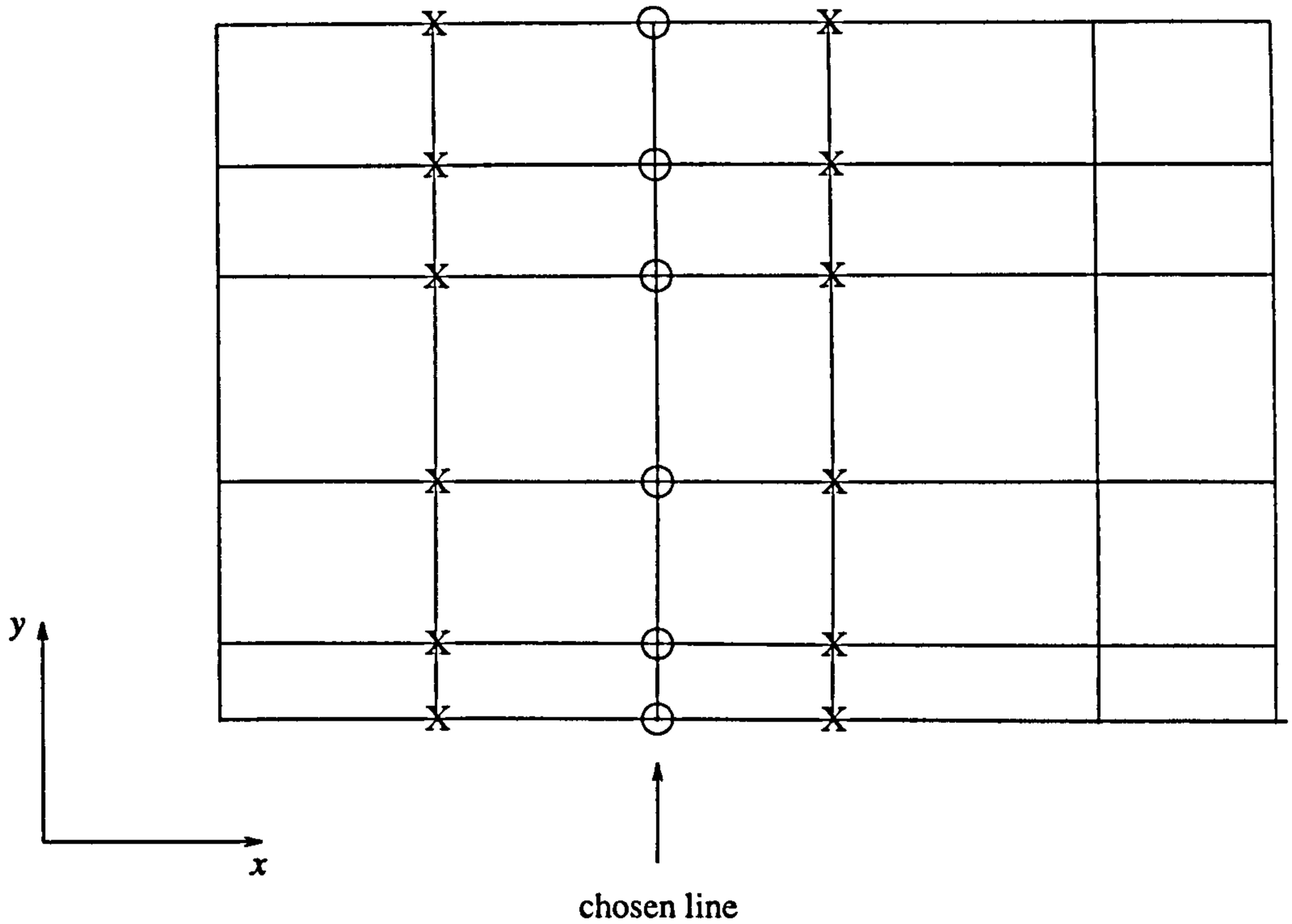

Figure D.4 Representation of the line-by-line method (after Patankar (1980)).

Each combination of X-O-X is then treated as a one-dimensional problem and the TDMA applied. This procedure is carried out for all lines parallel to the *y*-axis, after which those in the *x* and *z* directions can be considered. After several sweeps (*inner iterations*) of the field, the coefficients (a_P, a_E, a_W, etc.) are recalculated and the linear solver executed again to obtain better estimates of the dependent variables. Inner iterations are repeated until either the maximum number of inner iterations (MAXI) is attained, or until the residual reduction factor (RDFC) is achieved, whichever occurs first. The residual reduction factor after *n* iterations is the ratio of the residual (error in the linear equation) after *n* iterations to that when the solver was entered. The linear equation solvers used, along with the default MAXI and RDFC values are shown in Table D.2.

Table D.2 Details of linear equation solvers used for each equation.

Equation	Method	MAXI	RDFC
u_i	STONE	5	0.25
p	ICCG	30	0.1
H	STONE	30	0.1
k	LINE SOLVER	5	0.25
ε	LINE SOLVER	5	0.25

STONE - Full field Stone's method

ICCG - Preconditioned conjugate gradients

LINE SOLVER - Line relaxation

Note the high value of MAXI and RDFC for p and H, reflecting the computational effort necessary to obtain satisfactory solutions to these equations. The stringent value on H is only used in buoyancy-driven flows, otherwise, the same values as k and ε are used.

For more details regarding the linear solvers, interested readers should consult either Jones (1985) or Stone (1968).

D.6 Rhie Chow Interpolation

There still remains the task of calculating the velocity components at the control volume faces (see Equation (D-25)) in such a way as to avoid any chequerboard pressure or velocity fields. This is done using the Rhie Chow interpolation algorithm (Rhie and Chow (1983)).

Consider the discretised momentum equations at the grid *nodes* P and E (Fig. D.1), which can be written in the following general form (c.f. Eq. (D-26)):

$$u_P + [Bf(p)]_P = [Au]_P + S_P \qquad \text{(D-36)}$$

$$u_E + [Bf(p)]_E = [Au]_E + S_E \qquad \text{(D-37)}$$

Suppose there exists a discretised momentum equation at the cell face between grid nodes P and E. This may be assumed to have a similar form:

$$u_e + [Bf(p)]_e = [Au]_e + S_e \qquad \text{(D-38)}$$

The Rhie Chow methodology uses the solutions from equations (D-36) and (D-37) to approximate the solutions to Equation (D-38) as follows.

Suppose the right-hand-side of Equation (D-38) is given by the average of the corresponding terms of equations (D-36) and (D-37) so

$$u_e + \left[Bf(p)\right]_e = \overline{\left[Au\right]}_e + \overline{S_e} \tag{D-39}$$

The right-hand-side of (D-39) can then be given by the average left-hand-sides of equations (D-36) and (D-37):

$$u_e + \left[Bf(p)\right]_e = \overline{\left[Au\right]}_e + \overline{S_e} = \overline{u_e} + \overline{\left[Bf(p)\right]}_e \tag{D-40}$$

$$\Rightarrow \qquad u_e = \overline{u_e} + \overline{\left[Bf(p)\right]}_e - \left[Bf(p)\right]_e \tag{D-41}$$

The algorithm then assumes:

$$\overline{\left[Bf(p)\right]}_e = \overline{B_e}\,\overline{\left[f(p)\right]}_e \text{ and } \overline{B_e} \cong B_e$$

so the Rhie Chow interpolation formula can be written:

$$u_e = \overline{u_e} + \overline{B_e}\left(\overline{\left[f(p)\right]}_e - \left[f(p)\right]_e\right) \tag{D-42}$$

It can be shown (CFDS (1995)) that after velocity corrections have been formed, although the velocities at the cell faces satisfy mass conservation, those at the cell centres do not. These errors are called Rhie Chow errors and are normally small except in cases where there are discontinuities in pressure or the pressure gradient. Such situations may arise when the pressure gradient has to balance a strongly varying body force. This may be relevant in this research close to heat sources where there are large gradients in temperature.

These potential problems are overcome by employing an *improved Rhie Chow* algorithm. Here, the pressure gradient terms in the original algorithm are modified to include the body force term, B_i. This is done by replacing the, possibly *discontinuous* quantity, $-\frac{\partial p}{\partial x_i}$, with the *smooth* quantity, $B_i - \frac{\partial p}{\partial x_i}$.

The improved Rhie Chow algorithm is used throughout this research.

D.7 Control of the Iteration Process

D.7.1 Monitoring the Solution Process

Most CFD codes offer numerical methods for controlling the iteration process. These help to determine: the rate at which the solution is approached (rate of convergence); the stability of a solution; and whether indeed a solution is approached at all. In order to be capable of doing this, the user must have some interaction with the iteration process. This is offered via two interactive plots in CFX.

The first is a plot of the residuals, i.e. the error in each governing equation after each iteration. The residual, R_ϕ, is given by the difference between the left- and right- hand sides of Equation (D-16):

$$R_\phi = \sum_{nb} a_{nb}\phi_{nb} + S_{\phi_C}\Delta V - \left(\sum_{nb} a_{nb} - S_{\phi_P}\right)\phi_P \qquad \text{(D-43)}$$

For each equation, the magnitudes of the residuals are summed throughout the whole domain (one for each cell).

The second graph is a plot of the absolute values of the variables, (u_i, p, k, ε, H, and T), at some user defined monitoring point, after each iteration. Careful consideration should be given to the location of the monitoring point so that as much information can be gleaned from the absolute values as possible.

D.7.2 Controlling the Outer Iteration

Control of the outer iteration is possible by *under-relaxation*. This is used to control the amount by which a particular variable changes between iterations and in doing so, can help avoid possible divergence (movement *away* from the solution). Consider the following rearrangement of the final discretised equation (Eq. (D-16)):

$$\phi_P = \frac{\sum_{nb} a_{nb}\phi_{nb} + S_{\phi_C}\Delta V}{\left(\sum_{nb} a_{nb} - S_{\phi_P}\Delta V\right)}$$

$$= \phi_P^0 + \left[\frac{\sum_{nb} a_{nb}\phi_{nb} + S_{\phi_C}\Delta V}{\left(\sum_{nb} a_{nb} - S_{\phi_P}\Delta V\right)} - \phi_P^0\right] \qquad \text{(D-44)}$$

where ϕ_P^0 is the value of ϕ_P from the previous iteration and the term in the square brackets represents the change in ϕ_P produced by the current iteration. This change can be reduced by applying an *under-relaxation factor*, URF, $(0 < \text{URF} < 1)$ as follows:

$$\phi_P^r = \phi_P^0 + \text{URF}\left[\frac{\sum_{nb} a_{nb}\phi_{nb} + S_{\phi_C}\Delta V}{\left(\sum_{nb} a_{nb} - S_{\phi_P}\Delta V\right)} - \phi_P^0\right] \qquad \text{(D-45)}$$

where ϕ_P^r is the under-relaxed value of ϕ_P. This has the effect of making the solution matrix more *diagonally dominant*, which makes the set of solution equations more stable and increases the chance of convergence rather than divergence. The optimum value of α for each equation depends on the nature of the flow. However, most CFD codes do provide the user with a set of default values which are suitable for a wide range of flows. The values used in CFX are given in Table D.3.

Table D.3 Default under-relaxation factors used in CFX when implementing the SIMPLEC algorithm.

Variable	URF
u_i	0.65
p	1.0
H	0.7
k	0.7
ε	0.7
M_b	1.0

Note that pressure does not require any under-relaxation. This is because the SIMPLEC algorithm does not neglect the first term on the right-hand-side of Equation (D-31) (unlike the SIMPLE pressure correction algorithm, for example, where $\gamma = 0$ is used), and is thus sufficiently accurate so as not to require any under-relaxation to control exaggerated pressure corrections.

In some cases, despite the use of under-relaxation, it is still difficult to obtain convergence. Another type of under-relaxation is *false time-stepping*. This can be used in addition to, or instead of under-relaxation. False time-steps again control the amount by which a variable changes between iterations but does so by using a more physical under-relaxation factor based on the mesh and time scale over which the flow evolves, to give:

$$\alpha = \frac{a_P}{a_P + \frac{\rho V}{\Delta T}} \tag{D-46}$$

where: a_P = convection coefficient (see Eq. (D-19));

ρ = density;

V = cell volume; and

ΔT = false time-step.

Different false time-steps can be applied to different equations with the effect of accelerating or decelerating the rate at which the associated variable approaches its solution. The difficulty in using false time-steps is that a knowledge of the flow is required (prior to simulation) since the value of the time-step should reflect the

time over which the variable evolves. This difficulty can be approached by using the following expression:

$$t_f = \frac{\text{typical cell dimension}}{\text{typical velocity}} \tag{D-47}$$

where the typical cell dimension could be given by $\left(\frac{\text{area of domain}}{\text{number of cells}}\right)^{1/2}$ for a two dimensional flow, and $\left(\frac{\text{volume of domain}}{\text{number of cells}}\right)^{1/3}$ for a three dimensional flow.

D.7.3 Controlling the Inner Iteration

This method of controlling the solution procedure is less powerful, since each time the linear equation solvers are executed, only tentative coefficients are being used. Control is offered via the MAXI and RDFC variables shown in Table D.2. The user has to settle on a balance between drawing the most benefit from the set of coefficients, and carrying out excessive computation that would be based only on tentative coefficients.

In this research, all the default values were used for MAXI and RDFC (Table D.2).

D.7.4 Convergence Criteria

During an ideal solution process, the residuals should decrease, and the absolute variables should approach constant values. Eventually, the residuals will stop falling and possibly oscillate about constant values. This may indeed be a perfectly good solution to the problem. However, even if the variables have settled down to a constant set of values, the errors may still be unacceptably high. Therefore, there is a need for more quantitative criteria.

The residuals for each equation have the units shown in Table D.4. Using these units, it is possible to specify criteria that relate certain flow parameters to the equation residuals. For example, one might specify the following criteria on the enthalpy residual, He_{res}:

$$He_{res} \leq 1\% \text{ total heat into the domain (Watts)} \tag{D-48}$$

Table D.4 Units of residuals for each equation.

Equation	Units
Momentum	Kgm/s^2
Continuity	Kg/s
k	Kgm^2/s^3
ε	Kgm^2/s^4
Enthalpy	Kgm^2/s^3 (Watts)

D.8 Coordinate Transformation

Although the user of a CFD code defines a *physical* grid to capture the various physical phenomena of the flow, the equations are solved internally on a uniform, rectangular grid. Thus a transformation of coordinates is necessary from the 'physical' grid to the 'computational' grid.

The physical grid is based on the body fitted coordinate (BFC) system (§D.2). The basic idea is that the cartesian coordinate system in physical space, $x_i = (x, y, z)$ is transformed to a curvilinear coordinate system in computational space, $\xi_i = (\xi, \eta, \zeta)$ using a curvilinear transformation. The equations are then discretised in the computational space and the boundaries of the flow domain become the surfaces, $\xi_i = \text{constant}$. Although this makes the governing equations more complicated, it enables the boundary conditions to be implemented easily.

In order to transform from the physical coordinate system to the computational one, the chain rule can be used as follows:

$$\frac{\partial \phi}{\partial x_i} = \frac{\partial \xi_j}{\partial x_i}\frac{\partial \phi}{\partial \xi_j} = \overline{J_i^j}\frac{\partial \phi}{\partial \xi_j} \tag{D-49}$$

where ϕ is the dependent variable and $\overline{J_i^j}$ is the *inverse Jacobian matrix.*

To transfer back from the computational space, a similar formula is used involving the Jacobian matrix J_i^j as follows:

$$\frac{\partial \phi}{\partial \xi_i} = \frac{\partial x_j}{\partial \xi_i}\frac{\partial \phi}{\partial x_j} = J_i^j \frac{\partial \phi}{\partial x_j} \tag{D-50}$$

As already mentioned, this transformation makes the governing equations appear very complicated. For this reason, the analysis carried out in this chapter has assumed that the physical grid is a uniform, rectangular grid, so that $x_i = \xi_i$, giving $J_i^j = \overline{J_i^j} = 1$. Therefore the equations in computational space are exactly the same as those in physical space but with x_i replaced with ξ_i.

This may seem an over simplification. However, the curvilinear coordinate transformation only results in extra, more complex, coefficients. All the mathematical ideas and the form of the equations remain the same. However, the following important note should be borne in mind.

D.9 Important Note

CFX uses a *deferred correction* approach whereby conventional linearisation of the source term (Patankar (1980)) is achieved by absorbing the cross-derivative diffusion terms on the off-diagonals, resulting from the coordinate transfer (§D.8), into the source term on the right-hand-side of Equation (D-20). This can cause convergence difficulties on non-orthogonal grids due to poor diagonal dominance.

D.10 Summary of Appendix D

A method for linearising the governing equations of fluid flow using the finite volume approach has been presented. Details of the SIMPLEC algorithm for pressure correction along with the need for the Rhie Chow interpolation algorithm have been discussed. Methods used for solving the linearised equations have been outlined.